OPTICAL SOLAR REFLECTOR DEGRADATION: MODELLING, TESTING AND ORBITAL DATA EVALUATION

Rafael dos Santos Roque

Master's Dissertation of the Graduate Course in Space Engineering and Technology /Space Mechanics and Control, guided by Drs. Valeri Vlassov Vladimirovich, and Rafael Lopes Costa, approved in February 15, 2022.

URL of the original document:
<http://urlib.net/8JMKD3MGP3W34T/46DFE7P>

INPE

São José dos Campos

2022

OPTICAL SOLAR REFLECTOR DEGRADATION: MODELLING, TESTING AND ORBITAL DATA EVALUATION

Rafael dos Santos Roque

Master's Dissertation of the Graduate Course in Space Engineering and Technology /Space Mechanics and Control, guided by Drs. Valeri Vlassov Vladimirovich, and Rafael Lopes Costa, approved in February 15, 2022.

URL of the original document:
<http://urlib.net/8JMKD3MGP3W34T/46DFE7P>

INPE

São José dos Campos

2022

INSTITUTO NACIONAL DE PESQUISAS ESPACIAIS

Serviço de Pós-Graduação - SEPGR

DEFESA FINAL DE DISSERTAÇÃO RAFAEL DOS SANTOS ROQUE
BANCA Nº 015/2022, REG 139726/2019.

No dia 15 de fevereiro de 2022, as 09h, por teleconferência, o(a) aluno(a) mencionado(a) acima defendeu seu trabalho final (apresentação oral seguida de arguição) perante uma Banca Examinadora, cujos membros estão listados abaixo. O(A) aluno(a) foi APROVADO(A) pela Banca Examinadora, por unanimidade, em cumprimento ao requisito exigido para obtenção do Título de Mestre em Engenharia e Tecnologia Espaciais/Mecânica Espacial e Controle. O trabalho precisa da incorporação das correções sugeridas pela Banca e revisão final pelo(s) orientador(es).

Título novo: "Optical Solar Reflector Degradation: Modelling, Testing and Orbital Data Evaluation.".

Membros da Banca:

Dr. Fabiano Luis de Sousa - Presidente - INPE
Dr. Valeri Vlassov Vladimirovich - Orientador – INPE
Dr. Rafael Lopes Costa – Orientador – INPE
Dr. Douglas Felipe da Silva – Membro Interno – INPE
Dr. Gino Genaro – Membro Interno – INPE
Dr. Issamu Muraoka – Membro Interno – INPE
Dr. Elisan dos Santos Magalhães – Membro Externo - ITA

Documento assinado eletronicamente por **Gino Genaro**, **Tecnologista**, em 16/02/2022, às 13:36 (horário oficial de Brasília), com fundamento no § 3º do art. 4º do Decreto nº 10.543, de 13 de novembro de 2020.

Documento assinado eletronicamente por **Valeri Vlassov Vladimirovich**, **Tecnologista**, em 16/02/2022, às 14:06 (horário oficial de Brasília), com fundamento no § 3º do art. 4º do Decreto nº 10.543, de 13 de novembro de 2020.

Documento assinado eletronicamente por **Douglas Felipe da Silva**, **Tecnologista**, em 17/02/2022, às 08:24 (horário oficial de Brasília), com fundamento no § 3º do art. 4º do Decreto nº 10.543, de 13 de novembro de 2020.

Documento assinado eletronicamente por **Rafael Lopes Costa**, **Chefe de Divisão de Mecânica Espacial e Controle**, em 17/02/2022, às 13:40 (horário oficial de Brasília), com fundamento no § 3º do art. 4º do Decreto nº 10.543, de 13 de novembro de 2020.

Documento assinado eletronicamente por **Fabiano Luís de Sousa**, **Tecnologista**, em 17/02/2022, às 15:14 (horário oficial de Brasília), com fundamento no § 3º do art. 4º do Decreto nº 10.543, de 13 de novembro de 2020.

Documento assinado eletronicamente por **Elisan dos santos magalhaes (E)**, **Usuário Externo**, em 22/02/2022, às 08:24 (horário oficial de Brasília), com fundamento no § 3º do art. 4º do Decreto nº 10.543, de 13 de novembro de 2020.

Documento assinado eletronicamente por **Issamu Muraoka (E)**, **Usuário Externo**, em 22/02/2022, às 13:22 (horário oficial de Brasília), com fundamento no § 3º do art. 4º do Decreto nº 10.543, de 13 de novembro de 2020.

A autenticidade deste documento pode ser conferida no site http://sei.mctic.gov.br/verifica.html, informando o código verificador **9478496** e o código CRC **819A7AB0**.

Referência: Processo nº 01340.001119/2022-25								SEI nº 9478496

"Science cannot predict what is going to happen. It can simply calculate the likelihood that something has for happening."

Cesar Lattes

First and foremost to my family, friends and all colleagues that seek changing our world using science and technology.

This work is also dedicated to the memory of the millions of histories interrupted by the COVID-19 pandemic, especially to my cousin Mauricio, aunt Anadir and uncle Donizetti, whose presence has brought so much joy to my life.

ACKNOWLEDGEMENTS

Many people were determinant to the development of the present work, and I am deeply thankful for their help.

Respectfully to all faiths, I want to express my gratitude to God for watching things over and making events progress as good as they could be. Thanks be to God, whoever he/she/it is for you.

A great deal of credit is due to my parents Luiz Celso and Ruth Luciana for believing in me. The huge amounts of support and love they gave me are irreplaceable. To them as to others members of my family, thanks for the patience and comprehension while we faced off the most different challenges in life.

To my esteemed tutors Valeri and Rafael, I appreciate their willingness to accept the mission of enlightening my mind and putting so much energy on it. Thanks a lot for the productive discussions we had and for your enviable patience.

Thanks for the INPE's technicians and technologists that many times made efforts beyond their obligation in order to help me. A special thanks for Luiz Lavras from IEAv for the useful fabrication insights he provided to this research.

Lastly but certainly not least important, to the Brazilian people for the free and good quality education access they made me possible. I will do my best to honor those public funds and collaborate to this country attain the bright future it deserves.

x

ABSTRACT

The orbital environment is very challenging to space vehicles and for this reason, good thermal management is a requirement to make them able to accomplish their intended mission. Satellite thermal control systems (TCS) design has to account for the inherent wear caused by the harsh environment they are immersed into. Their conception needs to provide means for them to endure the intended lifespan of the mission. Space radiators are key components that allow internally produced excess heat to be dissipated to deep space through radiation, whereas limiting the entrance of undesired external heat loads such as from the Sun. Radiators are coated with special finishings that allow selective heat transit. Unfortunately, when degraded those coatings have a reduced capacity for limiting Sun radiation absorption because their optical absorptivity α tends to increase through time. Therefore, TCS design has to account for radiators critically reduced capacity that occurs in end-of-life. For this reason, the use of more stable coatings with reduced degradation rates is convenient to make radiators closely adequate to begin-of-life phase. Such attribute allows power savings with reduced need for electrical heating. OSR materials have these characteristics, but their inherent high fabrication variability makes their performance prediction a difficult task since no single established analysis method that currently exists stands out. An in-flight equipment (OSRA) was conceived, tested for space qualification and then integrated to CBERS 04A as the first Brazilian in-flight experiment for degradation assessment of radiator thermal coatings in real space conditions. Four samples compose the OSRA: white paint, black anodized and two OSR produced at INPE by two alternative technologies. Both analytical simplified nodal model and detailed numerical thermal mathematical model (TMM) with Sinda/Thermal Desktop RADCAD tool have been developed. The analytical model was used to perform preliminary analysis and enhance thermal behaviour understanding of the flight specimen. The detailed TMM was created to reproduce with better precision the assembly geometry and all internal couplings to account for possible heat deviations from basic thermal balance analytical equations. OSRA passed the Thermal Balance Test (TBT). Such TBT was recreated using a dedicated TMM version and then calibrated with the test results. Main internal parameters have been identified. A flight version of the TMM was refined with first telemetry data acquired after CBERS 04A has been launched in December 2019. The problem of α assessment through limited telemetry has revealed to be a more complicated task than anticipated: some unaccounted uncertainties, mostly in complex boundary conditions, that could affect the precision of degradation rates (Δα) identification have been found. Nevertheless, an attempt to quantify Δα for the thermal coatings was done. The results are plausible and explainable. As expected, the OSR Δα are lower than they are for the white paint. The treatment of two-year telemetry data from OSRA confirms exponential character of the degradation curve, i.e. in accordance with similar experiments flown by different satellites over the World.

DEGRADAÇÃO DE MATERIAIS REFLETORES OPTICOS SOLARES: MODELAGEM, TESTES E AVALIAÇÃO DE DADOS DE ÓRBITA

RESUMO

O ambiente de órbita é muito desafiador para veículos espaciais e por isso bom nível de gerenciamento térmico é crucial para permiti-los cumprir sua missão. O design de sistemas de controle térmico (TCS) de satélites precisa levar em conta o desgaste inerente causado pelo ambiente hostil em que são imersos. Sua concepção deve prover meios para que resistam toda a vida útil da missão. Radiadores espaciais são componentes fundamentais que permitem calor em excesso internamente produzido a ser dissipado para o espaço profundo via radiação, enquanto que limita a entrada de cargas térmicas indesejadas como a que vem do Sol. Radiadores são revestidos com acabamentos especiais que os permitem ter capacidade seletiva de trânsito de calor. Infelizmente, quando degradados estes revestimentos apresentam uma capacidade reduzida para limitar absorção de radiação solar porque sua absortividade α tende a aumentar com o tempo. Portanto, o projeto de TCS deve levar em conta a capacidade criticamente reduzida de fim de vida dos radiadores. Por essa razão, o uso de revestimentos mais estáveis com taxas de degradação reduzidas são convenientes para fazer os radiadores mais adequados à condição de início de vida. Tal atributo permite economia de energia devido a necessidade reduzida de aquecimento elétrico. OSRs têm tais características, mas sua grande variabilidade inerente a fabricação faz com que predições acerca da sua performance seja um desafio singular, pois não há unicidade nos métodos de análise estabelecidos ou alguma técnica que se destaque sobre as demais até o momento. Um equipamento de voo (OSRA) foi concebido, testado para qualificação espacial e então integrado ao CBERS 04A como o primeiro experimento de voo brasileiro para avaliação da degradação de revestimentos térmicos em condições espaciais reais. Quatro amostras compões o OSRA: tinta branca, preto anodizado e duas de OSR produzidas no INPE usando de tecnologias diferentes. Ambos modelos analítico simplificado nodal e numérico térmico matemático detalhado (TMM) com a ferramenta Sinda/Thermal Desktop RADCAD foram desenvolvidos. O modelo analítico foi usado para executar análises preliminares e incrementar o entendimento do comportamento térmico do espécime de voo. O TMM detalhado foi criado para reproduzir com melhor precisão a geometria da montagem e todos os acoplamentos internos para poder identificar desvios de calor previstos pelas equações analíticas básicas de balanço térmico. OSRA passou com sucesso pelo teste de balanço térmico (TBT). Tal teste foi recriado em uma versão dedicada do TMM para ser calibrado com resultados do teste. Parâmetros internos principais puderam ser identificados. Uma versão de voo do TMM foi refinada com as primeiras telemetrias disponíveis

após o lançamento do CBERS 04A em Dezembro de 2019. O problema de avaliar Δα através de telemetria limitada se mostrou mais complexo do que antecipado: algumas incertezas que influenciam no comportamento do sistema foram verificadas, principalmente no que se referem a condições de contorno complexas e que vêm a afetar a precisão das taxas de degradação (Δα). Entretanto, uma tentativa de quantificar Δα para os revestimentos térmicos foi feita. Os resultados são plausíveis e explanáveis. Como esperado, Δα para as amostras OSR são menores do que para a tinta branca. Tratamento de dados de 2 anos de telemetria vindas do OSRA confirma o caráter exponencial da curva de degradação, o que está de acordo com experimentos similares já voados por outros satélites do mundo.

Palavras-chave: Controle térmico de satélites. Revestimentos térmicos. Degradação.

LIST OF FIGURES

LIST OF TABLES

LIST OF ACRONYMS AND ABBREVIATIONS

AISI   American Iron and Steel Institute

AO   Atomic Oxygen

AWG   American Wire Gauge

bk   Black sample

BOL   Begin-of-Life

CAST   China Academy of Space Technology

CBERS   China-Brazil Earth Resources Satellite

EOL   End-of-Life

EM   Emergency Mode

E-beam   Electron Beam PVD technique

FD   Finite Difference

FR   NEMA designation for a flame retardant for a composite fiberglass reinforced epoxy material

GA   Genetic Algorithm

GEO   Geo-stationary Orbit

IEAv   Advanced Studies Institute (in Portuguese)

INPE   National Institute for Space Research (in Portuguese)

IR   Infra-red radiation

ISS   International Space Station

LEO   Low Earth Orbit

LIT   Integration and Tests Laboratory (in Portuguese)

MATLAB   Matrix Laboratory Software

MLI   Multi-layer insulation

NASA   National Aeronautics and Space Administration

NEMA   National Electrical Manufacturers Association

o1   First OSR sample

o2   Second OSR sample

OSR   Optical Solar Reflector

OSR1   First OSR sample

OSR2   Second OSR sample

OSRA   Experiment Unit

OSRB	Experiment Electronic auxiliary unit with shunts
PCB	Printed Circuit Board
PM	Payload Module
PVD	Physical Vapour Deposition
radk	Radiative conductance
ref	Reference point
RTV	Room Temperature Vulcanizing Silicone
SID	Information and Documentation Service (in Portuguese)
SINDA	Systems Improved Numerical Differential Analyser
SLPM	Simplified Lumped Parameter Model
SM	Service Module
SN	Serial Number
SSM	Second Surface Mirror
SPG	Graduation Service (in Portuguese)
STK	Satellite Tool Kit
Tt	Orbit period
TBT	Thermal Balance Test
TC	Thermocouple
TCC	Thermal Control Coating
TCS	Thermal Control Subsystem
TDI	Internal thesis and dissertations (in Portuguese)
TD	Thermal Desktop
TH	Thermistor
TMM	Thermal Mathematical Model
TVC	Thermal-Vacuum Chamber
TVT	Thermal-Vacuum Test
UV	Ultra-violet radiation
wt	White Sample

LIST OF SYMBOLS

α	Solar absorptivity, dimensionless
ε	IR Emissivity, dimensionless
σ	Stefan-Boltzmann constant, W/m²K⁴
ϕ_{alb}	Angle related incident albedo radiation coefficient, dimensionless
ϕ_{IR}	Angle related incident Earth emitted IR radiation coefficient, dimensionless
ϕ_S	Angle related incident solar radiation coefficient, dimensionless
A	Area, m²
B	Ratio between reflected solar radiation from Earth and incident solar radiation to it
C_m	Thermal capacity, J/K
D	Earth-Sun distance, AU
dn	Date of the year ordinal number, dimensionless
G_L	Parasitic conductive thermal coupling, W/K
G_R	Parasitic radiative thermal coupling, W/K
K_t	Linear contamination term, dimensionless
p	Time constant, s
q_{alb}	Inbound albedo flux radiation, W/m²
q_E	Inbound Earth's internally produced radiation, W/m²
$q_{IR,Earth}$	Inbound Earth's originated IR radiation, W/m²
q_S	Inbound solar flux radiation, W/m²
Q_{sat}	Heat produced within a spacecraft, W
Q_{out}	Rejected heat from a radiator, W
R_o	TBT experimental curves adjusting parameter, refer to eq. F.1, 1/s
t	Time, s
T	Temperature, K
T_{ref}	Reference temperature, K

T_{TVC} Thermal Vacuum Chamber shroud set temperature

SUMMARY

xxx

1 INTRODUCTION AND LITERATURE REVIEW

Spacecraft design is an engineering field that has to consider various factors influencing the vehicle's overall performance and capability to accomplish an intended mission.

Satellite structure and electronic equipment, for instance, must be kept within appropriate specified temperature limits along its entire lifetime.

The Thermal Control Subsystem (TCS) has huge influence on maintaining the satellite operational because space vehicles are expected to face harsh conditions in flight environment.

Externally mounted elements of TCS have huge exposure to the environment and thus prone to considerable degradation. Thus, to affirm that the TCS design needs to consider aspects that favours external thermal surface materials to conserve stability on their optical properties is no overstatement. Otherwise, the coatings may not provide adequate cooling capacity to the TCS at some point during the mission. This capacity is desired to last all mission time, from begin-of-life (BOL) to end-of-life (EOL).

1.1 Basic theoretical aspects and initial remarks

The TCS is the responsible for heat management and consequent temperature regulation of all satellite components, which shall be sustained within specified operational limits (KARAM, 1998).

While in orbit a satellite is exposed to a hostile thermal environment, which makes it to interact thermally with the surroundings by rejecting heat to deep space. In addition, its behaviour is influenced by incident radiation heat fluxes like direct solar radiation, reflected radiation by Earth (albedo), and terrestrial emitted infrared radiation (IR). Comparable heat exchanges occur exclusively by radiation, since there is no air to allow convection. This is vastly different from what it is observable in ground applications, where convection heat transfer prevails. Figure 1.1 illustrates those interactions.

1

Considering that radiation heat exchange is in general of relatively weaker intensity, it is necessary to optimize thermal control components and assemblies to allow reasonable heat management. One of the most important components for this purpose is the space radiator, which work as a thermal communication window between the vehicle and space environment. Through those devices excess heat from within is rejected towards the exterior (MESEGUER et al., 2012).

Figure 1.1 – Characteristic Thermal Environment in Space.
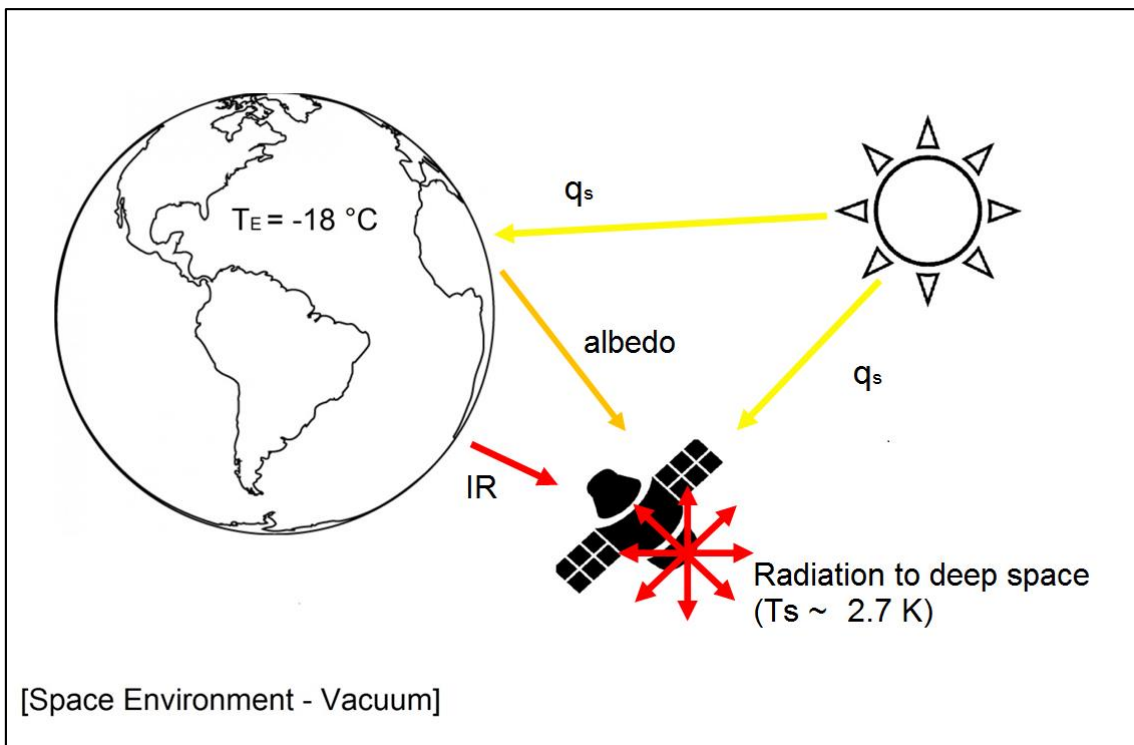
Source: Prepared by the author.

Space radiators make use only of radiation physical phenomenon as means to reject energy to the space environment. Radiation is a heat transfer mode based on emission of energy by electromagnetic waves (MORAN; SHAPIRO, 2006).

External heat fluxes can affect heat rejection capability of the radiator. The net steady state issued power, Q_{out}, rejected from a radiator may be calculated using

2

the Stefan-Boltzmann radiation law for grey bodies. If this Equation also considers undesirable heating from external sources, it becomes:

$$Q_{out} = \varepsilon\sigma AT^4 = Q_{sat} + q_s A + q_{alb}A + q_{IR,Earth}A \qquad (1.1)$$

Where A is the radiator area, ε is the surface emissivity and σ the Stefan-Boltzmann constant.

Satellite radiators may be designed in several configurations, but the simplest ones tend to be prominent. Figure 1.2 shows schematically the simplest and most used type of radiator: it consists of a designed cut opening in the thermal insulation blanket (MLI), making a region of the honeycomb panel exposed. It is required that this exposed area has an appropriate dimension and is finished with an adequate thermal coating with thermo-optical properties. A careful thermal design conception should make it thermally efficient.

Figure 1.2 – Schematics of a Simple Radiator Built on a Satellite Panel.

Source: Prepared by the author.

3
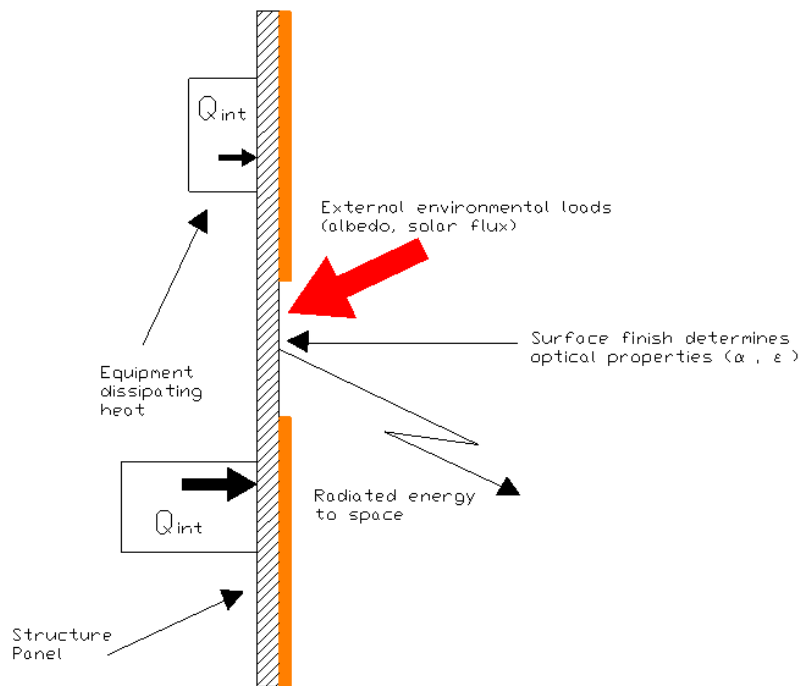
The capability of a surface to absorb irradiated energy in a given wavelength λ is conditioned by its absorptivity in this particular wavelength, α_λ. Referring to Kirchhoff's law, $\alpha_\lambda = \varepsilon_\lambda$. This law can also be applied to a range of wavelengths.

For satellites, the main external heat source comes from solar radiation. Fortunately, the characteristic temperatures of the Sun and those typical in spacecraft are hugely different, wherefore the spectrum is also different.

Related to this fact, black body theory says that, in this case, higher incident and emitted power densities are to be verified for different wavelengths (MESSENGUER et al., 2012). As a result, the emitted thermal radiation by the satellite surface is predominantly in IR band, meanwhile emitted radiation from the Sun has strong intensity in UV and visual bands (INCROPERA et al., 2011), as shown in Figures 1.3 and 1.4.

Using this particular relationship between internal and external heat sources, attempts are made in the industry for covering the area of the radiator facing space with materials featuring high emissivity in IR (ε_{IR}) and low absorptivity in the solar spectrum (α_s). The radiator efficiency is strongly related to the $\alpha_s/\varepsilon_{IR}$ ratio observed for this coating. White paints such as Chemglaze A276, CR107 and MAP SG121FD have corresponding properties and have been widely used in radiator assemblies, including on CBERS and Amazonia-1 satellite Brazilian programs.

The radiators shall be designed to remain effective in the hottest possible thermal scenario. These conditions are represented by the maximum thermal load combination and absorptivity when α is high, that is in EOL.

Figure 1.3 – Solar Irradiated Power Spectrum.
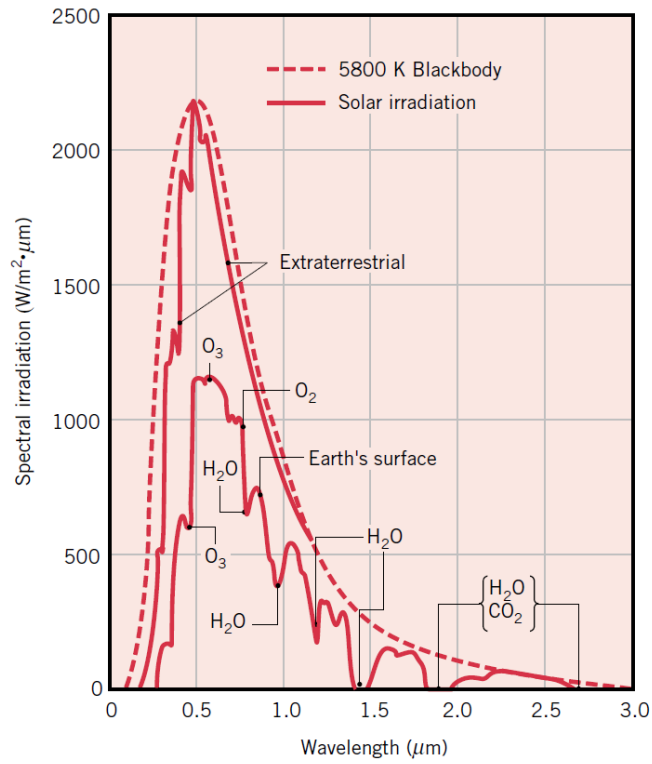
Source: Adapted from Incropera et al. (2011).

Figure 1.4 – Thermal Radiation Wavelengths.
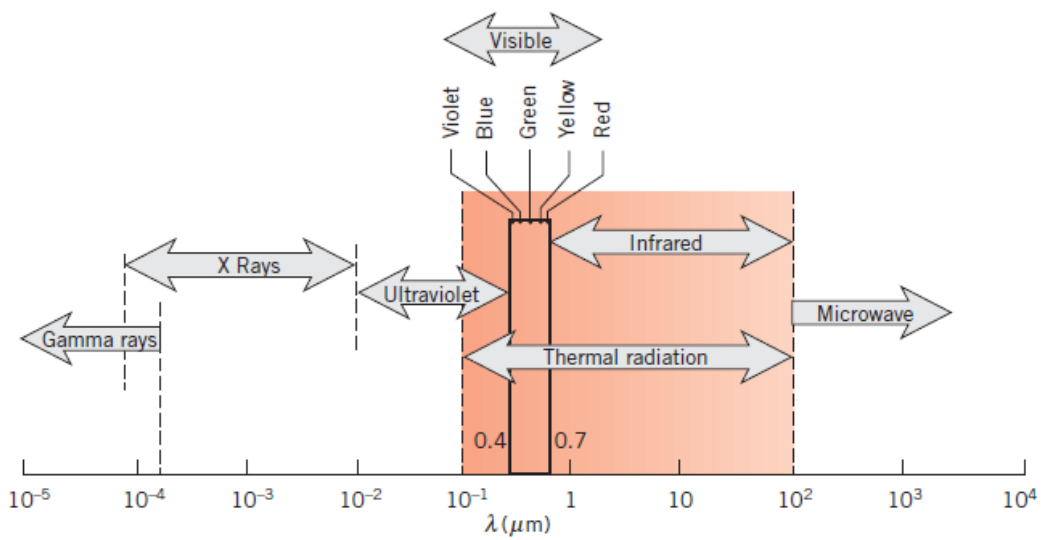
Source: Adapted from Incropera et al. (2011).

Regardless of being passive, radiators that are conceived using white paints reject more energy to space than desired on the first phases of a mission. Thus, such materials results on imposing colder temperatures to spacecraft electronic equipment. White paint usage may create the need to reheat those components as an outcome. Such redundancy consumes valuable on board electric energy. The use of electrical heaters and active control brings more complexity to the system and reduces TCS reliability. When used, paints that have appreciable degradation amplitudes make this effect more pronounced.

Alternatively, provision of adequate surface finishing to radiators is a topic that made different materials to be studied by other researches, and some of their registers can be found in the literature. Optical Solar Reflectors (OSR) are the most important. This technology comprises a class of advanced materials that show promising behaviour to such application.

In a few words, OSR are essentially mirrors that use thin films formed by metal layers over borosilicate or fused silica substrates that are expected to be transparent to the solar radiation and opaque to infrared. Layer configuration is critical to produce intended properties, and OSR are tailored to have low α levels. The technique used for their installation in a radiator surface allows them to be considered Second Surface Mirrors (SSM), and consists of attaching it on the layer deposited face. By this procedure, the aforementioned thin films are sandwiched between the finished surface and substrate. This makes the substrate a protective cover for the assembly, very important for chemical and mechanical stability. A usual configuration is presented in Figure 1.5.

Owing to the advantageous optical stability, radiators constructed using OSR materials allow their area to be minimized, and at the same time sufficient to cope with all mission phases. Due to very low magnitude of solar absorptivity, external solar fluxes over radiator will be mostly reflected and undesirable heating effect will be dumped; therefore stable thermal conditions can be expected likewise, and this is good for many spacecraft parts.

Figure 1.5 – Second Surface Mirror (SSM) Schematics.
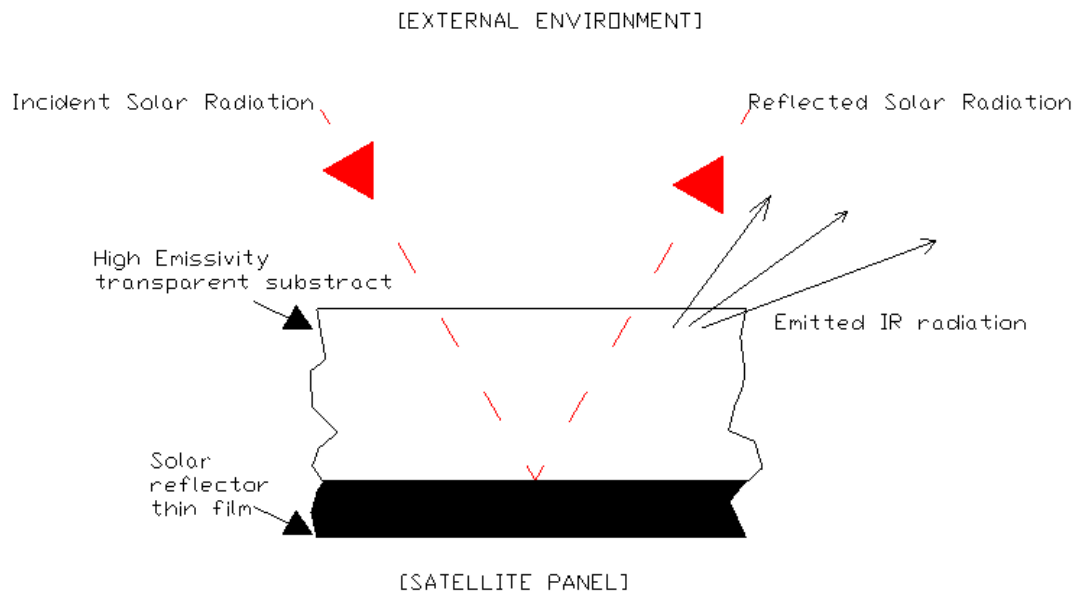
Source: Prepared by the author.

1.2 Literature review

The understanding of radiator coating materials degradation continues to evolve since the first vehicles sent to space. This Session offers a historical perspective of this process.

Factors like erosion caused by residual atmosphere, UV degradation of polymeric chains encountered in the paint materials, chemical interaction with volatiles condensed in the radiators (KARAM, 1998), thermal cycling and others have the potential do double absorptivity until end of life (EOL) is reached (JAWORSKE; KLINE, 2008). This increase in α reduces radiator efficiencies considerably, making satellite temperatures to rise.

Radiators that use white paints have the advantage of lower manufacturing complexity, despite of the inconvenience of having high degradation rates seen in their EOL optical properties. Samples studied going through a mission lifetime have experienced pronounced α increases (SCHAFER; BANNISTER,

1967). In other words, this coating resource is expected to evolve in the direction of higher absorptivity amplitudes.

Gilmore et al. (2002) report experiments in which good stability levels for the OSR optical properties were verified.

Indirect measurements of OSR optical properties seem convenient given that there are no autonomous methods reliable enough for direct measurement of optical properties during long time space flight (NENAROKOMOV et al, 2019).

Testing materials like OSR in actual orbital conditions has proved itself necessary because reliable information related to such coatings is hard to obtain in ground-based tests. This occurs because not all flight conditions are reproducible. Sometimes it is not completely clear which conditions must be accurately simulated (HASEGAWA, 2011). Exposure to facility-induced contamination adds up to the expected difficulties.

Schaefer and Bannister (1967) describe early attempts made to understand coatings response to in-flight degradation. Their work refers to an experiment put aboard satellites of the Pegasus program. A total of three experiments, one for each vehicle, were sent to Low Earth Orbit (LEO) trajectories.

Their proposed equipment, so called 'the thermal sensor package', has many physical resemblances to the one installed on CBERS 04A and is shown in Figures 1.6 to 1.8. It consists of four individual temperature measurement packages mounted in a solid aluminium case of round shape. The authors claim that it had large thermal mass and thus less prone to temperature fluctuations.

Essentially, the intention of Schaefer and Bannister (1967) was to expose a set of four different coated surfaces on the satellites to space environment, a different set each. All sets had a black reference sample. These coated surfaces were AISI 6064 thin aluminium disks that played their role as substrates. They were part of the testing packages mentioned before, which were also composed by titanium support rods.

According to Schaeffer and Bannister (1967), thin disks were adopted to accelerate thermal response. By its turn, the used supports were designed for

maximum strength and minimum thermal conductance. Thermal sensors were stick to backside of the substrate disks, which were also provided with a vapour deposited gold film on the inwards-oriented faces. This gold-coated side was planned to reduce radiation thermal coupling with the aluminium base case. Another thermal sensor has been placed on the case for reference.

Pegasus satellites had a cylindrical shape with two solar array wings. Their main axis Z was oriented to be tangent to the orbital trajectories. Simultaneously the spacecraft had a spinning movement about Z. The experiments were all positioned on the curved face and certainly had been exposed to albedo.

Figure 1.6 – Pegasus Thermal Sensor Case Schematic Top View.
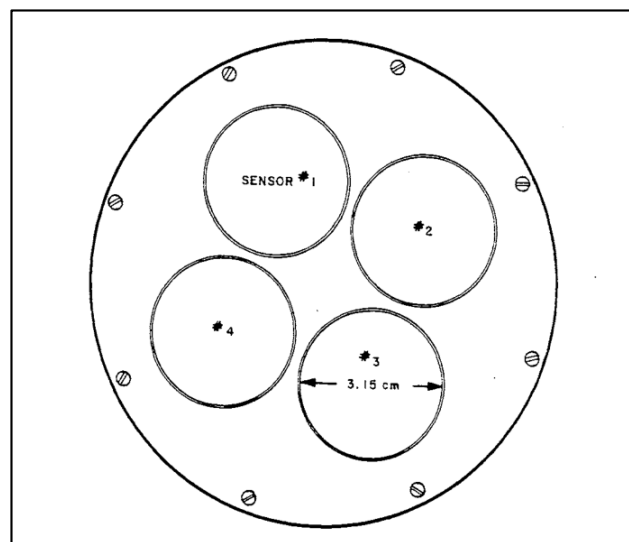
Source: Schaefer and Bannister (1967).

Figure 1.7 – Pegasus Thermal Control Coatings Experiment Package.
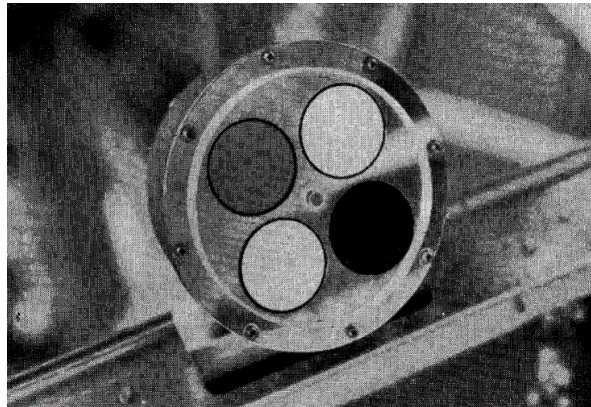
Source: Schaefer and Bannister (1967).

Figure 1.8 – Pegasus Thermal Sensor Schematics.
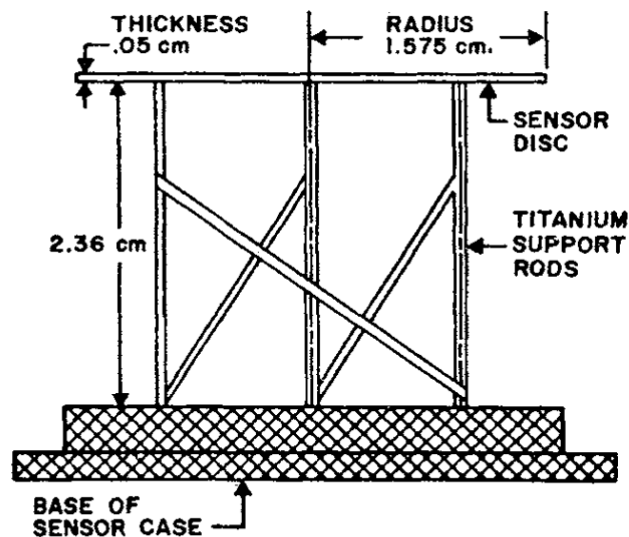
Source: Schaefer and Bannister (1967).

Schaefer and Bannister also claim that the thermal design is one of the most important considerations to a successful mission, thus it is relevant to know how temperatures develop along lifetime. This was done using selected assumptions to be applied in a direct inversion of a balance Equation 1.2, where authors adopt B as the ratio between reflected solar radiation from Earth and incident solar radiation to Earth.

10

$$C_m \frac{dT}{dt} = Q_i + \alpha q_s A + G_L (T_{ref} - T_i) + G_R (T_{ref}^4 - T_i^4) - \varepsilon\sigma A T_i^4 + (A\alpha B q_s + A\varepsilon_{IR} q_E) \qquad (1.2)$$

A noticeable feature was the presence of a term representing the radiative thermal coupling between the case reference point and disks G_R. Their line of thought was first to determine radiative and conductive couplings in ground based thermal cycling tests and then use selected on-orbit temperature data on the balance Equation. As they selected only peak temperatures, $dT/dt = 0$. Besides, the IR radiation emitted from Earth and albedo related terms were considered small enough to be disregarded in the temperature maxima. As the accurate spacecraft attitude was difficult to measure, when dealing with data the incident solar heat flux was determined first by analysing the black reference sample, then other samples data could be evaluated. In other words, the black samples were used as radiometers.

Although smart, Schaefer and Bannister studies leave some unanswered questions. No attempt was mentioned to assess whether the aluminium case temperatures were indeed homogeneous; this is a hypothesis, which is difficult to expect in real orbital conditions. Besides, the researchers assumed that all 4 thermal sensor unities of the 3 experiments flown (12 unities in total) had equal conductive and radiative thermal couplings, which is very unlikely to obtain even with flawless assemblage procedures and perfectly homogeneous materials. In addition to these not-accounted uncertainties, there is an effect of thermal inertia of the 'radiometer': the peak of its temperature does not match the peak of external flux (for nadir pointed attitude).

Another aspect to take into account is that the experiments are not readily reproducible: the solid aluminium case probably made the entire experiment prohibitively heavy, adding thermal inertia which may affect the measurements regardless of the sample disks having small masses and good thermal insulation levels.

The accumulated knowledge of the space environment throughout decades makes easier to question nowadays some of their assumptions. For example, it is known that for LEO trajectories Earth related heat loads are significant (GILMORE et al, 2002). Thus, prior knowledge that the samples were exposed to such loads would allow a more accurate assessment of the errors they were unaware to be including to their calculations. One finding that suggest that this may be case is their report on different degradation curves traced for the same materials. Given that all three spacecraft had very similar orbits, this is not expected.

Millard (1968) proposed an uncertainty analysis derived from the heat balance Equation applicable to a similar experiment. The initial Equation he has proposed is comparable to 1.2 and his subject was an experiment of the OSO 3 satellite, which had an approximately circular LEO orbit. The methodology used in the Equation analyses has common points to the error theory presented by Vuolo (1993). Based on the heat balance Equation, Millard derives mathematical relationships that express functionals resulting from different combinations between the original Equation and its partial derivatives. A graphic analysis for the expected error levels for each variable along orbital positions is also performed. He then complements these useful insights with a suggested iterative procedure intended to identify the most promising orbital points to source data from and calculate the needed optical properties with the least possible error margins per cycle. Unfortunately OSO 3 experienced problems with the recording module and provided only very limited data while in flight.

Curran and Millard (1977) developed another group of experiments in which Millard (1968) uncertainty analysis could be applied to larger amounts of data.

Curran and Millard designed degradation experiments to be included in actual radiators used in a series of 4 satellites, most likely with similar architectures and LEO trajectories. Details on these satellites used are not provided, probably due to their classified nature. As direct comparisons are made between experiments mounted on different satellites, it is reasonable to assume that they share common boundary conditions regarding the equipment installation.

Independently of the free interpretations it may lead to, their work was focused on investigating thermal control coatings (TCC) degradation specifically under satellite-produced contamination, which was the main acting mechanism. For that purpose, the chosen satellites seem to be attractive since their radiators had very cold average temperatures, around 200 K, thereby a preferential contamination condensation point.

Their plan was to assemble calorimetric units within the radiators is such a manner they could evaluate directional tendencies on the contamination related degradation to be observed. They used mainly one calorimetric unit configuration, shown in Figures 1.9 to 1.11, which was their second proposed design and had thermal couplings adjusted based on ground tests. Additionally, they describe partially a 23-node SINDA thermal mathematical model proposed in an attempt to reproduce the orbital data measurements. The amount of data collected on the experiment series was deemed insufficient, but it predicted the temperatures of the most long-lived satellite with remarkable proximity.

An interesting couple of findings by Curran and Millard draw special attention. Firstly, is that long-term data calculated absorptivity values tend to fit well to an exponential Equation as 1.3. The second is that the satellite indigenous produced contaminants vent paths have strong potential to affect radiators performance unevenly. Contamination sensors were included near some of the tested radiators, but the data they collected was not physically plausible.

$$\alpha_s = \alpha_o + (\alpha_m - \alpha_o)(1 - \exp(-t / p)) \tag{1.3}$$

Where p is a sample long-term degradation time constant.

Figure 1.9 – Contamination Focused Experimental Module Prior Installation.
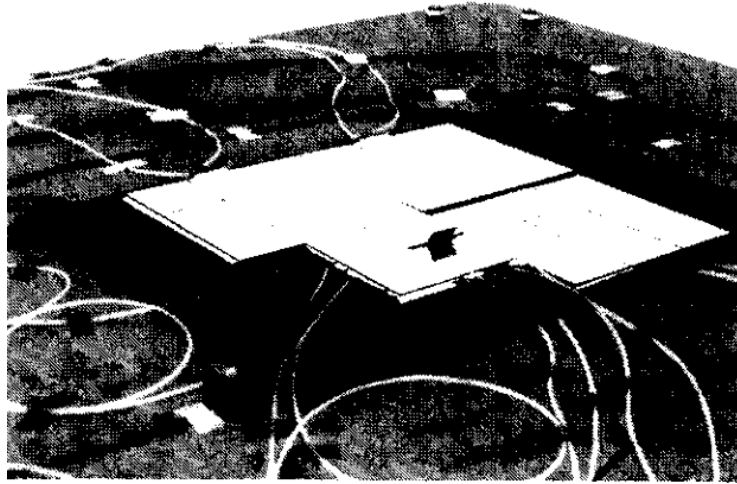
Source: Curran and Millard (1978).

In order to reduce parasitic heat fluxes as much as possible, the authors used fiberglass supports whenever possible instead of aluminium structure (Figure 1.10).

David Hall and Alfred Fote made very prolific efforts on degradation experimentation. That was made possible by using the degradation experiment flown in the SCATHA satellite, from which around 10 years of data could be gathered. Probably, it is one of the degradation experiments that was carried out on the longest timespan. In essence, the SCATHA had a fully experimental payload and described a quasi-GEO orbit (quasi Geosynchronous Earth Orbit).

In one of their first works, Hall and Fote (1980) described their tray based experimental setup, its location on the spacecraft, its construction and some aspects of the testing procedures. Notably, they used a thermal balance Equation like 1.2 as a basis and measured pertinent couplings and thermal capacity using respectively steady-state and transient data of a thermal balance test (TBT). The radiation thermal coupling between points of interest was also considered. Hall and Fote setup is depicted in Figures 1.12 and 1.13.

Figure 1.10 – Contamination Focused Experimental Module Schematics.
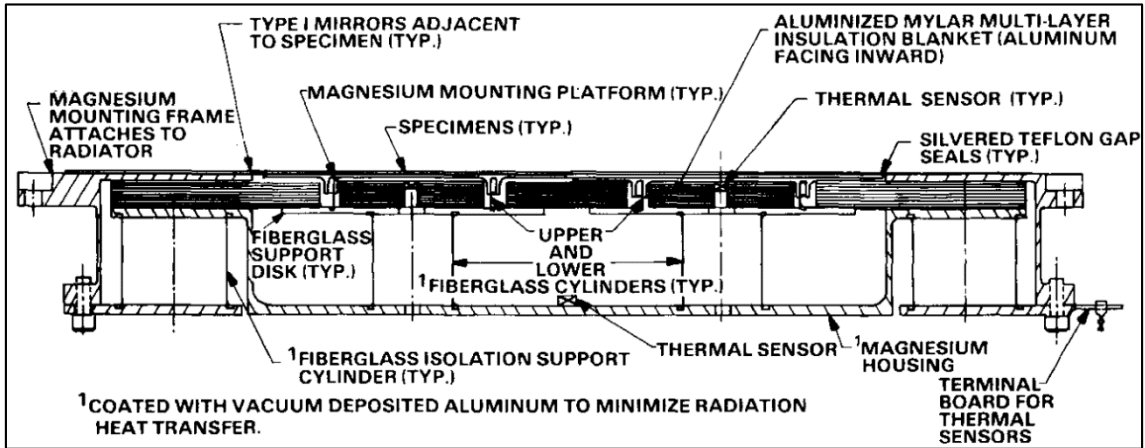
Source: Curran and Millard (1978).

Figure 1.11 – Contamination Focused Experimental Module in a Radiator.
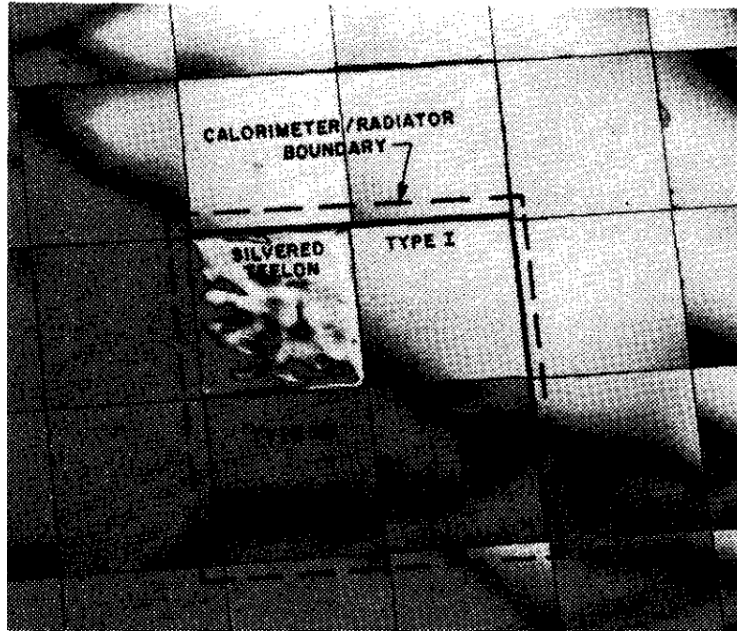
Source: Curran and Millard (1978).

Figure 1.12 – SCATHA TCC degradation tray based experiment.
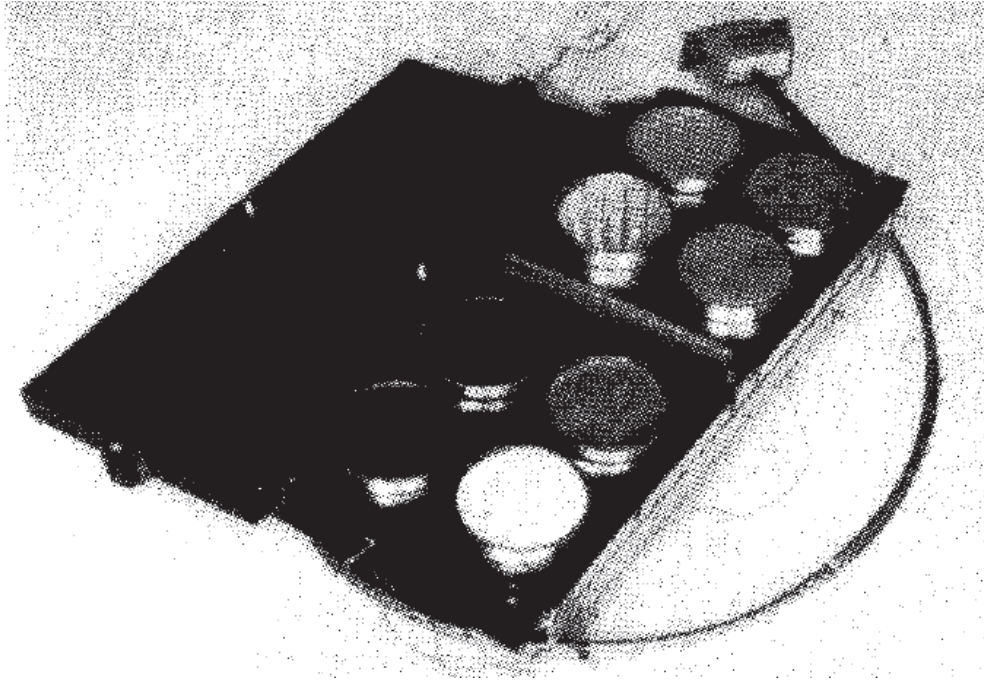
Source: Hall and Fote (1992).

A further contribution by Hall and Fote (1980) is their proposition of an algorithm to find the coatings optical properties, especially the absorptivity. Briefly described, this methodology consists of separating the balance Equation in other two: a non-time dependant and another time-dependent one. If flight data is used to solve them in the described sequence, they claim it is possible to iteratively reach the correct values for the desired properties. This work also presents the calculated values for the first mission years, from which they presume the absorptivity degradation curve is linear.

Figure 1.13 – Locations of MLI2-3/4 TCC Experiments in SCATHA.
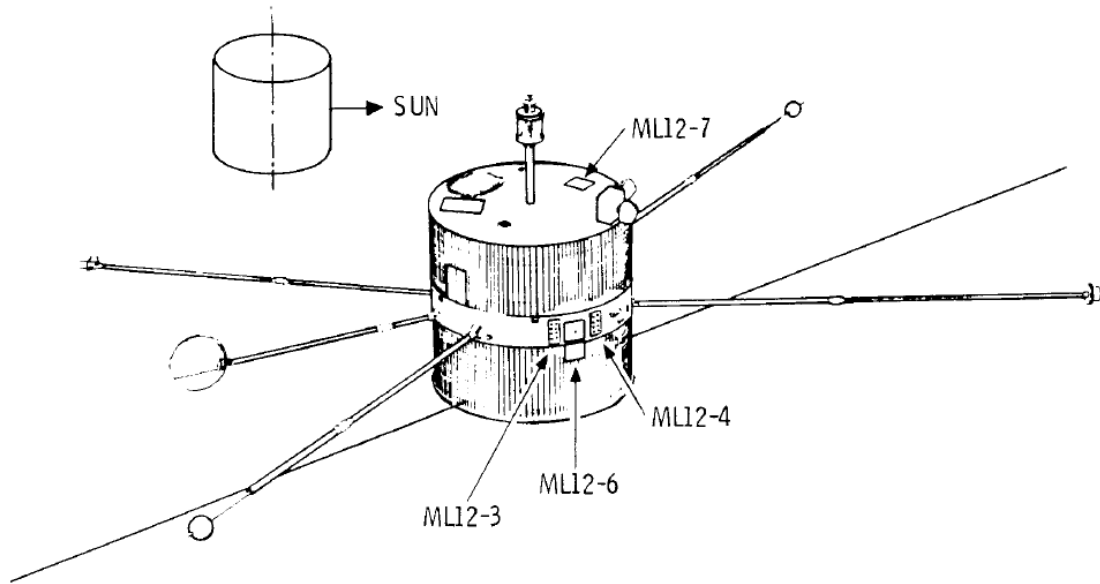
Source: Hall and Fote (1983).

However, Hall and Fote (1983) with further available data had a different view of this curve and at this time they propose that the absorptivity curve fits an exponential law similar to 1.3, but with added linear contamination term K_t as in 1.4.

$$\alpha_s = \alpha_o + Kt + (\alpha_m - \alpha_o)(1 - \exp(-t/p))$$ (1.4)

Finally, Hall and Fote (1992) conclude that for a coating considered space stable, i.e. degraded mainly due to contamination effects and not Space environment conditions, which is installed in an appropriately cleaned spacecraft assembled with space grade materials, a simpler Equation like 1.3 is good enough for a mathematical fit. Optical Solar Reflectors are considered the most stable space coatings.

Hyman (1981) presents his findings with another thermal control coating experiment carried on the COMSTAR satellites, intended for telecommunications and of geosynchronous orbit. He did not use a dedicated experiment, but instrumented OSR radiators attached to beacons of roughly constant heat dissipation. He uses maximum temperature data applied to the thermal balance Equation for direct inversion, but his thermal energy Equation has correction factors of undisclosed origin. A 14-node analytical thermal model has been used to compute partial derivatives estimations and to confirm the previously calculated absorptivity values. Unfortunately, there is no information on how this model was build and the author ultimately considered it inadequate. One remarkable conclusion Hyman draws is that there is evidence of OSR absorptivity deterioration progress depending upon incident radiation angle, i. e. the amount of energy to which the coating is exposed also has its weight in the process, not only the time exposure.

Naegeli (1992) adopted a different approach for OSR radiator degradation measurement that used many internal temperatures of the SPACENET satellites series. These are communications spacecraft and were kept in the geosynchronous orbit. He claims that it is possible to assess the degradation trends of the radiators using a weighted smoothing technique to determine overall satellite temperature mean difference throughout the service life. This is done by comparing internal temperatures in a given time 't' with the immediate post launch behaviour. The weights are defined depending on the intensity of the thermal coupling for a given temperature measurement point has to the studied satellite radiator.

Although this technique seems plausible and very practical to monitor any satellite during usage, it is not clear how other TCS components behaviour, such as thermal insulation blankets degradation, or internal dissipation gradual increasing (due to possible electronic equipment drifts and batteries natural wear) would affect the calculations using the proposed smoothing Equations. Most probably, this method is not applicable to a LEO satellite, which is exposed to transients on a much more frequent time basis.

From his finding, Naegeli concluded that both temperature rising and its related cause, that is the radiator absorptivity increase, occur in an exponential-like curve.

Additionally, he says that sunlight act as a catalytic factor for degradation. In other terms, it not only sums up the contamination degradation but also has the potential to enhance it further.

Lura et al. (1993) describe an experimental method to determine thermal control coatings optical properties using a ground test setup. Biering and Hagelschuer (1996) uses this method to execute a long time ground test to simulate UV radiation degradation only for a set of coatings. Probably due to temperature fluctuations on measured temperatures, they mention that a Kalman filter algorithm was necessary to estimate the coatings optical parameters of interest.

Leet et al. (1995) describe a ground-based degradation test designed in an attempt to simulate the charged particle related degradation of thermal control coating materials. Leet and collaborators studied the particle impingement load that the satellite CRRES was exposed as a reference, aiming to replicate them in a laboratory environment. This was accomplished partially using the AP-8/AE-8 radiation belt models, but the authors claim that low energy particle loads were hard to determine as they vary with the solar activity.

Remaury et al. (2003) briefly describe the principles of a degradation experiment flown in LEO satellite SPOT 2, that shares many similar aspects to the design developed at INPE. Their objective was to verify the degradation not only the behaviour of radiator-destined compounds like SG121FD white paint, but also thermal insulation intended materials. This experiment was named THERME and the temperature data allowed the researchers to verify that the protective coating had an increase that resembles an exponential grown. The value of the data for the radiator intended materials was questionable since the calculated absorptivity increased until satellite mid-life to reduce once again, as it had regenerated itself. By this time, other specimens were flying in SPOT 4 and 5. Another two specimens were planned to fly in HELIOS 2A and in a GEO (Geosynchronous Earth Orbit) satellite referred to as DEMETER.

Reumary et al. (2011) compiled the history of data available from the THERME aging experiment specimens of all mentioned satellites. Their objective was to create insights from the collected data that allow understanding the impact of different factors on degradation, since boundary conditions are different. For example, GEO satellites are not expected to suffer erosion caused by atomic oxygen and this reflects on the degradation curves. As in the newest space vehicles they have used multiple testing subjects, which were installed in different faces, the authors could also evaluate the installation placement impact on degradation.

Feng et al. (2007) describe a ground-based experimental setup prepared to simulate a GEO satellite charged particle scenario. Their analysis aims to understand how particle impingement influences satellite radiator coatings performance. Neutral charge particles were also tested. Similar to Leet et al. (1995), AE-8 radiation model was used to determine how particles were to be collided with the coatings.

Based on this model, an enhancement of particle load was employed to accelerate the ageing experiment. Different modulations of particle impingement were also adopted to reproduce solar activity variations. Nothing was proposed to accelerate UV radiation provoked degradation though. The authors claim that their results were equivalent to 8 years of degradation, found a fit to their data and extrapolated it to a 15 years scenario, so they could compare with flight data available of an unnamed spacecraft. The mathematical rule used for fitting is a second-order exponential similar to Equation 1.5.

$$\alpha_s = W + U.\exp(-t/p_1) + V\exp(-t/p_2) \tag{1.5}$$

Where U, V, W, p_1 and p_2 being fitting time-constant parameters with physical significance to be investigated.

Even though the authors affirm that their test was successful on predicting degradation, the results presented do not seem to support that. Compared to

the flight data available, the degradation observed has huge differences: one of the samples tested ended up with an absorptivity value less than half of that verified in flight.

The described outcome confirms how challenging is to reproduce orbital conditions and makes the described testing methodology questionable. Hasegawa and Kauder (2011), who did a similar experimental study, have also encountered this reduced degradation seen on lab test results.

Anvari et al. (2009) made a case study using a simple numerical model. One small LEO cube shaped satellite model was built on Thermal Desktop Sinda/Fluint, which had the entire zenith oriented face used as a radiator. After different modelled coatings comparison, they concluded that optical stability indeed helps to reduce substantially a satellite overall temperatures at EOL.

At a first glance, Kang et al. (2011) work may seem completely unrelated to space radiators thermal coatings degradation. They study wood optical properties alterations caused by the exposure to the elements, mainly sun radiation. However, they employ an interesting inverse method to do so, and their approach is general enough to be tested in other applications.

In essence, they use the Gauss-Newton iteration to minimize the root mean square differences between a parameter-dependent analytical model and a data-dependent 1D numerical model proposed by the authors.

Regrettably, their work was inconclusive. They credit this outcome to the likely inadequate analytical Equation used. It was proposed using building materials handbooks that do not necessarily reflect the reality of the wood samples considered. Given that wood is very variable in composition, this reasoning may be accurate and thus does not rule out the use of this methodology in other applications.

In what concerns inverse methods, Colaço et al. (2006) made a concise compilation of many inverse methods applied to heat transfer that could be attempted to solve the coating degradation problem. They summarize aspects and explain execution procedures of purely analytical methods, stochastic variants and hybrid techniques. Their work is very rich in references, which they

make to many consolidated authors on the inverse problems area, such as Alifanov (1994) and Özisik (2000).

Liao et al. (2015) have created a method to predict in-orbit performance degradation of thermal control coatings, which is now registered in a filed patent on behalf of the Shanghai Satellite Engineering Research Institute.

Concisely explained, the method referred is based on a simplified form of the balance Equation applied to any in-flight experiment. This Equation form considers Earth emitted IR and albedo effects, but disregards a temperature point of reference and thus the thermal couplings it would have to the samples.

As inputs, it uses only the measured temperatures of the samples and the incident radiation angles of the Sun and albedo. The previously mentioned simplified balance Equation, written in terms of absorptivity, is represented by Equation 1.6 in a simplest way:

$$\alpha_s = \frac{\varepsilon(\sigma T^4 - \phi_{IR} q_{IR})}{\phi_s q_s + \phi_{alb} q_{alb}}$$

(1.6)

Where ϕ_{IR}, ϕ_s and ϕ_{alb} are angle related coefficients to the incident fluxes in the samples that were originated as Earth emitted IR, solar radiation directly from the Sun and solar reflected radiation, respectively.

The inventors advise to obtain four calculated values of α in a daily basis by using peak temperatures. They also suggest to make use of a specific software to determine the orbital dynamics instantaneous radiation applicable angles, for example the Satellite Tool Kit (STK). The daily calculated points put in an α versus t plot should then be fitted to a predefined exponential mathematical law as Equation 1.7. Parameters a, b and c are to be found.

$$\alpha_s(t) = \alpha_s(0) + a\left\{1 - \exp\left[1 - (1 + b.t)^c\right]\right\} \qquad (1.7)$$

Liu et al. (2016) use the above mentioned patented procedure to manipulate satellites temperatures data produced by degradation in-flight experiments. A statistical degradation model based on a Wiener degradation mathematical process has been proposed. It is intended to simulate the degradation curves using incremental amounts of collected data at any point of the spacecraft service life. This approach takes into account the fact that the measurements are subjected to random measurement errors, which were assumed to manifest itself in the same format of a white noise. However, how the transient behaviour of the experiment structure and samples could be tackled remains an open point. Besides, it is not clear how the inevitable parasitic heat couplings between the sample and experiment structure could be accounted for.

Nenakomov et al. (2019) explain in details a numerical algorithm for parameter estimating that determines the needed optical properties for thermal control coatings subjects. In this promising approach, they use the complete form of a heat balance Equation and a coupled analytical orbital dynamics model to predict pertinent radiation angles from the spacecraft attitude.

Piegari and Flory (2018) do a review on space application coating degradation agents. Jaworske and Kline (2008) end-of-life coating analysis seems to support their claims. Miller and Banks (2010) complement such discussions showing photographic evidence gathered during maintenance on the Hubble telescope. Some factors that they mention are the action of atomic oxygen, micrometeorite impacts, presence of contaminants, thermal cycling, ionized particle absorption and UV wearing.

Atomic oxygen (AO) is specially relevant to LEO satellites and due to the high velocity impact on the coatings, is able to remove material through abrasion. In the flight environment, AO may also cause wear by chemically combining with coating material, which is gradually removed away from the spacecraft.

Thermal cycling is a phenomenon that can modify the optical properties of coating materials by either changing the refractive index of translucent solids, like OSR substrates, or by inducing stresses on the thin film deposits that cause cracks. Figures 1.14 and 1.15 illustrate this damage mode.

Figure 1.14 – Cracks Caused by Thermal Cycling Induced Stresses.

Source: Piegari and Flory (2018).

Figure 1.15 – Magnified Cracks Caused by Thermal Cycling.
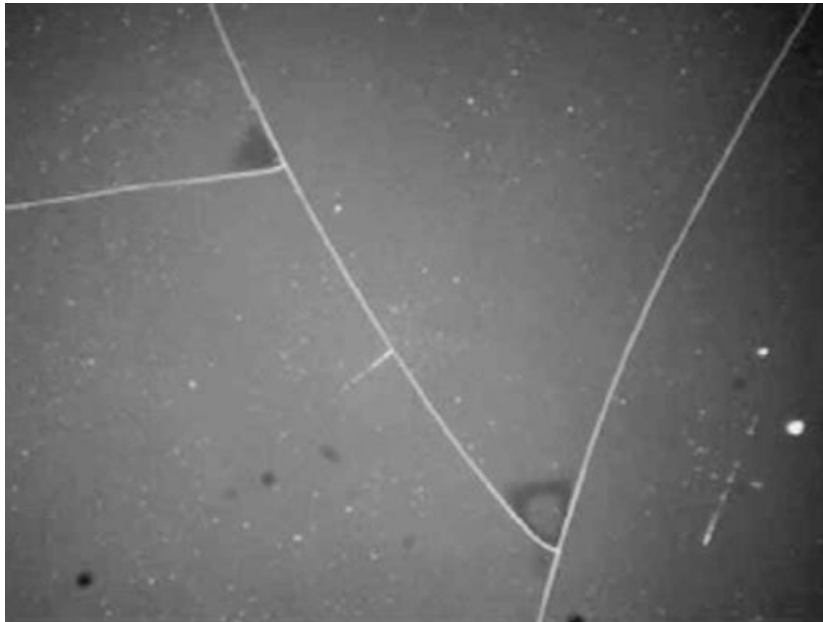
Source: Piegari and Flory (2018).

Piegari and Flory (2018) also mention that long-time exposure to UV radiation can induce change in optical properties of satellite thermal control thin-film devices. Accumulated solar radiation charges may cause translucent material such as the OSR substrates and solar array cover glasses to darken. Another failure mode triggered by UV radiation is the polymerization of organic deposits formed on the coatings. Figure 1.16 shows how a high energy radiation-induced polymerization can produce globules of condensed material that can alter materials optical behaviour.

Micrometeorite impacts should be also a factor taken into account, since the mechanical energy they have may physically damage the coatings. The destructive nature of such events can enhance the action of other degradation mechanisms. For example, a crack on the OSR substrate would expose the silver layer to higher oxidation speeds. Figure 1.17 illustrate the effects of a micrometeorite impact on a silver plate exposed in the International Space

Station (ISS), and its black oxidation areola gives an idea of how detrimental impacts can be.

Figure 1.16 – Deposit of polymerized material in a translucent substrate.
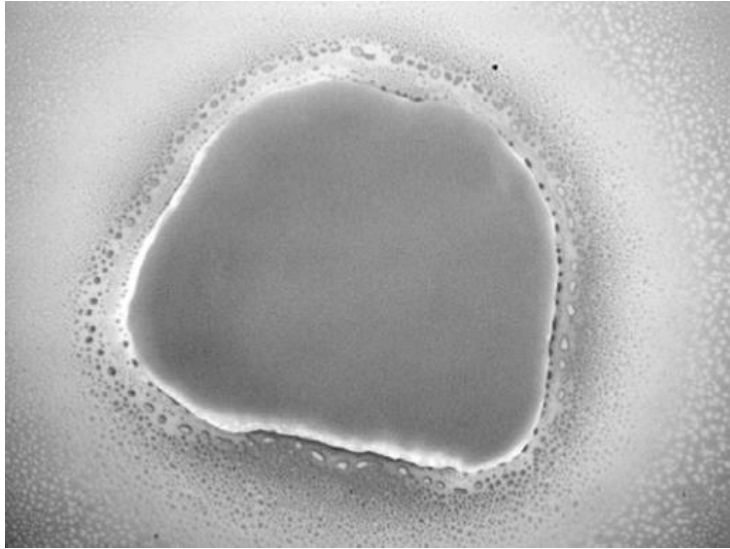
Source: Piegari and Flory (2018).

Figure 1.17 – Micrometeorite impact on an exposed silver tray at ISS.
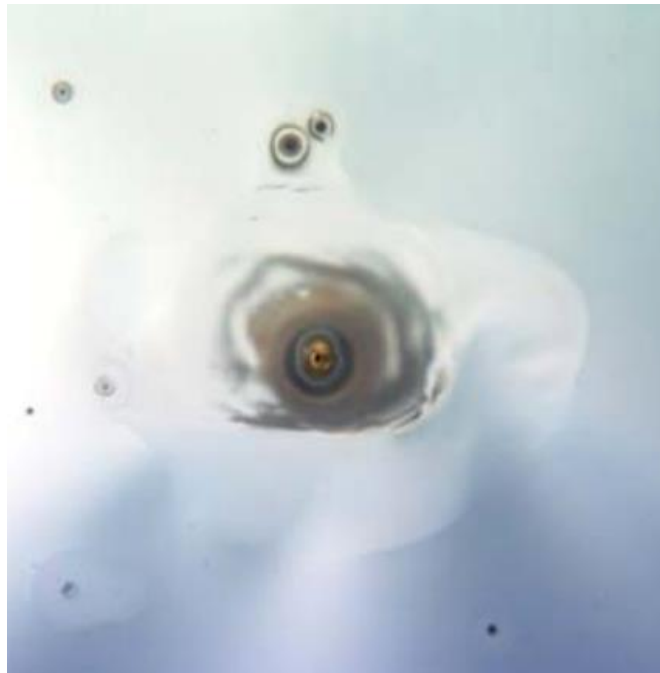
Source: Miller and Banks (2010).

After initial subsidies provided by the literature review, the present work is structured in topics chosen to represent the chronological line of though regarding the theme. Chapter 2 has more information on the aims pursued. Chapter 3 describes the equipment design used for orbit data collection. Chapters 4 and 5 presents details on the thermal testing used for equipment qualification. Chapter 6 is dedicated to the thermal mathematical model used to represent the physical system. Chapters 7 and 8 are brief sections that present preliminary conclusions drawn from comparisons between laboratory data and the thermal mathematical model (TMM). Chapter 9 presents an analytical perspective of the problem analysed and useful remarks used to enhance the TMM. The efforts of this work culminate on Chapter 10, in which actual orbital data is presented along an analysis on how they can be used with the TMM to deduce absorptivity degradation rates. Finally Chapters 11 and 12 summarize the main ideas and conclusions produced from this study.

2 MOTIVATION AND OBJECTIVES

Continuous development of satellite technology is critical for a country to preserve its interests and sovereignty. In order to drive costs down, longer lifespans and increased reliability are helpful.

The thermal control subsystem (TCS) has a strong influence on lifespan qualities of many spacecraft parts. This is why it is important to optimize TCS components on design as best as possible. Radiators are one of the most relevant of those elements, and for that reason, innovations proposed are welcome.

OSR family of coatings is a strong candidate to increase radiators performance and thermal optical properties stability. Before it can be used in real applications, designers need to be able to gather information for assessing the predictability of its attributes during an entire satellite mission, from BOL to EOL.

Therefore, to depend upon a reliable methodology to evaluate OSR degradation behaviour is essential for new technological endeavours in this area.

This work aspires to investigate and make propositions of such methodology. A greater focus is desired towards a numerical approach to the problem of assessing thermal coating degradation based on available telemetry data from a real flight equipment.

2.1   Problem description

Means for deducing indirectly optical properties from thermal control coatings temperature readings are diverse and not always straightforward. Apart from possible innovations, existing methods show different levels of adequacy for a given mission. While customisable, their provided results are susceptible to high variability just like the coatings they analyse.

Besides, information on the degradation predictability of some thermal control coatings for space applications is not widespread in the literature. As mentioned before, there are investigations made in the past but details are consistently

supressed. Since spacecraft design possibilities are linked to the heat it can manage, these are understandable instances. Still, it is necessary to overcome this information gap to achieve technological independence.

Literature suggests that degradation rates are different for distinct orbit inclination, altitudes, satellite attitudes and pointing. Therefore, it is very important to direct these very costly studies towards the missions planned by the national strategy Space program, which is PNAE for Brazil.

For that reason, the primary problem to be tackled consists of how to obtain indirectly the solar absorptivity degradation curves of the OSR and other thermal coatings flown in CBERS 04A as the OSR Equipment based only on the available temperature telemetry. Adjacently, to comprehend how the ideas prospected in the literature are applied to the experiment, and how they compare and correlate to each other. In addition, to evaluate how feasible newly proposed methods are.

2.2 Objectives

This work is oriented towards the following primary objectives:

a) To develop a detailed Thermal Mathematical Model (TMM) of the coating degradation OSR Equipment developed by INPE, which is in-flight on the CBERS 04A satellite.

b) To perform numerical tests as means of assessing the obtained absorptivity values from the different techniques evaluated.

And additional objectives:

c) To contribute on in-situ OSR technology of electric beam deposition and to produce the OSR samples to be tested and qualified for assembling into OSRA INPE equipment.

d) To make proper adjustments of the TMM using specific Thermal Balance Test data of the OSRA equipment.

e) To conduct theoretical studies to propose a complementary analytical model.

f) To apply the developed methodology towards extracting the absorptivity information from the CBERS 04A flight telemetry data currently available.

2.3 Methodology

Methodologies adopted in the execution of this study are:

a) Create the detailed geometry for the TMM based on the CBERS 04A OSR Equipment drawings and using the thermal analysis software Thermal Desktop Sinda/Fluint;

b) Define the nodal mesh, materials thermal properties, surface optical properties, thermal couplings, radiation analysis groups definition and imposed heat;

c) Based on theoretical considerations, numerical tests and software limitations, to impose adequate discretization and parameterization levels to the model, in order to make the TMM flexible enough;

d) From the preliminary TMM, to produce other variants that simulate different boundary conditions the experiment has been exposed to along its development cycle: ground test and orbital operation;

e) Inspired by the data produced in the thermal balance test, perform sensitivity analyses on the TMM to allow adjustments on the parameters that approximate the thermal behaviour of the numerical model as best as possible to experimental data;

f) Observe how the TMM behaves compared to the available flight telemetry data in to better reproduce the flight boundary conditions;

g) Proceeding from the correlated TMM, to identify the sample absorptivity magnitudes and signs of possible coating degradation from the available telemetry data;

h) Derive a simple lumped parameter analytical model from theoretical considerations and information found in the literature;

i) Propose algorithms to process the theoretical model-generated data to reduce inherent errors, using telemetry flight data and TMM results as a benchmark.

3 OSR EXPERIMENT – CBERS 04A

Indeed, one of the most interesting OSR materials assets is their optical properties flexibility, i.e. their ability to be optically tailored to a specific application. Unfortunately, this is counterbalanced by the high variability thin film fabrication is exposed to (OHRING, 1991). To deal with this problem, some film compositions have been previously investigated at INPE/ITA (BOATO et al., 2017) as well as some concerning manufacturing processes.

The most promising layer combination found, made of Aluminium, Silver and Chrome, had been reproduced and manufactured in the Thermal Laboratory of INPE/DIMEC (Figure B.4) and then undergone through qualification procedures including thermal shock test and TVT acceptance test (photo in Figure C.3). This was an opportunity for other INPE collaborators to add further innovations, yet unpublished, to the manufacturing process and storage in the sense of making the parts high quality and reproducible. Manufactured samples using this technology were successful in all ground tests, and then were installed to OSRA CBERS 04A flight equipment. This is the final phase into complete in-situ OSR qualification and validation. The CBERS 04A satellite has been launched in December 2019 in a Sun-synchronous Low Earth Orbit (LEO). The telemetry data it gathers is in 12-bit resolution and shall be used to evaluate indirectly performance and degradation of OSR samples. Such equipment physical aspect is presented in Figure 3.1.

Figure 3.1 – CAD Model of the Planned OSR Degradation Equipment.
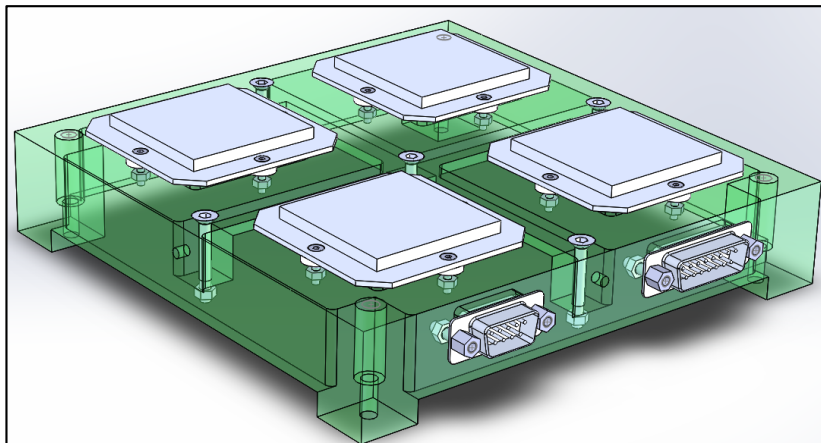
Source: INPE (2021).

3.1 Experiment description

The INPE OSR Experiment is, as shown in Figure 3.1, a box-shaped device defined by its chassis represented in green colour. It has been conceived to provide adequate support for the internal components of the assembly.

This frame is a machined box, made of FR4 composite material that is composed of fiberglass-reinforced epoxy resin, which is frequently used in the electronics industry as a dielectric substrate for printed circuit boards (PCB). Inherently this is an electrical and thermal insulating material and is very stable dimensionally due to the low thermal expansion coefficients verified. FR4 has a notable strength-to-weight ratio and meets the outgassing requirements of the mission.

From a block of raw material, the reference chassis was manufactured by boring and milling processes.

On the inside, the box has reinforcing ribs and ledges that provide increased assembly rigidity and attachment points to the lid. Inside details are shown in Figure 3.2.

Externally four corner ledges are distinguishable and serve as contact interfaces to the mounting panel. Space grade Velcro hook pieces are glued to the outward faces and are expected to provide fastening points to the MLI blanket.

Passing holes through the thinnest regions of the top surface in a total of sixteen are intended to allow sample support fixation. These are aligned to the midpoints of cut squares made on this surface. Other holes had been bored on the lateral faces to give fixtures to the electrical connectors and electrical grounding points.

In the box top face are bolted four AISI 7075 aluminium sample holders, which are spaced from the top surface by a set of FR4 machined washers.

The box assembly weights about 530 grams, and each sample support around 12 grams.

Further information related to the equipment construction is reported in Appendix A.

Figure 3.2 – Inside details of the chassis from the bottom isometric view.
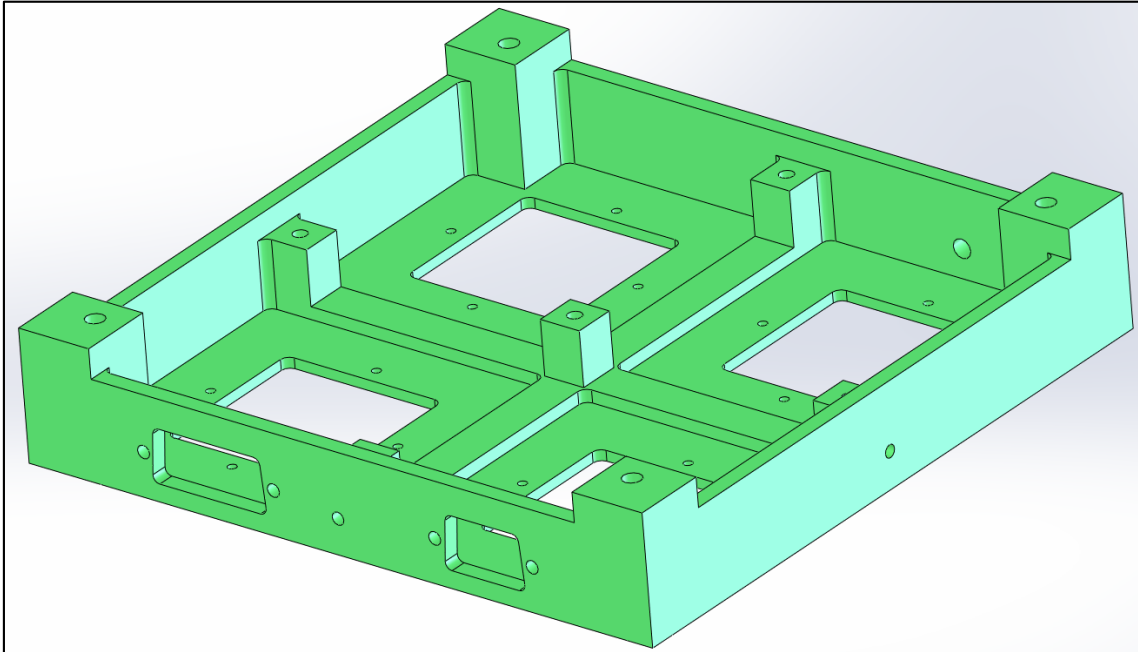
Source: INPE (2021).

3.2 Coating samples

The specimens that make the set being studied comprise two OSR samples with similar layer configuration, one MAP SG121FD white paint and one is black anodized aluminium. The physical vapour deposition (PVD) technology used is what differentiates both OSR samples, where one of them has been created from electron beam (E-beam) and the other was made using magnetron ion sputtering. Sputtering is considered a faster, cheaper and more convenient manufacturing process, which brings some advantages such as dispensing the aluminium binding layer due to the ionic bonding phenomenon; while e-beam follows already established and proven technology.

Referring to Figure 3.3, the E-beam OSR #1 sample is located in the left-hand sample holder, opposite to the connector side; the black anodized sample is the other one far from the connectors, to the right; the front left sample is the MAP

SG121FD white paint, and the front right is the sputtered OSR #2. From this point onwards, the box lateral to which connectors are attached will be adopted as being the front side.

Additional details regarding the fabrication of the samples are presented on Appendix B.

A logical relationship between the sample coatings is what guides the set choice, which is based on the following rationale:

a) the black coating may serve as an optically inert reference since its solar absorptivity is already very high, which makes it useful for deducing incident heat fluxes;

b) the white sample is a comparison reference since its use is widespread and its degradation characteristics are known in the literature and informed by manufacturer datasheet;

c) the remaining two OSR samples are the investigation's main subjects.

The samples were distributed aiming to maintain the temperature distribution as symmetric as possible.

Figure 3.3 – Layout of the Samples Set.
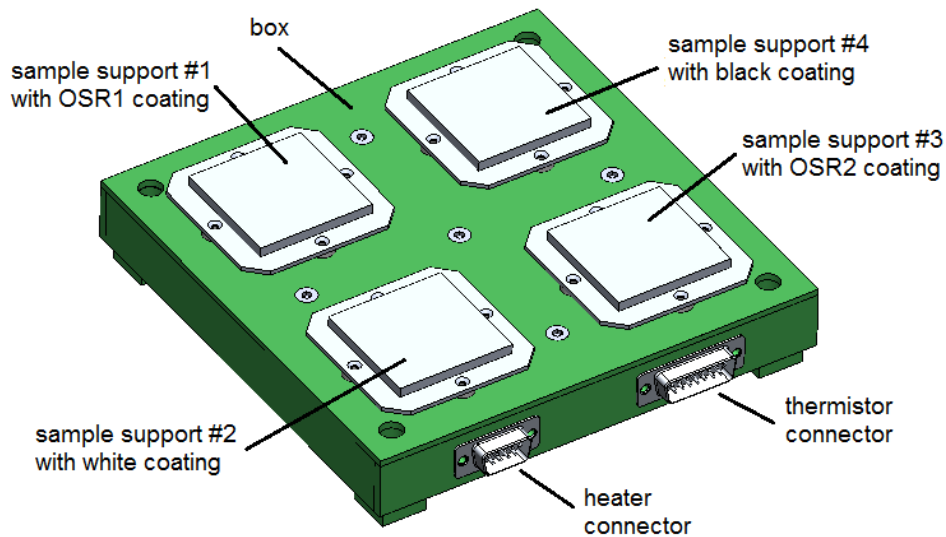
Source: Vlassov and Costa (2019).

3.3 Experiment flight behaviour expectations

The equipment installed in CBERS 04A is subjected to the external heat fluxes posed by a Sun-synchronous LEO trajectory, which orbit is projected to endure around 100 minutes. It was installed at the Z- satellite side, therefore the samples are always zentith-oriented to receive only direct Sun flux; no Albedo or Earth infrared heat flux may affect the measurements.

Standardized assembly procedures employed were defined to enhance the experiment survivability to the launch and orbital phases loads. Expectations are that such procedures were sufficient to allow the experiment to conserve its thermal characteristics as best as possible, keeping its thermal couplings similar to what can be deduced from ground test data.

Even though the assembly is lightweight, given the fact that large characteristic time constants are expected due to very small area for heat exchange, the experiment will likely have not enough time during the orbit period to reach and sustain a steady-state regime; the transient regime will be the only mode of samples temperature behaviour while in orbit.

The samples experience heating and cooling cycles regardless of the state of the heaters. Such thermal cycles are caused by the spacecraft transit through Sun-illuminated and eclipsed orbital phases.

Conversely, these thermal modes relative to the experiment are not anticipated to always share exactly the same characteristics with similar thermal modes that the entire spacecraft will go through.

Exceptionally, the only deviation that may occur to the mentioned cycles is due to the impact of the satellite entering Emergency Mode. When activated, this operation mode alters the satellite attitude to orient Z- and the solar array towards the Sun, which serves as an inertial reference. In this case samples will also receive Albedo and Earth IR heat fluxes, which will disrupt nominal measurements.

Figure 3.4 shows a CAD model of the Z- surface of the satellite with OSRA attached to it. Figure 3.5 is a photo taken of the same surface days prior to satellite launch. Figure 3.6 illustrates the expected trajectory of CBERS 04A.

Figure 3.4 – Satellite Z- Surface CAD Model with OSRA Attached.
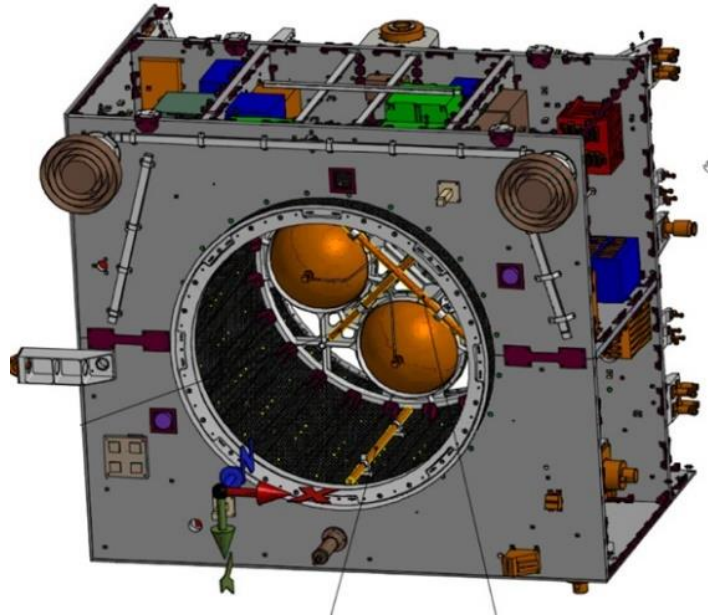
Source: Prepared by the author.

Figure 3.5 – Satellite Z- Surface Photo with OSRA Attached before Launch.

Source: Prepared by the author.

Figure 3.6 – Screenshot of the Satellite Expected Trajectory Animation.
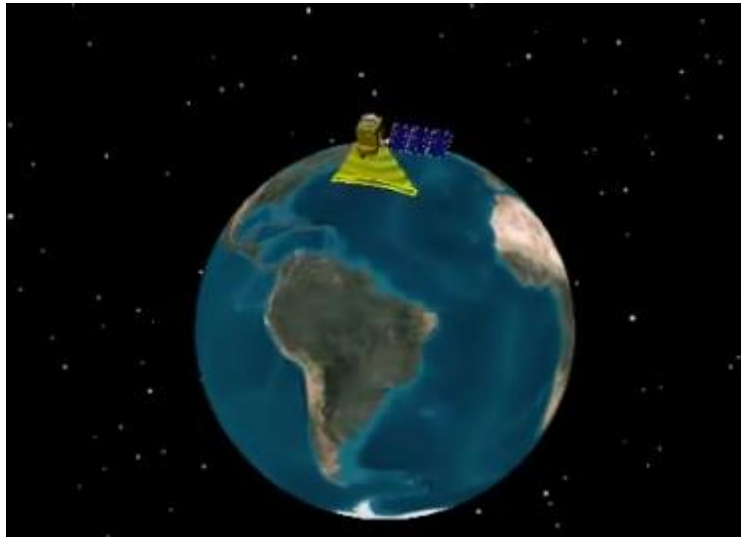
Source: Prepared by the author.

In regular operation, the experiment is designed to dissipate heat in a more predictable regimen. The electrical heaters are planned to be turned on most of the in-flight time, thus remaining in this state for the majority of the orbital cycles performed, which allow the samples to remain in the typical satellite radiator's temperature range.

Even if the spacecraft is illuminated, it can cast a small amount of shadow over the experiment caused by Antennas on the surface the box is mounted. However, the cyclic nature of the orbital movement will dictate illumination intensities experienced in a sinusoidal-shaped law. Consequently, the measured temperatures forecast is also of cyclic nature and probably fits a composed sinusoidal law.

The main difference in terms of thermal behaviour between orbital phase and ground tests is that during TBT the near steady-state regimen is achieved, besides being helpful to perform TMM precise parameter adjusting.

Throughout the mission lifetime, the OSR coating samples' optical properties are suspected to follow two general tendencies. Emissivity is likely to remain almost unaltered, whereas the solar absorptivity will probably increase.

Consequently, it will cause an increase in mean temperatures of the samples for the same boundary conditions.

This absorptivity rise behaviour is attributed to the action of mechanisms such as atomic oxygen (AO) erosion, condensation of satellite-originated volatile contaminants and propulsion ejected particles, bombardment by high-energy charged particles and degradation through UV flux.

The aforementioned effect also applies to the MLI blanket external layer, which will probably lose efficiency with time. Given the geometric complexity of this component, the insulating characteristics are prone to some degree of variability among different points of its surface. These effects can be predicted in the mathematical model, which will be used for data treatment.

4 UNIT TESTS DURING CBERS 04A SATELLITE TBT AND TVT

A joint TBT and TVT for the entire CBERS 04A satellite has been carried out. On the occasion, the space vehicle assembly status was close to the flight configuration, with most of its equipment on board. This was seen as an opportunity to identify improvements in the OSR degradation equipment, so it has been attached to the spacecraft for this event.

Equally important was the possibility this joint test has brought to the OSR Experiment TMM conception, which at this stage may require some simplifying strategies to be feasible. The data generated in this test could be used to judge whether proposed simplifications were reasonable or not, as well as to evaluate the satellite panel interface influence.

The equipment serial number 1 (SN01) was used as a specimen.

4.1 Test setup and procedures

Originally, the TBT stages were intended for satellite flight model thermal characterization and qualification, while simulating maximum cold and hot temperatures predicted for the spacecraft under flight conditions. In other words, worst-case operational scenarios.

For the OSR degradation equipment, it was useful to verify the box design adequacy. Another possibility was to check how the box assembly thermally interacts with the satellite panel at the point it was to be installed, and also with other vicinity equipment. Similarly, it was intended to verify how OSR Sample Unit (OSRA) temperatures were affected by boundary conditions closest as possible to the flight configuration. Additionally, all the electrical interfaces had their capability to work together assessed, including the 12-bit thermistor telemetries, heater lines and their telecommands, satellite cables and the OSR Electronic Unit (OSRB).

Aside from the TBT, a total of 8 stages of TVT were performed in alternate extreme cold and hot temperature plateaus, not counting the transients inherent to between those stages. As extreme conditions, they imposed to the satellite

thermal scenarios that go beyond project constraints. This is an qualification requirement for stress screening and for investigating workmanship issues. The TVT pattern can be also used for the additional adjustments of the OSRA TMM.

In order to execute this joint test, the assembled satellite was positioned within a big scale thermo vacuum chamber (TVC) that has generous dimensions: its entrance measures 6 x 8 m. The satellite was properly accommodated above a cold plate cart. Orbital heat inputs were simulated by means of infrared arrays (IRAs) and film heaters applied to MLI surfaces to simulate external heat fluxes to all satellite surfaces. This configuration is illustrated using the satellite geometric representation of Figure 4.1.

Figure 4.1 – Comparison of Satellite Test Configuration with IRAs.
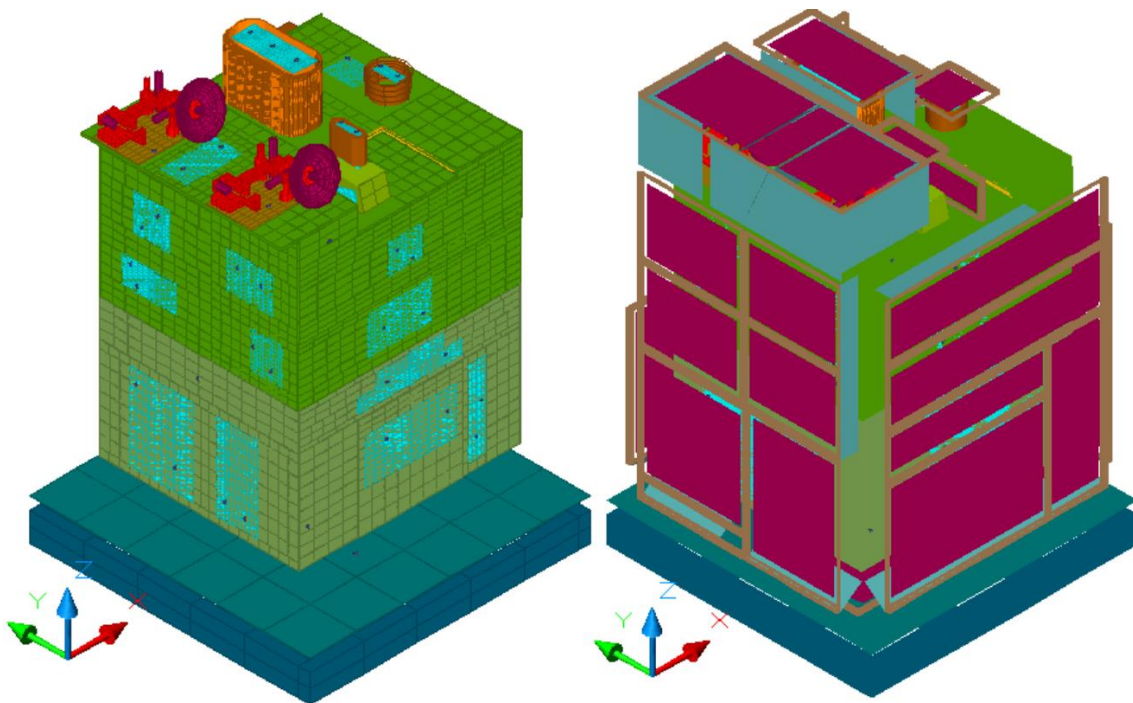
Source: Adapted from Henghui et al. (2019).

Heat loads applied to each heating device were individually determined based on their level of exposure, the orientation of the face they were installed, and derived from the orbit illuminated and eclipse periods.

41

Considering that many parts used in this test were destined for flight and that some thermal stresses could go beyond the project limits, temperatures of critical elements were closely monitored by thermistors and many termocouples. The test sequence profile is shown in Figure 4.2. Numerical labels identify different test stages.

Figure 4.2 – CBERS 04A Combined TBT and TVT.
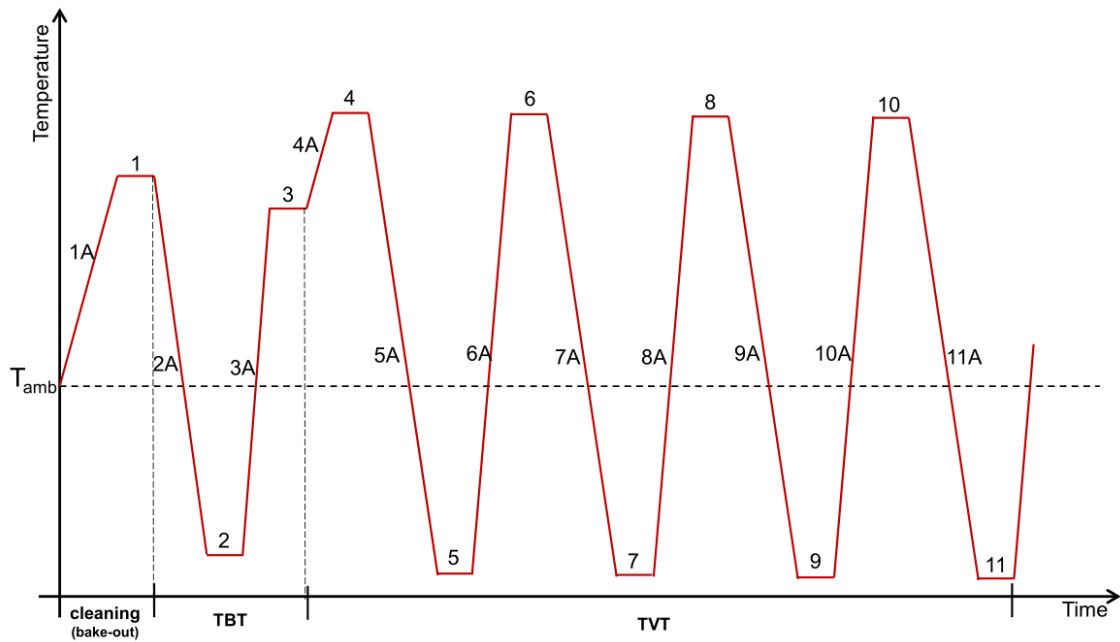
4.2   Results related to the OSR experiment

The temperature curves relative to the OSR Experiment in the CBERS 04A combined thermal tests are represented in Figure 4.3.

In both TBT and TVT hot phases, if electrical heaters were kept turned on the experiment samples tended to be in higher temperature levels compared to the box. This scenario changes when heaters are turned off, as noticeable in instants close to the end of day April 2nd, 2019. At this point, curves reveal that OSR2 and white samples, that is the front samples, remain at temperatures above the FR4 box regardless of the electrical heaters being inoperative. Such

effect suggests that indeed samples on the front, i.e. the pair that lay close to the connectors, may suffer stronger influence of thermal conductive couplings to the satellite through the cables.

Conversely, opposite relative tendencies between samples and box were verified while in the test cold phases, which samples seem to behave as expected of radiators, keeping temperatures below the levels seen in the reference box.

Sharp temperature decreases could be verified when heaters were turned off at TBT, which means that the experiment is capable of reacting in a relatively short timespan to changes in heat inputs (temperature valleys in Figure 4.3).

Unusual straight-line behaviour of the curves may be verified during TBT-TVT testing between March 27th and 28th , and also between March 30th and 31st. Since it was possible to acquire reasonable temperature data after those events, it seems that they were unrelated to any mechanical attachment problems with the experiment, but electrical continuity issues could not be disregarded.

In general, when heaters statuses were kept undisturbed for longer periods of time, the temperature curves presented parallel movements, i.e. they tend to be coupled while reacting to changing shroud temperatures, which confirms the functionality of the OSRA internal thermistors.

General temperature ranges were between -20 to -10 °C for the hot cases, which correspond to average temperature levels for satellite radiators. In the cold cases all samples went below 60°C.

Figure 4.3 – OSR Experiment Temperatures on Satellite Combined Test.
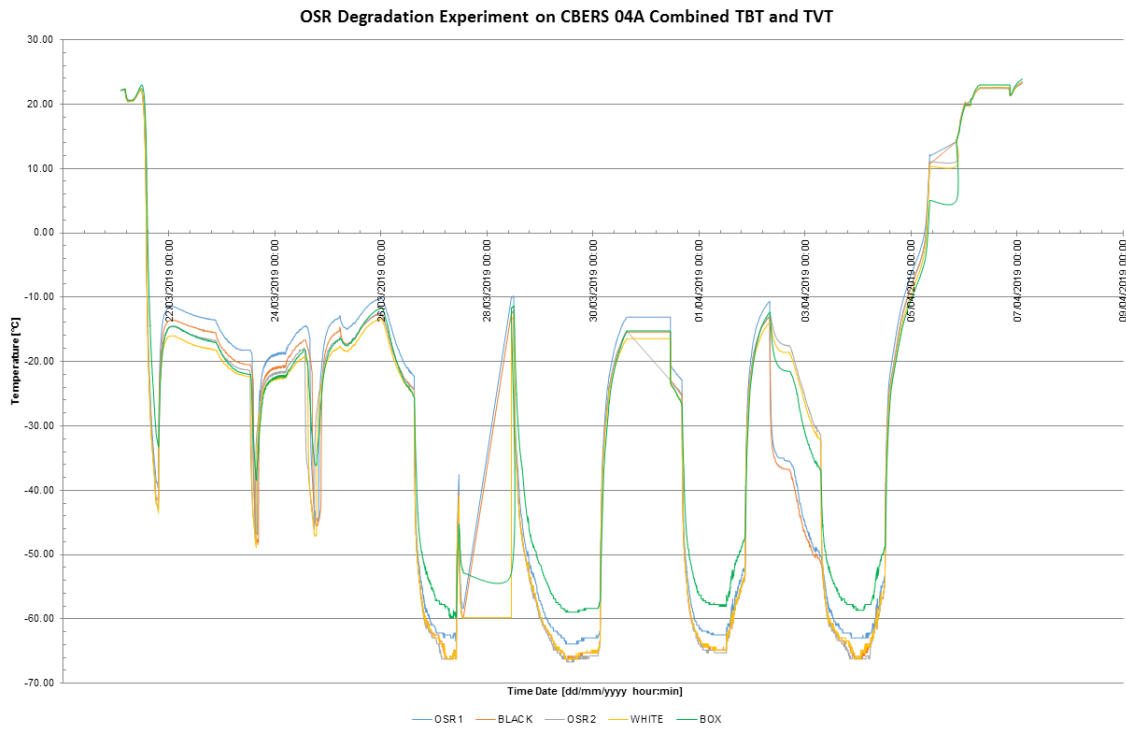
Source: Prepared by the author.

4.3   Results appreciation

Mechanically the OSR Experiment seems resilient, since no isolated abnormalities on temperature curves could be observed. In other words, all temperature curves made solidary movements in reaction to the transient testing conditions.

Heaters remained operational throughout the test, being responsive when demanded by telecommands. Turn on capabilities seem adequate for the orbit conditions.

The thermal responsiveness of the experiment shows that the design is indeed well-positioned to reflect the constantly changing temperatures as expected over orbital cycles.

After the satellite testing, based on obtained results, a rework was performed over the OSRA SN01 unit. Particularly, changes in the MLI geometric design and fixture techniques were performed to improve insulation capacity. Likewise, an additional MLI blanket was proposed to be attached to the internal surface of the box lid. On this occasion, the samples were changed to ones recently produced and not contaminated during satellite TBT-TVT. All these reworks resulted in the assembly of an identical unit, which was approved to flight nevertheless: OSRA SN02.

5 UNIT THERMAL BALANCE TEST (TBT)

Despite being a qualification procedure commonly executed at system level, which was already executed using SN01, performing thermal balance tests at equipment level for the flight model, to be carried out with OSRA SN02, was considered crucial.

The geometric complexity of the experimental unit demanded detailed temperature mappings, so the thermal couplings could be precisely identified. This level of detail is coherent with the necessary adjustments for the detailed numerical representation desired in the model.

The TBT Session refers to OSRA SN02 separate test carried out at INPE/LIT laboratory on September 2019, before being attached to CBERS 04A satellite for launch. To avoid thermally induced stresses prior to flight, after this TBT SN02 was fitted with new coating samples, which were manufactured in the same batch as the ones tested. Therefore, it is believed that the shared batch makes the tested and flown samples similar enough.

5.1 Test setup and objectives

In this test, the parameters over boundary conditions to be imposed are well controlled, and anticipated thermal scenarios emulate the equipment in-flight operation. Some stages of this test involve not only predicted cold and hot cases, but intermediate conditions as well. Both steady-state and transient OSR behaviour can be assessed from the data produced.

Furthermore, the unit TBT was conducted to verify and validate the adequacy of the design criteria, the thermal effectiveness of the used materials and assembly techniques adopted. Also, it is intended to assess whether the unit is capable of maintaining the expected temperature limits.

Regarding the basic setup of the test, the following configuration has been used: the experiment specimen is mounted on a temperature-controlled interface plate, which sits isolated in a baseplate inserted into a 46hermos-vacuum chamber (TVC). The interface plate has independent temperature

control in such a way that it is always maintained in levels above the chamber internal shroud when required. Figure 5.1 illustrates this configuration.

Figure 5.1 – Unit TBT Basic Configuration.
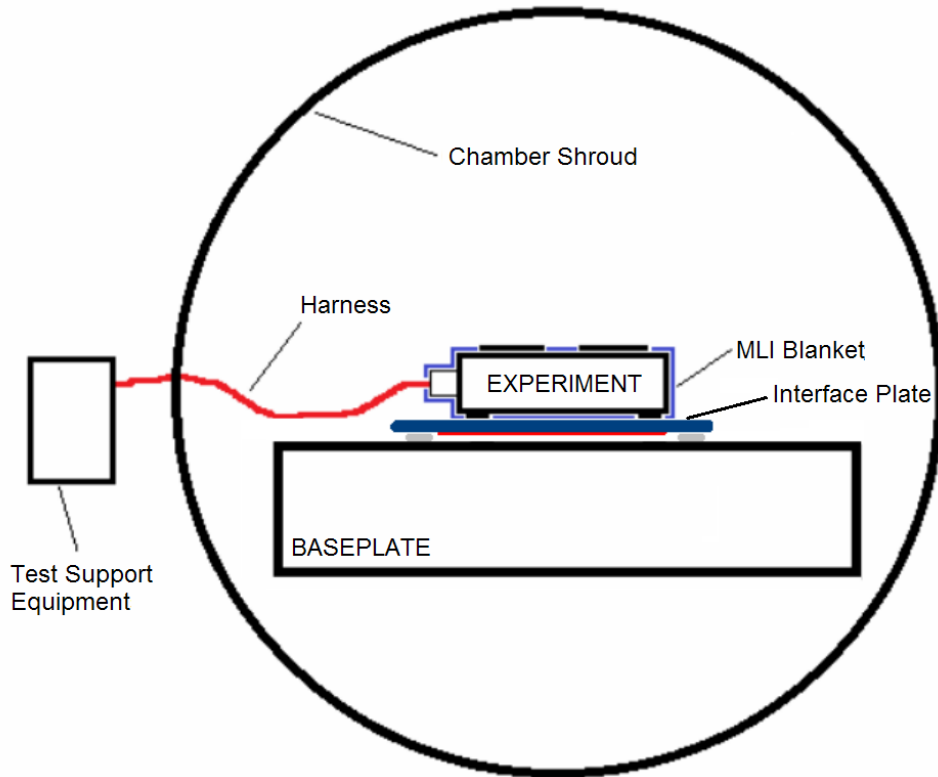
Source: Adapted from Vlassov and Costa (2019).

The chamber used has 250 L of volumetric capacity, is equipped with a pumping set capable of reaching high vacuum grade (lower than 10^{-5} Torr) and counts with scavenger plate and contamination detectors. The chamber thermal shrouds have temperatures controlled by embedded tubing with gaseous and liquid N_2.

Communication of the experiment to the external support equipment is done using a harness that is fixed to a feed-through connector plate. The external equipment include the power supplies, heater controllers, thermistors and data acquisition system.

Additional temperature-sensing elements were employed in order to instrument points of the experiment that have strategic value. Some of the test thermocouples were positioned to acquire temperatures of points that include box laterals, box feet, MLI internal and external faces and lid internal and external faces: twenty thermocouples were installed in this parts. Extra 4 redundant thermocouples were added to the samples and 6 to points in the box. Thus, a total of 30 thermocouples were used attached to the specimen.

Certain thermocouples were distributed on the surfaces in such a way to allow heat flow direction inferences. This is the case of the sensors placed in the box top inner surface. Their positions in the box are illustrated in Figures 5.2 to 5.4.

Figure 5.2 – Box Upper Wall and Lateral Thermocouples (TC).
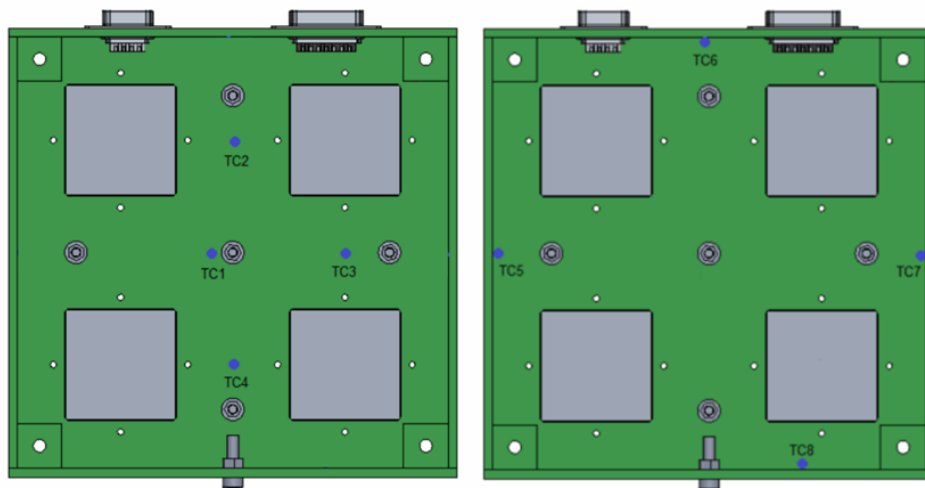
Source: Adapted from Vlassov and Costa (2019).

Figure 5.3 – Lid Thermocouples (TC).
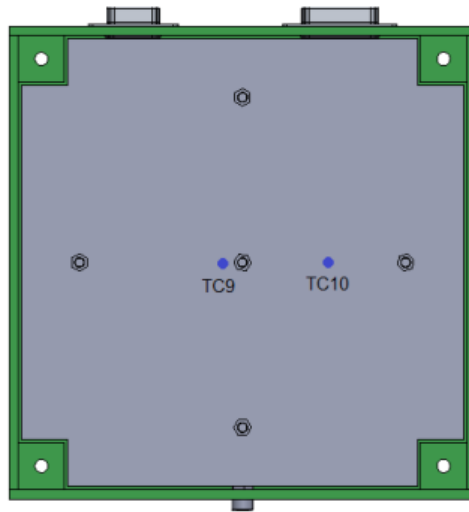
Source: Vlassov and Costa (2019).

Figure 5.4 – Feet and Box Top Thermocouples (TC).
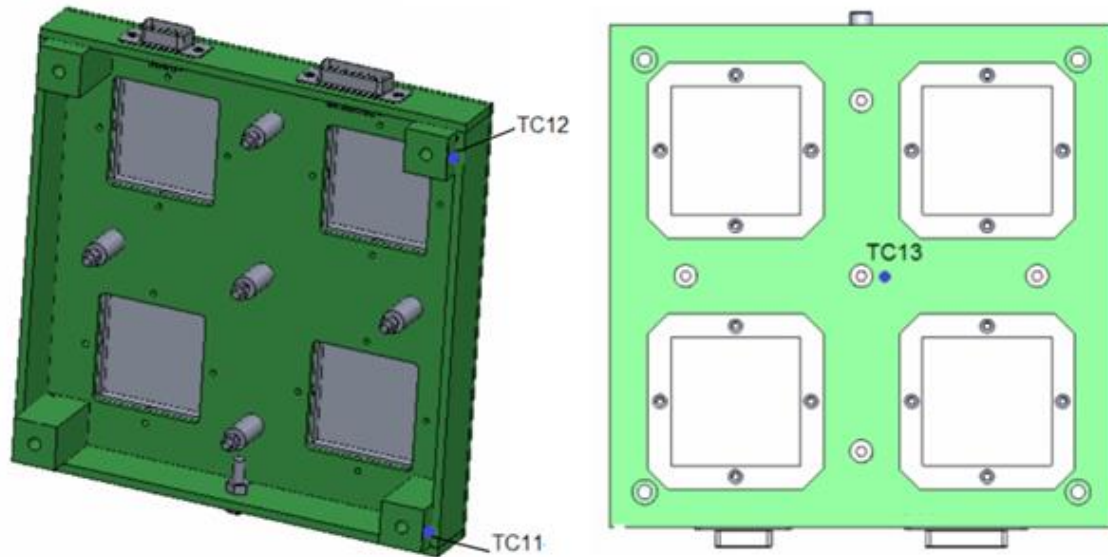
Source: Adapted from Vlassov and Costa (2019).

5.2 Execution procedures

For the TBT to be carried out with the described set, the external heat fluxes were simulated by setting the chamber shroud temperature. In order to determine the required T_{TVC} temperatures of the shroud, a system of two

thermal steady-state balance Equations was used for rough estimation. It is an approximation defined around the OSR samples.

In an eventual thermal state of equilibrium under orbital simplified conditions, the heat emitted by the OSR samples via radiation is equal to the absorbed radiation added to the electrically generated heat imposed. In the TBT condition, the heat produced by heaters shall be equal to the net heat exchanged via radiation between experiment and shroud. To equalize the in-flight and test conditions, the sample temperatures T_{OSR} shall be equal to both. Mathematically those relations are expressed by Equations 5.1 to 5.2. The T_{TVC} is obtained through the solution of these Equations by T_{OSR} elimination:

$$\varepsilon_{OSR}\sigma A T_{OSR}^4 = \alpha_{OSR} q_s A + Q \qquad (5.1)$$

$$Q = \varepsilon_{OSR}\varepsilon_{TVC}\sigma A(T_{OSR}^4 - T_{TVC}^4) \qquad (5.2)$$

$$\therefore T_{TVC} = \sqrt[4]{\frac{\alpha_{OSR} q_s}{\varepsilon_{OSR}\sigma} - \frac{(1-\varepsilon_{TVC})Q}{\varepsilon_{OSR}\varepsilon_{TVC}\sigma A}} \qquad (5.3)$$

All obtained estimates for the TBT, calculated with Equation 5.3, are shown in Figure 5.5. Four temperature levels were defined with the purpose to simulate the OSR samples possible condition combinations: 1) beginning of life (BOL) in the cold case, 2) OSR BOL in the hot case, 3) OSR EOL in the cold case and 4) OSR EOL in the hot case. These phases are represented in the Figure respectively by plateaus 3, 4, 5 and 6. As they progress, temperature of the interface mounting plate is maintained in 10 °C. Cold case and hot case

terminologies are meant to represent the moments of maximum and minimum Sun inbound radiation experienced by the satellite.

Beyond plateaus, transient regions are also represented in Figure 5.5 and are labelled with the suffix 'A'. They start when the shroud set temperature is altered and are considered to end when the chamber reaches the new set temperature. This new set shroud temperature is then actively controlled.

After a chamber transient phase ends, a controlled steady-state plateau begins following conditions as listed below:

a) Temperature variation in the experiment samples equal or less than 0.2°C/h for the minimum of 1 hour.

b) If it endures for a period of 4 hours without satisfying the previous condition.

Figure 5.5 – Temperatures Imposed to the Shroud in Unit TBT phases.
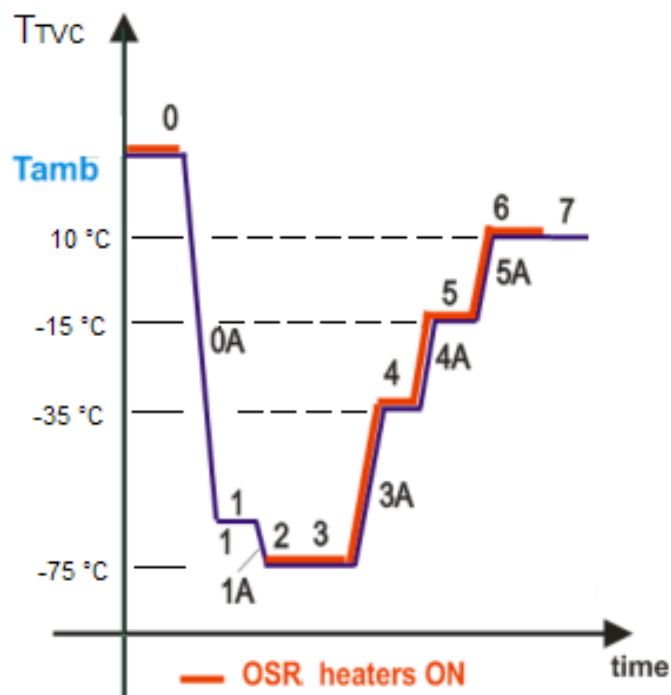
Source: Adapted from Vlassov and Costa (2019).

As expressed in Figure 5.5, the samples heating elements were kept turned on most of the time. When operated, all heaters were switched on and off at the same time. Among the phases labelled in the Figure, the main objects of interest were the ones from 3 to 6, transients included. The transient regimen can be especially useful to deduce characteristics such as the time constant and thermal capacities of OSRA parts. Preceding phases 0 to 2 are also useful for investigation, but they are less real-life representatives as they serve as preparation stages. A TVT followed this TBT in a joint test, so phase 7 also serves for preparatory purposes.

Temperature data was read and recorded once each 30 seconds by the Data Acquisition System (DAS).

After chamber closure and decompression, a hot soak procedure (phase 0) was conducted to eliminate adsorbed volatiles and any residual facility contamination, just like a bake-out procedure. A temperature change in the interface plate is the difference between phases 2 and 3, brought from -5 °C to 10°C for the rest of the test.

5.3   Results

A selected output dataset is shown in Figures 5.6 to 5.8, which contain temperature data collected from the thermistors installed on the 5 points of interest chosen in the experiment box. They represent phases 3A to 6, but it is possible to also extract the final temperatures reached in phase 3 from Figure 5.6. One interesting highlight is on the relative distribution of the temperature curves that was preserved, and their tendencies which were very similar throughout these stages.

Regardless of their very low sample mass, the thermal inertial of the samples is very high: a 4-hours soak at shroud constant temperature may not be enough for the samples to reach steady-state. This occurs due to the very small heat exchange area of the samples an thus such a transient behaviour shall be taken into account on real flight data treatment, situation in which cycles occurs once each 100 minutes approximately.

Indeed it can be verified from test data that the transient processes are really very slow. In spite of OSR equipment being lightweight, the time constant seems to be of great magnitude: the steady-state was not completely achieved after the soak time adopted. It confirms the assumption that while in-flight, the only OSR operational status to be observed is the transient mode.

In contrast to the OSR2 sample curve relative position obtained, temperatures of these thermistors were expected to better approach the ones of OSR1. Later on, a permanent temperature shift was discovered and has been present even at initial conditions where all OSRA temperatures should have been equivalent. To be used for TMM adjustments, it was performed special calibration procedures based on the TCs temperatures during the TBT. The calibrated curves are presented in Figures G.1 to G.3 from Appendix G; from them, it is possible to observe that only OSR2 temperatures changed significantly: their curve is now much closer to the OSR1 and is now positioned above the white sample curve.

An additional noticeable phenomenon is a curve bump seen in the Figure 5.8. This was caused due to the TVC temperature erroneously set for -10 °C, but the aim was actually to set it in +10 °C. This mistake was corrected in a time around 4000 s of this phase, but its occurrence meant that less time was available for temperatures to develop once again. Perhaps, doing a curve extrapolation will be convenient to make a safer usage of this data while in TMM adjustments.

Tables 5.1 and 5.2 summarize information on the heaters and samples that were used in the TBT and now are part of the flying OSR Experiment assembly.

It is relevant to mention that some degree of controversy surrounds the optical properties true values. As reported in Table 5.2, the listed properties are as they have been measured just before the experiment unit integration to the satellite for the launch procedures in September 2019.

However, values up to 0.148 were found for the white paint solar absorptivity on previous measurements, while the 0.087 value seems too low. In the literature, works such as Remaury and colaborators (2011) report measured values as 0.19 ± 0.04. Duzellier et al (2018) provide data that corroborate the previous.

Similarly, the manufacturer provides 0.20 ± 0.02 as BOL solar absorptivity for the SG121FD.

On previous optical measurements at INPE, the black anodized sample has shown different results as well, with solar absorptivity placed up to 0.949.

Therefore, it is realistic to consider that OSR sample optical measurements were also exposed to undesired shifts from the real value.

Figure 5.6 – Experiment Thermistors TBT Temperature Curves for 3A and 4.
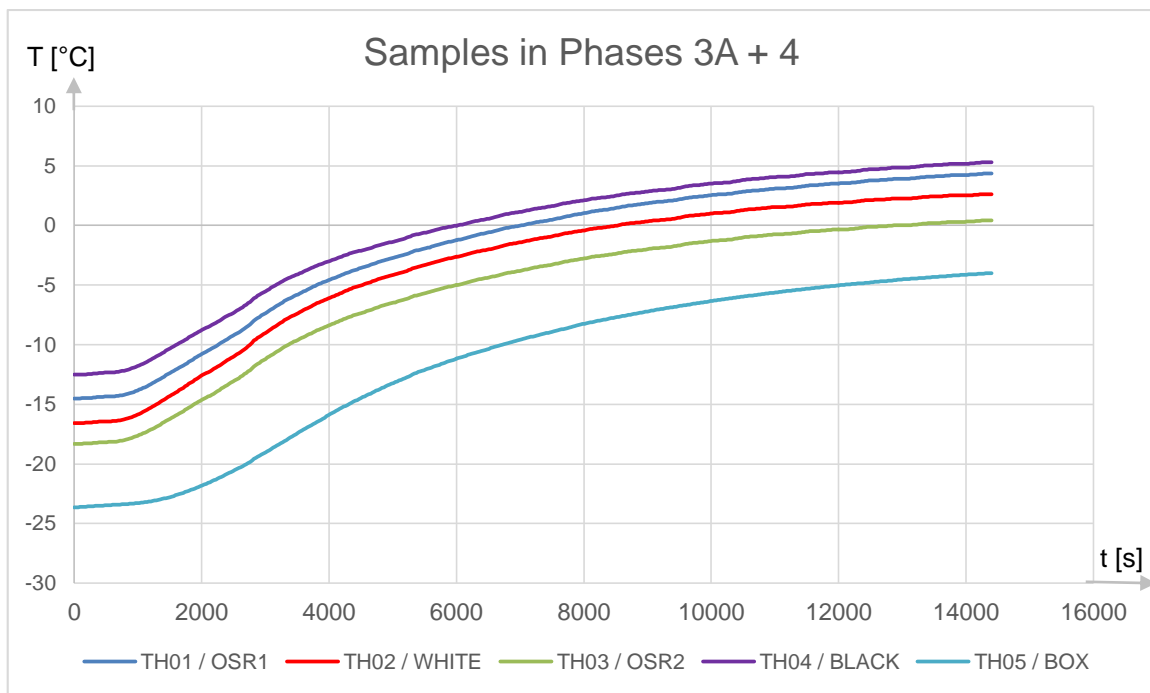
Figure 5.7 – Experiment Thermistors TBT Temperature Curves for 4A and 5.
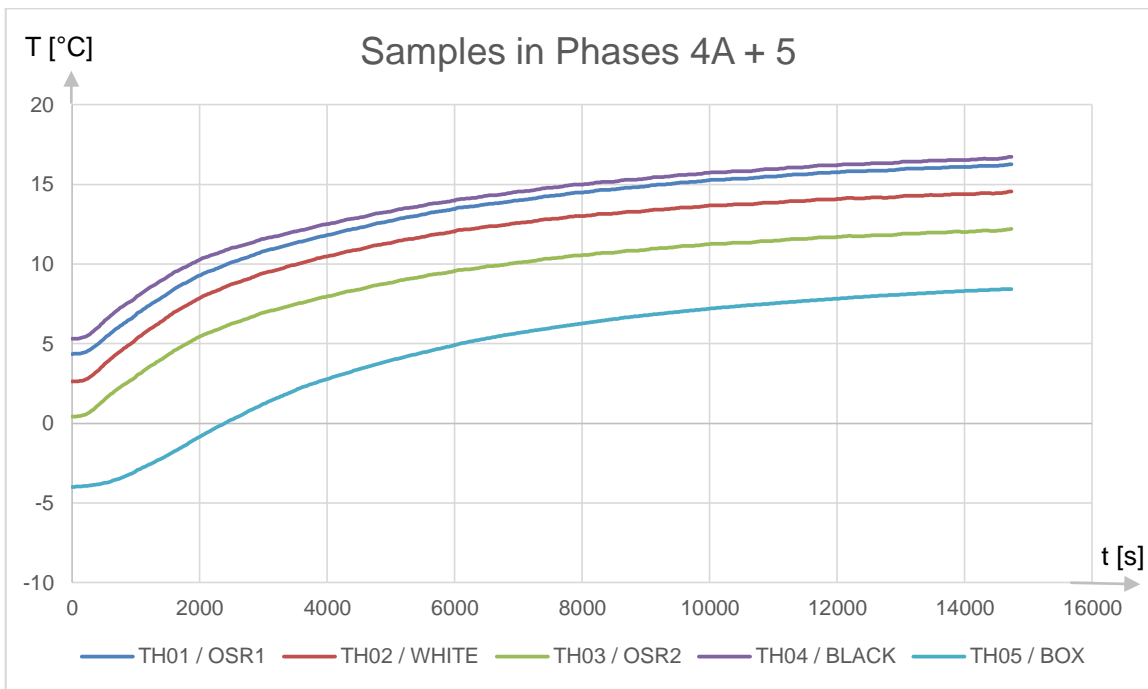
Source: Prepared by the author.

Figure 5.8 – Experiment Thermistors TBT Temperature Curves for 5A and 6.
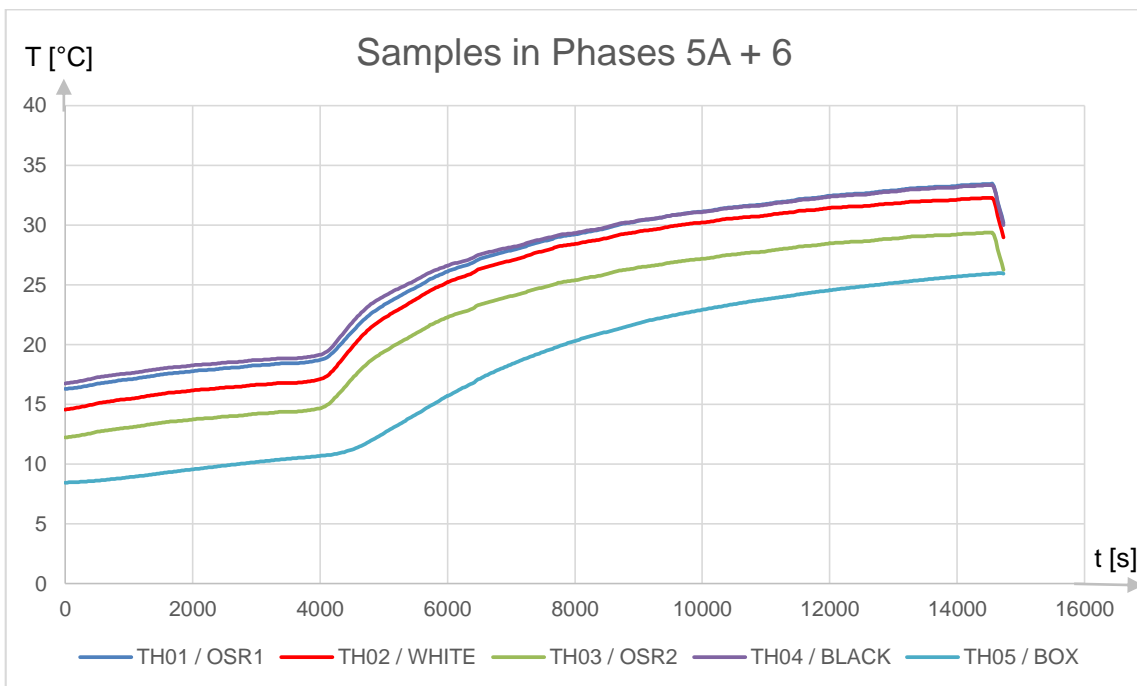
Source: Prepared by the author.

Table 5.1 – Sample Electric Heaters Characteristics.

ID	Sample Coating	Heater Resistance [Ω]	Estimated Circuit Resistance* [Ω]	Estimated Power Dissipation [W]
1	OSR1	147.0	550.24	0.38065
2	White Paint	153.2	553.44	0.39213
3	OSR2	152.6	555.04	0.38835
4	Black Anodized	152.7	555.84	0.38749

*Considers OSRB electronic box resistances and 4 meters of AWG24 wiring.

Table 5.2 – Pre-flight Samples Optical Characteristics.

Sample	Measured Absorptivity	Measured Emissivity
OSR1, Set/2019	0.031 ± 0.002	0.822 ± 0.008
OSR1, April/2019	0.037 ± 0.016	0.852 ± 0.014
White Paint, Set/2019	0.087* ± 0.005	0.866 ± 0.010
White Paint, Mar/2018	0.148* ± 0.001	0.919* ± 0.010
OSR2, Set/2019	0.034 ± 0.006	0.829 ± 0.011
OSR2, April/2019	0.043 ± 0.004	0.833 ± 0.013
Black Anodized, Set/2019	0.919** ± 0.002	0.887 ± 0.011
Black Anodized, Mar/2018	0.949 ± 0.002	0.893 ± 0.007

*true value is disputed ; **values up to 0.97 in the literature.

5.4 Comments and conclusions

Independently of OSR2 temperatures corrections being performed, and the fact that it has very close optical properties if compared to OSR1, its curve will likely remain below the one correspondent to OSR1. This relation is because the samples positioned closer to the connectors are better coupled thermally to the experiment box and electrical cables with exposed connectors, which can act as radiation fins that provide additional cooling.

By the end of all temperature plateaus, the criteria for temperature stabilization for the steady state regimen was not met, thus the stages finished at the maximum time limit. Such deadlines had to be observed nonetheless due to facility available time limitations, i.e. the 4 hours period have to be respected.

However, these temperature rates comply mostly with MIL-STD-1340D standard of 1 °C/h maximum for temperature stabilization criteria, which is less strict and also defined to a system level. If this would be enough for TMM adjustments is yet to be seen. In this case, curve fitting for extrapolation could be an option to discover the curves limit steady-state temperatures. An alternative for extrapolation could be using transient simulations reproducing test times, in which the same temperature profiles of the TVC would be used as an input to the simulation. Certainly, the last is more computing time demanding.

6 NUMERICAL THERMAL MATHEMATICAL MODEL (TMM)

A numerical reproduction of the physical experiment has been developed using the software platform Thermal Desktop Sinda/Fluint. This software package is a standard tool used at INPE, NASA and CAST. Such representation is also referred as the Thermal Mathematical Model (TMM), which is capable of simulating the thermal behaviour of a given system.

Essentially, it represents the geometric collection of virtual entities that in turn are divided as discrete elements. These are interrelated in accordance to thermal couplings and boundary conditions. Inherent physical laws govern their interactions. The TMM uses the finite difference (FD) method for the solution.

The adopted philosophy allows the TMM to be used for different investigation scenarios.

Currently the TMM is made of approximately 7230 nodes unevenly distributed. A high nodal resolution was adopted in regions of the equipment where it is believed that more complex heat pathways occur. Extra nodes were also used in parts that are made of insulator materials, which tend to present greater temperature gradients.

The definition of nodal resolution is not an exact science and may depend on multiple factors, but for simple thermal systems theoretical fundamentals can usually provide good guidance. Its TMM demanded continued symbolic parameters testing to compare solver runs output temperature fields with ground tests data. This strategy has proven a more straightforward approach. Figures 6.1 and 6.2 illustrate the TMM geometry with and without MLI blankets, respectively.

Figure 6.1 – Experiment TMM External View with MLI Blanket.
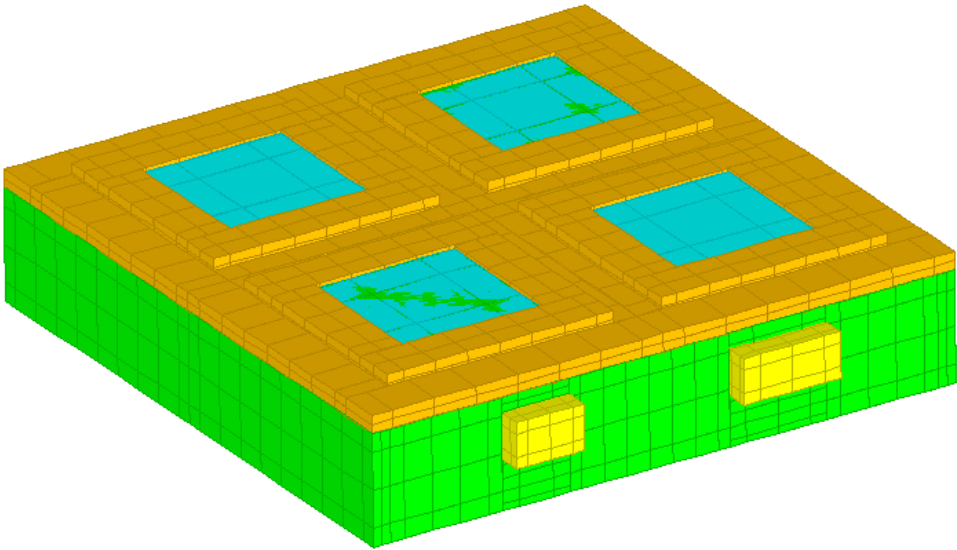
Source: Prepared by the author.

Figure 6.2 – Experiment TMM External View without MLI Blanket.
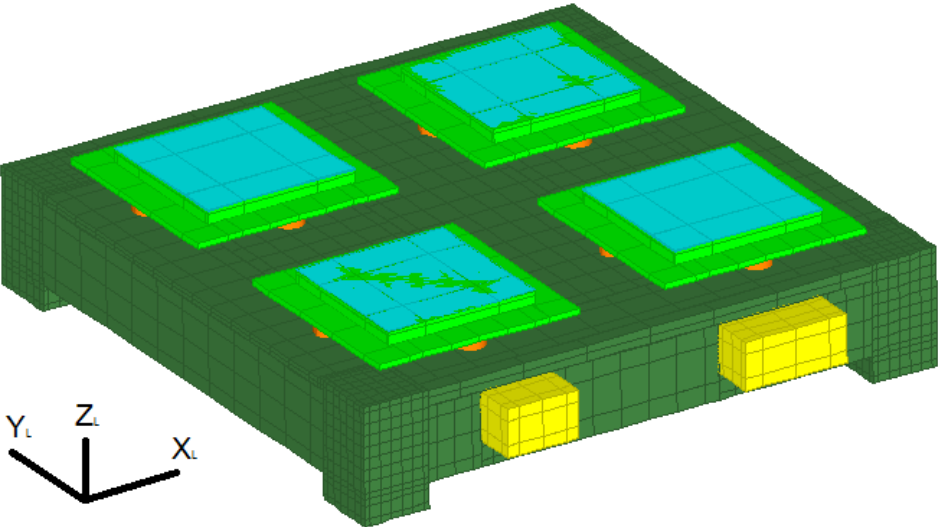
Source: Prepared by the author.

6.1 Geometrical model description

As intended, the TMM was modelled in subdivided blocks that approximate the actual geometry.

Aiming to establish thermal cohesion among the blocks within a single part, heat flow smoothness is emulated by defining strong thermal coupling between adjacent blocks. This is also the reason why only edge nodes were used to discretize the blocks: nodes of adjacent blocks are kept adjacent as well, which contributes to preserving heat flow directionality on the interfaces.

When put in contrast, Figures 6.1 and 6.2 reveal a prominent feature: the MLI blanket geometry is modelled in many blocks, which was done to allow blanket thickness variation as well as the nodes to be parameterized. All the blocks that compose the MLI have their edges size parameterized to cope with thicknesses between 5 and 12 mm.

Beyond variable thickness, the MLI blanket has humps around the sample holders. They were defined to accommodate the holders while maintaining a constant thickness in this area. Details of the inside of the MLI blanket can be observed in Figure 6.3. The double colour pattern used in the blocks have no special meaning: it has been chosen only for visual reference. It is worth noting that the MLI bottom edges touches on the satellite panel. Another important feature of the blanket is its anisotropic material definition.

Initially, it was intended to leave a gap (say, of 1 mm) between the FR4 box and MLI blanket to simulate radiation heat exchange. Nevertheless, it was verified that this feature would increase prohibitively the computational cost. Therefore, current MLI blanket "touches" the experiment.

An examination on the MLI Figure 6.3 also shows that block symmetry and size homogeneity were priorities. To respect these principles in the front face was challenging because connectors disturb the geometrical balance in this region.

Figure 6.3 – Inside of the External MLI Blanket Model.
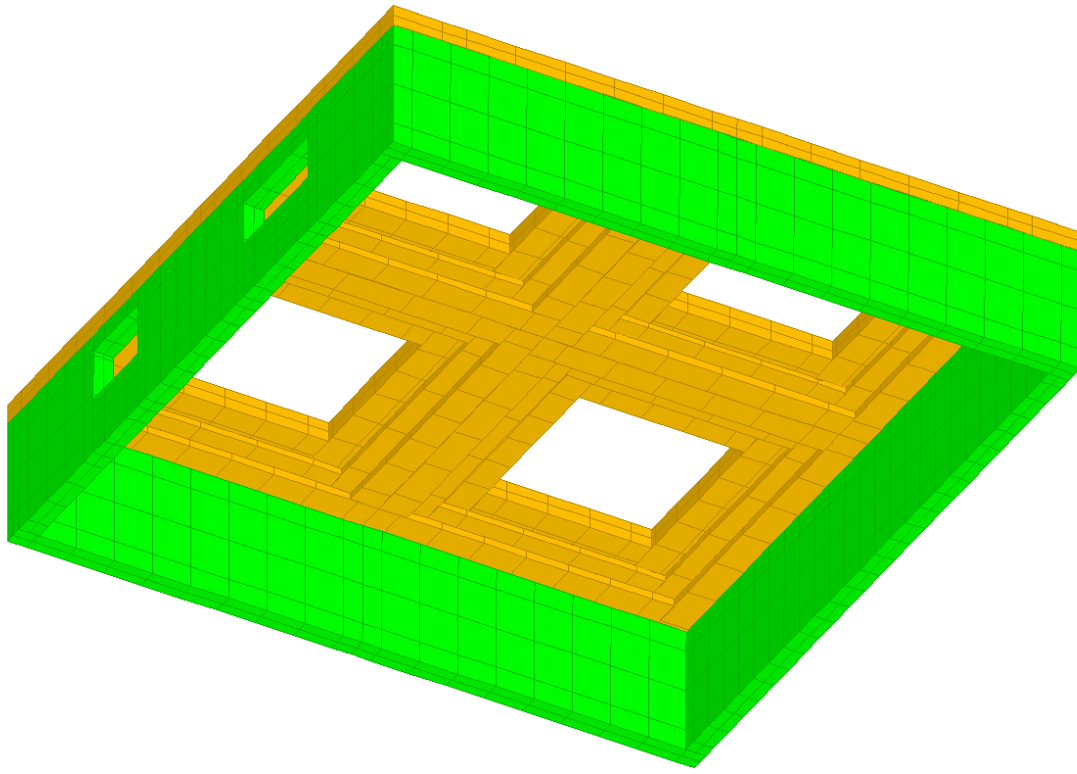
Source: Prepared by the author.

Similar principles oriented the modelling of the FR4 box, but this part demanded different intricacies. On its external blocks, an enhanced nodal resolution was added to the corner feet, where the real experiment has holes to accommodate attachment bolts. Besides, the corner blocks have contact to the mounting surface (either a TVC plate or a satellite panel) and act as a heat bridge between laterals and the top. Figure 6.4 illustrates the box blocks layout. Once again, the modelling of the front face was challenging and demanded a breakdown in 6 blocks. Examination of Figure 6.4 also reveals that the feet representative blocks top surface also is part of the box top. No perforation was modelled to represent the bolts housing, neither the bolts themselves were modelled. Different anisotropic factors to the thermal conductivities were defined to represent bolts and holes effect. In what concerns the conductive properties, typical FR4 anisotropic specs were used for a material laminated

parallel to the top plane. In other words, conductive behaviour in the box is the same in X_L and Y_L directions on the local coordinates system, but conductive properties in Z_L are different. At least 2 nodes were used through the thicknesses direction.

Figure 6.4 – External Blocks of the FR4 Box Model.
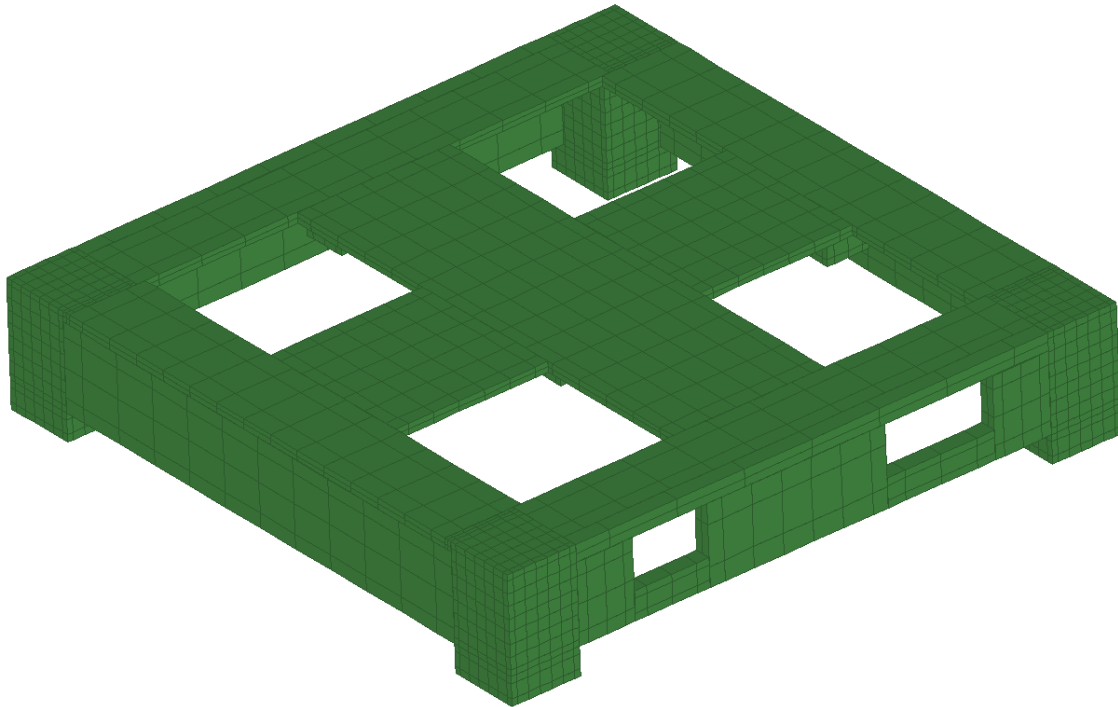
Source: Prepared by the author.

On the inside the box is composed of blocks that represent lid support ledges and ribs separately, which were nonetheless coupled thermally to represent a solid structure. They can be observed in Figure 6.5. Similarly to the feet, these ledges on the real equipment have pass-through holes for bolts housing. This time, however, they are intended to bolts that hold the lid in place. Neither the holes nor bolts were geometrically represented in the model, but conduction factors were used to emulate their impact. It is possible to verify in Figure 6.5 that edges fillets were not represented, and this is due to the limitations of the used software platform.

Figure 6.5 – Internal Blocks of the FR4 Box Model.
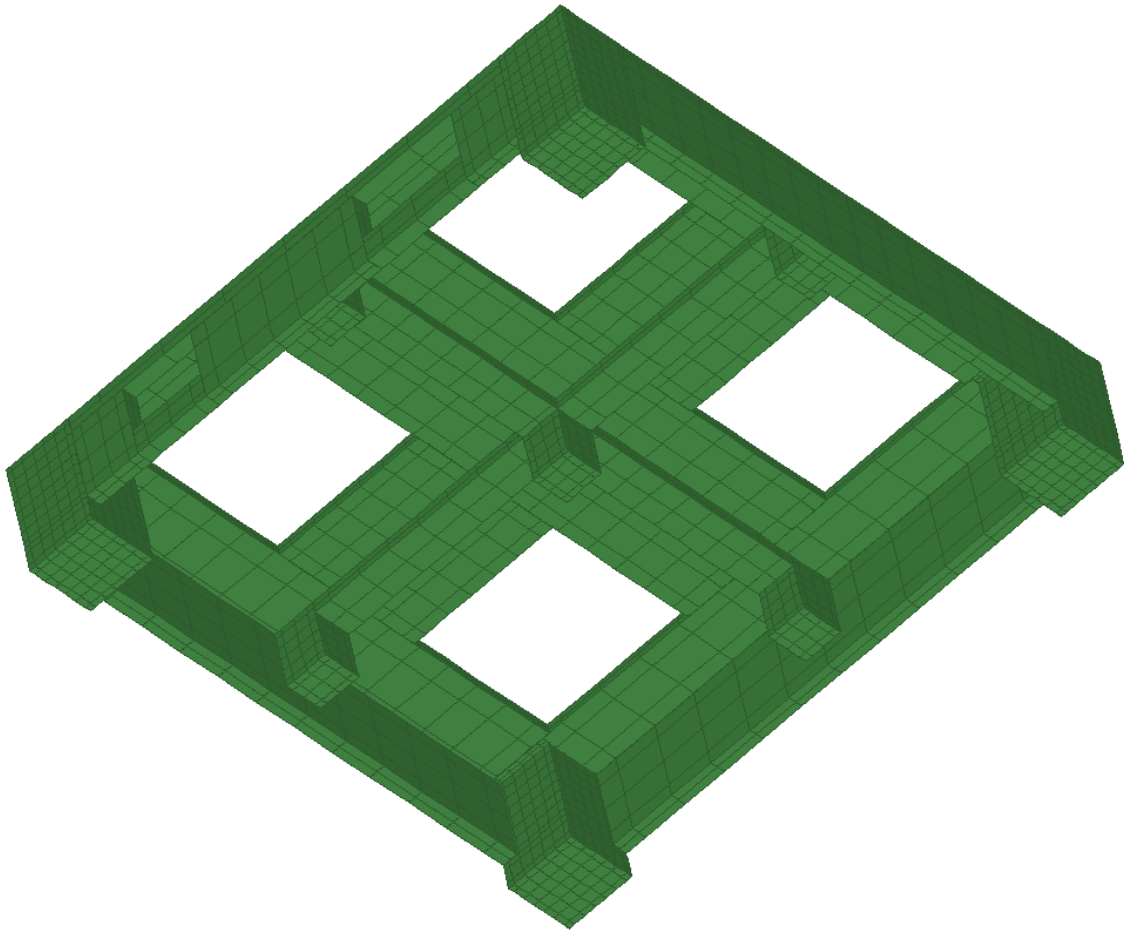
Source: Prepared by the author.

In the real experiment, machined FR4 plain cylindrical washers were used to mount and insulate thermally the aluminium sample holders on the box top and they were represented geometrically in the model. Metal bolts were represented by an increased conductive factor to the axial direction. The washers are represented in Figure 6.6 in orange colour.

Above the washers group stand the models of the 4 sample holders modelled using properties of the AISI 7075 aluminium alloy. Their octagonal skirts were represented by square ones instead and the internal slot is present.

Figure 6.6 – Washers Models Positioned in the Box Top Surface.
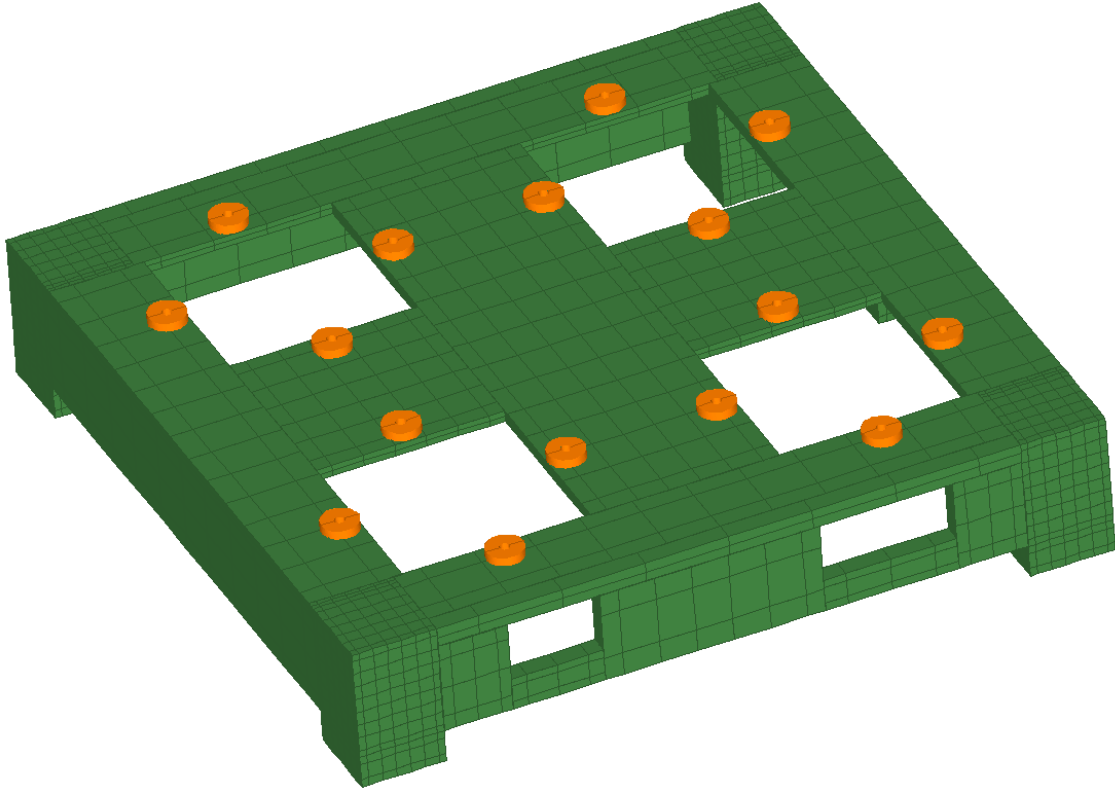
Source: Prepared by the author.

Coating samples are modelled using slim bricks as thin plates and are positioned on the top of the sample holders stands. On the other hand, RTV566 layer that attaches OSR samples to the stands were represented as contact factors. One of the samples is shown as the aqua-blue surface in Figure 6.7. From this Figure, it is possible to verify that a 3 x 3 mesh was used to discretize the sample, which may seem coarse but higher node densities were used were tested and no significant changes in the temperature calculations could be identified. Concerns with possible inaccuracies produced by radiation reflection in satellite flight conditions motivated meshes up to 7 x 7 to be tested. It is believed that the aluminium sample supports high conductance played an important role on this test since it contributes to evenly spread the temperatures.

Figure 6.7 – Sample Model on the Top of a Holder.
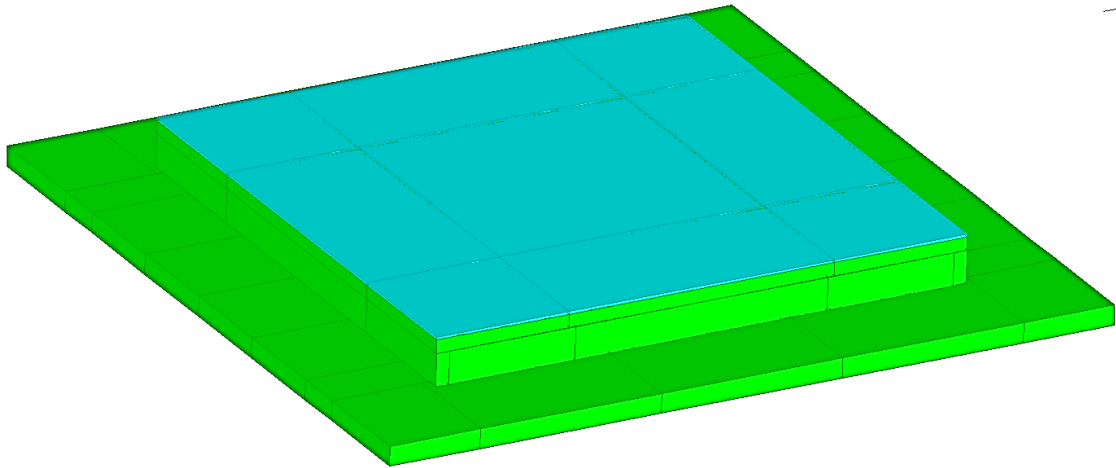
Source: Prepared by the author.

Since the sample supports material has high thermal conductivity, no important temperature gradient is expected and heat loads were applied directly on them. Thermistors were modelled as very small square surfaces at the tip of the conductors used to represent the cables. Such details are better seen in Figures 6.8 and 6.9.

The electrical cables function as heat conductors from points on the sample holders to other points in the equipment assembly. Some of them are attached to the representatives of the connectors. These connectors have slightly different widths and were modelled using a similar logic: they were divided in three blocks of which one is in the interior environment, one in the exterior of the box, and the last is within the respective front face wall hole.

A closer look to the connectors shows that the conductors are not attached to their centre. This has been done on purpose, in an attempt to simulate the asymmetric disposition of the cables on the connectors. Besides, as real connectors are composed of different materials, triaxial anisotropic conductive properties were assigned to them, which have preferential conductance in the metallic pins direction.

Figure 6.8 – Heat Loads and Conductors Applied to the Sample Holders.
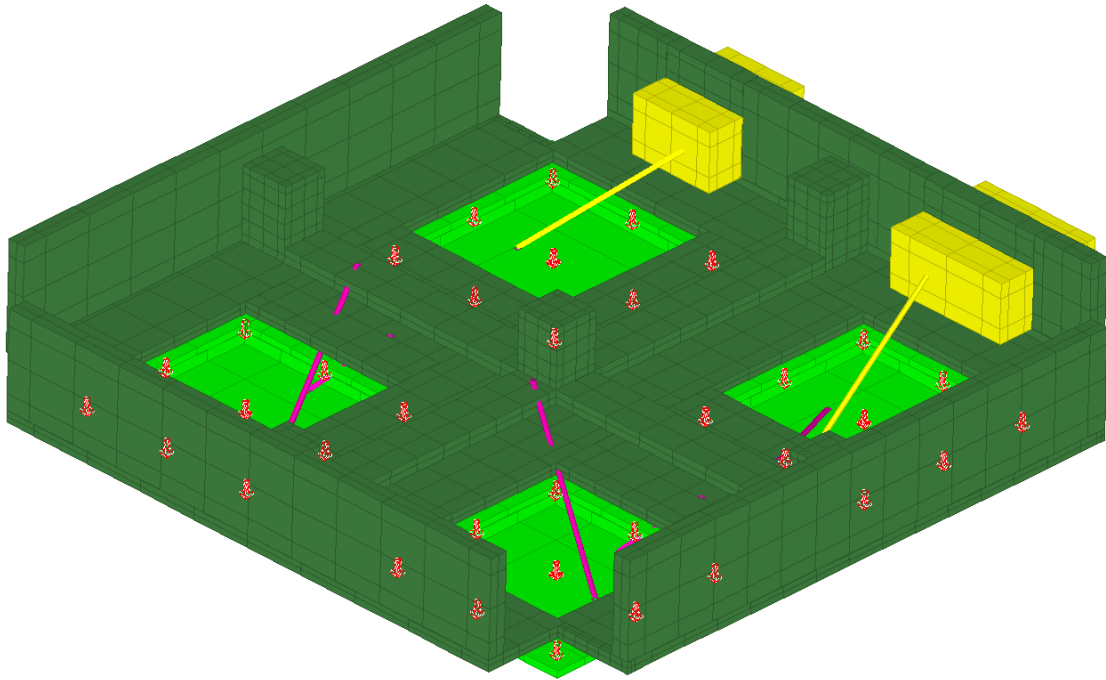
Source: Prepared by the author.

Figure 6.9 – Cable Terminals on the Sample Holders.
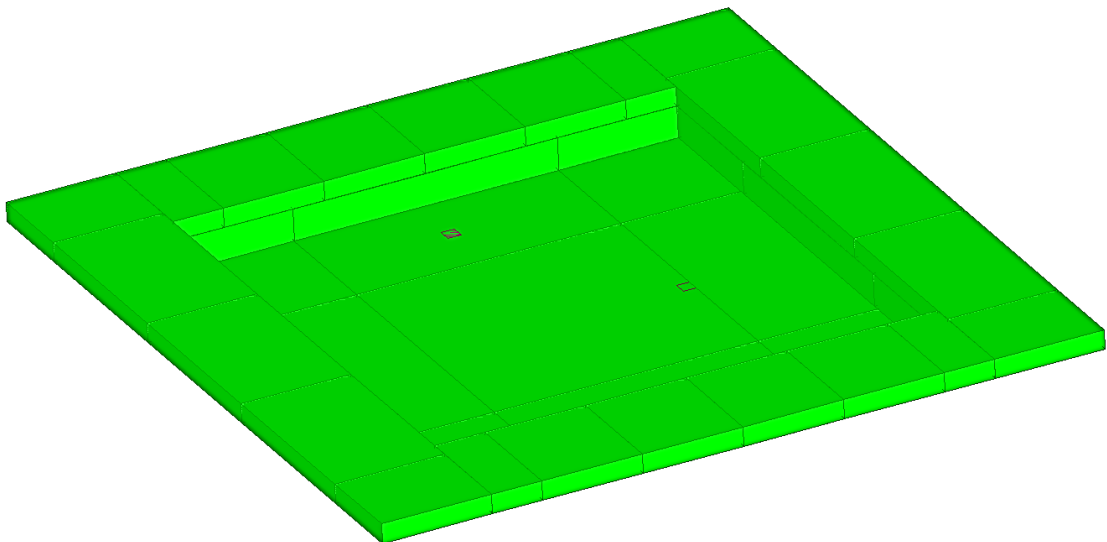
Source: Prepared by the author.

In what it concerns the closing lid, its simple geometry was closely replicated. Pass-through holes were not modelled, but interface contact factors were used to represent them. Numerical grid resolution was reduced in this region because it remains protected from the external environment and for that reason less exposed to temperature gradients. Externally to the lid, MLI coating blocks copy its shape. On the internal surface, MLI was not modelled in blocks and is represented only by arithmetic nodes, which is a usual approach for MLI simulation. Figure 6.10 illustrates the FR4 lid in pink colour with its correspondent external MLI. Meanwhile, 6.11 shows how they fit in the box.

Figure 6.10 – FR4 Lid Top View with Corresponding MLI External Blanket.
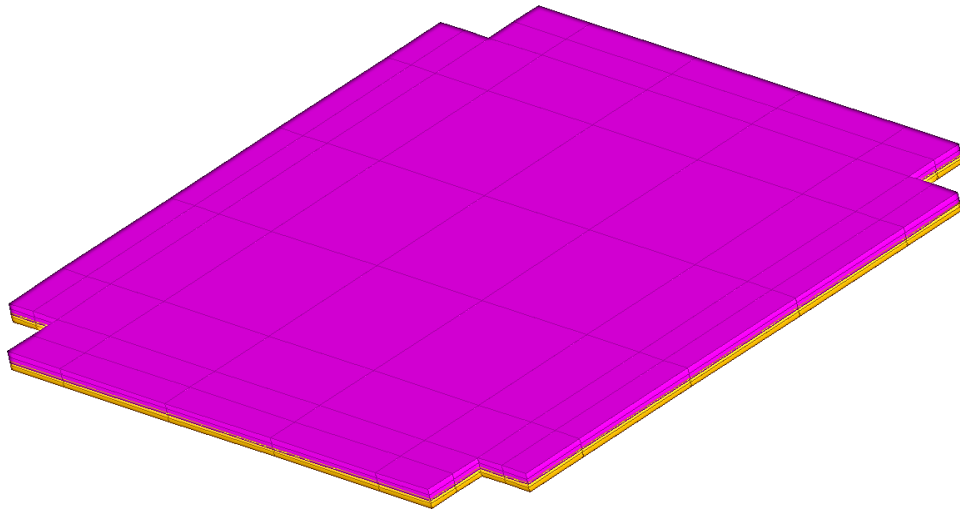
Source: Prepared by the author.

Lastly, an examination of Figure 6.11 also reveals that when the lid and its MLI are in place, a gap is formed between the mounting panel, the free MLI surface, and feet internal oriented surfaces. Both FR4 lid and MLI do not touch the lateral faces, only the internal mounting ledges.

Figure 6.11 – FR4 Lid and Corresponding MLI Fitted to the FR4 box.
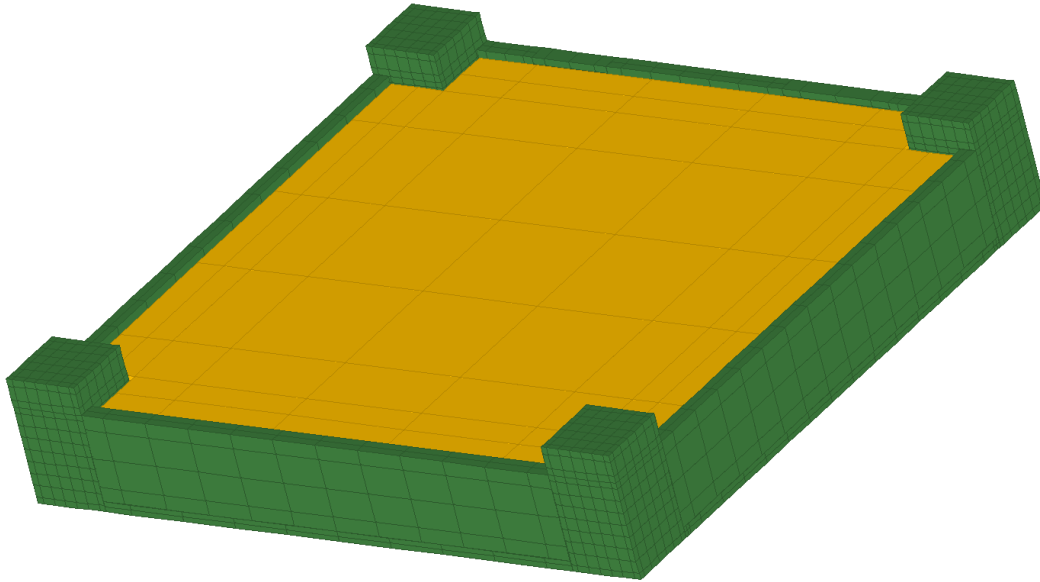
Source: Prepared by the author.

6.2 Simplifying assumptions

Regardless of the desired level of detail to be reproduced in a numerical model, simplifications are adopted frequently. This practice is motivated by reasons that range from software limitations to intentional reduction of the computational cost.

As mentioned before, the external MLI blanket is modelled by blocks but does not interact with the box surfaces using radiation simulation techniques. Thermal coupling using this technique, which is built-in on Thermal Desktop/Sinda, rely on radiative conductances (radks) established between surfaces. Its execution demands random ray sampling from each of the nodes via Monte Carlo stochastic algorithm, which makes it costly to be computed repeatedly. In the OSR Experiment TMM, ray tracing was used to calculate the radks.

Unfortunately, constant computations of radks were required on the adjustment process since MLI blankets usually have properties determined by manufacturing processes of great variability.

An equivalent contact conductance was used instead as an approximation, and was proposed based on optical properties available in the literature (GILMORE, 2002). Such conductive coupling has been considered as reference values, but probably does not reflect the exact thermal insulation qualities of the real MLI.

MLI blanket thermal performance depends on factors that are not easy to control, predict and replicate. For example, the blanket may assume non-homogeneous thicknesses in different points of its area due to different venting patterns on launch and thus have eventual spots of internal contacts with spacer nets. Thicknesses are also affected by bends on the blanket, which are plentiful on this specimen. Additionally, blanket accommodation and compaction levels can also change under influence of vibrations produced by the launch vehicle.

Because of the explained elements that affect MLI performance, higher variations in temperatures when compared to test data were considered acceptable as long as adjustments of other assembly parts were kept feasible.

Furthermore, an extra assumption had to be made to the external MLI geometric representation to guarantee coherence on their temperature fields. The problem resides in the fact that MLI conduction properties are anisotropic and they change orientation in different faces of the box caused by their bends on the edges.

As the software cannot bend the finite difference blocks, on the corners they irredeemably touched themselves in directions of different conductive properties. For instance, at junctions MLI lateral blocks in-plane direction had to interact with the normal direction of the MLI top blocks.

In this case, if the surface contacts between blocks were established they had roughly the same effect as if no contacts were used at all: temperature contours would develop unnatural steps in this region.

This phenomenon was verified on both MLI and box. Node merging between adjacent blocks was considered to solve this issue, but adopting it would eliminate the possibility for editing the MLI mesh progressively, i.e. if any hidden

errors were to be encountered, fixing it would require rebuilding the MLI model over and over again.

The solution proposed consists of "sewing" the MLI corners with linear conductors between pairs of adjacent nodes at corners junctions. Such a solution was work intensive and reduced nodal flexibility of the external MLI, but seems to have solved the issue.

Assumptions were made to also represent other features of the TMM. Blocks that represent perforated zones in the real experiment had their conductivities multiplied by factors that represent the influence of the holes and bolts.

Notable examples include the corner feet and internal ledges. Parallel to the axial direction of the bolts, equivalent conductance was reduced by the transversal area of the bolt, but on the other hand increased by the presence of the metallic bolt itself.

Similarly, on directions perpendicular to the bolts installed the resulting conductivity has reduction defined by the rectangular transversal area that represent the material removed on the hole.

For the connectors, which have their axial thermal conductivities determined based on estimations of material composition, this task was performed by visual reference, and for this reason was expected to be prone to higher uncertainties.

The bonding of heaters and thermistors to the slot face within the sample holders covered a significant part of its area. Then, the resulting optical properties of this surface are different from that of machined aluminium. Thus, the effective emissivity and thermal capacity had to be estimated. Figure 6.12 shows how this bottom face is covered with attachments.

Figure 6.12 – Sample Holder Bottom Attachments.
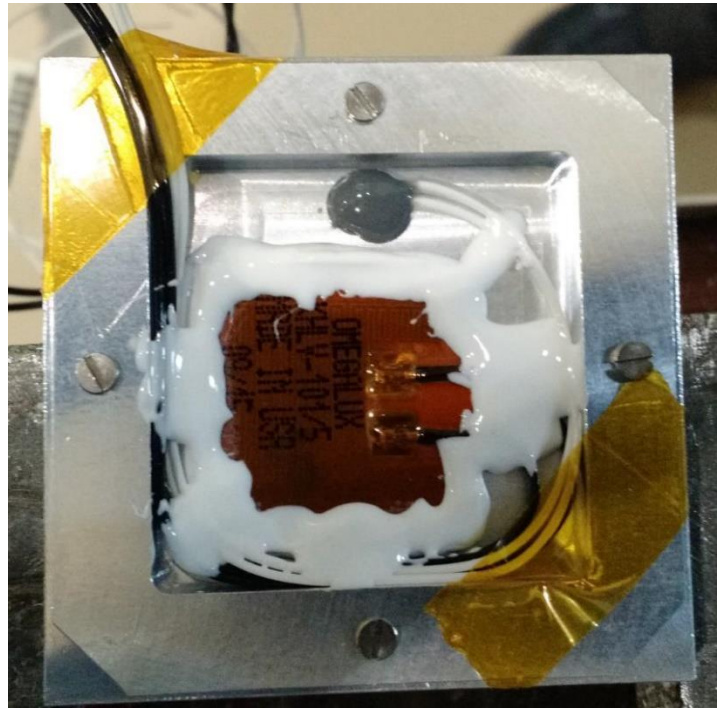
Source: Costa et al. (2018).

Additionally, all those attachments needed a reasonable quantity of binder as observable in Figures 3.5 and 6.12, which means that the holders' subassembly had its mass altered. Therefore some freedom of adjustment was allowed to the sample holders thermal capacity when it comes to transient simulations as well as their thermal contacts.

Linear conductors represent the cables and have conductance estimated based on their diameters. They were not represented on all of their lengths, but only connecting the sample holders to the closest contact point on the box. Their layout is illustrated in Figure 6.13.

Figure 6.13 – Comparison of the Modelled Conductors to the Real Cables.
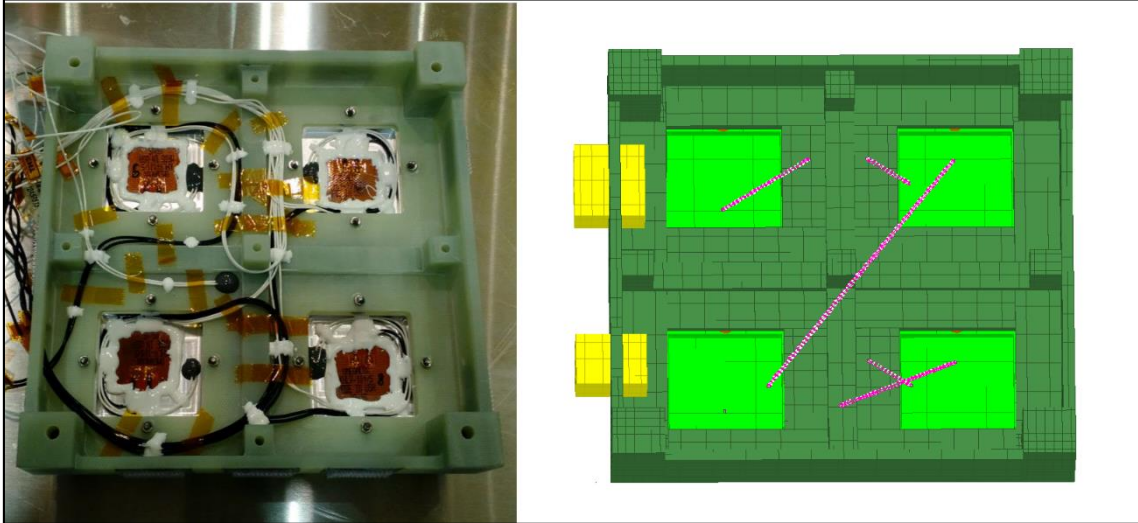
Source: Prepared by the author.

Finally, in order to represent the different environments the equipment was exposed to, two different TMM models were created: one for ground test simulation and another for flight representation. This separation was considered helpful for keeping the simulated cases organized.

The internal setup and parameters are equivalent for both, but external couplings and boundary conditions are different, thus the use of two models avoids some recurrent manual modifications needed to execute case studies runs.

6.3 Model parameterization

Definition of symbols to parameterize the pertinent heat transfer properties was broadly used along the TMM. Their use made some tasks easier to perform, like sensitivity analyses and parameter tuning. At times, they also served to test compositions of thermo physical and optical properties proposed to some parts, such as the aforementioned case of the holders slot face.

Mainly, parametric symbols were used in areas of the model where the thermal behaviour was of difficult predictability Boundary conditions were also conveniently represented by symbols.

Given the considerable amount of detail the proposed geometry for the TMM, many parametric symbols were created. They can be grouped in different classes:

a) Contact conductance/resistance adjustments. Each of the separated surfaces of parts that touch each other had parameters defined that quantify their particular contact conductance. In adjustment procedures, they were varied within plausible ranges during sensitivity analyses.

b) Directional conductivity tailoring. As mentioned previously, some blocks used to build a composition to represent a given part have a special feature: they had also to capture characteristics of accessory components that were not geometrically represented in the TMM, as bolts for instance. Thus, factor parameters were defined to some blocks that can enhance or reduce their effective conductivities in a given direction. Examples of such blocks are the feet and internal ledges.

c) Block soldering. In order to make separated blocks to behave as a continuous solid, they had to be thermally coupled by virtual high intensity surface conductances. However, numerical limits exist to these virtual couplings: if they were defined with too high values, source terms seem to be affected in such a way that the software was less capable of balancing transport Equations.

d) Linear conductor approximations. Linear conductors are used to model different phenomenon like conduction on the cables.

e) Temperatures of boundary conditions. On the TMM variants some points could be seen as boundary conditions. Symbols were assigned to them to easily assess the impact they may have on the TMM. Examples: mounting panels and chamber shroud temperatures, space node.

f) Optical properties of surfaces. Even though emissivity and absorptivity can be measured on the ground with reflectometers, changes to these properties are not uncommon. They may occur between lab testing and orbit deployment. Causes vary, but range from facility contamination to orbit induced oxidation.

g) Heat loads. Sun flux, heater input and satellite internally produced heating are prone to variations and for this reason were also parameterized. For example, sun flux parameter was used to replicate environmental conditions throughout the year.

h) Ageing factors. In order to facilitate modification of degradable thermo physical and optical properties during the orbital mission lifetime, they were written in expressions with secondary symbols as terms that express the state of known degradation of a given property. Linear aging model is assumed for any property p:

$$p = (1-s)p_{BOL} + sp_{EOL} \tag{6.1}$$

Where s is relative to the mission life, varied from 0 to 1.

i) Variable dimensions. Some components were planned to be studied when they assume different geometries. Notably, this is the case of the MLI external blanket. Parameters related to the dimensions of the blocks were defined in function of the desired thickness, which is also a symbol.

j) Property weighting. Parameters were also defined for use in properties compositions. They are applied in locations where the estimation of a hybrid property is related to another characteristic of the subassembly. To cite an example: the mean optical properties of the slot surface of the sample holders, which estimation depends on the area of the attached components (binder, heater, cables, etc.).

6.4   Radiation analysis groups

The participating surfaces on the radiation heat transfer were separated into different radiation groups to organize and reduce TMM computational cost.

In total, three radiation groups were used. The first contains the experiment external surfaces and surfaces of the vicinity. Meanwhile the second contains surfaces oriented inwards, to the inside of the box. The last group is made of surfaces within the gap between mounting the panel and lid external MLI.

For visual reference, these groups are illustrated in Figures 6.14 to 6.16. Comparing TMM versions intended to replicate ground tests and flight, the external group was the one with most differences. Active faces are shaded in green colour.

Figure 6.14 – External Radiation Group Active Faces.
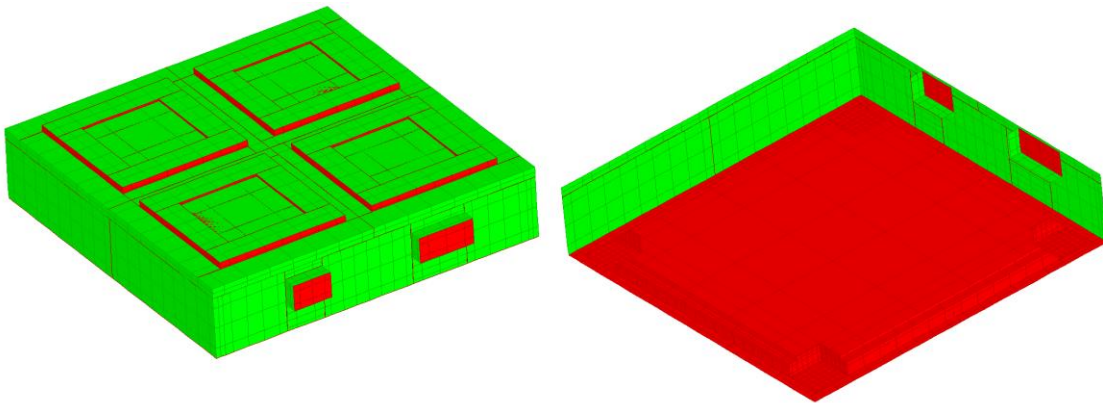
Source: Prepared by the author.

Figure 6.15 – Gap Cavity Radiation Group Active Faces.
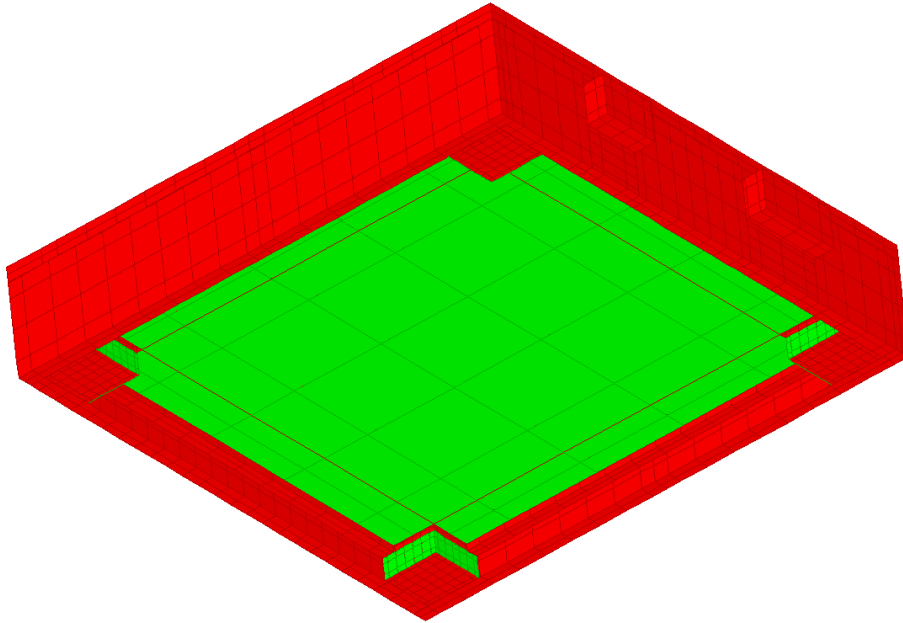
Source: Prepared by the author.

Figure 6.16 – Internal Radiation Group Active Faces.
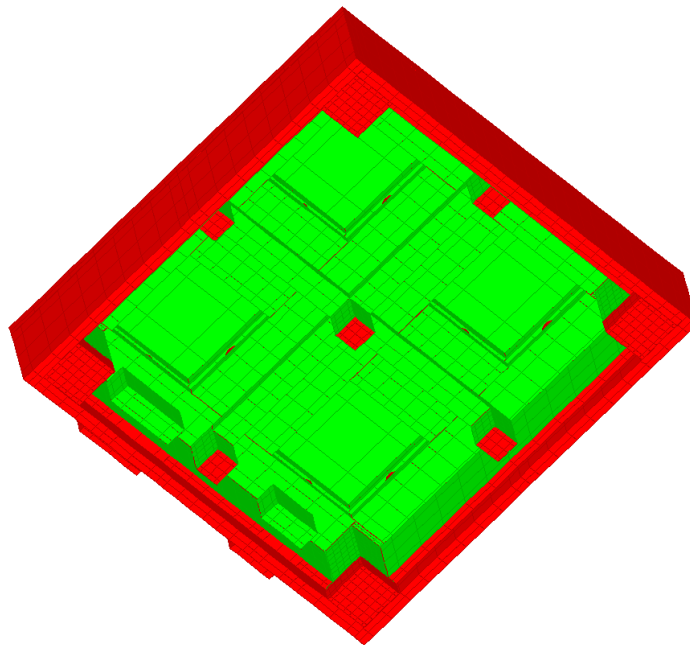
Source: Prepared by the author.

The ground test representative has a vicinity made of TVC shroud and the mounting plate. On the other hand, the flight case vicinity is made of satellite closest panels, antennas supports and space node. The internal radiation group is the same in both cases. The only surface modified in the gap group between TMM versions is the experiment mounting substrate.

It is possible to recognize in Figure 6.14 that the tips of the connectors were maintained out of the radiation group. This was adopted because linear connectors were already attached to the tips.

An examination to the Figure 6.15 shows that sections of the internal surfaces of the box MLI see the gap cavity but are not included in this radiation group. This was adopted because the real external MLI laterals are bent outwards in the region of the edges that are closer to the mounting substrate.

At last, it is possible to verify in Figure 6.16 that all internal surfaces are active, including the bottom surface of the skirts in the sample holders. Washers were not included because they add complexity to the Monte Carlo ray tracing without considerable gains. The top face of the lid, which is removed from Figure 6.17, also participates in this radiation group and is MLI insulated with a dedicated geometry, similar to the box MLI.

6.5 Parameter adjustment echniques

Parameters adjustment is an important task to obtain a representative and reliable TMM. This stage consists of applying modifications to the symbolic parameters defined in the model, which shall approach the model thermal behaviour to the experimental data.

Primary information used as a reference for the adjustment procedures was the data gathered from SN02 FM TBT, executed in September, 2019. Further details of this test were described in Chapter 5.

Frequently, parameter setting relies on repeating solver runs with the model on different parameter configuration. Thus, the general tendency is that the more

parameters a model has, the longer it takes to close the gap between output and experimental data.

Firstly, the process begins setting all the parameters to theoretically estimated values. Ideally, empirical Equations found in the literature could be used as references, but they not always are precise and available.

Silva (2014) for instance, details strategies used to determine equivalent conductances of satellite structural elements. Additionally, he describes experimental findings on MLI effective properties TVC testing. His approach to insulating washers had been adopted in this TMM.

Fontenot and Whitehurst (1968) present a useful method for the prediction of bolted joint resistance given an applied torque, which was also used to estimate conductance values.

Costa (2018) discusses factors that influence the contact interface resistance, which had to be taken into account.

An illustrative example on the technique used for computing equivalent conductance is described on Appendix I.

The described adjustment process that follows is also schematized in the flowchart in Figure 6.17.

Figure 6.17 – Parameter Adjustment Flowchart.
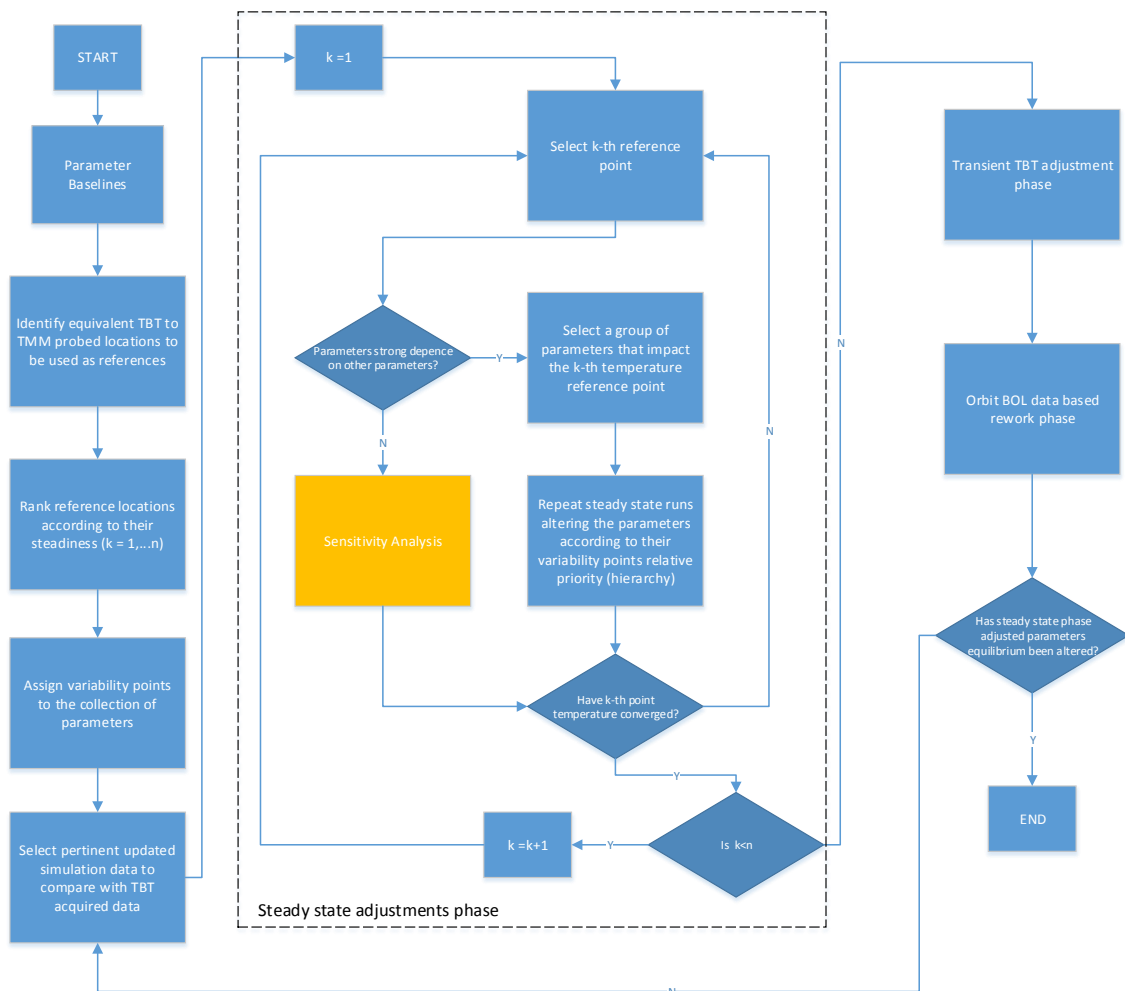
Source: Prepared by the author.

6.5.1 Steady state cases adjustments

The same temperature sensor points were observed in the TMM, both thermistors and thermocouples.

The acquisition points that present reduced temperature amplitudes (less sensitivity) are considered steadier. Thus, following a ranking defined by the steadiness level, a priority order is established among temperature probing locations.

It was detected by numerical tests and sensitivity analysis that temperature monitoring points that are less prone to temperature variations when exposed to the same testing conditions conformed better to the experimental data before other less stable points could do so.

In general, steadier temperature points are part of higher thermal capacity components such as the FR4 box, and are linked to more insulated regions.

The following novel strategy for the adjustment procedure of the model was developed.

From all parameters, a subgroup of parameters is chosen arbitrarily. This subgroup is composed of parameters that are suspected of being linked the present TMM adjusting point.

Next, the parameters in this subgroup are classified into arbitrary groups of enhanced variability. To these variability groups were fit the following criteria:

a) materials, which nature can facilitate thermal properties inconstancies.

b) fabrication processes, which usage has poorly mapped thermal developments.

c) assembly procedures, which can influence the contact thermal resistances and areas for internal radiation heat transfer.

d) bridging locations, which tend to present non-intuitive heat flows directions.

e) special features, which rely on theoretical estimations that may be inaccurate.

If a given parameter is within one or more of the above criteria, it is assigned a score that corresponds to the number of criteria met. Examples: if a parameter meets 2 criteria, it scores 2 points; if another parameter meets 5 criteria, it scores 5.

After ranking the temperature probing locations, picking one of them according to their hierarchy, selecting a subgroup of parameters linked to the picked point,

and assigning variability scores to the parameters of this subset, an iterative adjustment process can then be kick-started using TBT steady-state data.

The principle is to first try making steadier temperatures approach the correspondent test data within a ± 2 °C margin in one of the TBT temperature plateaus.

This is done by acting exclusively in the elected subgroup of parameters that were mentioned before.

Within a given subgroup of parameters that is linked to a temperature probing location in the TMM, the tuning process for adjustment should respect a hierarchy between the parameters themselves. The higher the variability score of a parameter, the higher priority it has on modifications.

Alternatively to the parameter variability score approach, a sensitivity analysis may be performed to measure how each of the parameters impact on the temperature of TMM location currently being adjusted.

The process described in the previous paragraphs is then repeated for the remaining TMM temperature monitoring probe locations.

After the lower ranking location is adjusted, one should return to the higher ranking location and repeat adjustments once again.

This iterative repetition is deemed necessary because the first locations adjusted may be affected by temperature adjustments of the lower ranking locations that follow. It is expected to make the temperatures converge, though.

At this stage, since only steady-state is analysed, the parameters that have an impact only on the heat capacity shall not be used.

6.5.1.1 Example of parameters hierarchy assessment

Supposing that one thermal conductivity parameter is under scrutiny and that it is applicable to a FR4 washer. It will be referred to as 'washer thermal conductivity'.

As it relates to a part that is made of composite material, it scores one point according to variability criterion 'a'.

The machining process used to produce the washer does not influence on its conductivity, no point scored due to criterion 'b'.

The same applies for the bolting procedure, which does nothing to the washer internal conductivity, no point for criteria 'c' then.

Heat on washers goes from holders to box in heating conditions and otherwise in cooling, then as the heat flow direction is pretty predictable no points are scored according to criterion 'd'.

As the modelled washers represent both real washers and attaching bolts, this conductivity may reflect a composed conductivity and thus it is classified as having a special feature, which makes it meet criteria 'e' and scores an additional point.

A total of 2 out of 5 points were accumulated for the 'washer thermal conductivity' parameter.

On the other hand, if a 'foot interface conductance' was put under scrutiny, it would score a total of 4 points out of 5, as follows.

This interface conductance depends on the contact of composite material, thus its variable thermal properties can affect the junction. So one point is scored for meeting criterion 'a'.

The machining process is related to the interface finishing and thus affects the interface conductance magnitude. An additional point for criterion 'b' is scored.

Used torque on assembly may affect the interface conductance as well, then it makes this parameter score on criterion 'c'.

Heat flow directions are intuitive while the experiment heats or cools, no point due to criterion 'd'.

Finally, the interface conductance also concentrates the bolt heat interaction with the mounting panel and this makes it a special feature, scoring in criterion 'e'.

When compared, 'foot interface conductance' has more points of enhanced variability than the 'washer thermal conductivity' parameter. Therefore, between these two, the referred interface conductance will be of higher hierarchy and therefore a priority on the symbolic parameters adjustment efforts.

As this parameter classification process is arbitrary, the same weight was attributed to all variability criteria. Their weighting could be an object of future investigation, though.

6.5.2 Transient cases adjustments

When the TMM parameter setup is evaluated in terms of transient behaviour, the TBT transient curves shall be used as reference.

They can be closely replicated by imposing variable boundary conditions in the TMM as arrays of TBT measured temperatures of TVC.

Besides, in order to reduce the time spent on adjustments, only the thermistors temperatures may be used as a reference at this stage.

The curve adjustments may now be performed by first tuning the parameters of properties that were not altered before. In other words, the only parameters that impact the heat capacity.

For the adjustment OSR degradation experiment TMM, tuning the individual sample holders and FR4 heat capacities was enough to adjust the curves.

Other parameters altered on steady-state cases may also be of some impact, but they pale in comparison to heat capacities relevance.

6.5.3 Orbit data rework

In order to enhance the experiment representativeness further, BOL preliminary orbit data may be used as a reference to act over parameters that were not possible to deal with in a laboratory environment. As examples of such parameters, one may consider MLI blanket solar absorptivity or MLI thickness.

Alternatively, parameters that express quantities that may vary from the experimental setup to the satellite panel mounting may also be explored, such as the feet interface contact resistance to the mounting panel. These parameters are in general external to the box assembly.

It was discovered that the tune up of some parameters based on-orbit data insights has been capable of altering the parameter equilibrium obtained in the previous phases, which were based solely on ground test data. This produced an additional iterative loop procedure.

Previous phases had to be revisited to find alternative sets of variables that were capable of delivering the same results. As many parameters were used, different combinations indeed produced similar results.

6.6   Sensitivity analysis

Based on the detailed TMM, a comprehensive sensitivity analysis was performed. With relative small variation of some parameters, dp/p, the responses in 5 OSRA temperatures (4 samples and box) have been obtained for its orbital maximum and minimum values (dTmax/T, dTmin/T). Therefore, the non-dimensional sensitivity coefficient K of a temperature variation δT in response to small variation of a parameter p is defines as:

$$K_p^T = \frac{\delta T}{\delta p}\frac{p}{T}$$

(6.2)

The flight TMM final version has shown sensitivity to selected parameters as reported on the Table 6.1, which can be complimentary to the parameters classification procedure proposed before and may be helpful to solve ambiguities.

Table 6.1 – Flight TMM parameter Sensitivity.

Input / variation in parameter:	Output Responses:									
	$T_{o1,min}$	$T_{wt,min}$	$T_{o2,min}$	$T_{bk,min}$	$T_{bx,min}$	$T_{o1,max}$	$T_{wt,max}$	$T_{o2,max}$	$T_{bk,max}$	$T_{bx,max}$
Temperature of satellite panel	2.81E-1	2.76E-1	2.66E-1	2.81E-1	3.37E-1	2.68E-1	2.56E-1	2.55E-1	1.99E-1	3.37E-1
OSRA MLI thickness	1.09E-2	-0.95E-2	1.27E-2	0.85E-2	0.20E-2	1.16E-2	1.95E-2	1.16E-2	-0.35E-2	0.46E-2
OSRA MLI external emissivity	-6.69E-2	-6.81E-2	-6.38E-2	-6.48E-2	-7.03E-2	-6.78E-2	-6.88E-2	-6.68E-2	-4.84E-2	-6.68E-2
Thermal contact conductance btw. feets and panel	5.73E-4	5.64E-4	6.45E-4	5.16E-4	7.05E-4	-1.41E-3	3.16E-3	2.52E-4	1.64E-3	1.05E-3
Effective thermal conductance with connector	1.13E-2	6.49E-4	9.59E-4	5.31E-4	-2.80E-4	~0	2.22E-3	-2.90E-4	-4.10E-3	3.46E-4
Power supply voltage	1.58E-1	1.53E-1	1.73E-1	1.56E-1	1.06E-1	1.36E-1	1.29E-1	1.50E-1	1.00E-1	0.93E-1
Sample subassembly thermal capacities	1.36E-2	1.39E-2	1.39E-2	1.54E-2	1.17E-2	-1.17E-2	-1.32E-2	-1.15E-2	-2.73E-2	0.39E-2
FR4 box effective thermal capacity	5.16E-3	5.79E-3	6.19E-3	6.42E-3	10.81E-3	-3.66E-3	-2.79E-3	-4.41E-3	-3.38E-3	-11.9E-3
Absorptivity of bk sample	6.19E-3	7.73E-3	5.92E-3	6.14E-3	8.39E-3	4.69E-3	9.72E-3	7.62E-3	1.55E-1	2.45E-2
Emissivity of bk sample	-8.97E-3	-1.16E-2	-9.85E-3	-5.83E-3	-1.53E-2	-7.73E-3	-1.03E-2	-1.26E-2	-7.13E-2	-1.82E-2
Absorptivity of wt sample	4.47E-3	5.53E-3	4.36E-3	3.93E-3	5.32E-3	4.73E-3	3.33E-2	4.65E-3	3.29E-3	8.16E-3
Emissivity of wt sample	-1.86E-2	-6.06E-2	-1.72E-2	-1.47E-2	-2.51E-2	-1.27E-2	-6.23E-2	-1.16E-2	-7.68E-3	-2.19E-2
Absorptivity of o1 sample	-7.97E-5	-1.89E-4	-2.32E-4	-2.65E-4	-1.98E-4	8.38E-3	-2.95E-4	1.71E-4	-1.00E-3	4.61E-4
Emissivity of o1 sample	-5.98E-2	-7.05E-3	-4.53E-3	-4.37E-3	-1.08E-2	-6.56E-2	-6.62E-3	-2.54E-3	-6.66E-3	-1.15E-2
Absorptivity of o2 sample	7.87E-4	1.11E-3	1.47E-3	9.54E-4	1.25E-3	3.8E-4	1.44E-3	1.89E-2	6.80E-4	2.69E-3
Emissivity of o2 sample	-1.43E-2	-2.20E-2	-7.03E-2	-1.68E-2	-2.33E-2	-6.98E-3	-2.22E-2	-7.25E-2	-1.07E-2	-2.14E-2

From Table 6.1 its is possible to observe that solar absorptivities have increased influence to maximum sample temperatures, whereas IR emissivities on minimum temperatures. Interestingly, the OSR1 sample seems coupled to the connector in such a way that almost no influence is perceived by its maximum temperatures. Unsurprisingly, a high dependence of the temperature contours hinge on the satellite panel temperature and on the electrical power dissipated by heaters.

7 TMM PARAMETER CORRELATIONS BASED ON THE TBT

7.1 Boundary conditions for TBT test environment TMM

In order to mimic TBT boundary conditions, the test setup digital twin was reproduced in detail for the TMM.

As shown in Figure 7.1, the box sits on a pink coloured surface that simulates the intermediate base plate, which has temperature independently controlled from the shroud. This plate is made from stainless steel and its surfaces are mostly exposed, without insulation attached.

The shroud is represented as the hollow orange cylinder, which one of its ends has been suppressed in Figure 7.1.

Figure 7.1 – TBT Geometry Replicated on the TMM.
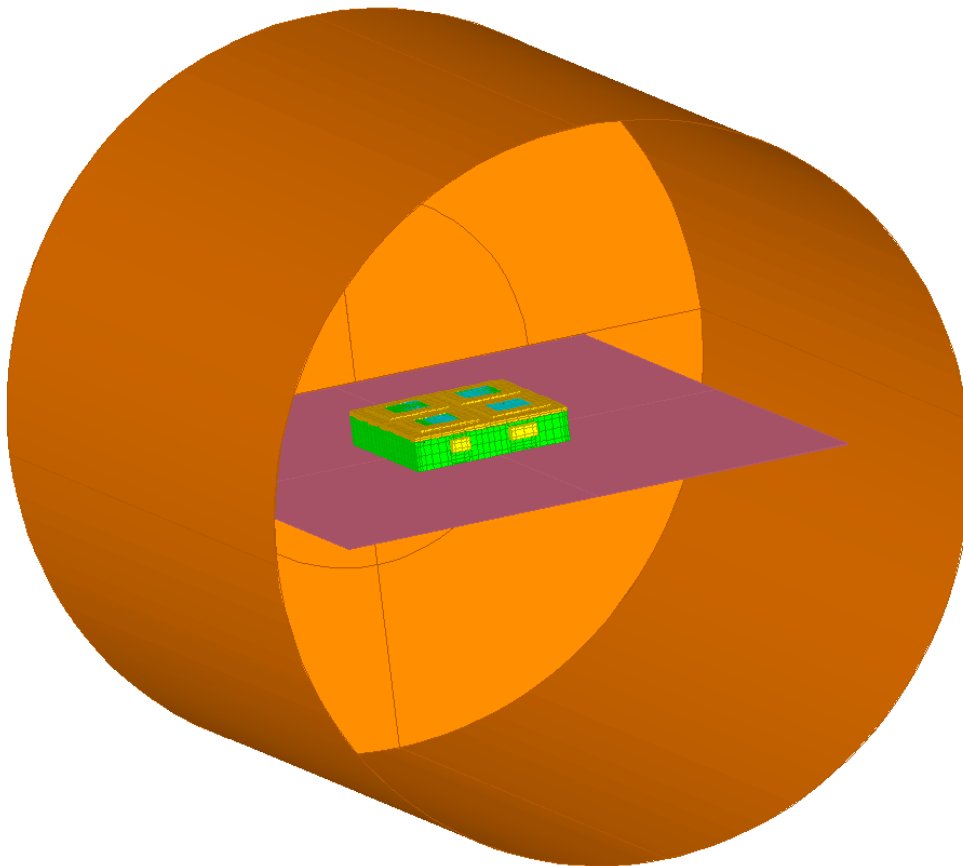
Source: Prepared by the author.

Different boundary conditions strategies were used depending on the phase of the TBT that was employed as reference.

On steady-state TBT temperature plateaus, the chamber and the plate were configured as boundary nodes to assume constant setup temperatures.

Subsequently, as transient phases were studied the chamber and plate temperatures were not kept constant. Instead, their behaviour followed the same path of the measured temperatures on the real components that took part in the TBT, which have typical variations. Thus, their temperatures were defined by arrays of temperature and time values acquired during the test.

7.2 Main parameter adjustments

As a means of reference, Table 7.1 condensates some important parameters adjusted based on the unit TBT acquired data.

Table 7.1 – Selected Adjusted Parameters.

Parameter Description	Value
Relative contact conductance between feet and plate	8 W/m²K
External MLI thickness	0.005 m
Relative contact conductance between MLI and holders laterals	12 W/m²K
Lid internal MLI effective emissivity ($\varepsilon*$)	0.01
Heaters thermal load	0.405 W
FR4 thermal capacity	800 J/kgK
Sample holders subassembly composed thermal capacity	1400 J/kgK
Washers interface contact conductance	0.03 W/K
Contact conductance between MLI and box to emulate radiation	0.15 W/m²K

8 TMM COMPARISON TO FLIGHT DATA

8.1 Boundary conditions for the flight environment TMM

During the flight, the assembly mounted in the satellite experiences boundary conditions that are different from the test environment.

The main difference is exposition to heat loads in the solar spectrum, which were not simulated during the ground tests. Beyond radiation inputs, the experiment sits on a satellite panel that is made of honeycomb aluminium panels covered by MLI blanket. The panel may vary its temperature to some extent due to electronic equipment attached to the opposite (internal) side of the honeycomb structure being used or not.

Close to the experiment mounting points, two antennas and the star sensor are positioned. Due to their proximity, they were anticipated to produce shadows and additional heat loads from reflected radiation towards the box. Their influence, therefore, was thought to be considered only in what relates to optical phenomena. For that reason, they were modelled on the in-flight TMM version according to surface information available on 'as-built' mechanical datasheets.

The equipment was mounted in panel SM-15, but SM-16 and the external part of the SM-05 cylinder were also added because they also make view contact the experiment, Figure 8.1.

For solar heat load calculation, CBERS 04A typical orbit parameters and attitude were used as inputs. Those made the satellite to cross the Equator descending at 10:30 a.m. local time (± 10 minutes), which means that the angle between right ascension (RA) of Sun and RA of the satellite descending node is 22.5 ± 2.5°.

Also considering the orbit inclination (of 97.8963°±5°) and variation of the Sun declination (from -23.4° to +23.4°) along the year, geometrical calculations lead to a value of the β angle (between Sun vector and orbit plane) from 12.5° and 27.9° during the year. As the Z- surface is normal to the orbit plane, the maximum possible solar heat input is reduced by a factor of cos(β).

In other words, if hot and cold case solar constants are about 1420 W/m² and 1330 W/m² respectively, the expected peak solar heat inputs to be experienced on Z- face are approximately 1255 to 1386 W/m² for the hot case and 1175 to 1298 W/m² for the cold case. Muraoka (2017) has predicted a similar scenario, as shown in curves plotted in Figures 8.2 and 8.3, for cold case (June 22, descending passage time of 10:40h, orbit inclination 98.8963°) and hot case (December 22, descending passage time 10:20h, orbit inclination 98.8963°), respectively. Keplerian orbit parameters used in the TMM for the orbit are represented in Figure 8.4 for the hot case scenario.

Figure 8.1 – Satellite Vicinity Geometry Replicated on the TMM.
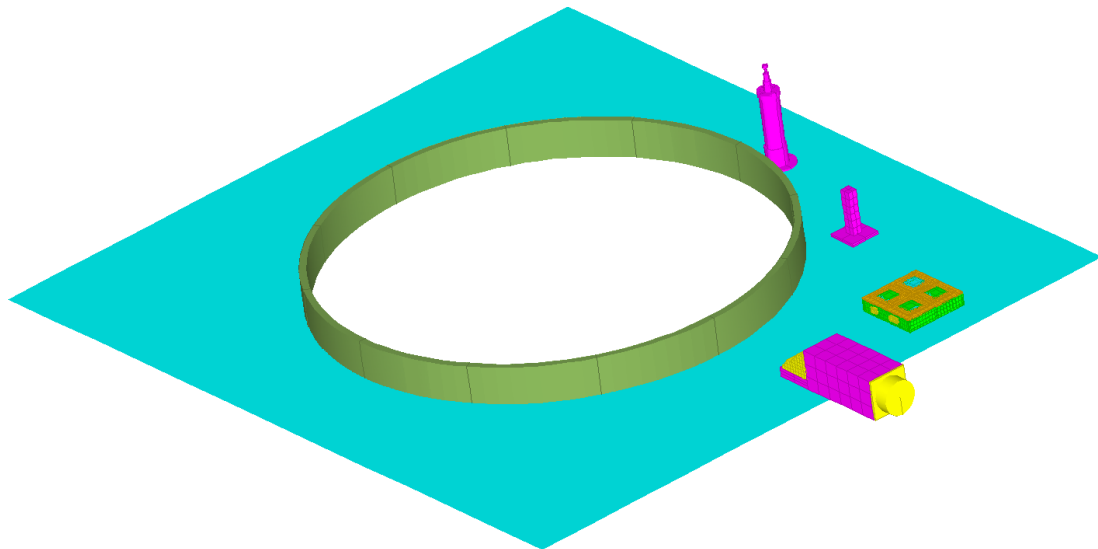
Source: Prepared by the author.

Initially, the satellite panels temperatures were expected to be kept at about 20 °C, but telemetry later confirmed that SM-16 temperatures are maintained on approximately 15 °C. There are no temperature sensors on the panel SM-15 where OSRA is installed. However, it is expected that the panel average temperature should not run out far from SM16 temperature. The MLI blanket

that protects the panels is configured to use the same setup as the satellite TBT.

The real equipment mounted to the satellite had differences on its MLI blanket compared to the one used in ground tests, which makes it prone to additional variability in flight. Such differences were fastening lines that touched the sample holders, and the outermost layer of aluminized kapton that is thinner and it has an additional ITO layer. The thinner layer is expected to affect the MLI solar absorptivity.

Figure 8.2 – Calculated Incident Solar Flux for Nominal Cold Case.
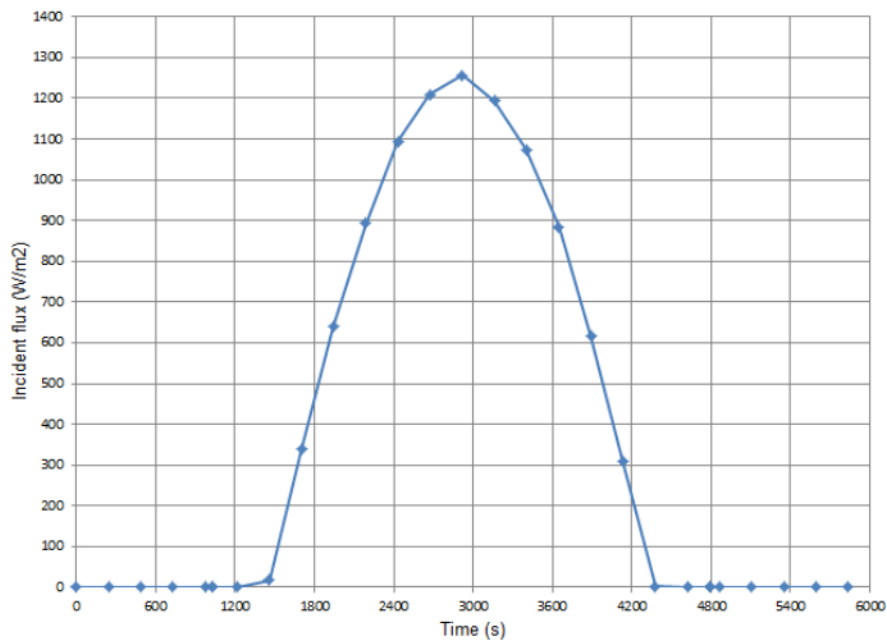
Source: Muraoka (2017).

Figure 8.3 – Calculated Incident Solar Flux for Nominal Hot Case.
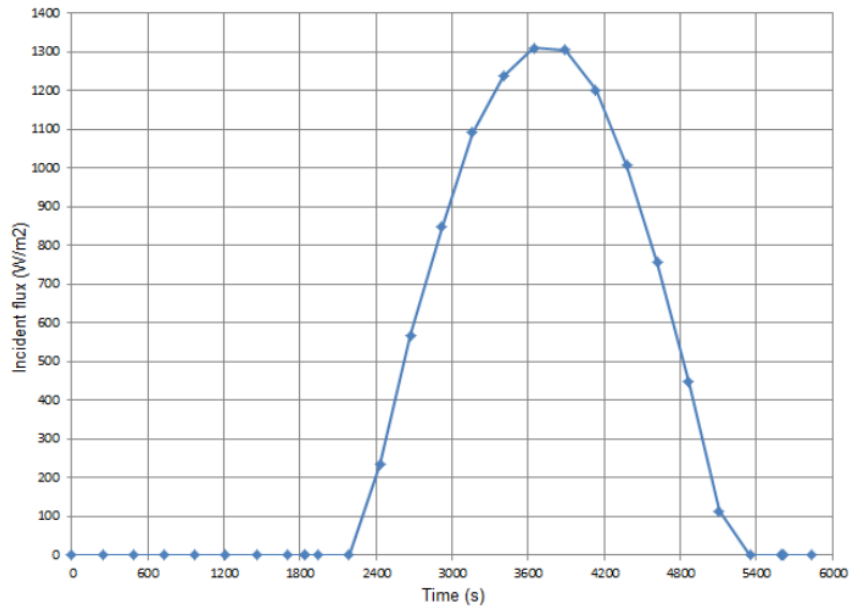
Source: Muraoka (2017).

Figure 8.4 – TMM Orbit Keplerian Elements for hot case.

Source: Prepared by the author.

8.2 Preliminary results

A comparison between in-flight data and TMM output can be made if one contrasts Figures 8.5 and 8.6, which are a sample of cold case temperatures and a selected timespan of simulation results.

91

As observable in these Figures, maximum temperatures are compatible. Occurring peak temperature order also is replicated on the TMM. Temperature ranges are plausible and the temperature derivatives seem to be quite similar.

On a first glance, OSR2 seems like an exception to the good agreement between data and simulation. But this temperature is not represented with the needed correction in Figure 8.5, as its thermistor imposes a shift to temperatures as verified during unit TBT.

For the cold case TMM output represented on Figure 8.6, the solar absorptivity of the white paint is $\alpha_{wh} = 0.26$, and for the OSR samples $\alpha_{o1} = \alpha_{o2} = 0.07$. The white paint absorptivity was performed based on measurements presented by Reumary et al. (2011) for MAP SG121FD in a similar satellite and time, and OSR absorptivities adjustments followed.

Unfortunately, in-flight data from the hot case was not available. However, TMM projected temperature curves are drawn in Figure 8.6. It is possible to notice that temperatures the eclipse phase remain almost unaltered between 8.5 and 8.6. This effect is desired because at this phase only additional accumulated heat has to be the predominant factor that affects the minimum temperatures.

In general, it is possible to infer that the TMM has acquired promising capabilities for reproducing the samples' thermal behaviour.

Figure 8.5 – Cold Case In-flight Data Sample.
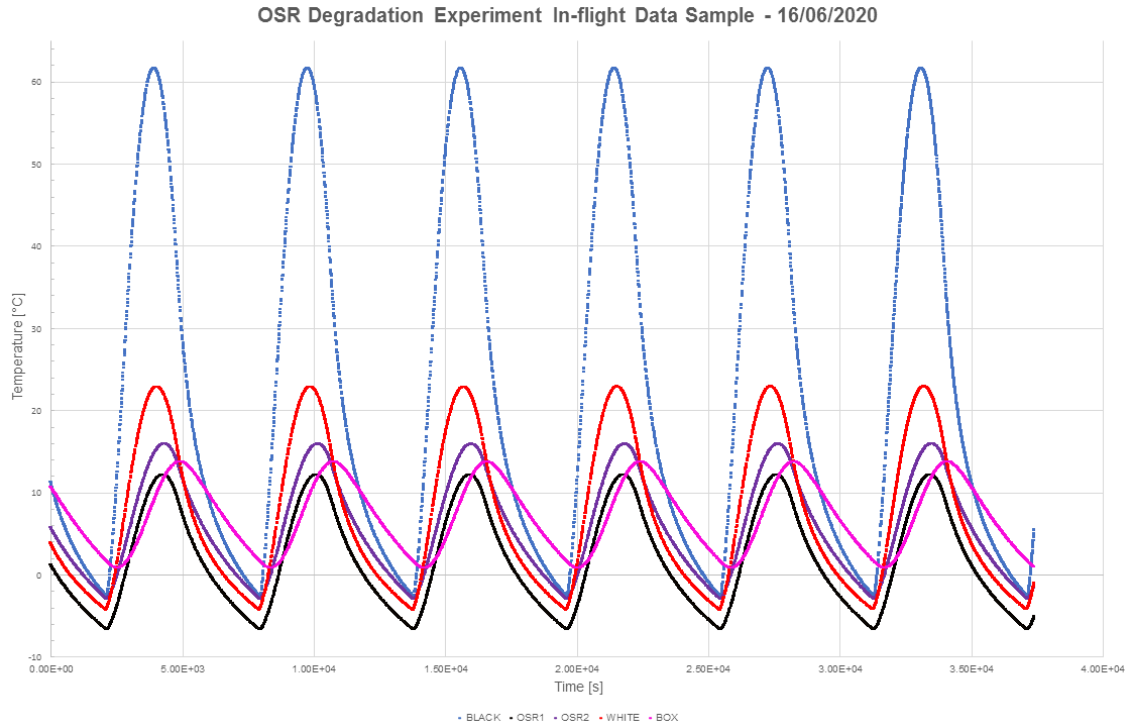
Source: Prepared by the author.

Figure 8.6 – Preliminary TMM Orbit Curves on Cold Case.
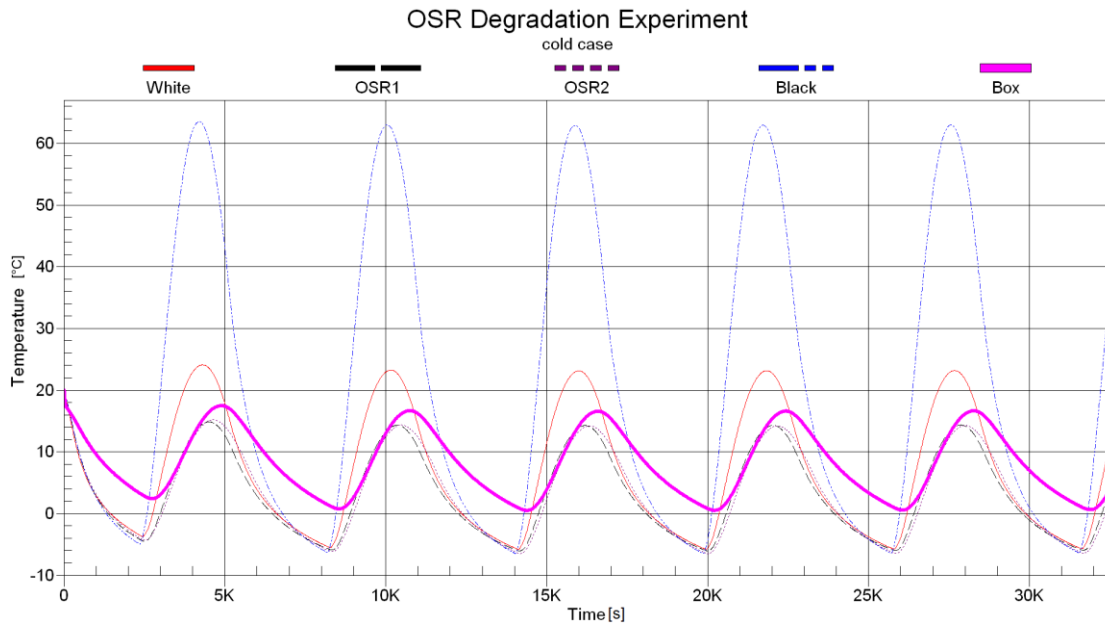
Source: Prepared by the author.

Figure 8.7 – Preliminary TMM Orbit Curves on Hot Case.
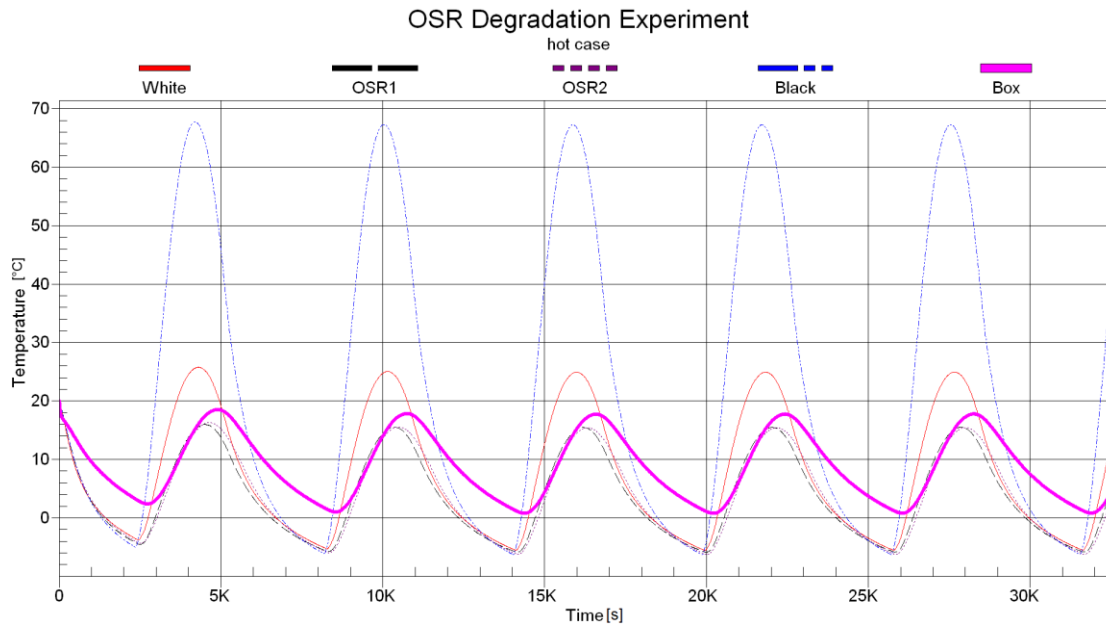
Source: Prepared by the author.

9 ALGEBRAIC ANALYTIC MODEL

In parallel to the detailed numerical TMM development, an approach to use simplified analytical models was also explored. Such models may help to understand better the thermal interaction and mutual influence of main parameters of the OSRA samples. The analytical models may also predict the sample temperatures general tendencies and derive useful preliminary results.

The first concepts involved methods to deduce the absorptivity of the samples simply by manipulating the basic thermal balance Equation used to represent the heat coupling on each sample. To be more specific, the primary idea was to use temperature telemetry data on them as inputs so to indirectly calculate α values. The basic transient thermal balance for each of the samples in relation to a common reference point is mathematically described by the following expression:

$$C_m \frac{dT_{sample}}{dt} = Q_{heater} + \alpha q_s A + G_L (T_{ref} - T_{sample}) - \varepsilon \sigma A T_{sample}^4 \tag{9.1}$$

Where C_m is the sample's thermal capacitance, q_s is the heat flux in solar spectrum (deduced from the reference sample – black anodized), A is the sample's area, G_L is the parasitic thermal conductive coupling between a sample and a selected reference point which represent average box temperature. Other terms may be present: for example, additional parasitic couplings in the box interior, but this tends to be of reduced importance and will be omitted at this point for simplicity for a while.

Notably, the inversion of Equation 9.1 reveals that a direct data extraction may be exposed to measurement noise. Beyond this initial claim, Millard (1968) has investigated algebraically many additional uncertainties the balance Equation is subjected to.

Hence, there is a need for developing a data conditioning algorithm to smooth the acquired information. This algorithm may shed some light to aspects of the problem and can be attempted using the known boundary and tie conditions.

Alternatively, if one considers the fact that the layout of the proposed experiment makes it complex in geometric terms, it is reasonable to assume that a mathematical model based solely on Equations originated on 9.1 is prone to poorly mapped thermal interactions. An oversimplified model may not provide all necessary details of multiple and not well defined heat transfer links acting between the points of interest. Since multiple trajectories for heat flows in the interior of the experimental box are possible, alternatives to represent the problem should be considered.

A refined numerical model (TMM) used to represent more accurately the geometric nuances has the potential to be a powerful tool and provide means to solve this inverse problem, but at a cost of considerable computational resources. Consequently, analytical means to solve this problem retain some appeal.

9.1 Simplified lumped parameter model (SLPM)

The present experiment model is composed of 4 transient heat balance Equations that can be expressed mathematically by Equations 9.2 to 9.5.

$$C_{m,o1}\left(\frac{dT_{o1}}{dt}\right) = Q_{h,o1} + \alpha_{o1}q_s A + G_{L,o1}(T_{box} - T_{o1}) - \varepsilon\sigma A T_{o1}^4 \qquad (9.2)$$

$$C_{m,wt}\left(\frac{dT_{wt}}{dt}\right) = Q_{h,wt} + \alpha_{wt}q_s A + G_{L,wt}(T_{box} - T_{wt}) - \varepsilon\sigma A T_{wt}^4 \qquad (9.3)$$

$$C_{m,o2}\left(\frac{dT_{o2}}{dt}\right) = Q_{h,o2} + \alpha_{o2}q_s A + G_{L,o2}(T_{box} - T_{o2}) - \varepsilon\sigma A T_{o2}^4 \qquad (9.4)$$

$$C_{m,bk}\left(\frac{dT_{bk}}{dt}\right) = Q_{h,bk} + \alpha_{bk}q_s A + G_{L,bk}(T_{box} - T_{bk}) - \varepsilon\sigma A T_{bk}^4 \qquad (9.5)$$

Where the indexes o1, wt, o2, and bk were adopted as a convention indices to identify samples of coatings OSR1, white paint, OSR2 and black anodized respectively. Alternatively, a general Equation for any sample 'i' may be written as:

$$C_{m,i}\left(\frac{dT_i}{dt}\right) = Q_{h,i} + \alpha_i q_s A + G_{L,i}(T_{box} - T_i) - \varepsilon\sigma A T_i^4 \tag{9.6}$$

As all samples share the same surface area A, a common symbol was adopted for all samples. Although the electric heaters used in the assembly have slight differences in their resistance, they are close enough to assume that are capable to dissipate the same heat Q_h for each sample. It is worth remembering that all heaters are connected to the same voltage source offered by the satellite bus of 28V, which is regulated and very stable.

9.1.1 Temperature curves typical characteristics

The best SLPM solution found up to the present date was developed based on some preliminary findings from: analyses of typical orbit characteristics, balance Equations rewriting attempts, as well as temperature data from the first TMM versions.

Although inaccurate, such temperature data was fundamental to understand sample temperatures general tendencies, which were later confirmed with actual flight data.

Before diving into the mathematical specificities of the referred solution, it is necessary to explore some of the concepts these analyses produced.

Firstly, the experiment temperatures were found to have a repetitive behaviour that can be broken down into phases. These phases may have some variations in shape and duration, but are likely to occur in a regular orbit cycle without

special manoeuvres. Figure 9.1 demonstrates the aspect of the temperature curves.

Figure 9.1 – Typical In-Flight Behaviour of the Sample Temperatures.
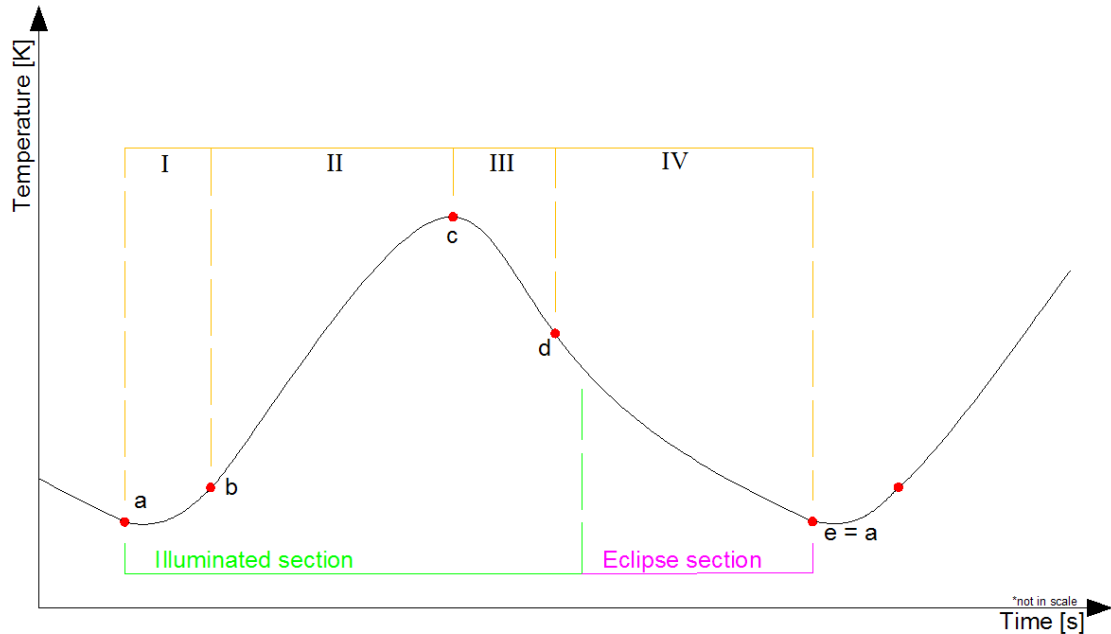
Source: Prepared by the author.

A total of four stages and five notable points are highlighted on Figure 9.1. In the orbital arches that correspond to these stages it is possible to observe:

a) on stage I that both first and second temperature time derivatives are positive, thus $dT_i/dt > 0$ and $d^2T_i/dt^2 > 0$.

b) on stage II that the first temperature time derivative is positive whereas the second is negative, thus $dT_i/dt > 0$ and $d^2T_i/dt^2 < 0$.

c) on stage III that both first and second temperature time derivatives are negative, thus $dT_i/dt < 0$ and $d^2T_i/dt^2 < 0$.

d) on stage IV that the first temperature time derivative remains negative whereas the second is then positive, thus $dT_i/dt < 0$ and $d^2T_i/dt^2 > 0$.

Meanwhile, in what concerns the points labelled in Figure 9.1:

a) at point 'a' is where the illumination period begins and by convention will be considered the starting point of a given orbital cycle.

b) at point 'b' occurs a sign change only on the second temperature time derivate and marks the first inflexion point.

c) at point 'c' is the maximum temperature of a given orbital cycle. At this point, the temperature time derivative $dT_i/dt = 0$

d) at point 'd' occurs again a sign change only on the second temperature time derivative and marks the second inflexion point.

e) at point 'e' is the orbit trajectory closing of a given cycle, thus it coincides with the 'a' point of the subsequent orbit.

9.1.2 Orbit impact on the temperature curves

A relevant factor worth noting is the non-smoothness of the curves. In other words, there are temperature points that do not have time derivatives defined. This is the case for all 'a' points, if they are put rigorously on the exact moment the samples illumination is triggered. This lack of continuity is exaggerated when represented by the shape of the curve in Figure 9.1. Due to the thermal systems inherent inertia, this phenomenon is tenuous and for that reason much harder to be visually identified.

Fortunately, to identify algebraically where an illuminated section starts is not complicated. Most of the stage IV is when the samples are free to cool down without external heating from the Sun. Therefore, if the samples ever had enough time to complete cooling, their temperatures would describe a decaying exponential curve.

However, as already mentioned time is never enough for a steady-state to occur during one orbit period. At the transition between phases IV and I, the cooling curve is abruptly disturbed when the illumination again hits the samples. Such movement resembles a step signal applied to the samples, although it is a

step input of tiny proportions. This is the reason why the curves are not differentiable at the moment a cycle eclipse-illumination transition occurs.

Alternatively, 'a' can be placed seconds after the actual starting point of the illumination period. Given that one orbital cycle occurs roughly every 6000 seconds, considering 'a' as an approximation of the actual starting point inserts negligible errors to calculations performed using the temperature data. Again, such approximation is possible due to the inherent inertia of thermal systems.

As a result, points 'a' temperature time derivatives may now be used as reference. Thus, 'a' of a given orbital cycle is the first data point where both derivatives are positive.

From the definition of 'a' points locations, it is possible to pinpoint other important reference points not identified in Figure 9.1.

One of such remarkable points is the illumination apex 'b*', i.e. the location in the orbit arch that the Sun illuminates the samples in the closest possible direction to their normal. The illumination apex point 'b*' shall not be confused with the temperature maximum point 'c'. Both points refer to different concepts. Points 'b*' and 'c' may coincide, but not necessarily it happens.

As mentioned before, point 'c' is the temperature maximum and for that reason represents a good calculation reference since its first derivative is theoretically zero. This point has been observed to not be simultaneous for all samples. Besides, it is believed that the time delay from the illumination apex that is associated to each sample curve is related to each of the sample subassemblies thermal capacity.

The third remarkable point is the one located at the transition from an illumination period to an eclipse.

In order to find where these points are located in the temperature curves, the orbital mechanics of the spacecraft has to be taken into account, since these points depend on the spacecraft attitude. Such dependence exists because the spacecraft can cast a shadow on itself: when some of its faces see the Sun

directly, others remain protected from light. Figure 9.2 illustrates this phenomenon.

Figure 9.2 – Satellite Casting a Shadow on Itself.

Source: Prepared by the author.

Considering the fact that the CBERS 04A satellite describes an approximately circular Sun-synchronous orbit at 628.6 km of altitude, the satellite is illuminated on about 65% of the orbital cycle period of 97.25 min. However, the zenith-oriented face in which the OSR Experiment is installed has shorter illumination time than the satellite has. This face is only illuminated from the moment it becomes parallel to the solar vector onwards. This persists until Z- face stops being illuminated, which happens in the next moment it is once again parallel to the solar vector. In Figure 9.2, where the equipment and satellite are represented in green and pink, respectively.

Doing the trigonometric calculations, this mentioned time window corresponds to a 179.994° orbit trajectory arch, out of the total 360°. Therefore, the illuminated period corresponds approximately to half a period.

Hence, it is expected that the illumination peak to occur on the middle of the illuminated section of the temperature curves. If a full period is Tt, the illumination apex corresponds to a quarter Tt counted from point 'a'. By turn, the illumination arch ends at a half of Tt counted from point 'a'.

Analyses from temperature data acquired from TMM simulations and flight telemetry have revealed that the illumination apex takes place moments before the temperature maximum point 'c' due to thermal inertial of the samples. Besides, the end of the illumination section happens moments after the second inflexion point 'd'. This is a common behaviour among all samples, but those time differences vary from sample to sample.

An interesting hypothesis presumes that this time shift is caused by a degree of heat accumulation on the FR4 box. Thus, some of the heat from the maximum illumination power would find its way to the box through the MLI blanket, and then have enough time to be stored on the box, to be once again conducted to the samples' subassemblies and finally emitted by the samples tens of seconds later. Another hypothesis is that this may be linked to a radiative coupling between reference box parts and samples. Either way, the SLPM and its best solution found would need to be modified to cope with them.

For the sake of simplicity, these hypotheses were put aside for a while. They will be revisited if the solution to the SLPM to be described in the following paragraphs proves itself ultimately inadequate.

Having defined where the selected notable points on the temperature curves can be found, it is easier to understand the proposed solution to this SLPM.

9.1.3 Algorithm for conductive thermal coupling and thermal capacity

The analytic problem is defined by Equations 9.2 to 9.5 that have supposedly 4 unknown parameters each: α, G_L, C_m and q_s. Thus, a total of 4 Equations and 16 unknowns is available.

Fortunately, these unknown parameters have different degrees of relevance in different stages of the orbit. Relations that have this nature can be engaged in a systematic procedure to eliminate the unknowns one by one.

Supposing that a dataset from a given series of orbital cycles is available which is made of n different data points per cycle. Ideally, these data points have to be equidistant from one another by a Δt time step.

This is not a requirement, though. If the data available is not evenly distributed in time, a least squares fitting can be attempted. From the fitted function, evenly distributed data points can be artificially generated. Such a procedure would add complexity to an algorithmic implementation, because it has to be repeated every orbit cycle.

Regardless of the means used, the data analysis begins with these n data points per orbit. Now using one of the curves of the dataset as a reference, its point 'a' can be defined as 0Tt. Then, one should look specifically to the temperature data that belongs to the [0Tt, +½Tt] timespan. This interval considers only the illuminated section of the orbit and places the illumination apex at the centre.

To start with an illuminated period, instead of an eclipse, is counterintuitive because the solar heat input terms of the heat balance Equations are not zero. Nevertheless, this approach is justifiable by the fact that the illuminated period has a centre point easier to identify, and to the following method this was proved to be an important attribute.

In addition, one may consider the illumination apex as the 'zeroth' time point. This adds to the supposition that equal amounts of data points are placed before and after the illumination apex, and they are always equidistant by a time step Δt. Then, it is possible to select and compare pairs of data points that are symmetrically distant from the zeroth time point. The pairs of selected points are illustrated in Figure 9.3.

Figure 9.3 – Formation of Pairs of Symmetrical Data Points.
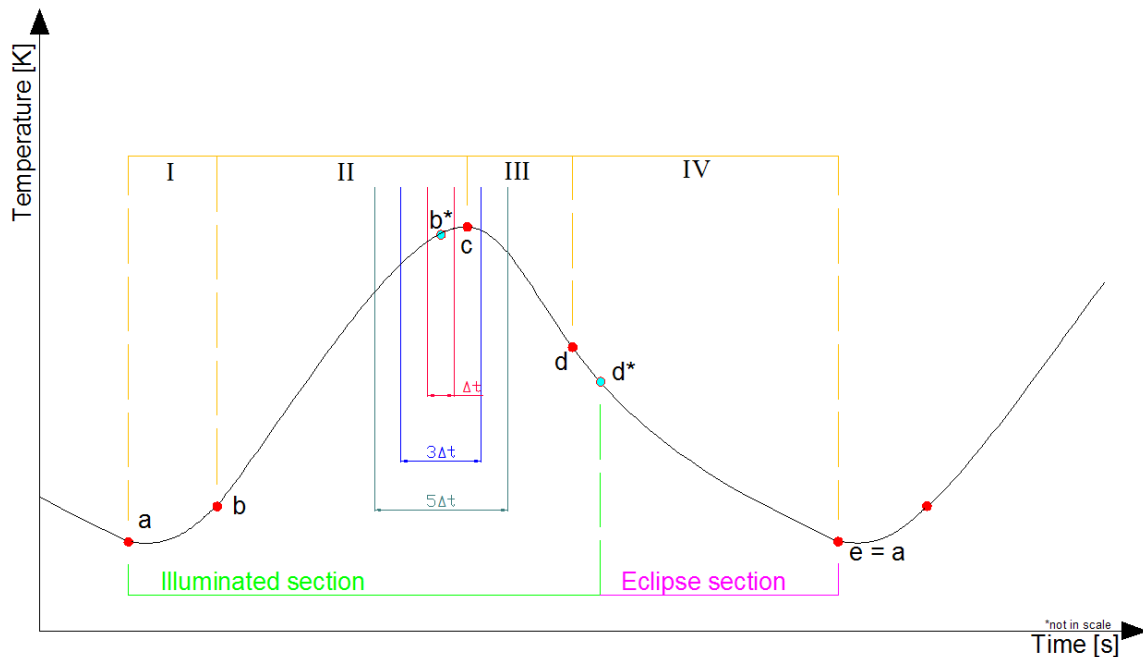
Source: Prepared by the author.

Differently from the previous image of the typical temperature curve, the illumination apex and illumination end point are now represented as b* and d*, respectively.

The pairs of symmetrical points indicated on Figure 9.3 have an interesting feature: in a selected orbital cycle they experience the same level of Sun illumination.

When the related heat balance Equations for the pair of points distant $\Delta t / 2$ are compared, they eliminate each other illumination terms. For any sample 'i', in mathematical terms it becomes:

$$C_{m,i}\left[\left(\frac{dT}{dt}\right)_{+\Delta t/2} - \left(\frac{dT}{dt}\right)_{-\Delta t/2}\right] = (Q_h - Q_h) + \alpha_i A\left(q_{s,+\Delta t/2} - q_{s,-\Delta t/2}\right) +$$

$$+ G_{L,i}\left[(T_{box} - T_i)_{+\Delta t/2} - (T_{box} - T_i)_{-\Delta t/2}\right] - \varepsilon\sigma A[(T_i^4)_{+\Delta t/2} - (T_i^4)_{-\Delta t/2}] \tag{9.7}$$

$$C_{m,i}\left[\left(\frac{dT}{dt}\right)_{+\Delta t/2} - \left(\frac{dT}{dt}\right)_{-\Delta t/2}\right] = G_{L,i}\left[(T_{box} - T_i)_{+\Delta t/2} - (T_{box} - T_i)_{-\Delta t/2}\right] - \varepsilon\sigma A[(T_i^4)_{+\Delta t/2} - (T_i^4)_{-\Delta t/2}] \tag{9.8}$$

Adopting Equation 9.8 as a reference, a pair of data points equally distant from the illumination apex can provide one expression with two unknowns: the thermal conductance G_L and the heat capacity C_m.

Such a procedure might be repeated for all other pairs of points that can be formed within one orbit timespan. If a total of n data points are available per cycle, $n/2$ correspond to the illuminated section. Then, those $n/2$ points can produce $n/4$ pairs and thus $n/4$ Equations with the same two unknowns, G_L and C_m.

These unknowns are thermo-physical properties of the equipment that are not expected to vary from one data point to another. Consequently, they can be determined by many systems of 2 Equations formed from the $n/4$ Equations available. A combination without repetition of the $n/4$ Equations in groups of 2 Equations results in $(n^2 - n)/32$ possible systems of Equations per orbit cycle. By turn, from this group of systems of Equations, when they are solved $(n^2 - n)/32$ values are produced for each of the unknown parameters. Any valid solution method can be employed to solve those systems of Equations, but Cramer's rule has proved easier to automatize the process. Then, in a simpler way , the average values of these two unknowns shall be calculated. Alternatively, a least squares method can also be applied once the matrix has rectangular format.

9.1.4 Errors embedded to the calculations

Large amounts of calculated values will be created. Despite of the data volume produced, it is desirable to make it easier to generate a sample intended for statistical inference. Statistics is a convenient tool to be used in this application because there are many error sources affecting the analytical solutions to the SLPM, which unfortunately is a rough approximation of the real physical system. Errors have such a presence that makes them difficult to quantify objectively.

In fact, the solution algorithm adopted also creates additional error sources. For example, in the case of the aforementioned algorithm, it is hard to define precisely when the illumination apex occurs because the orbit is not exactly a perfect circle. The illumination apex exact location may be also subjected to variations of Sun activity: a sudden peak of impinging changed particles can disrupt the equipment regular thermal behaviour. Another error source is the assumption that symmetrical data points are seamlessly equally illuminated, and this may not be the case. These add to errors from telemetry, temperature probes, fitting issues (if needed) and others.

Even though errors are still present, when compared to other solution methodologies attempted previously this algorithm was the one that produced the most consistent results for G_L and C_m. Seemingly, the errors are smaller too. This may be justified in the fact that this method avoids Equation terms with higher order derivatives, multiplication operations with derivatives or among unknowns. Such avoidance tends to make errors to propagate less (Vuolo, 1993).

Mostly, the remaining errors embedded in the calculations appear to be of random characteristics. By applying a normality statistical test on the samples obtained from the data set used in the study, it was possible to verify that the calculated values for G_L and C_m are either quasi-normally or normally distributed. The Kolmogorov-Smirnov normality test was the one employed for this task.

However, tests using this calculation method revealed that the amount of data produced was not enough to feed a good quality inference for the G_L and C_m true values. For instance, data histograms had considerable dispersion and resulted in high uncertainty margins.

Efron and Tibishirani (1993) detail procedures called 'bootstrap' that is a family of methods used for assigning measures of accuracy to statistical estimates. This toolbox is widely applied to problems of different fields, and is related to the concept of 'bootstrap sample'. The principle of construction of a bootstrap sample can be used to enhance the reliability of the empirical samples available for G_L and C_m.

Bootstrapping are resampling methods, and the bootstrap sample it requires is a simple concept. It consists of producing a normally distributed sample from the original sample, given that the last is representative of the studied phenomenon and normally distributed as well. The bootstrap sample is built drawing randomly elements from the original sample, but with replacement. Parameter N affects the quality of the bootstrap sample and is the number of resamples per individual value in the original sample. For example: if the original sample consists of n = 30 individuals, a N = 10 parameter produces an equivalent bootstrap sample of n* = 30.10 = 300 individuals. Generally, applications of the bootstrap sample use parameter N ≤ 4000, but this number is not a boundary.

Given that a quantity is the result of a physical phenomenon that inherently has errors of random nature, it tends to be represented by a normal distribution. The normal distribution is continuous, therefore it is an expression of a hypothetical infinite sample of this quantity. An infinite sample represents precisely how the population behaves. However, for many reasons to measure a quantity infinite times is not feasible. This is why limited empirical samples are in general rather considered. If an empirical sample represents the reality of a quantity but is not big enough to narrow down uncertainties for inference, an equivalent bootstrap sample may be used instead.

Indeed the bootstrap sample was used to make G_L and C_m inferences. The effect it produces is to bring the empirical sample closer to an ideal and infinite sample that is the normal distribution. Put differently, the bootstrap sample emulates the population the original sample comes from. However, this procedure is calculation-intensive and thus feasible only via computer algorithms.

It has been included in a MATLAB code used to implement this proposed analytical model solution. The best compromise between sample enhancement and required computing power was verified for N ≈ 2000.

Some preliminary results are presented in Section 9.4.

9.1.5   Inbound sun flux calculation

Having obtained reliable values for G_L and C_m of each sample, the Sun illumination flux q_s may now be calculated from the black reference sample temperatures.

Adoption of the black sample is a natural choice in this stage because its properties are the most stable, making it the reference sample. The high solar absorptivity of the black anodized surface is α_{bk} that is known beforehand from ground measurements. This property is expected during spacecraft lifetime. Besides, as this sample is positioned in the same plane of the others it receives the same amount of illumination.

Therefore, to calculate the sun flux the rewritten balance Equation 9.9 may be used only with data points that correspond to the illuminated section. Using Equation 9.9 makes no sense on eclipse sections of the orbit. The resulting curve anticipated is a sine type function.

$$q_s = \frac{C_{m,bk}\left(\dfrac{dT_{bk}}{dt}\right) - Q_h - G_{L,bk}(T_{box} - T_{bk}) + \varepsilon\sigma A T_{bk}^4}{\alpha_{bk} A} \qquad (9.9)$$

9.1.6 Samples absorptivity

Considering that all samples share the same Sun energy flux term in their thermal balance Equations, it can now be calculated a sample of α_i values each of the samples but the black anodized. The obtained calculated sample has shown itself normally distributed most of the times. Equation 9.10 is then used to compute the desired absorptivity from data of illuminated section.

$$\alpha_i = \frac{C_{m,i}\left(\dfrac{dT_i}{dt}\right) - Q_h - G_{L,i}(T_{box} - T_i) + \varepsilon\sigma A T_i^4}{q_s A} \qquad (9.10)$$

In the case when the heat flux magnitude is known from other satellite sensors or calculated separately, point 'c' in the temperature curves where the first derivative is 0, Equation 9.11 may be used instead:

$$\alpha_i = \frac{-Q_h - G_{L,i}(T_{box} - T_i) + \varepsilon\sigma A T_i^4}{q_s A} \qquad (9.11)$$

Here, it is supposed that the conductance $G_{L,i}$ is already estimated.

Some preliminary results to this calculations are also presented in Section 9.4.

9.2 Advantages related to analytic approaches

Methods developed to help with the absorptivity problem that work under an analytic perspective may be a valuable component to a toolbox.

Firstly, it tends to require less processing time if compared to the TMM developed for the same purpose. As a comparison, the numerical model built on Thermal Desktop Sinda/Fluint 4.8 on its present state needs about 18 hours to compute temperatures for 30 orbit cycles. The analogous analytic algorithm implemented using a MATLAB routine in the same computer is executed in about 25 minutes time. Many performance optimization can still be added to this algorithm, though.

Secondly, analytic models are capable to enhance the understanding of the heat behaviour on the principal components of the equipment. Different variants of analytic models can be readily created and used to evaluate the most relevant heat paths, and to identify where complex phenomena like radiation may be disregarded and where it cannot.

Lastly, the analytical models have potential to be reformulated as inverse problems to use appropriate methods to estimate the sample absorptivity values by a most optimal way.

In the other hand, if the analytical model is oversimplified even the most sophisticated inverse methods may not give accurate results. Usually, using simplified analytical models and expressions implies that an experiment has to be built with close-to-ideal insulations and avoiding parasitic heat losses in all elements; and be exposed to exact and carefully controlled strict boundary conditions.

Unfortunately, this is not the case of OSRA: a lot of space qualification requirements had to be satisfied during the OSRA conception and construction stages in order to equipment be considered capable to be aboard CBERS 04A, which did not allow time-costly closer-to-ideal tests to be executed.

9.3　Challenges related to analytic approaches

As referred previously, a computer routine was written to execute the algorithm that corresponds to the best solution method for analytical models found to this date, which is the one described in Session 9.1. This routine has produced interesting results.

Using TMM produced data from both cold and hot cases as inputs, the algorithm consistently calculates the same values for α, G_L, C_m and q_s. These also do not change between routine runs.

However, the analytically calculated α does not correspond to the optical property defined directly on the detailed TMM. A drift is always found to influence the calculated α. For instance, if for an OSR sample $\alpha = 0.05$ in the TMM, calculated value by analytical model is $\alpha = 0.12$. A similar behaviour is seen for the white sample, but in this case the alpha difference is $\Delta\alpha \cong 0.02$, that is proportionally much smaller.

Additionally, the obtained curves for the heat flux q_s look promising. They are in the scale expected, but still less than the anticipated values. For example, q_s is predicted to reach the samples in a cold case with 1220 W/m² of maximal intensity, meanwhile the corresponding cold case calculated with Equation 9.9 reaches a peak of about 950 W/m² as shown in Figure 9.4.

A sinusoidal pattern has been reproduced, but the illumination curves are not symmetrical probably due to not precise capacity estimation. This effect has to be studied further.

Figure 9.4 – Example of Sun Heat Flux Curves of Calculated Values.
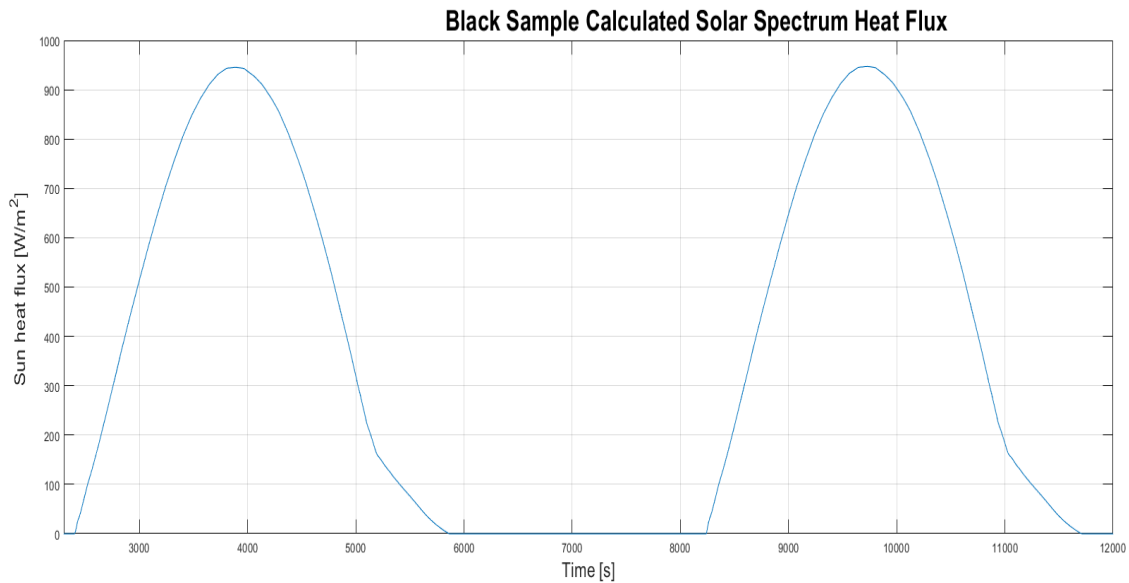
Source: Prepared by the author.

Furthermore, unexpected behaviour was identified by using TMM temperature outputs produced from induced changes of α in the TMM, which in turn had been used as test inputs in the studied analytical model.

For this experiment, different data sets were produced from exactly the same TMM parameters setup, except from α. For example, a small change in OSR α from 0.05 to 0.07 made the analytical algorithm to calculate different values for G_L and C_m. This is believed to unlikely for the physical experiment. This finding suggests that poorly mapped phenomena still have significant weight on the experiment heat transfer. At the same time, the SLPM fails to properly represent such phenomena.

Therefore, it is possible to infer that the SLPM needs to be reformulated. Similarly to the strategy by Schaefer and Bannister (1967), a radiative internal thermal coupling seems necessary to be defined. Hall and Fote (1983) also considered this coupling as an additional term in the samples thermal balance Equations.

Moreover, an alternative SLPM node layout also may prove adequate. In order to represent thermal accumulation on the box, a capacitance may be added to the reference temperature. Additionally, as the MLI blanket is not ideal, an additional node can represent the heat leakage it may pose. Those new features will need new extended balance Equations represented by 6 differential Equations.

$$C_{m,o1}\left(\frac{dT_{o1}}{dt}\right) = Q_{h,o1} + \alpha_{o1}q_s A + G_{L,o1}(T_{box} - T_{o1}) + R_{L,o1}(T_{box}^4 - T_{o1}^4) - \varepsilon\sigma A T_{o1}^4 \tag{9.12}$$

$$C_{m,wt}\left(\frac{dT_{wt}}{dt}\right) = Q_{h,wt} + \alpha_{wt}q_s A + G_{L,wt}(T_{box} - T_{wt}) + R_{L,wt}(T_{box}^4 - T_{wt}^4) - \varepsilon\sigma A T_{wt}^4 \tag{9.13}$$

$$C_{m,o2}\left(\frac{dT_{o2}}{dt}\right) = Q_{h,o2} + \alpha_{o2}q_s A + G_{L,o2}(T_{box} - T_{o2}) + R_{L,o2}(T_{box}^4 - T_{o2}^4) - \varepsilon\sigma A T_{o2}^4 \tag{9.14}$$

$$C_{m,bk}\left(\frac{dT_{bk}}{dt}\right) = Q_{h,bk} + \alpha_{bk}q_s A + G_{L,bk}(T_{box} - T_{bk}) + R_{L,bk}(T_{box}^4 - T_{bk}^4) - \varepsilon\sigma A T_{bk}^4 \tag{9.15}$$

$$C_{m,box}\left(\frac{dT_{box}}{dt}\right) = G_{L,o1}(T_{o1} - T_{box}) + R_{L,o1}(T_{o1}^4 - T_{box}^4) + G_{L,o2}(T_{o2} - T_{box}) + R_{L,o2}(T_{o2}^4 - T_{box}^4) +$$
$$G_{L,wt}(T_{wt} - T_{box}) + R_{L,wt}(T_{wt}^4 - T_{box}^4) + G_{L,bk}(T_{bk} - T_{box}) + R_{L,bk}(T_{bk}^4 - T_{box}^4) +$$
$$G_{L,MLI}(T_{MLI} - T_{box}) + R_{L,MLI}(T_{MLI}^4 - T_{box}^4) \tag{9.16}$$

$$C_{m,MLI}\left(\frac{dT_{MLI}}{dt}\right) = \alpha_{MLI}q_s A_{MLI} - \varepsilon\sigma A_{MLI}T_{MLI}^4 + G_{L,MLI}(T_{box} - T_{MLI}) + R_{L,MLI}(T_{box}^4 - T_{MLI}^4) \tag{9.17}$$

In this system of Equations, transient balances have been added to the box and MLI, besides the internal radiative links defined through 'radk-s' R_i.

113

In order to either enhance future analytical models or propose new approaches, alternative complementary techniques are mentioned in Appendix E.

9.4   SLPM preliminary results

In addition to the Figure 9.4, the analytical algorithm has produced other useful outputs to the coating degradation research. Figures 9.5 to 9.12 show outputs for the calculated values of G_L and C_m from a bootstrap sample N = 2000 which was by its turn sourced from an output of the TMM for 30 consecutive orbit cycles.

A bell shape with central tendency, characteristic to the normally distributed samples, is observable on the outputs histograms, providing visual compliance to what Kolmogorov-Smirnov test suggests from calculated bootstrap samples.

A noticeable feature from the Figures is the calculated G_L for the black sample, which is an order of magnitude smaller than others. TBT acquired data suggests that these values for the black sample are closer to reality. Therefore, further investigation to identify the reason G_L discrepancies exists to other samples is required.

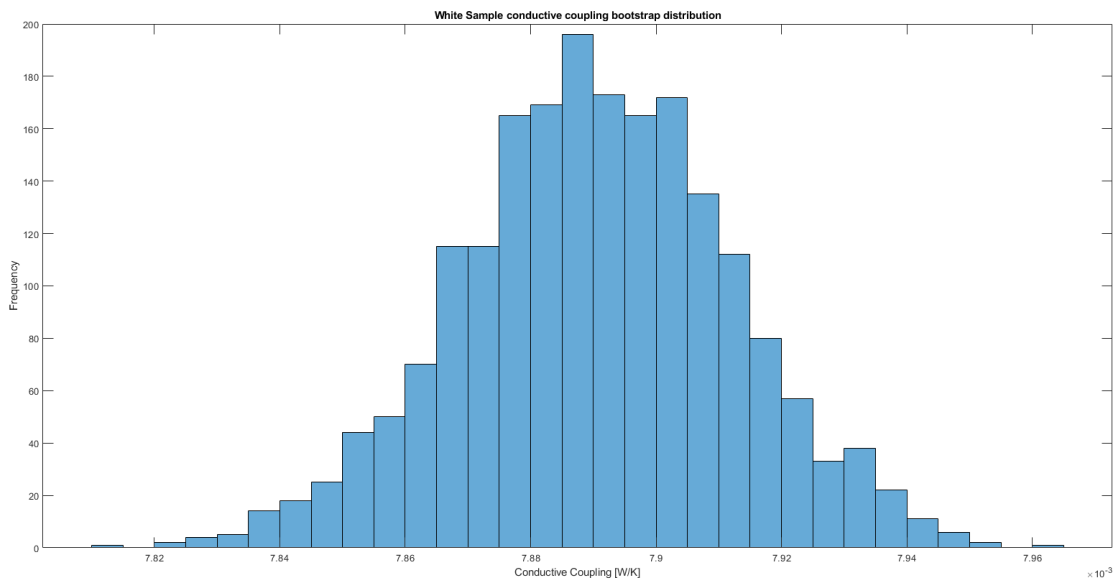Following Figures 9.5 to 9.8 show the G_L outputs for all 4 samples, and 9.9 to 9.12 the C_m outputs.

Figure 9.5 – SLPM Calculated OSR1 G_L.
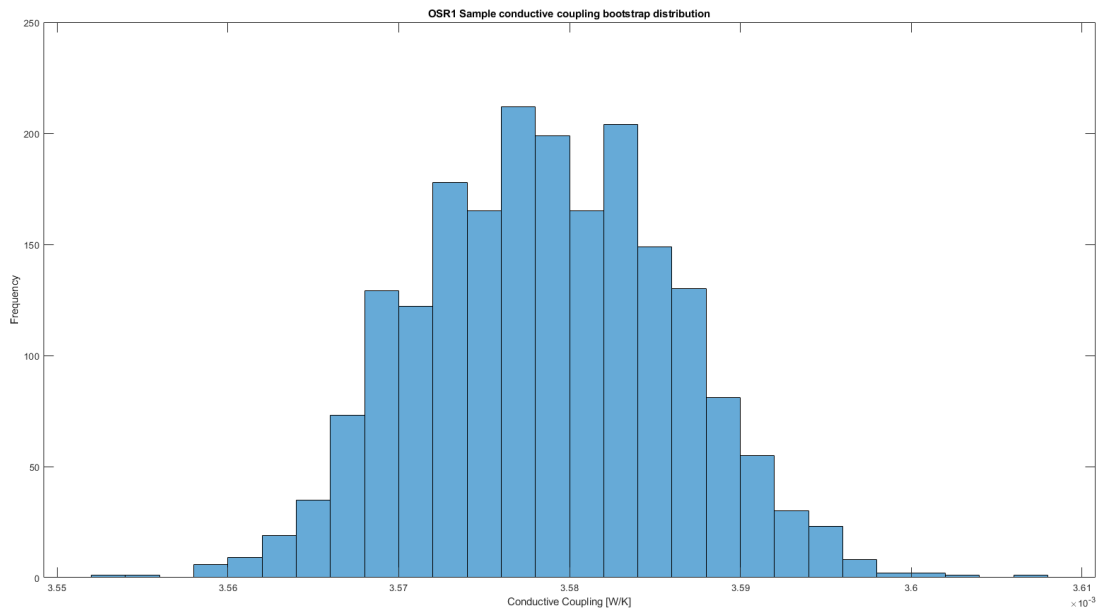
Source: Prepared by the author.

Figure 9.6 – SLPM Calculated White Paint G_L.

Source: Prepared by the author.

Figure 9.7 – SLPM Calculated OSR2 G_L.

Source: Prepared by the author.

Figure 9.8 – SLPM Calculated Black Anodized G_L.

Source: Prepared by the author.
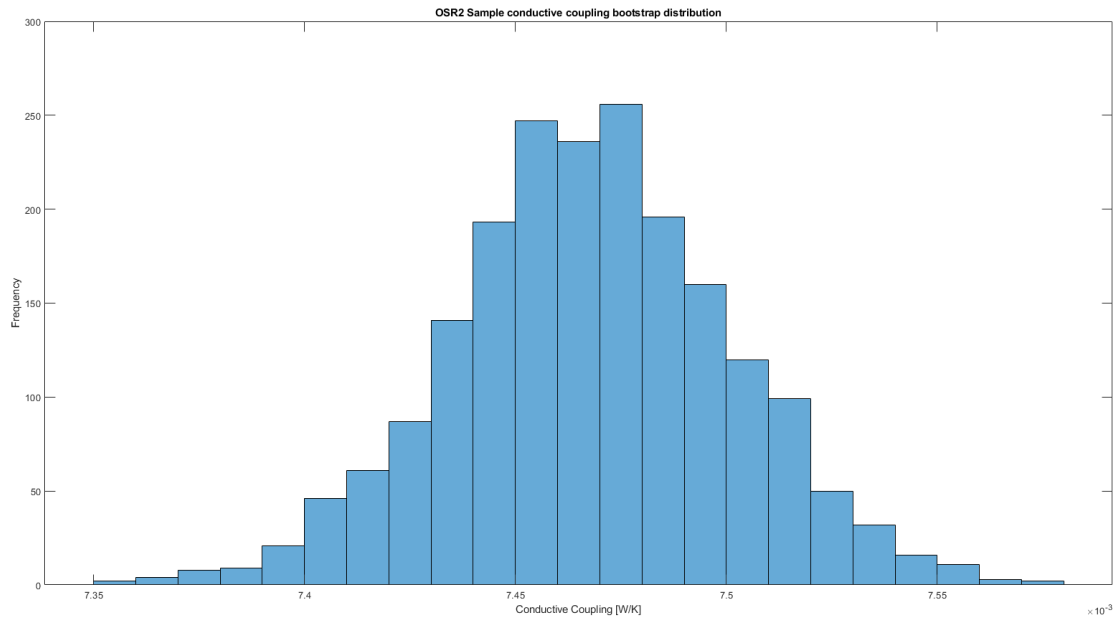
Figure 9.9 – SLPM Calculated OSR1 C_m .

Source: Prepared by the author.

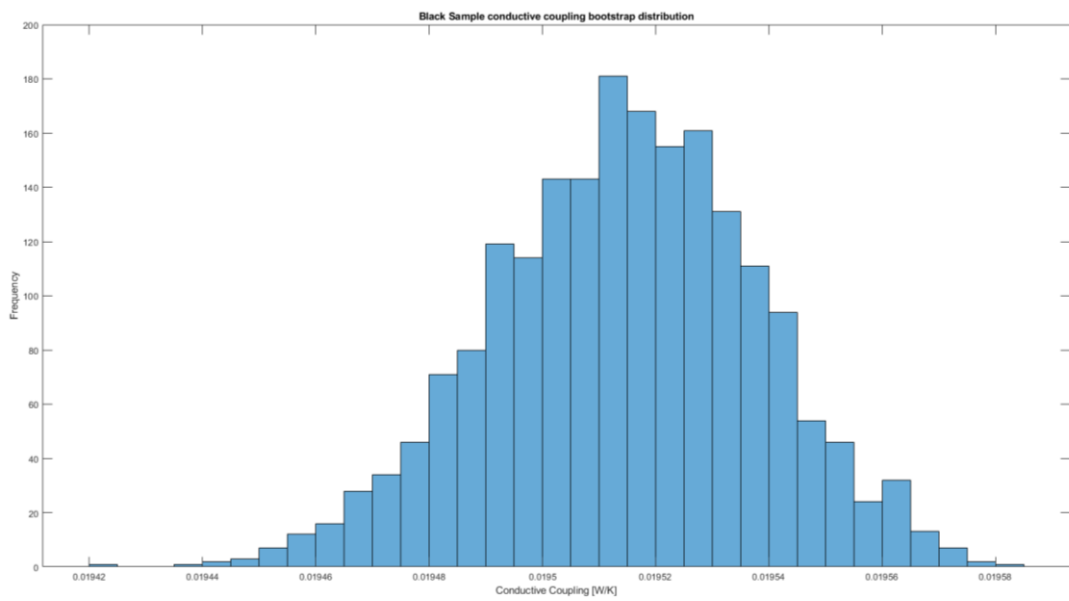Figure 9.10 – SLPM Calculated White Paint C_m .

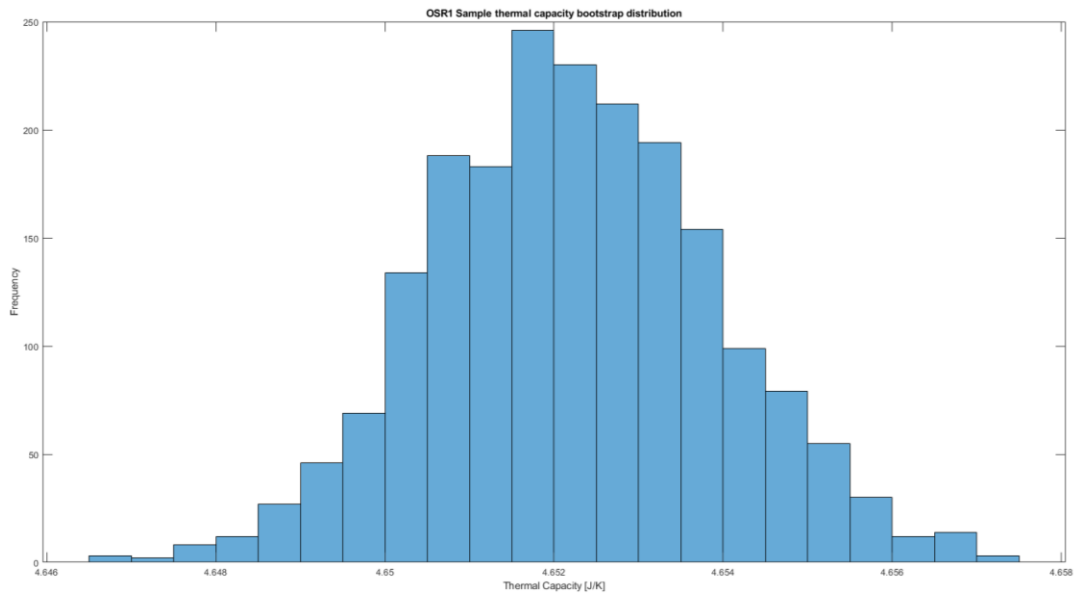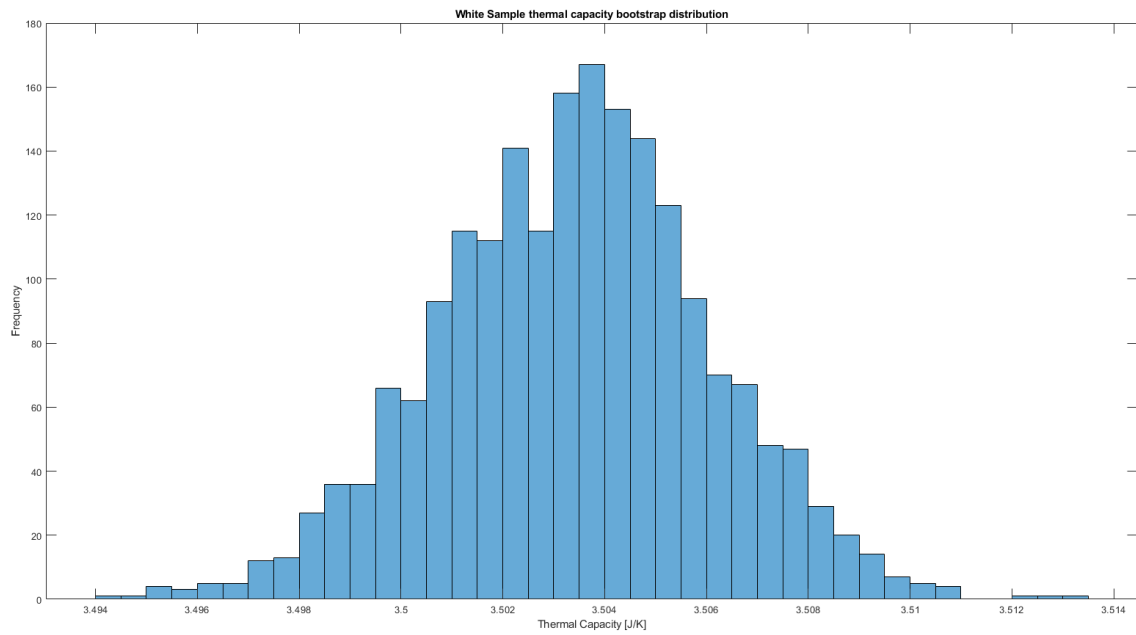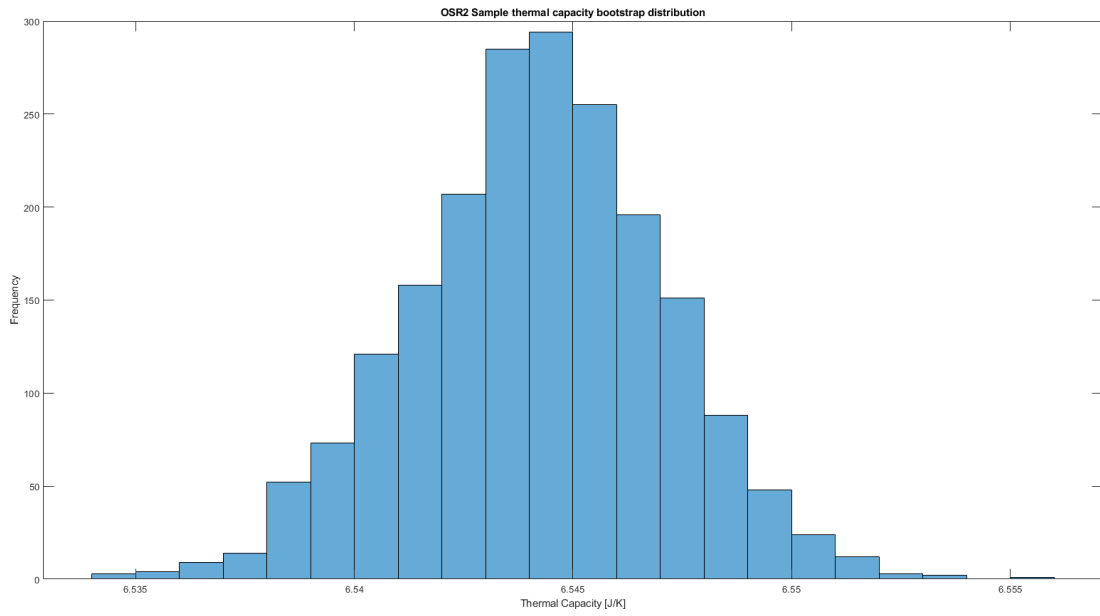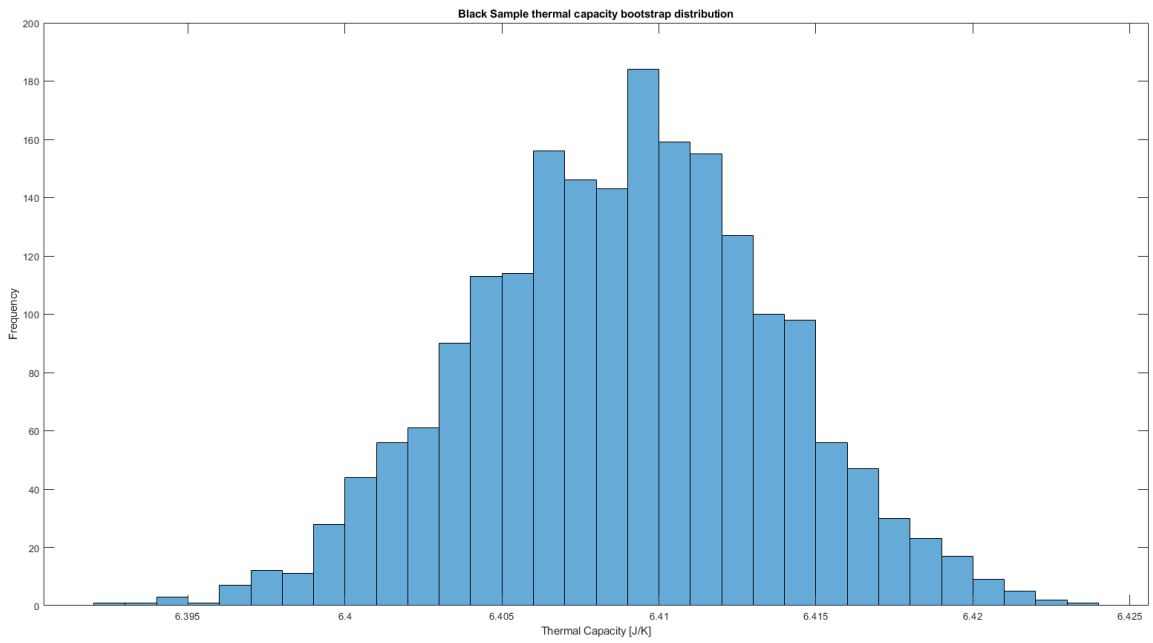Source: Prepared by the author.

117

Figure 9.11 – SLPM Calculated OSR2 C_m.

Source: Prepared by the author.

Figure 9.12 – SLPM Calculated Black Anodized C_m.

Source: Prepared by the author.

From data reported by Figures 9.4 to 9.12 and Equation 9.11, it was possible to calculate corresponding solar absorptivity for the samples and they are presented in Table 9.1.

Table 9.1 – Preliminary SLPM calculated α for BOL.

	TMM input reference	SLPM calculated from TMM output
α_{o1}	0.10	0.1822
α_{o2}	0.10	0.1348
α_{wt}	0.20	0.2306

Calculated α data suggests that the SLPM still needs enhancements. Another factor that may have influenced on the presented results are the TMM outputs used by SLPM as inputs, because at the time of algorithm execution test the data sourced from the TMM was of a version that was not calibrated well enough to reproduce correctly the BOL orbital conditions.

However, similar SLPM tests were performed with a small sample of telemetry data from June, 2020 which was the only flight data available at the time. From such data, which was not from BOL either, only 5 orbital cycles could be sourced and this was not enough to produce normally distributed bootstrap samples. Similar tendencies in the calculations for q_s, α, G_L and C_m to the aforementioned could be visualized.

Actually, more tests need to be performed from actual flight data but not before adding a routine to the algorithm to automate the data conditioning process, which is usually very time-consuming. In other words, a routine that separates data per orbit cycle, fits it in a representative time-dependent Equation, and from this fit it is expected to extract equally distributed time-stepped data for

usage as an input to the SLPM. Such input characteristic is a pre-requisite to this algorithm to function.

This improved analytical model, which is based on nodal method, may approach better the real details of the OSRA assembly. However, it is still a work in progress. Even after completion, it may not be enough to represent distributed parameters and temperature maps, as well as accessory constructive elements like connectors, electric cables, bolts and peculiarities of MLI installation; all of which produce thermal influences that are not negligible.

Naturally, the use of numerical techniques such as the finite difference method that approximate the analysed continuous thermal system by smaller discrete entities bears the possibility to better replicate details and represent distributed characteristics more accurately. For this reason, it is believed that such model serves better to more precise degradation rates identification throughout the entire mission.

Such detailed finite difference TMM was developed. Next chapter presents the main results acquired from it.

10 MAIN RESULTS OBTAINED WITH TMM

Given the various approaches available to tackle the sample degradation problem, it has been decided that a greater focus must be dedicated towards the numerical models which could replicate all constructive details of the OSRA assembly, including connectors and cables. This choice seemed to be more robust and best suited to the current knowledge of the complex heat paths believed to occur in the CBERS 04A OSRA Equipment.

10.1 TBT numerical simulations

Using as reference the test data from the TBT, the corresponding TMM has been adjusted to reproduce temperatures seen in the laboratory thermal-vacuum test. Further details regarding thermistors acquired data correction are reported in Appendix G.

The TMM temperatures outputs are shown in Figures 10.1 to 10.3, which may be directly compared to Figures 10.4 to 10.6 (G.1 to G.3) made from test data.

Figure 10.1 – Temperature curves for the TBT simulation phases 3A+4.

Source: Prepared by the author.

121
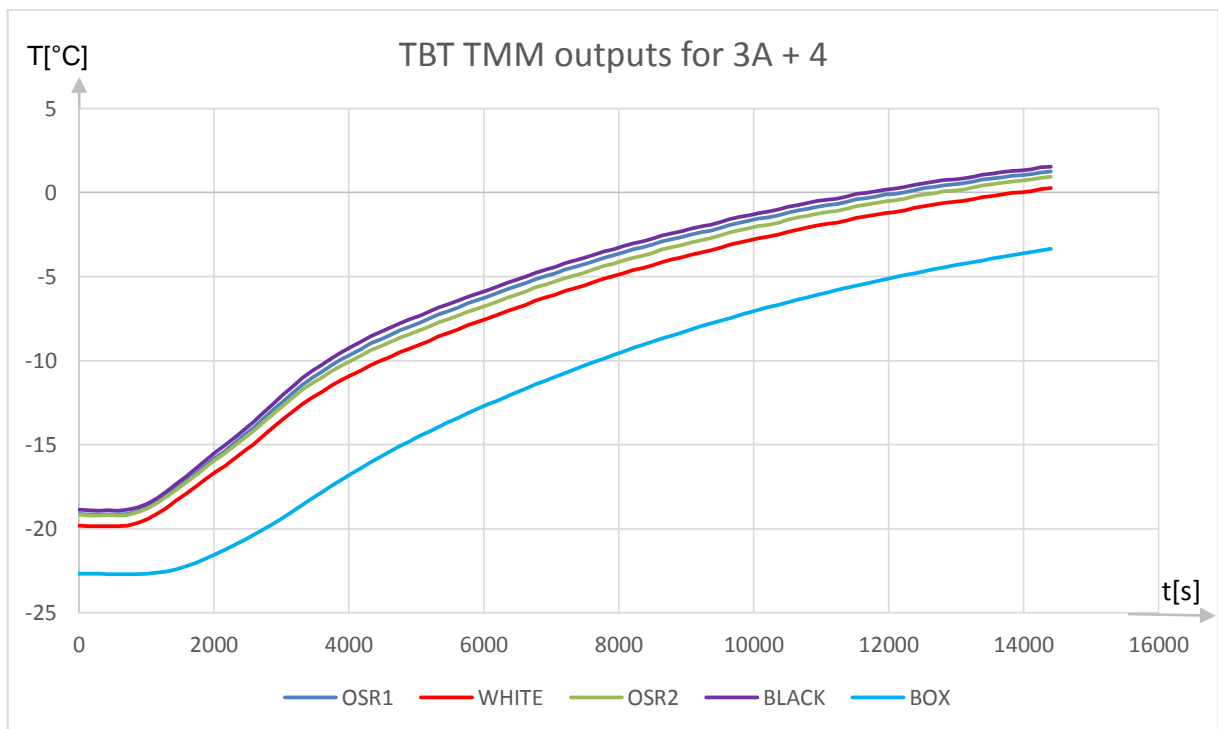
Figure 10.2 – Temperature curves for the TBT simulation phases 4A+5.
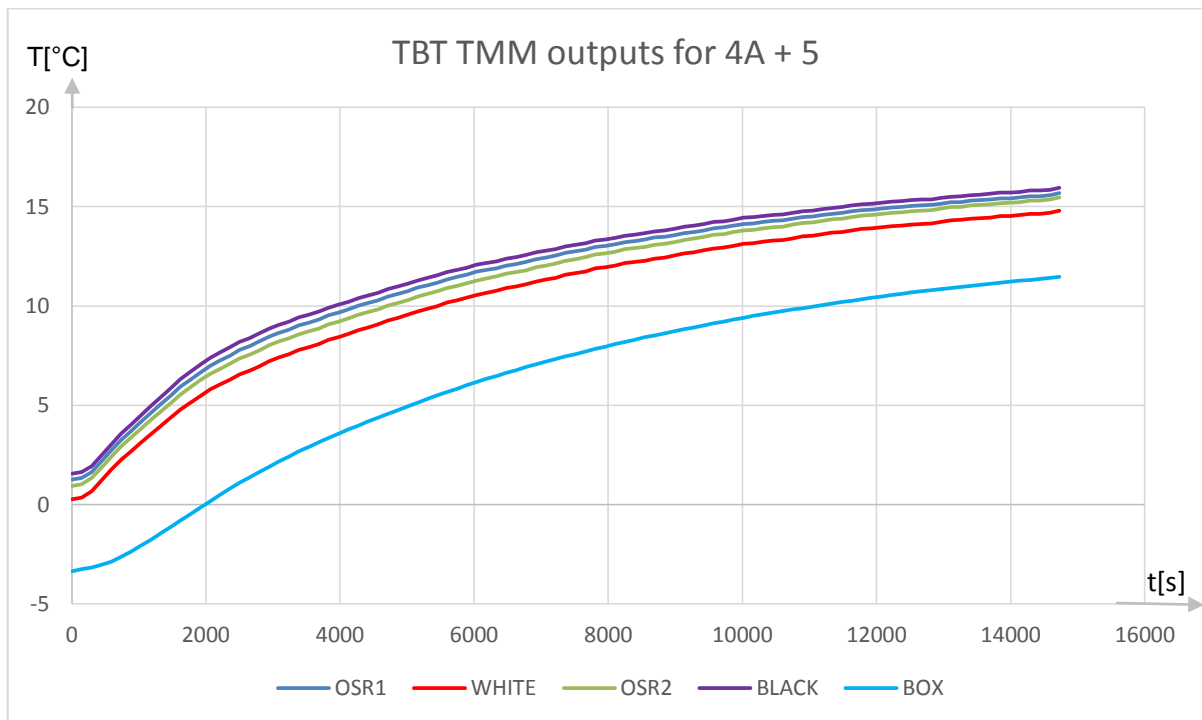
Source: Prepared by the author.

Figure 10.3 – Temperature curves for the TBT simulation phases 5A+6.
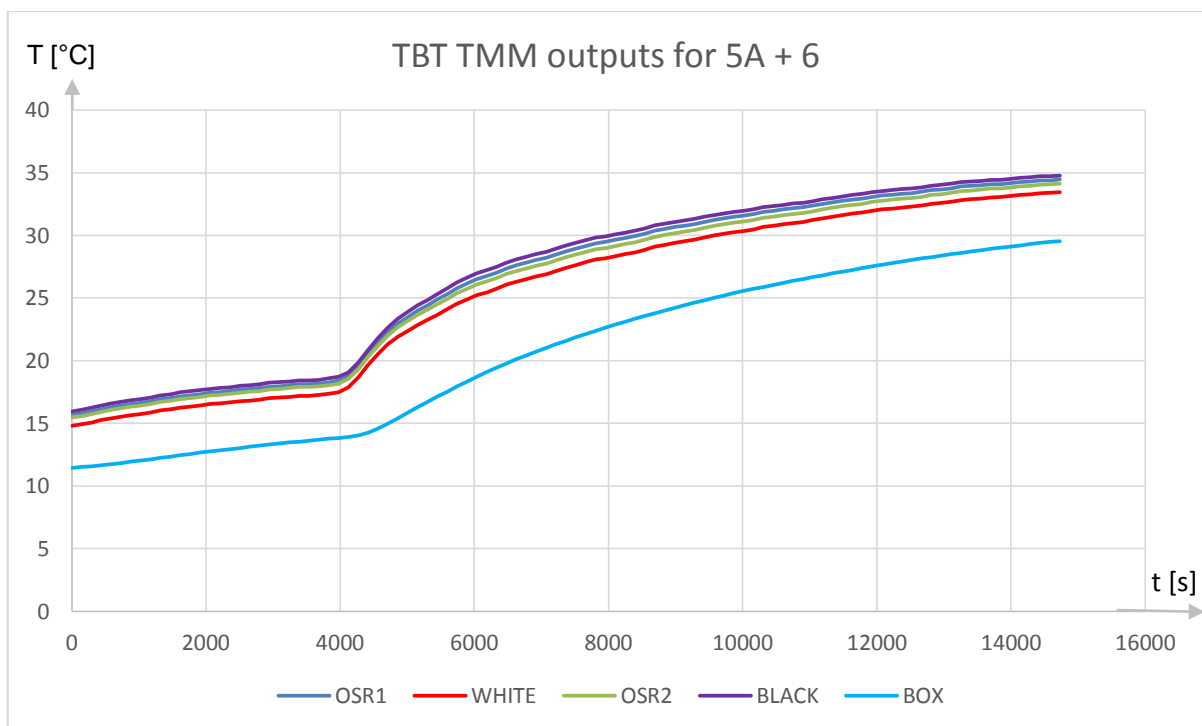
Source: Prepared by the author.

Figure 10.4 – Corrected Experiment Therm. TBT Temps. For 3A and 4.

Source: Prepared by the author.

Figure 10.5 – Corrected Experiment Therm. TBT Temps. For 4A and 5.
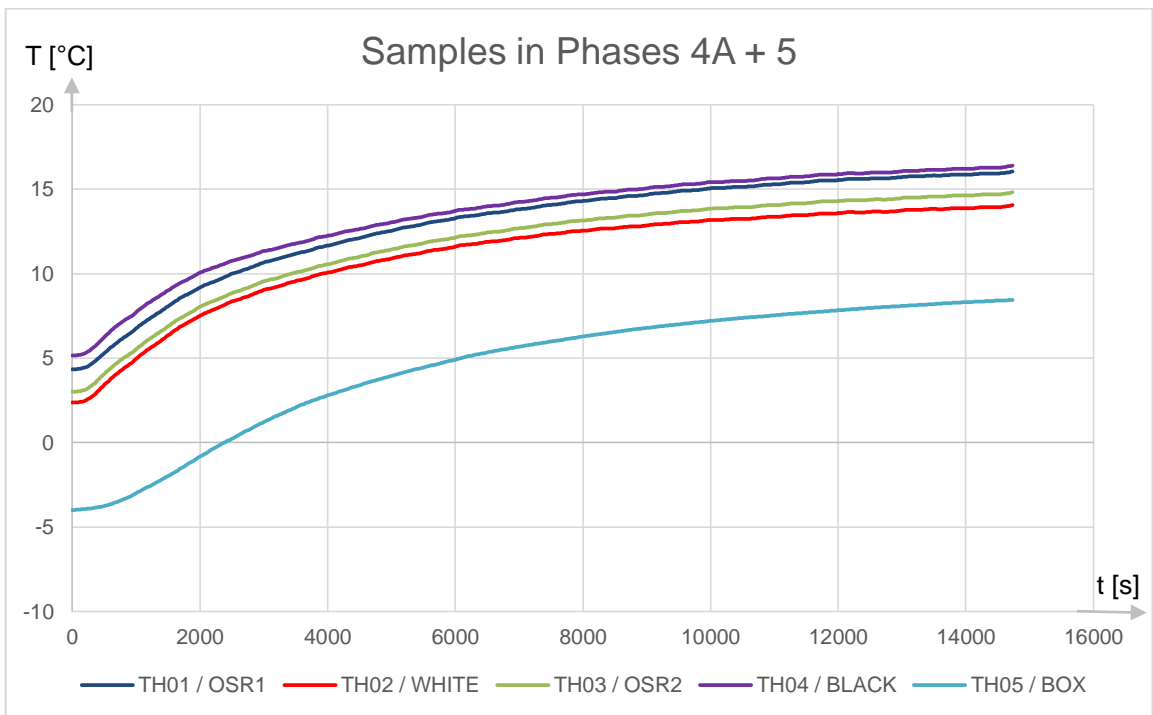
Source: Prepared by the author.

Figure 10.6 – Corrected Experiment Therm. TBT Temps. for 5A and 6.
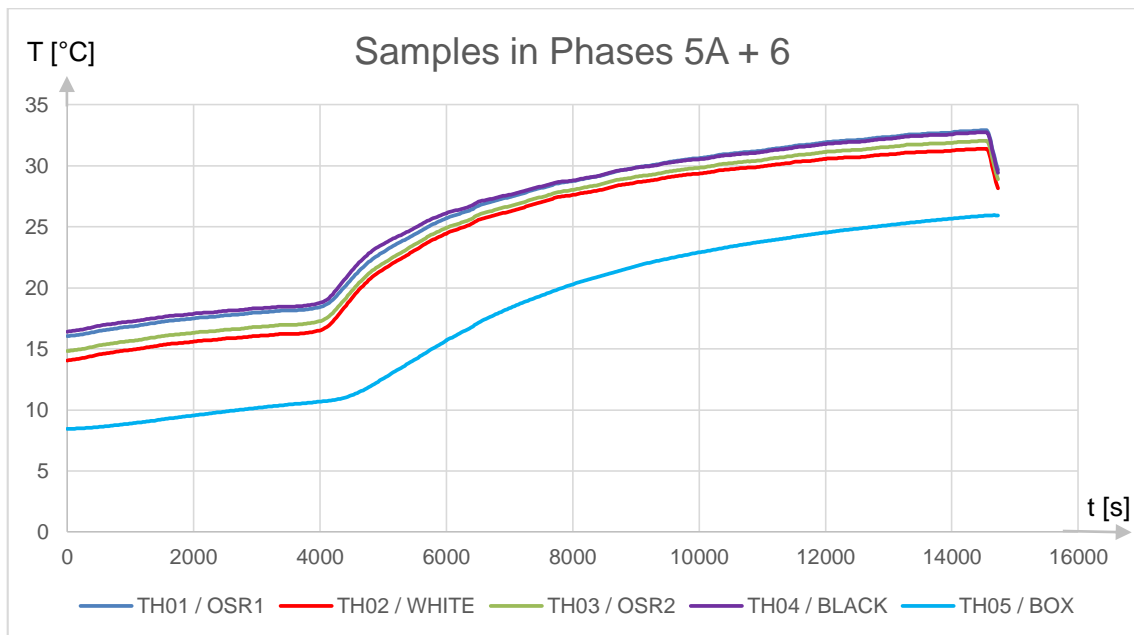
Source: Prepared by the author.

An examination of the curves makes evident that the TMM has a good agreement with the measured data gathered in the laboratory. The simulation temperatures are mostly within the range of ± 2 °C from the test data.

However, the resulting parameters set imposed to the model represents a compromise solution. The knowledge of the typical flight temperatures fr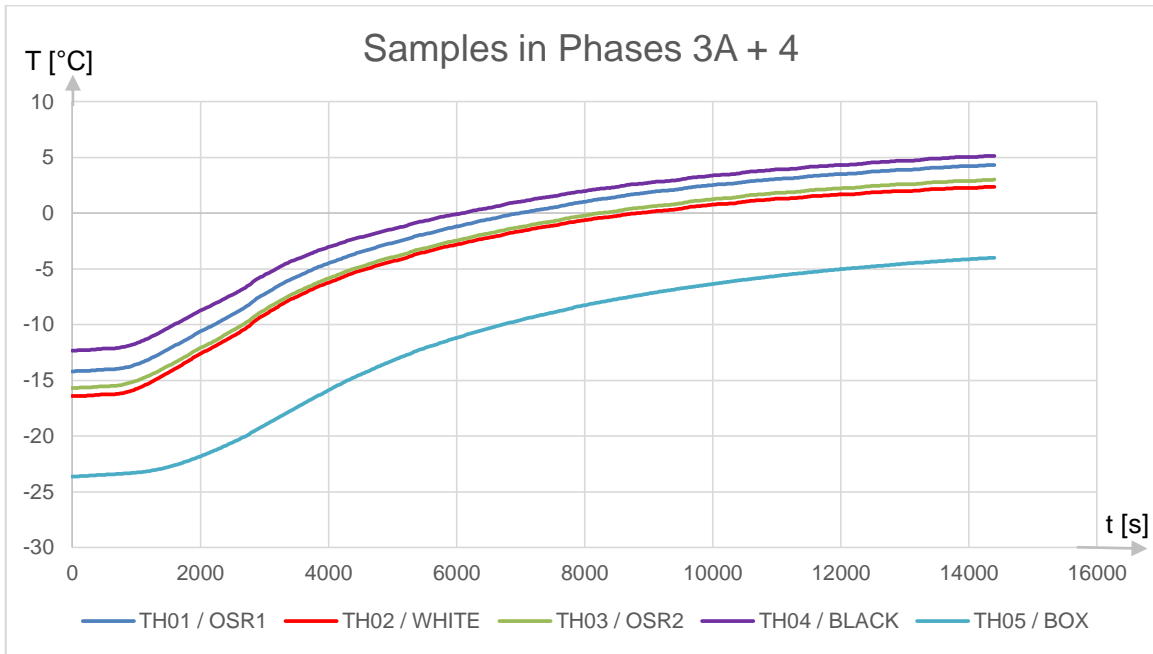om telemetry has encouraged a greater focus to be dedicated to the 4A+5 phase. This is why all temperatures seem to comply to the ± 2 °C aim at this phase, including the one related to the box reference.

Meanwhile, the target range has been achieved for the aforementioned phase, slight violations were allowed to take place on the other two phases. At 3A+4, this criteria has been relaxed to ± 3 °C for the black sample temperatures higher than -10°C. Black anodized and OSR1 samples were allowed to go beyond ± 3 °C thresholds for colder scenarios since -10°C or less is unlikely to occur in flight as data suggests. This phenomenon is an improvement opportunity and is probably linked to the position of those samples in the box since both are opposite to the side of the connectors.

Such enhanced difficulties encountered to calibrate the TMM on colder temperatures is believed to be related to the nature of the numerical method itself. The finite difference method used to calculate the physical parameters compute them only in the nodes, and this feature requires that the mathematical formulation use derivatives of pertinent Equations as a rate approximation. In the case of the present TMM, this implies that greater temperature gradients through the domain is an attribute that reduces the chances of errors and miscalculations between neighbour nodes. Conversely, the temperatures seen on the physical model are quite homogeneous for colder ranges.

Similarly, the box temperature was allowed to go beyond the initial intended range in the warmer instants of 5A+6 phase, but still within the less strict ± 3 °C range. This was not considered a major concern because box temperatures during the flight do not reach temperatures close to 25°C, even in a hot case scenario.

Some features seen in the flight telemetry data are present in the TBT as well, such as the curve arrangement. In both cases, the samples that seem to be best coupled to the box are, in decreasing order: the white paint, OSR2, OSR1 and black anodized. Curves grow closer together in the numerical simulation though.

An interesting general tendency of the temperatures behaviour could be observed. When compared to their respective TBT data counterparts, the TMM obtained curves have lower temperatures at 3A+4, approximately the same levels of temperature at 4A+5, and higher levels at 5A+6. It is believed that this is caused by non-linearity phenomena being approximated by linear laws in the modelling.

A further aspect worth noting is the proximity of the OSR samples temperature curves, which initially suggests that both samples share very similar boundary conditions internally to the experiment unit. Another hypothesis to consider is that they have similar initial optical properties, which pre-launch measurements seems to support.

Examination of the curves reported on appendix F, using Equation F.1 as a reference, it was verified that the time constants of the curves for the samples in both TBT data and TMM are compatible, which was expected since they produce similar temperature curves. The exception is the box for the 5A+6 phase, which has a non-negligible greater time constant in the TMM, but that likely should not degrade quality of the flight TMM because the telemetry suggests that this is temperature range is untouched by the box reference.

For example, the samples time constants for the 3A+4 phase may be calculated within the range of approximately 4000 to 4500 [s]. This range is 3700 to 4450 [s] for the 4A+5, and it is placed around 3100 to 3700 [s] for the 5A+6. Such changes in the time constant were not expected and suggest that the samples are exposed to varying effective thermal capacity.

Conversely, the time constants on increasing order are for the white sample, OSR1, OSR2, black sample and finally the box. This effect seems systematic and could be verified for all experimental TBT phases.

Such findings underlined the necessity to propose changes to the analytic model described in Section 9. Counterintuitively, the black anodized sample does not have the best behaviour to be considered as the reference that defines the starting point of the illumination phase within an orbital cycle. Future updates of the analytic model shall incorporate this phenomenon. Future experimental unit construction could also have modifications that keep the black sample support slightly lighter, thus prone to reduced thermal capacity.

Figures 10.7 to 10.11 show a direct comparison between experimental TBT gathered data and numerically reproduced TBT temperatures by the TMM.

Figure 10.7 – OSR1 curves from experiment and numerical model.

OSR1 sample TBT temperature comparison
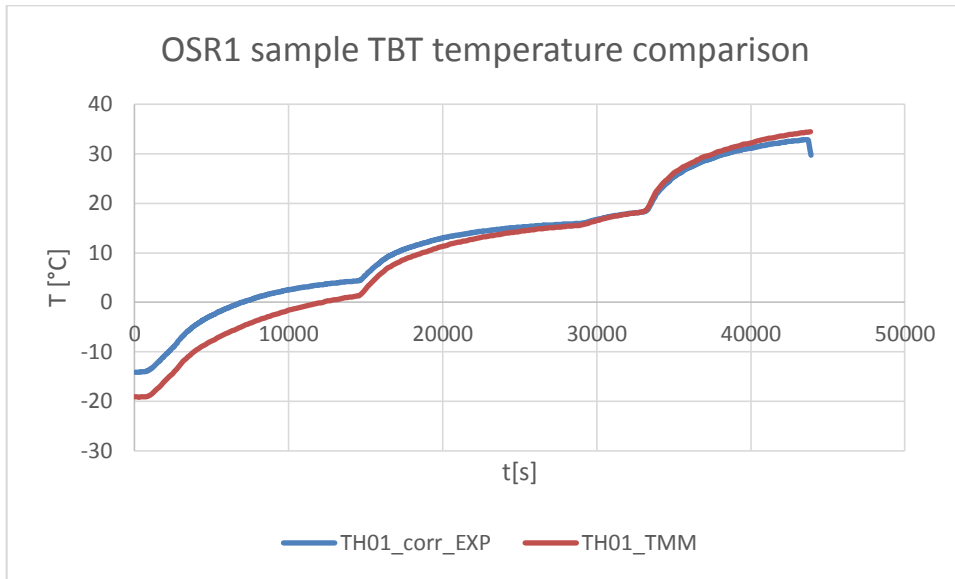
Source: Prepared by the author.

Figure 10.8 – White paint curves from experiment and numerical model.

White sample TBT temperature comparison
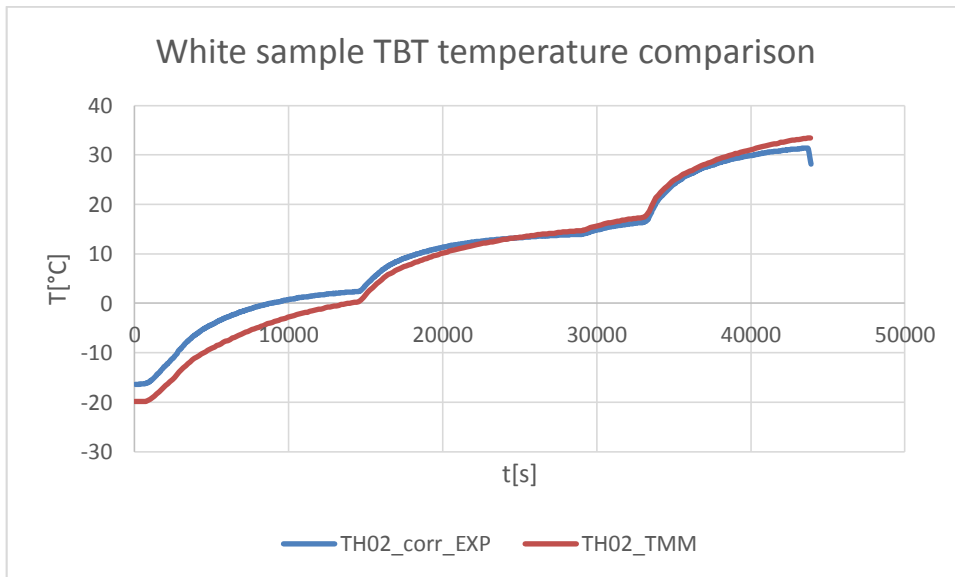
Source: Prepared by the author.

Figure 10.9 – OSR2 curves from experiment and numerical model.

OSR2 sample TBT temperature comparison
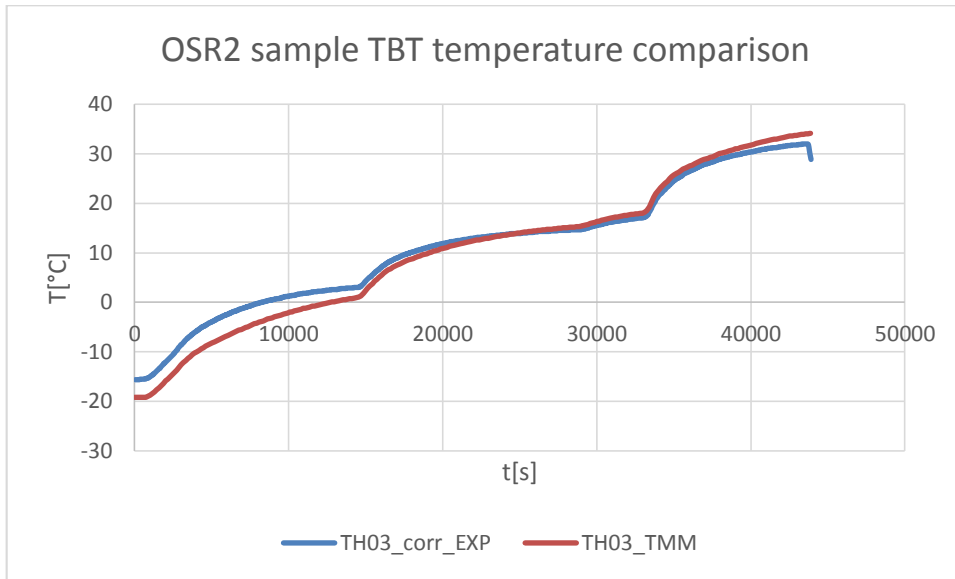
Source: Prepared by the author.

Figure 10.10 – Bk anodized curves from experiment and numerical model.

Black sample TBT temperature comparison
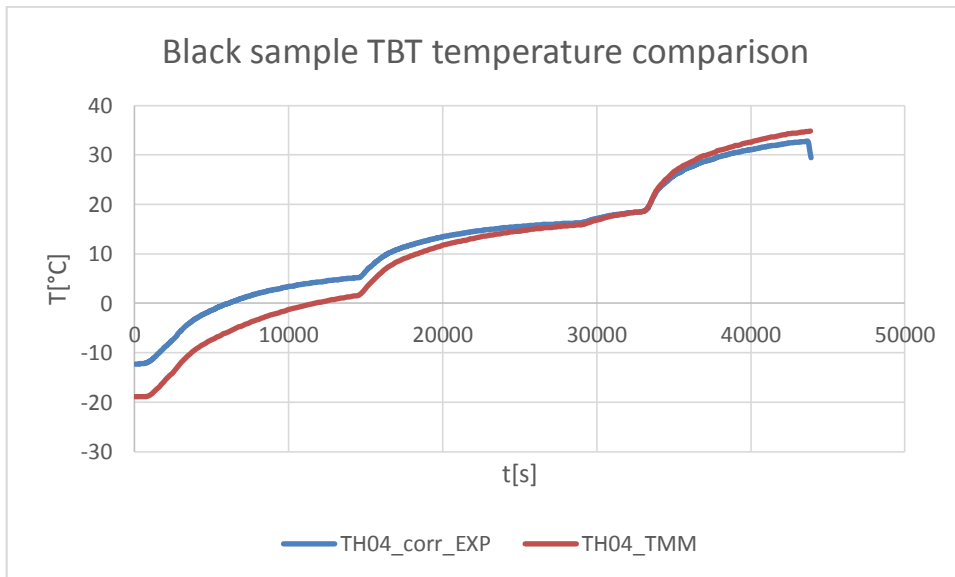
Source: Prepared by the author.

Figure 10.11 – Box curves from experiment and numerical model.
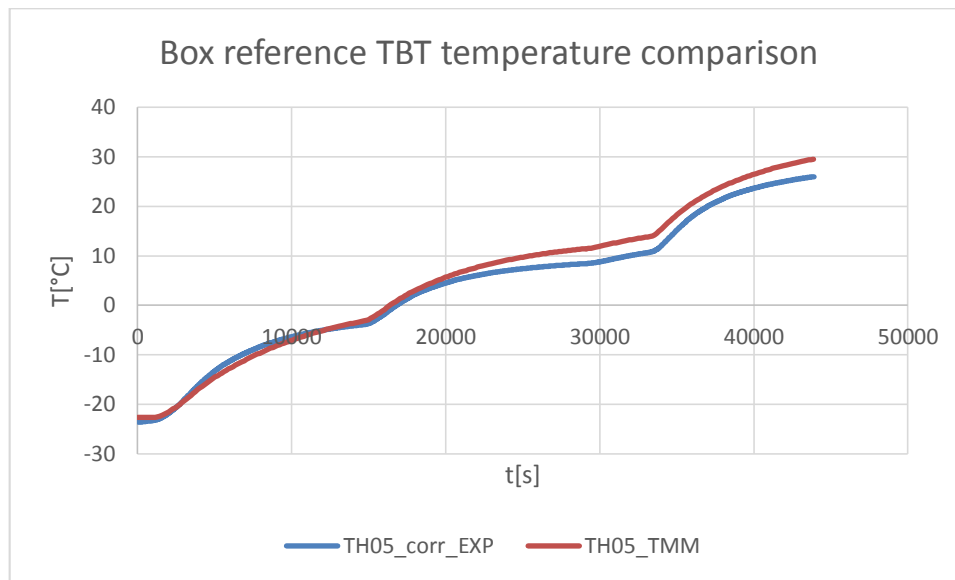
Source: Prepared by the author.

10.2 Flight numerical simulations

One of the first tasks to define the orbit TMM parameters was to choose which telemetry data point was to be considered the time zero reference.

Ideally, the initial reference data point would be produced just after the satellite attitude was stabilized following the vehicle launch, which occurred on December 20th and 24th 2019, respectively. However, the equipment fitted heaters had to be kept turned off for approximately 20 days, being energized only on January 11th, 2020. Thus, on a first glance data from this date could be regarded as the initial reference. A data sample from this date is reproduced in Figure H.1 from Appendix H.

However, when compared to data shown in Figure H.2 collected only 12 days after the first telemetry available with the heaters turned on, it is possible to notice that sample temperatures are significantly higher on January 11th. This is unexpected and is characteristic of a degradation reversal, which is physically implausible. No unusual satellite attitude occurred either.

Additionally, it is possible to verify comparing H.1 and H.2 that even the temperatures at the end of the eclipse are higher for January 11th than the

observed for January 23rd. This suggests that the optical behaviour of the experiment might be affected by its boundary conditions history.

Data has been collected from January 26th. This sample was not reproduced as a Figure because it resembles very closely the data shown in Figure H.2. Data from Figure H.3, from February 1st, show that the phenomenon that caused temperature evolution occurred between January 11th and 23rd ceased. Another data point was collected from February 15th reveals peak temperatures slightly reduced when compared to the H.3 Figure, in a difference of less than 0.25°C.

A hypothesis that could explain the unusual temperature difference between January 11th and 23rd is that the 20 days of heaters off made the samples unit into a preferential zone for volatile condensation. This seems reasonable especially taking into account that the initial days of the mission tend to produce an enhanced amount of volatiles. Presumably, the activation of the heaters caused a bake-out phenomenon to the experiment, which needed days to progress. After the bake-out was concluded, the samples probably recovered optical properties levels that are compatible with the values expected from BOL.

A hypothesis that still has to be verified is possible changes in the satellite panel average temperatures where the OSRA equipment was installed, due to change in power dissipation modes of the electronic equipment installed on the other side of the panel. Also, the satellite bus voltage variation, which could impact the heater's dissipations was verified and no issues were found.

Therefore, as the initial data reference for calibration of the Flight TMM the sample from January 23rd was chosen. This implicates that the data considered as the initial point is already 33 days old from the launch date. For example, Remaury et al (2011) report sensible degradation for the same white paint placed in the satellite SPOT5, which was also oriented towards space. The SPOT5 is a LEO satellite with orbit parameters comparable to CBERS 04A, and was launched in April 2002. For May 2002, Remaury and collaborators could verify that the white paint showed $\Delta\alpha \approx +0.035$. Hence, making the TMM replicate the observed temperatures for January 23rd 2020 demanded to allow some degree of freedom for the sample absorptivities to vary.

Another aspect that impacts the equipment entire behaviour, and therefore needs to be considered, is the temperatures reading shift seen for the OSR2 sample. Figures 5.6 to 5.8 show the uncorrected temperatures from the thermistors seen on the TBT, which reveals that the OSR2 temperatures are lower than the OSR1 ones in the raw data. The correction Equations listed in Appendix G, when applied to the TBT data approached successfully all sample temperatures to the corresponding thermocouples and showed that the OSR samples had very similar temperature points. The OSR2 corrected temperatures for the TBT were slightly under OSR1 corrected temperatures, though. This is seen in the Figures of the Appendix G.

However, the flight raw data shows that OSR2 temperatures are higher than the ones for OSR1 even prior to correction. When applied to the flight data, the correction enhanced the pre-existing gap between samples OSR2 and OSR1 even further. A hypothesis to interpret such finding could be that the boundary conditions might have been altered between TBT and flight deployment, perhaps by a thin margin. In the future, this claim has to be investigated further.

If boundary condition changes had indeed occurred, they may be linked to factors such as: different MLI blanket that was used in flight, different physical accommodation of the blanket that may have occurred during launch, and changes in the box feet couplings to the satellite unevenly altered by launcher vibrations. Further possibilities like asymmetrical damage to the MLI blanket by micrometeoroids or uneven venting patterns, and the possibility that the MLI touches the aluminium sample holders' skirts unevenly need to be also studied.

Moreover, if some sort of boundary condition change has taken place it may have minor effects on the thermal behaviour and may have happen only due to factors that are not easily reproducible in the laboratory with the resources available. This is why it is believed that, wherever the case, the boundary conditions reproduced in the TBT are still valid.

Additionally, the noticeable in-flight difference in the temperature levels experienced by OSR samples 1 and 2 could be explained either by their different position relatively to the connector side, or by their different principle of

131

fabrication: each fabrication technique may produce samples with different susceptibility to the initial degradation the experiment was exposed to. Additional scrutiny needs to be carried on this issue.

Examination of the order temperature peaks that occur in the telemetry does not seem to support the hypothesis that black sample has the higher time constant as measured from TBT data because the black sample produces the first peak of a given orbital cycle. Perhaps the amount of mass affected between box reference and sample is different in orbit conditions when compared to TBT conditions. For example, solar heating thought MLI blanket could play a role in this phenomenon. Another reason is that the absorbed heat flux on the black sample is much higher than on the other samples, therefore the intensity of heating is higher and the black sample gets increased temperature change rate. Once the black sample achieves higher temperatures, the intensity of cooling external flux goes down is also higher. Nonetheless, it is possible to verify that peaks occur in the following order: for the black anodized, white paint, OSR1, OSR2 and box reference. The flight TMM reproduces this same temperature peak order.

Figure 10.12 – Flight TMM temperatures TD output for BOL – 5 orbits.
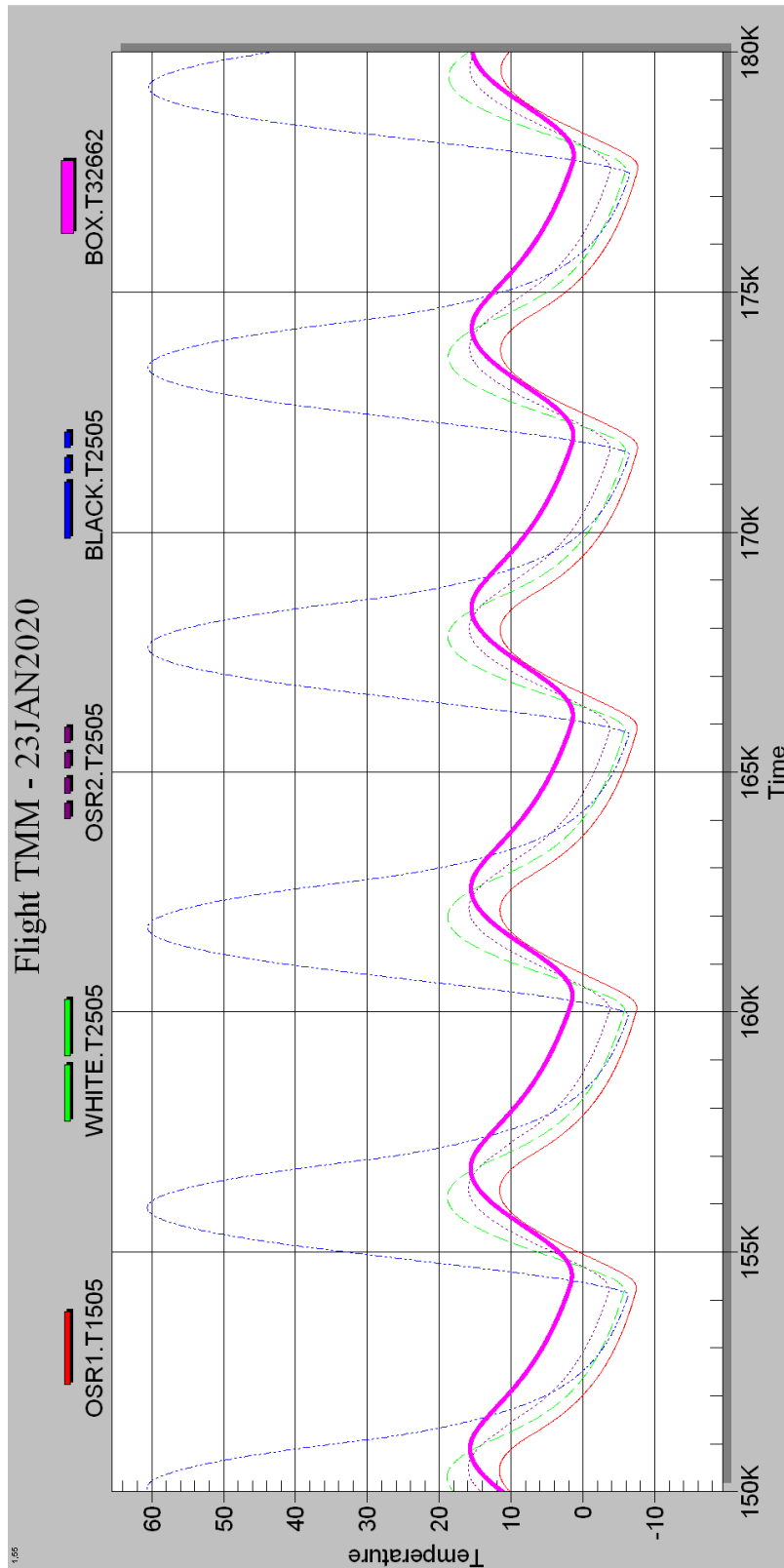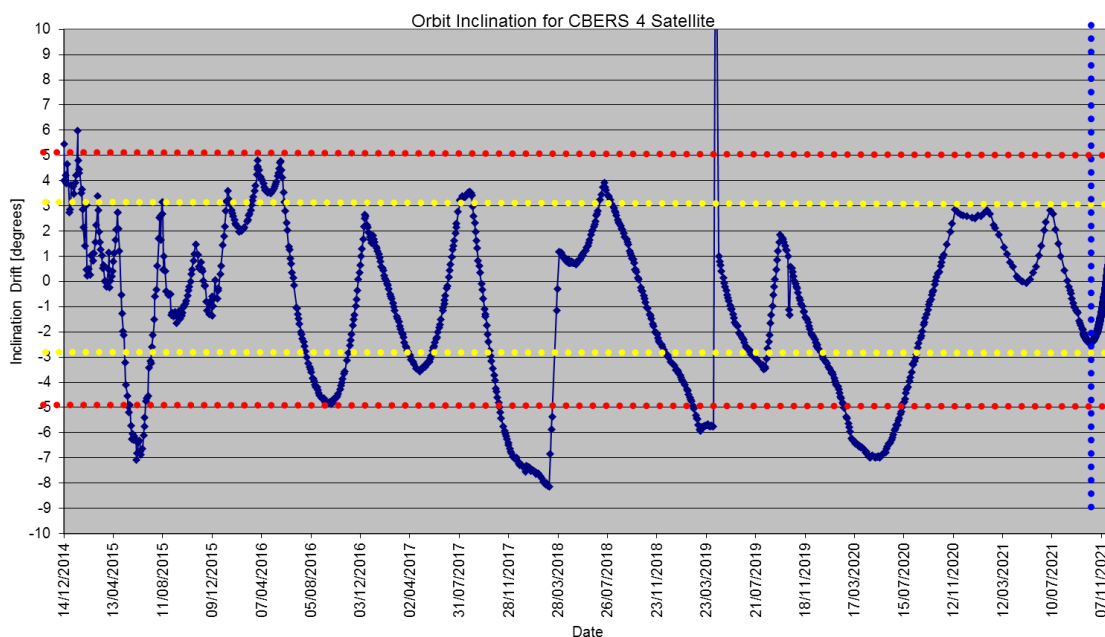

Source: Prepared by the author.

Based on the previous claims, it was possible to calibrate the TMM for the conditions experienced by the degradation unit at BOL. Figure 10.12 illustrates the outputs obtained from the TMM, which compared to Figure H.2 appears to be able to reproduce the temperatures from telemetry successfully.

Before additional analysis, another concern to be tackled was the influence the orbit inclination drift could have on the coating samples temperatures. Unfortunately attitude data for CBERS 04A was not readily available, but according to INPE's satellite command centre the CBERS 04 satellite attitude data offers a comparable history to what could be verified for the CBERS 04A. Figure 10.13 summarizes this history. Examination to this picture allows inferring that the inclination threshold adopted by INPE is of ± 5°. When left undisturbed in the maximum inclination, CBERS 04 tends to migrate to minimum acceptable inclination in about 4 months. However, corrections are frequent as they keep the satellite mostly within ± 5°. Therefore, it is considered acceptable an analysis considering these inclination extremes applied to the experiment in order to verify temperature changes, if any.

Figure 10.13 – Orbital Inclination history for CBERS 04.

Source: Prepared by the author.

A case study was proposed to verify the inclination variation influence using the TMM reconfigured to a cold case scenario. Imposing to the model the approximate solar constant characteristic of June 16th. Figure 10.14 illustrates the results presumed from the TMM considering non-degraded samples. Figures 10.15 and 10.16 illustrates the results for the same presumed non-degraded samples to the same date, but for a -5° inclination drift and a +5° additional inclination. The cold case was preferred to this study since that any variations in the effective solar constant would be more perceptible, since it represents a higher percentage of the maximum attainable solar constant for this date of the year.

Numerical simulation outputs for these cases suggest that temperature changes to the samples in the drift case were very small. The outputs also suggest that in the case of additional inclination, the peak temperatures decreases less than 1°C for the samples and 2°C for the box reference. Therefore, if inclination affects a given data telemetry point, it tends to reduce temperatures only if the satellite is in inclination exceeding the requirements.

Figure 10.14 – Nominal TMM output for 16/06/2020 and preserved samples.
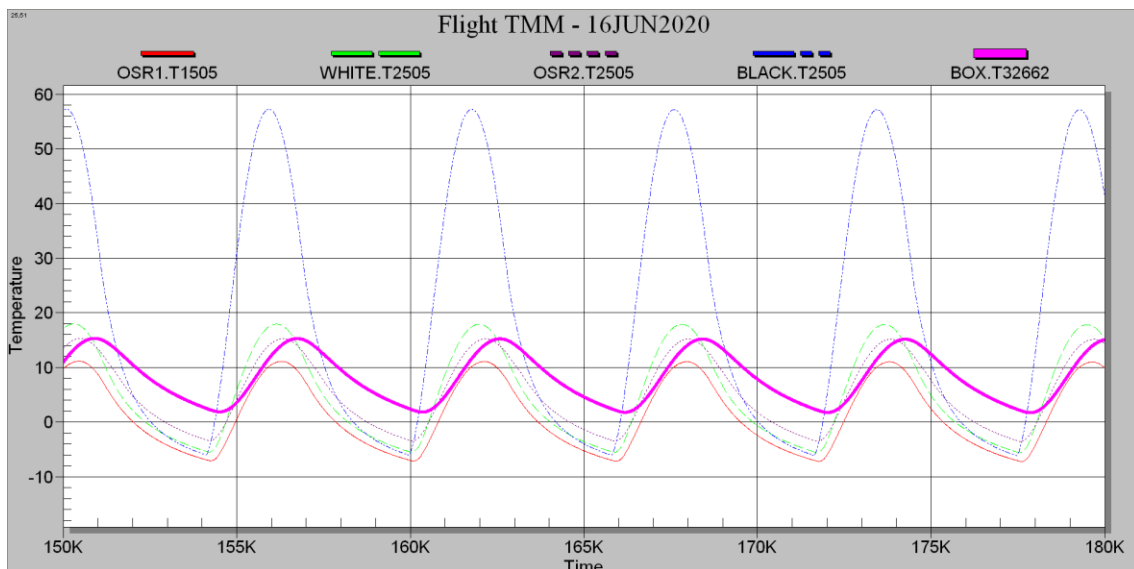
Source: Prepared by the author.

Figure 10.15 – Drifted TMM output for 16/06/2020 and preserved samples.
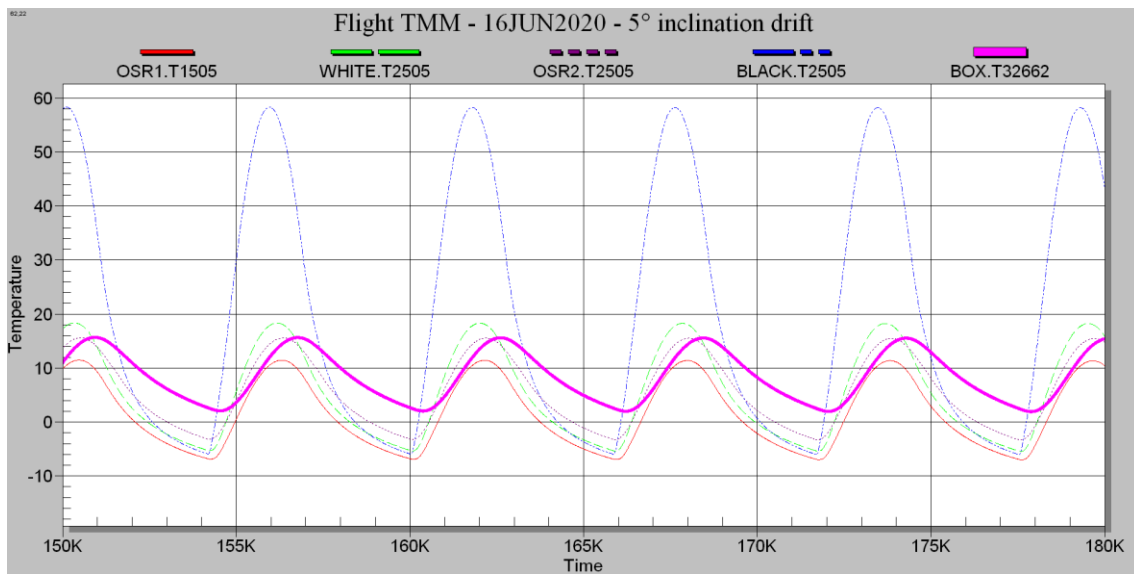
Source: Prepared by the author.

Figure 10.16 – Inclined TMM output for 16/06/2020 and preserved samples.

Source: Prepared by the author.

In other words, if the orbital inclination varies (thus the Equator passing time varies) within allowed limits, it produces almost no effects to the temperatures: only a slight reduction occurs when compared to the nominal orbit.

This conclusion leads to another pertinent question. When compared, data for cold cases from Figures H.5 and H.9 show that the black sample peak temperatures increase after 1 year, from +60.5°C to +62.5°C. Due to the fact that both telemetry data samples were collected under similar solar heat loads, this increase was not expected. Put differently, the black sample may not be completely inert as first thought. On the other hand, it is not possible to say unequivocally that the black sample has degraded, because factors difficult to measure may play a role in the results. For instance, this temperature difference may have been produced by satellite panel temperature variation since the minimum temperatures increase about 2°C as well.

Finally, the numerical model was used to perform additional computations that simulate the behaviour of the experiment in time periods analogous to the ones seen in the Appendix H Figures. Their outputs could be appreciated on Figures 10.17 to 10.21. It is important to underline that these results were obtained by only changing the solar radiation load, as they presume that the samples maintain non-degraded. This has been done on purpose to compare to the telemetry data using calculations.

Figure 10.17 – Nominal TMM output for 14/11/2020 and preserved samples.
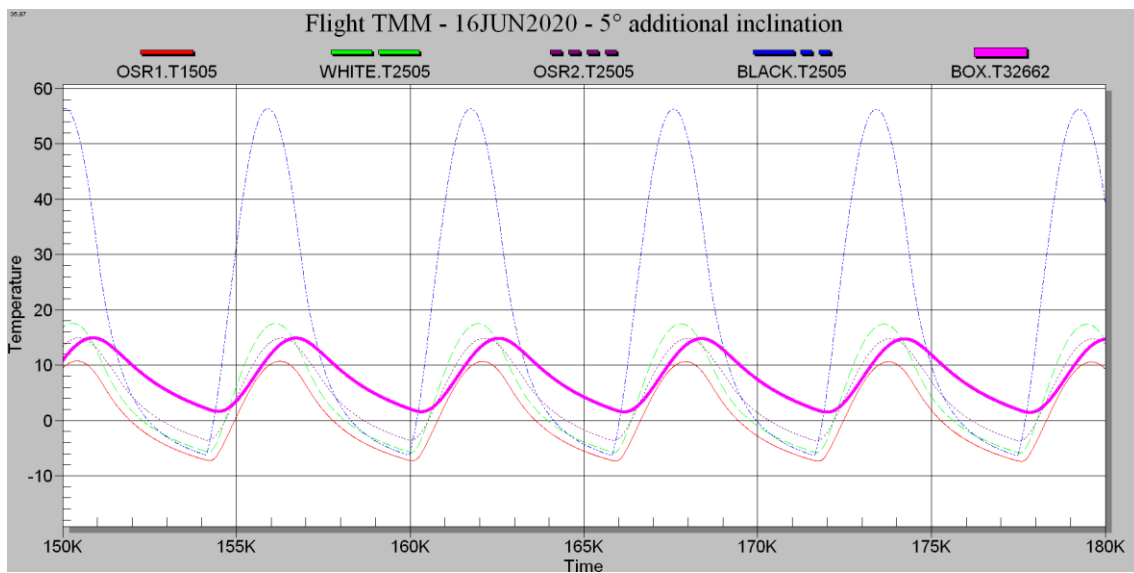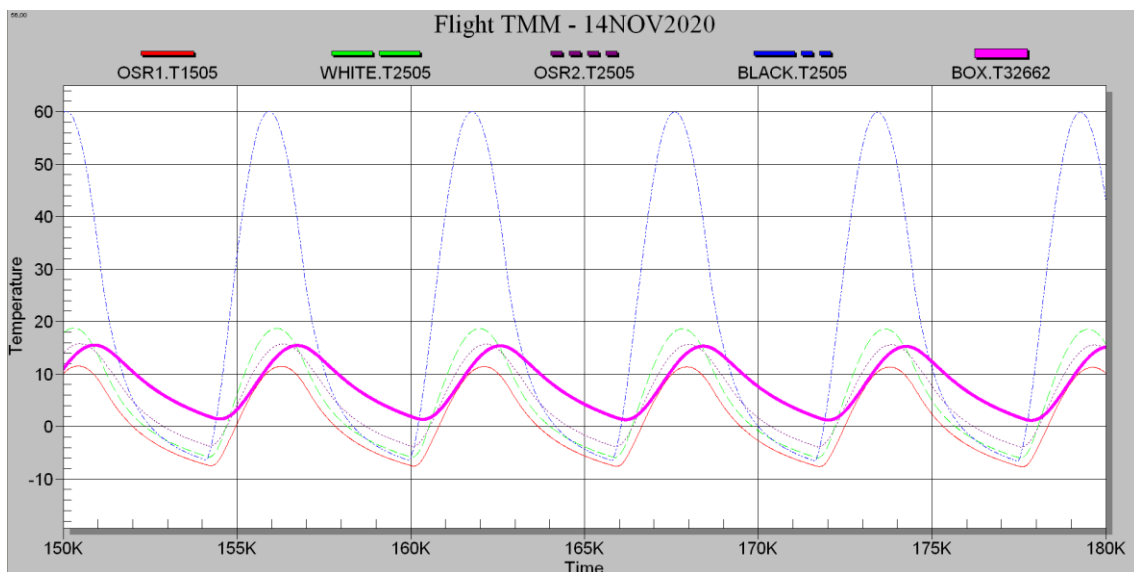

Source: Prepared by the author.

Figure 10.18 – Nominal TMM output for 20/12/2020 and preserved samples.
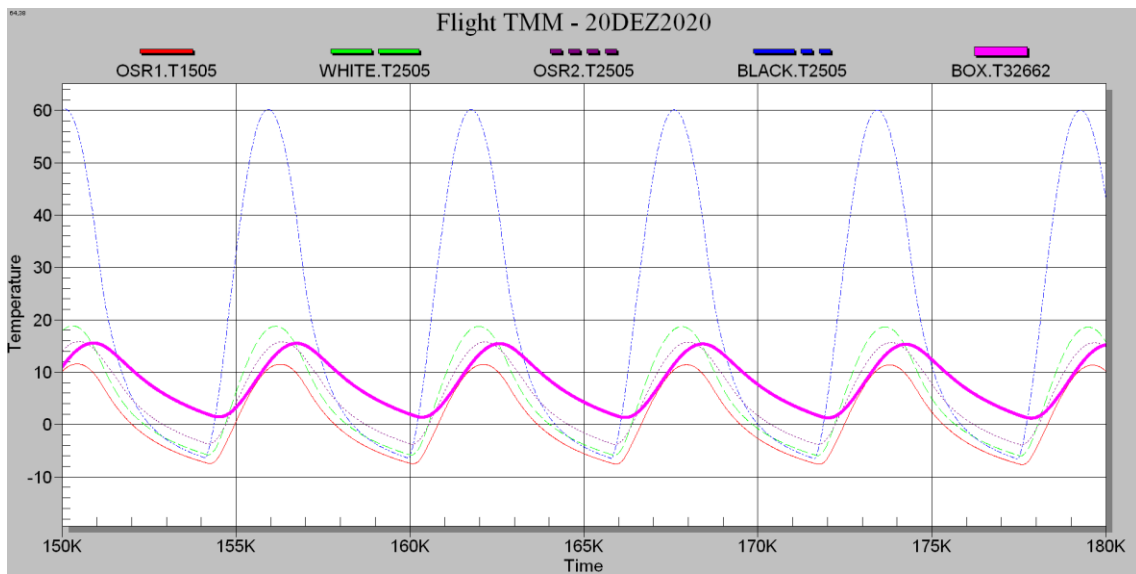
Source: Prepared by the author.

Figure 10.19 – Nominal TMM output for 19/04/2021 and preserved samples.
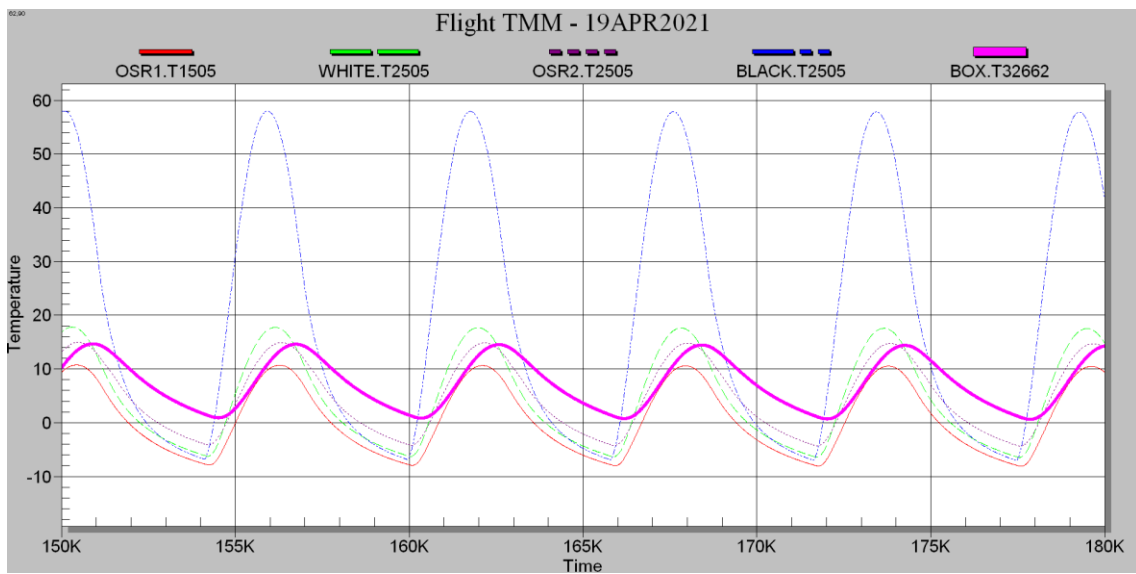
Source: Prepared by the author.

Figure 10.20 – Nominal TMM output for 25/06/2021 and preserved samples.
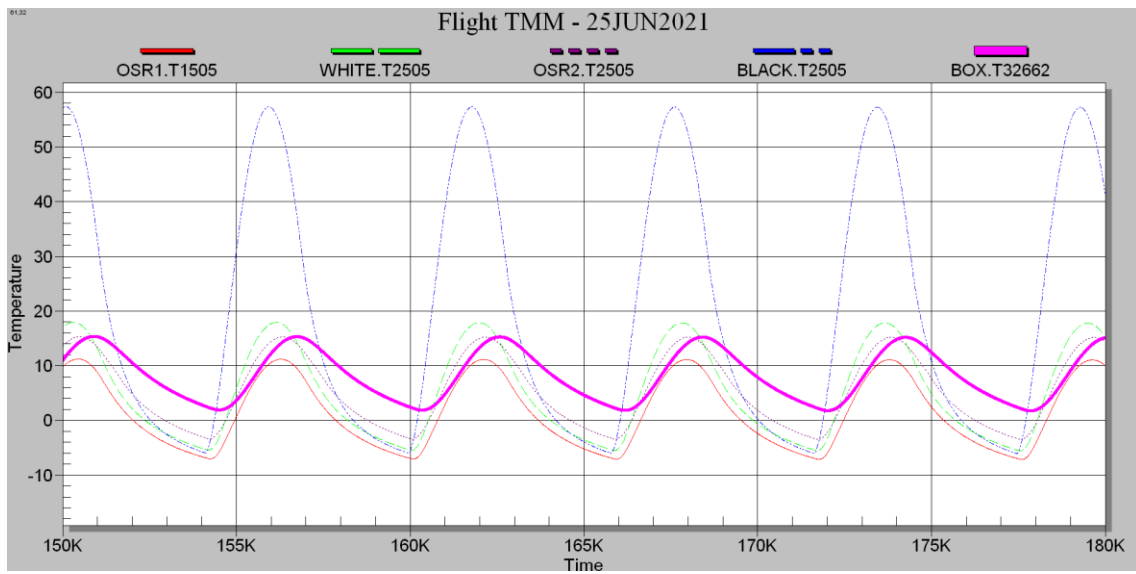
Source: Prepared by the author.

Figure 10.21 – Nominal TMM output for 30/11/2021 and preserved samples.
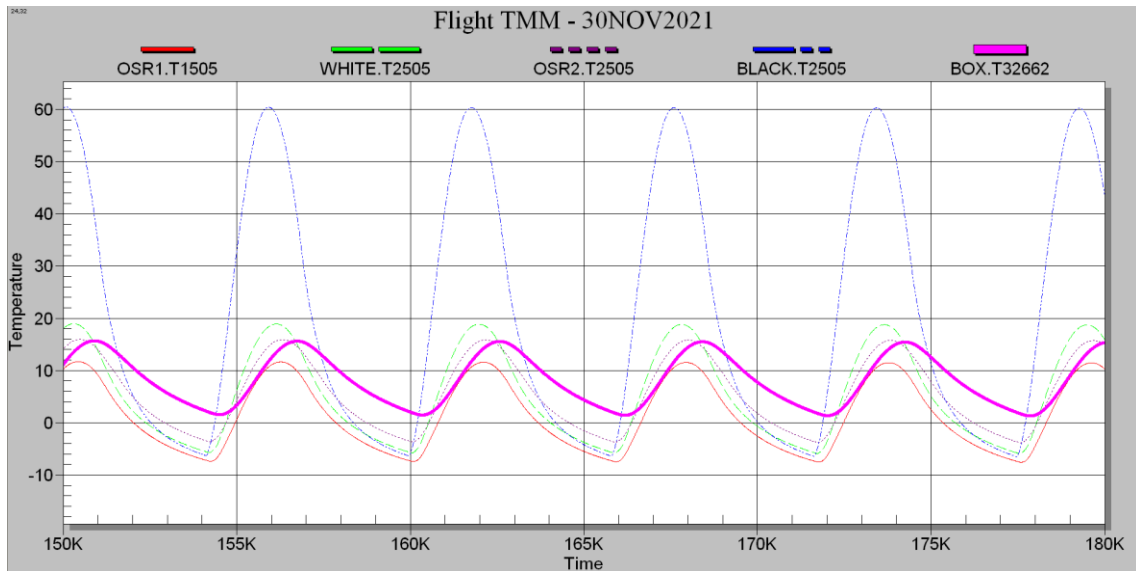
Source: Prepared by the author.

As means of illustration, Figures 10.22 and 10.23 show typical temperature distribution (in different color scales) for a black sample peak and valley temperature, respectively.

Figure 10.22 – Equipment temperature distribution in a Black sample peak.
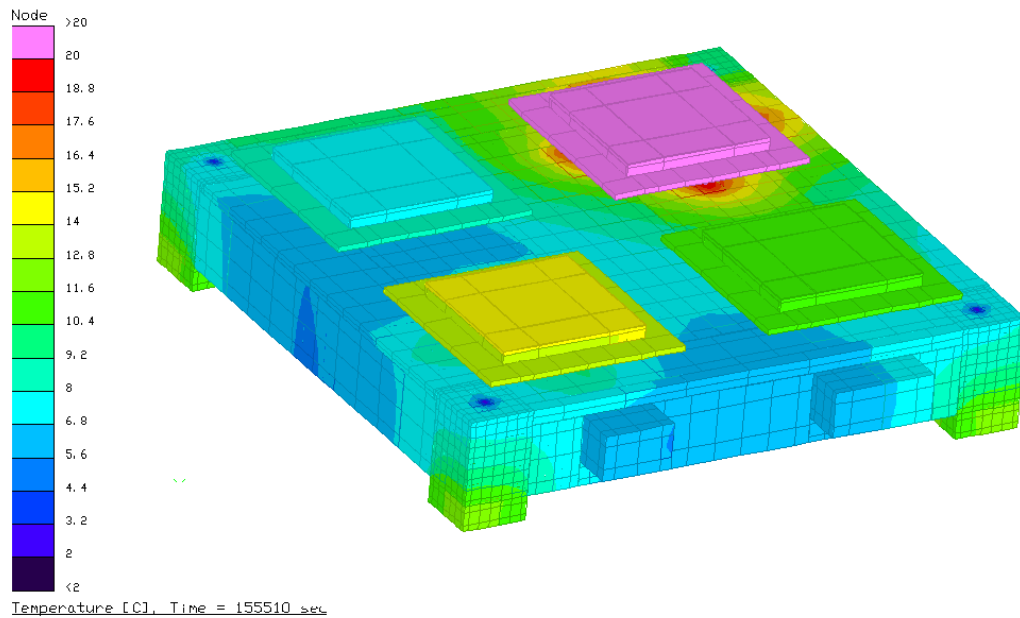
Source: Prepared by the author.

Figure 10.23 – Equipment temperature Distribution in a Black sample valley.

Source: Prepared by the author.

140
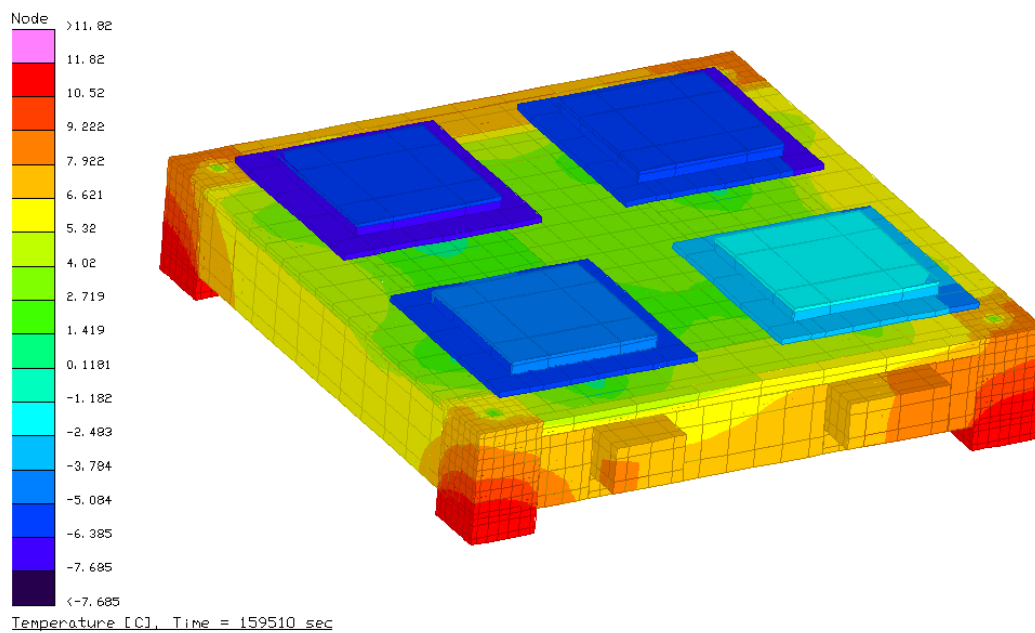
10.3 Sample degradation assessment

Firstly, it is required to acknowledge the initial optical properties adopted in the TMM for the samples. They are listed in Table 10.1 and consider 1 month of estimated degradation. OSR2 needed to include an enhanced α to comply with telemetry data, which may support the hypothesis that the samples reacted to the initial condensation differently.

Table 10.1 – BOL Flight TMM Samples Optical Properties.

Sample	Measured Absorptivity	Measured Emissivity
OSR1	0.042	0.853
White Paint	0.183	0.880
OSR2	0.090	0.810
Black Anodized	0.949	0.870

Concurrently, the solar heat load adopted in the TMM tested cases was calculated using Equations 10.1 and 10.2 combined.

Gilmore (2002) states that the inbound solar flux for a given Earth orbit position may be obtained as a function of its current distance D to the Sun:

$$q_s = \frac{1367.5}{D^2} \ [\text{W/m}^2] \tag{10.1}$$

Where D is given in astronomical units (AU). For a given day dn of the year, the distance D may be also calculated using the modified Kepler Equation:

$$D = 1 - 0.01672\cos[0.09856(dn - 4)] \tag{10.2}$$

In which dn is the desired day of the year, being dn = 1 for January 1st .

In order to evaluate the samples Δα, it is possible to use the TMM outputs by comparing them to their analogous telemetry counterparts. Assuming that they are exposed to equivalent boundary conditions, and they are reproduced in the TMM, their compared heat balance Equation for a given sample allows inferring that the assessment on increased absorptivity seen in the real equipment can be done on the base of temperature differences between telemetry and TMM output in terms of the net dissipated energy changes. In mathematical terms:

$$\Delta\alpha = \frac{\varepsilon_O \sigma (T_{real}^4 - T_{TMM}^4)}{q_s}$$

(10.3)

Using peak temperatures, it is possible to calculate Δα with fewer uncertainties, since temperature derivatives are closer to zero. Table 10.2 lists the peak temperatures for points in the experiment flight history that have the best quality telemetry data available.

Table 10.2 – Peak Temperatures for Selected Experiment Ages.

ID	Telemetry temps. [°C]					TMM temps. [°C]				
	16JUN20	14NOV20	19APR21	25JUN21	30NOV21	16JUN20	14NOV20	19APR21	25JUN21	30NOV21
o1	12.148	14.886	14.818	14.677	16.904	11.076	11.431	10.641	11.144	11.580
wt	22.334	27.220	27.754	27.681	30.515	17.907	18.677	17.686	17.873	18.864
o2	18.688	20.582	21.367	21.128	23.522	15.231	15.704	14.857	15.263	15.863
bk	61.033	64.734	63.287	62.537	66.237	57.241	59.992	57.946	57.357	60.379

From the information organized in Table 10.2, Δα rates are finally calculated using Equation 10.3 with temperatures in Kelvin. The results of such calculations are organized in Table 10.3.

Table 10.3 – Calculated Δα.

Sample ID	Δα					ε_o
	16JUN20	14NOV20	19APR21	25JUN21	30NOV21	
o1	0.0036	0.0112	0.0139	0.0121	0.0174	0.852
wt	0.0175	0.0331	0.0401	0.0401	0.0457	0.919
o2	0.0120	0.0163	0.0224	0.0207	0.0258	0.833
bk	0.02127	0.0259	0.0297	0.0293	0.0321	0.893
$q_s[W/m^2]$	1325	1398	1356	1323	1406	

The calculations performed to complete Table 10.3 may also be performed to other points of the illuminated phase of orbital cycle, but corresponding points have to be correctly selected to be compared. Data from the above Table can be used to find exponential law fittings, similar to the one chosen by Duzellier et al (2018), which are shown on Figures 10.24 to 10.28.

Figure 10.24 – Degradation of the solar absorptivity for OSR1.

Model	Exponential
Equation	y = y0 + A*exp(R0*x)
Plot	Δα OSR1
y0	0.01775 ± 0.00525
A	-0.02793 ± 0.01083
R0	-0.00394 ± 0.00347
Reduced Chi-Sqr	4.70814E-6
R-Square (COD)	0.90843
Adj. R-Square	0.81687
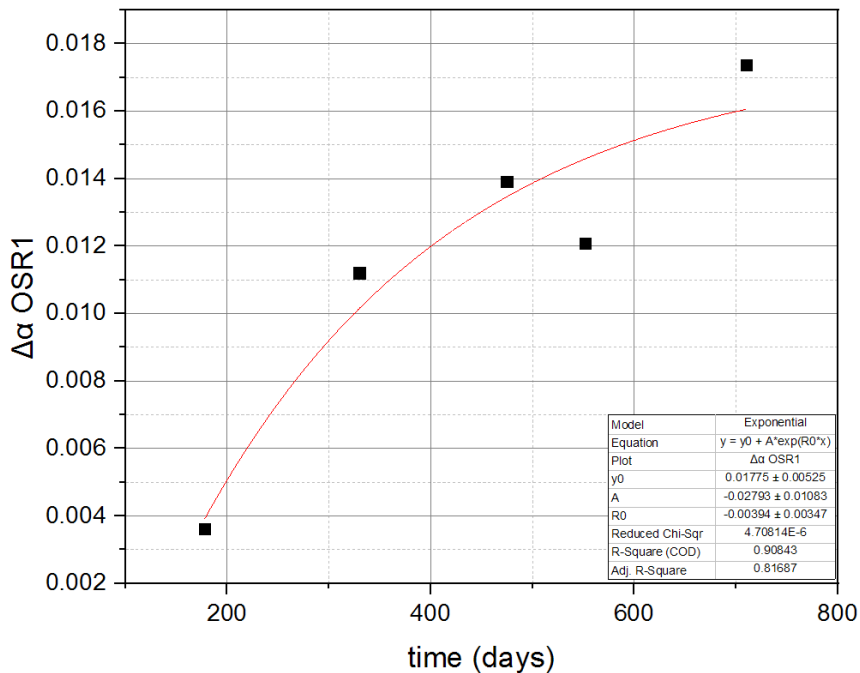
Source: Prepared by the author.

Figure 10.25 – Degradation of the solar absorptivity for White Paint.

WHITE sample absorptivity increase rates

Model	Exponential
Equation	y = y0 + A*exp(R0*x)
Plot	Δα WHITE
y0	0.04736 ± 0.00308
A	-0.0663 ± 0.01018
R0	-0.00453 ± 0.0012
Reduced Chi-Sqr	2.4768E-6
R-Square (COD)	0.98951
Adj. R-Square	0.97902
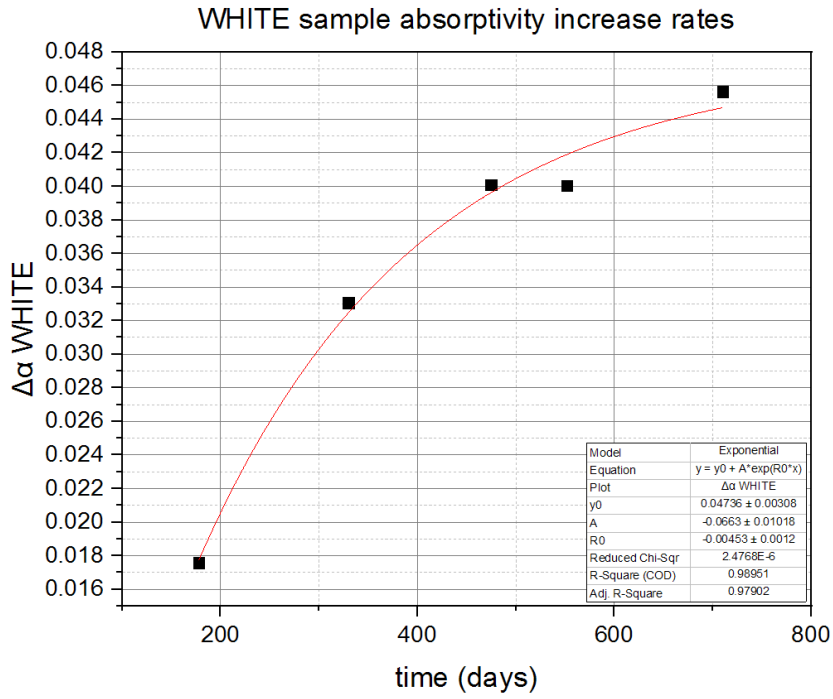
Source: Prepared by the author.

Figure 10.26 – Degradation of the solar absorptivity for OSR2.

OSR2 sample absorptivity increase rates

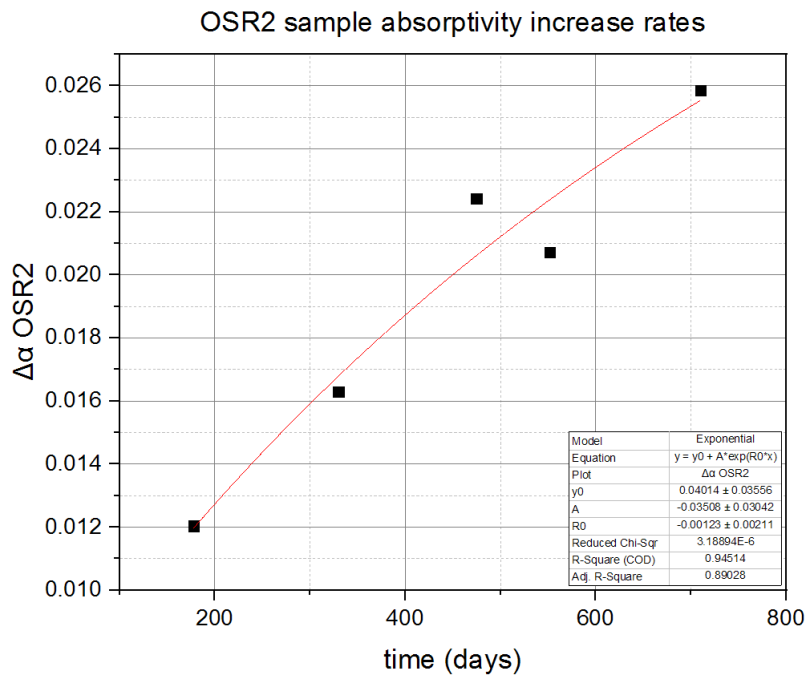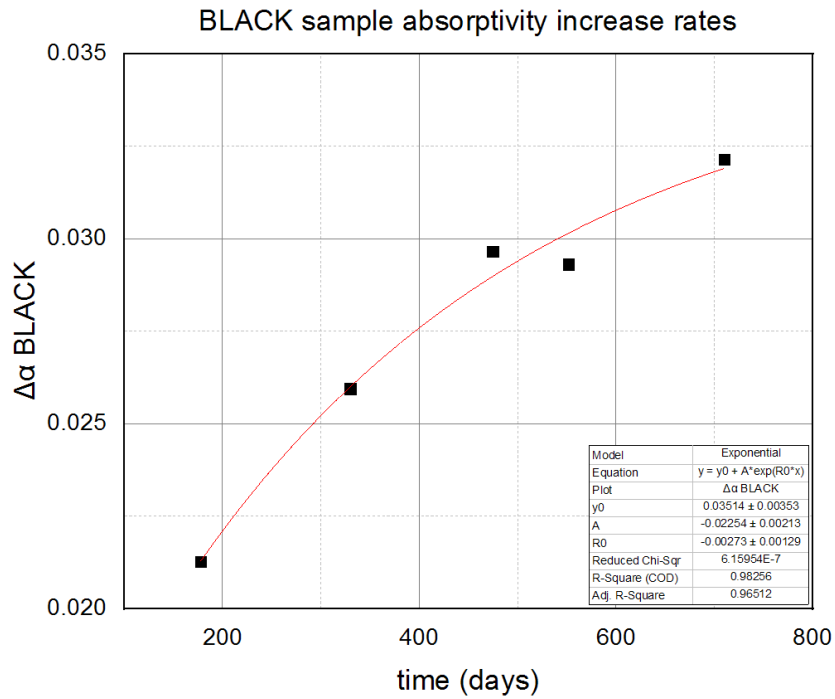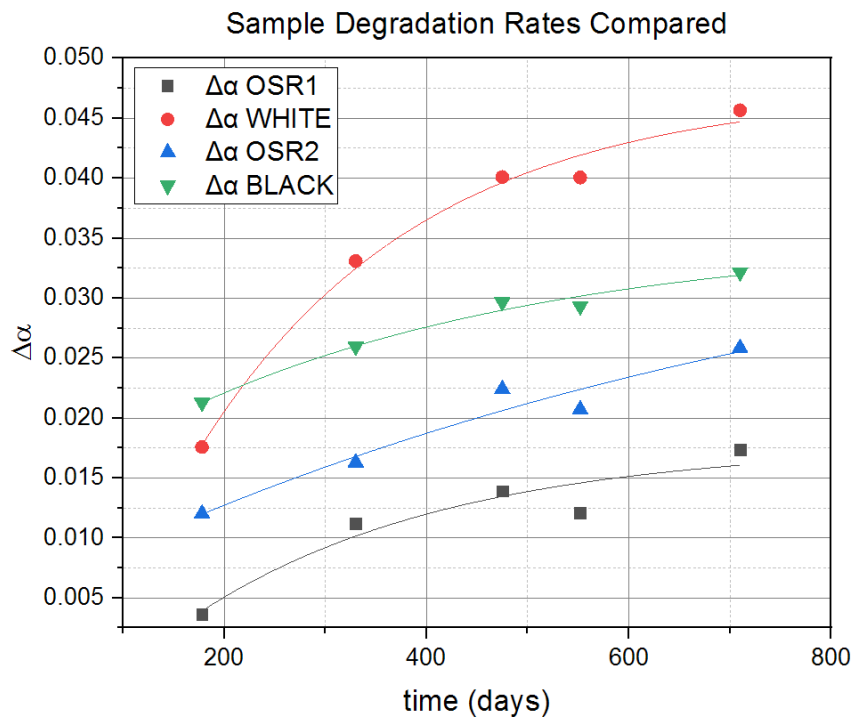| Model	Exponential
Equation	y = y0 + A*exp(R0*x)
Plot	Δα OSR2
y0	0.04014 ± 0.03556
A	-0.03508 ± 0.03042
R0	-0.00123 ± 0.00211
Reduced Chi-Sqr	3.18894E-6
R-Square (COD)	0.94514
Adj. R-Square	0.89028

Source: Prepared by the author.

144

Figure 10.27 – Degradation of the solar absorptivity for Black Anodized.

Source: Prepared by the author.

Figure 10.28 – Degradation curves in contrast.

Source: Prepared by the author.

145

Satisfactory agreement to the calculated data could be verified to the exponential fit adopted, but uncertainties to the parameters are considered to be excessive. The use of more data points from telemetry is believed to reduce such uncertainties.

Figures 10.24 to 10.28 compile the insights produced by the proposed methodology and on a first glance suggest that the black sample is indeed exposed to some degree of degradation. This is not necessarily true, though, because Figure 10.24 hints that the black sample degraded at speeds that are comparable to the OSR samples, which is not reasonable to think since black anodized has already very high absorptivity that makes its increase window substantially smaller. Besides, the black sample is not exposed to the same degradation mechanisms as the OSR sample is. The anodized aluminium is not prone to suffer from UV-sensitive chemical reactions degenerative effects, for instance.

An alternative interpretation to increase in the black anodized sample absorptivity as represented in Figure 10.27 is that the sample itself did not degrade, but the boundary conditions on the experiment evolved in such a way that produces an apparent increase in the black sample α.

In other words, it is believed the temperature increase in the black sample may be replicated in the calculations not as an effect of an increased α, but instead as an effect of the boundary condition changes, like gradual increase in the satellite panel temperature or a decreased efficiency of the experiment insulation, or both.

These supposed gradual changes in boundary conditions, even if not defined, could be corrected to stabilize the black sample property variations. This correction may be inserted in the TMM by changing a parameter that is capable to produce this effect, for example the solar heat flux magnitude. A procedure that could be explored to produce such artificial correction is to propose a factor that reduces the acting sun flux from Equation 10.3 considering that the temperature difference from real and expected values (from experiment and TMM) is maintained. Put differently, if the temperature difference is still the

same and the 'corrected' sun flux is smaller, the equivalent effect of changes in boundary conditions is mathematically created.

Therefore, if Equation 10.3 is rewritten in terms of a correction factor f:

$$\Delta\alpha = \frac{\varepsilon_O \sigma(T_{real}^4 - T_{TMM}^4)}{q_s f} \qquad (10.4)$$

And this factor is written in terms of the fitted values for the black sample from Figure 10.27 as:

$$f = \alpha_{o-bk}[1 - (0.03514 - 0.02254e^{-0.00273})] \qquad (10.5)$$

Where α_{o-bk} is the BOL solar absorptivity for the black sample at the real equipment.

If the results from Table 10.3 are computed again now using Equation 10.4, the calculated Δα for samples become represented in Table 10.4. Figures 10.29 to 10.32 correspond to the corrected results..

The increased degradation rates are about 11.2 % higher for 16/JUN/2020 and 12.4 % higher for 30/NOV/2021.
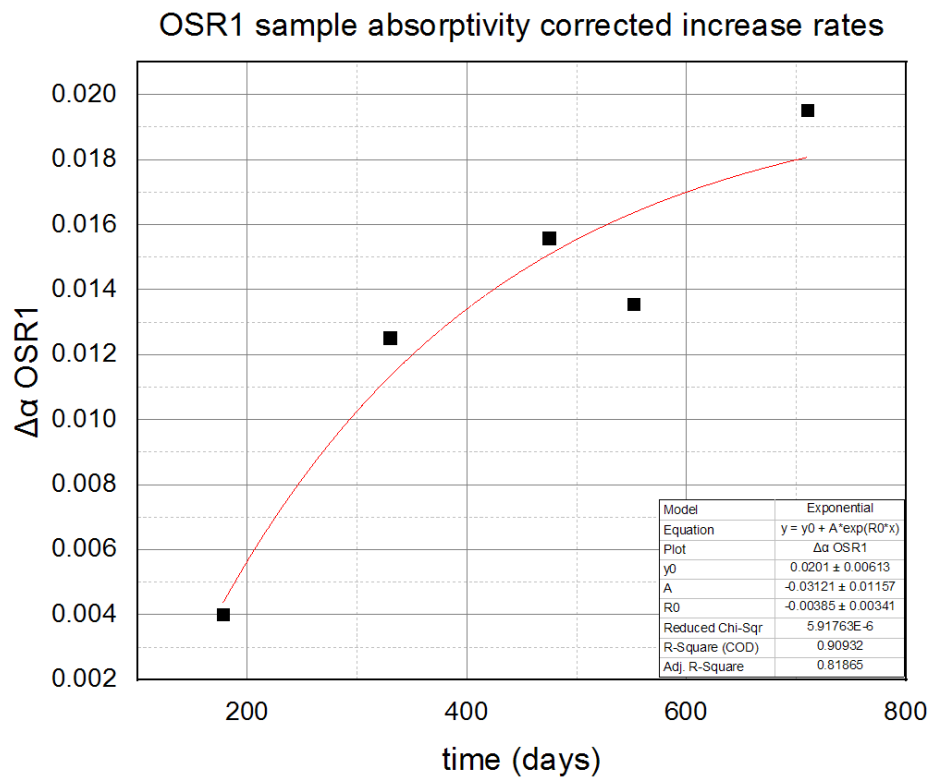
In any case, it is believed that the behaviour of the curves may produce interesting conclusions when contrasted. Figures show higher degradation rates for the white sample when compared to the OSR samples. At the same time, OSR1 appears to degrade slightly slower than OSR2.

Table 10.4 – Recalculated Δα.

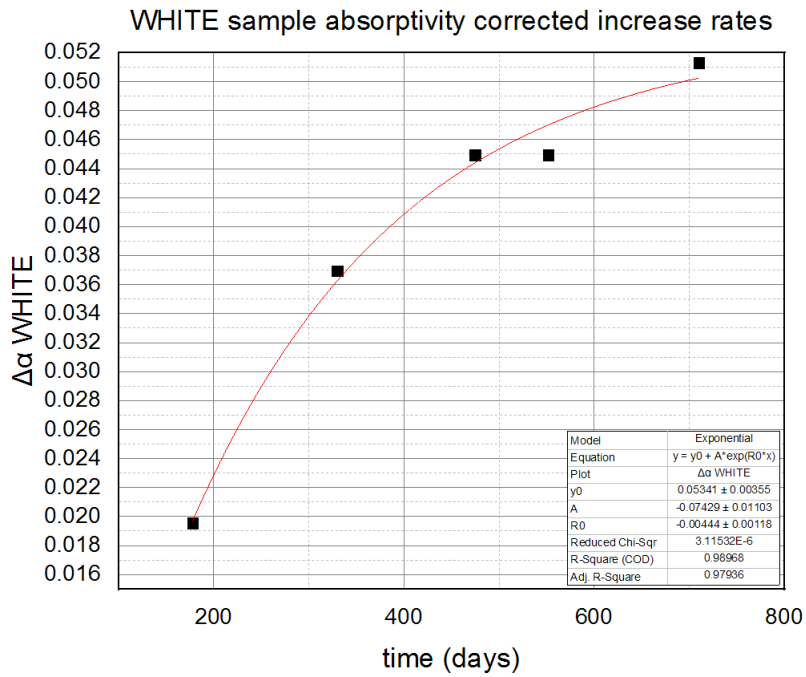| Sample ID	Δα					ε_o
	16JUN20	14NOV20	19APR21	25JUN21	30NOV21	
o1	0.0040	0.0125	0.0156	0.0136	0.0195	0.852
wt	0.0195	0.0369	0.0449	0.0449	0.0513	0.919
o2	0.0134	0.0182	0.0251	0.0232	0.0291	0.833
$q_s[W/m^2]$	1325	1398	1356	1323	1406	

* $\alpha_{o-bk} = 0.919$

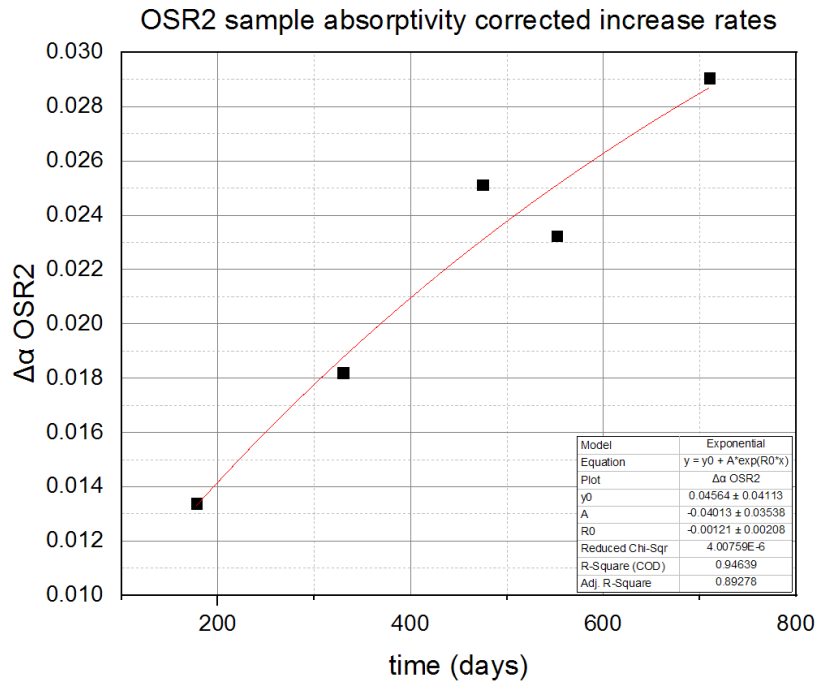Figure 10.29 – Corrected degradation of the solar absorptivity for OSR1.

Source: Prepared by the author.

148

Figure 10.30 – Corrected degradation of the solar absorptivity for Wt. Paint.

WHITE sample absorptivity corrected increase rates

Model	Exponential
Equation	y = y0 + A*exp(R0*x)
Plot	Δα WHITE
y0	0.05341 ± 0.00355
A	-0.07429 ± 0.01103
R0	-0.00444 ± 0.00118
Reduced Chi-Sqr	3.11532E-6
R-Square (COD)	0.98968
Adj. R-Square	0.97936

Source: Prepared by the author.

Figure 10.31 – Corrected degradation of the solar absorptivity for OSR2.

OSR2 sample absorptivity corrected increase rates

Model	Exponential
Equation	y = y0 + A*exp(R0*x)
Plot	Δα OSR2
y0	0.04564 ± 0.04113
A	-0.04013 ± 0.03538
R0	-0.00121 ± 0.00208
Reduced Chi-Sqr	4.00759E-6
R-Square (COD)	0.94639
Adj. R-Square	0.89278

Source: Prepared by the author.

149

Figure 10.32 – Corrected degradation curves in contrast.
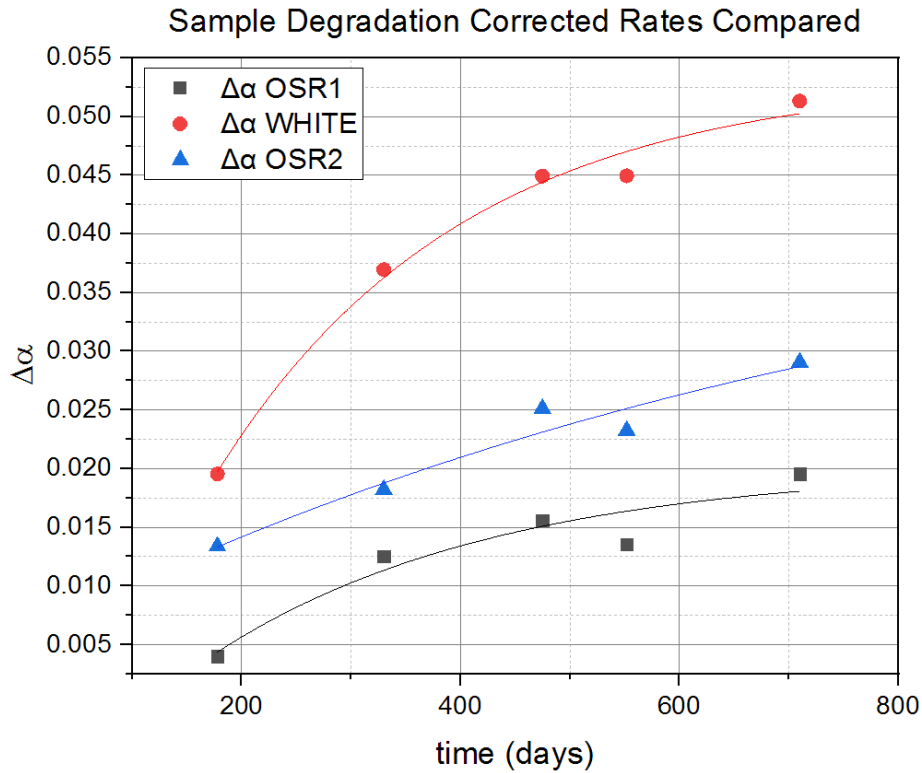
Source: Prepared by the author.

However, with eight years of data Duzellier et al (2018) found an asymptotic value α = 0.58 for the white paint, which is more than what Figure 10.25 implies. Therefore, it is possible that the real degradation curve behaviour is different from what the aforementioned Figures show.

Alternatively, there are other factors that may imply this difference. Some examples are: different attitudes, different orbit parameters, different intensity of propulsion pluming, among other factors contrasted from OSRA/CBERS 04A and the referred source data (Duzellier et al, 2018). For example, the OSRA position on CBERS 04A is arranged by such a way that the sample surfaces are tangential to the satellite velocity vector: this avoids the samples being affected by Atomic Oxygen fluence, which as known, is a big factor for white paint degradation. Ideally, this analysis needs a longer database timespan to produce more assertive results.

150

11 FINAL REMARKS

Spacecraft thermal control coatings development, as noticed through the research, is not a simple endeavour. From design concept to fabrication and performance evaluation, many nuances have been found to make a difference in the understating of how they could enhance a TCS design effectiveness.

As mentioned before, greater focus was dedicated to the numerical approach with detailed TMM to the degradation problem. This is why this work is only an excerpt of a much wider range of possibilities that are to be explored to tackle this inverse problem, which may be done for example by refining the analytical models and algorithms.

Telemetry data acquired from the flight experiment has shown signs of temperatures behaving possibly with hysteresis, i.e. dependent on the equipment's boundary conditions history.

The TMM developed to tackle this problem provided many useful insights for future research. At the same time, it has proven a very time-consuming resource while in the calibration process. For this reason to enhance automation in parameter testing is suggested. As an approximation, the numerical simulation also indicates that non-linear phenomenon is likely to influence the real experiment more vigorously at some temperatures, especially in the colder ranges. The inherent non-linearity of the problem is shall be better studied.

Comparisons between telemetry data and TMM seem initially to point towards a black sample degradation. This possibility cannot be disregarded, due to anodized layer thinning for example, but is however intuitively unlikely. A reasonable explanation to this observation is the modification of the boundary conditions of the system while in-flight, which by its is turn may range from changes in the satellite operational schedule and power dissipation to the reduction in the insulation effectiveness throughout time. Some factors of such changes are, for instance, MLI external layer absorptivity degradation which is very likely but does not importantly affect the blanket insulation. The last

possibility has been carefully considered since the minimum temperatures increase in time, as shown in Table 11.1.

Table 11.1 – Peak and Min. Temperatures for Selected Experiment Ages.

ID	Telemetry peak temps. [°C]					TMM peak temps. [°C]				
	16JUN20	14NOV20	19APR21	25JUN21	30NOV21	16JUN20	14NOV20	19APR21	25JUN21	30NOV21
o1	12.148	14.886	14.818	14.677	16.904	11.076	11.431	10.641	11.144	11.580
wt	22.334	27.220	27.754	27.681	30.515	17.907	18.677	17.686	17.873	18.864
o2	18.688	20.582	21.367	21.128	23.522	15.231	15.704	14.857	15.263	15.863
bk	61.033	64.734	63.287	62.537	66.237	57.241	59.992	57.946	57.357	60.379
	Telemetry minimum temps. [°C]					TMM minimum temps. [°C]				
	16JUN20	14NOV20	19APR21	25JUN21	30NOV21	16JUN20	14NOV20	19APR21	25JUN21	30NOV21
o1	-6.345	-4.726	-4.696	-4.756	-3.482	-7.219	-7.668	-8.103	-7.153	-7.586
wt	-4.226	-2.577	-2.379	-2.237	-0.788	-5.647	-6.026	-6.496	-5.603	-5.938
o2	-0.193	1.476	1.448	1.307	2.682	-3.576	-3.928	-4.389	-3.522	-3.841
bk	-2.492	-0.889	-0.972	-1.111	0.182	-6.129	-6.584	-7.031	-6.087	-6.500

Interestingly, in the TMM the colder minimum temperatures were observed for April time, which is unexpected since this is not the satellite cold case situation. Shadows imposed by the vicinity protuberances may be a reasonable explanation for this phenomenon.

For future flight equipment iterations, some design changes were suggested throughout this text to make the data produced easier to interpret. In addition to the claims made in the previous sections, it is suggested that future experiments SNs also consider the following modifications such as: to reduce sample subassembly 4 contact points to the FR4 box to a single one; and attempt to propose an alternative to the MLI blanket insulation design, which

could be less intricate and easier to reproduce. It is also suggested to evaluate design features that do not sum up to the complexity of heat paths, such as avoiding cables to be thermally attached to points near bolts and washers used to fix the supports.

To conclude, it is believed that this work is an attempt to solve an intricate problem and shall be seen as a part of a wider research branch. Given the degradation aspects explored in this work, it is believed that knowledge in the theme has been enhanced, and for this reason it is also believed that the project was conducted in compliance with the intended objectives.

12 CONCLUSIONS

The following results and main conclusions can be detached:

1) OSR samples qualified for flight have been produced by the author on INPE's installations using previously developed technology of e-beam deposition. Additional innovations were added to the fabrication and storage of the samples though, which were necessary to enhance quality and reproducibility of the specimens.

2) The abovementioned OSR along other 3 samples have been assembled in OSRA module with author and other colleagues from the thermal engineering group contributions. The OSRA module passed successfully through all qualification tests in order to meet CBERS 04A environment conditions. OSRA is the first thermal coating experiment of INPE and Brazilian space missions history.

3) Differently from analogous experiments launched previously by other countries, the sample supports were equipped with heaters which power adjusted by such a way that the sample average temperatures would approximate the average temperatures seen by radiators used on other CBERS series satellites. This aspect will increase the practical applicability of the OSRA results to the Brazilian missions in thermal control designs that use OSR radiators.

4) OSRA has passed through a Thermal Balance Test carried out in a vacuum chamber located at INPE/LIT and conducted by the thermal group with active participation of the author. The TBT results were, to this date, treated solely by the author.

5) The analytical nodal model of OSRA has been created to better understanding of the thermal behaviour of the OSRA, considering main internal couplings. Some analyses have been performed.

6) A study and numerical tests have been performed to evaluate if the nodal model could be used as a principal base for assessment of coatings degradation rates by inverse methods; the conclusion derived from this

154

study is that the nodal model can not represent all internal details and peculiarities of the real assembly, which influence on the sample temperature variations. More detailed finite difference thermal mathematical model (TMM) with distributed parameters is needed.

7) Detailed TMM of the OSRA was developed within the SINDA Thermal Desktop environment which is a NASA proven tool. Some of the main features of this TMM are the following:

   a. Detailing and reproduction of OSRA geometry and constructive details with fine spatial and volumetric numerical grids over the OSRA box, internal plate and MLI blankets;

   b. Geometrical reproduction and thermal parameterization of electrical connectors and wires that also act as additional conductors and contribute to parasitic heat losses;

   c. Detailed simulation of internal radiative heat transfer between all elements of the assembly;

   d. Inclusion in the model all contact thermal resistances between insulated washers, box, plate and MLI blankets;

   e. Deep parameterization of the TMM to have the possibility to perform effective correlation with experimental results.

8) The TMM was correlated with TBT results and then improved with first telemetry data acquired after the satellite was launched in December 2019.

9) First estimation of OSR and white paint degradation during the initial 2 year period of CBERS 04A flight was performed based on developed technology. The degradation rate of OSR samples was quantified; this rate is lower than for white paint, as expected.

10) After completion, CBERS 04A mission will allow INPE to obtain a complete lifelong useful database regarding the stability of thermal coatings produced with in-house technology This will allow, then, having full flight qualification and being adopted in the Brazilian Space Program.

REFERENCES

ALIFANOV, O. M. **Inverse heat transfer problems.** Berlin, Germany: Springer-Verlag, 1994. 359 p.

ANVARI, A.; FARHANI, F.; NIAKI, K. S. Comparative study on space qualified paints used for thermal control of a small satellite. **Iranian Journal of Chemical Engineering**, v. 6, n. 2, p. 50-62, 2009.

BIERING, B.; HAGELSCHUER, D. Improvements of a thermal method for the determination of solar absorptance and thermal emittance of spacecraft coatings. In: INTERNATIONAL CONFERENCE ON ENVIRONMENTAL SYSTEMS, 26., 1996, Monterrey, CA, USA. **Proceedings…** 1996. 6 p.

BOATO, M. G. **Development of the fabrication process for a reflective optical surface for satellite thermal radiators** (in Portuguese). 2014. 141 p. (DCTA/ITA/DM-085/2014). Dissertation (Master in Aeronautical and Mechanical Engineering – Aerodynamics, Propulsion and Energy) – Aeronautical Technology Institute (ITA), São José dos Campos, 2014. Available from: http://www.bd.bibl.ita.br/tde_busca/arquivo.php?codArquivo=3164 . Access in: mar. 2019.

BOATO, M. G.; GARCIA, E. C.; SANTOS, M. B.; BELOTO, A. F. Assembly and testing of a thermal control component developed in Brazil. **Journal of Aerospace Technology and Management.** v. 9, n. 2, p. 249-256, 2017.

COLAÇO, M J.; ORLANDE, H. R. B.; DULIKRAVICH, G. S. Inverse and optimization problems in heat transfer. **Journal of the Brazilian Society of Mechanical Science & Engineering**, v. 23, n. 1, p. 1-24, 2006.

COSTA, R. L. **Experimental study of the contact thermal resistance between equipment and satellite structural panels** (in Portuguese). 2018. 247 p. (INPE-07.25.19.19-TDI). Thesis (PhD in Space Engineering and Technology – Space Mechanics and Control) – National Institute for Space

Research (INPE), São José dos Campos, 2018. Available from: http://urlib.net/8JMKD3MGP3W34R/3RGPJQH. Access in: out. 2019.

CURRAN, D. G. T.; MILLARD, J. M. Contamination/degradation measurements on an operational satellite thermal control surfaces. In: FLETCHER, L. (Ed.). **Heat transfer and thermal control systems**. New York, NY, USA: American Institute of Aeronautics and Astronautics, 1978. p. 263-289.

CURRAN, D. G. T.; MILLARD, J. M. Results of contamination/degradation measurements on thermal control surfaces of an operational satellite. In: AIAA THERMOPHYSICS CONFEFENCE, 12., 1977, Albuquerque, NM, USA. **Proceedings…** 1977. 15 p.

DUZELLIER, S.; PONS, C.; REMAURY, S.; NABARRA, P. Influence of test conditions and variability of end-of-life solar absorptance of thermal control materials. In: INTERNATIONAL SYMPOSIUM ON MATERIALS IN SPACE ENVIRONMENT (ISMSE), 14., 2018, Biarritz, France. **Proceedings…** 2018.

EFRON, B.; TIBSHIRAMI, R. J. **An introduction to the bootstrap.** Dordrecht, The Netherlands: Springer Science+Business Media, 1993. 452 p.

FENG, W.; DING, Y.; YAN, D.; LIU, X.; WANG, W.; LI, D. Space combined environment simulation test on α_s degradation of GEO satellite thermal control coatings. **Spacecraft Environment Engineering**, v. 24, n. 2, p. 27-31, 2007.

FONTENOT, J. E.; WHITELUST, C. A. **A method to predict the thermal conductance of a bolted joint.** Baton Rouge, LA, USA: NASA, Jan, 1968. Report NASA/TM – 68-33514. Available from: <https://ntrs.nasa.gov/citations/19680024042>. Accessed on: set. 2019.

GILMORE, D. G. **Spacecraft thermal control handbook:** fundamental technologies. El Segundo, CA, US: The Aerospace Press, 2002. 837 p.

HALL, D. F.; FOTE, A. A. α_s/ε_H Measurements of thermal control coatings on the P78-2 (SCATHA) spacecraft. In: AIAA THERMOPHYSICS CONFEFENCE, 15., 1980, Snowmass, CO, USA. **Proceedings…** 1980. p. 467-486.

HALL, D. F.; FOTE, A. A. α_s/ε_H Measurements of thermal control coatings over four years at geosynchronous altitude. In: AIAA THERMOPHYSICS CONFEFENCE, 18., 1980, Montreal, Canada. **Proceedings…** 1980. 11 p.

HALL, D. F.; FOTE, A. A. 10 year performance of thermal control coatings at geosynchronous altitude. In: AIAA THERMOPHYSICS CONFEFENCE, 26., 1991, Honolulu, HI, USA. **Proceedings…** 1991. p. 467-486.

HALL, D. F.; FOTE, A. A. Thermal control coatings at near geosynchronous altitude. **Journal of Thermophysics and Heat Transfer**, v. 6, n. 4, p. 665-671, 1992.

HASEGAWA, M. K.; KAUDER, L. R. Space environmental evaluation of white conductive thermal control coatings. In: AIAA THERMOPHYSICS CONFEFENCE, 42., 2011, Honolulu, HI, USA. **Proceedings…** 2011. 9 p.

HENGHUI, M.; VLASSOV, V. V.; COSTA, R. L. **CBERS 04A TVT and TBT specification.** Technical Report no. RBB-TRP-2098/00(04A). São José dos Campos: National Institute for Space Research (INPE), 2017.

HYMAN, N. L. Solar absorptance degradation of OSR radiators on the COMSTAR satellites. In: AIAA THERMOPHYSICS CONFEFENCE, 16., 1981, Palo Alto, CA, USA. **Proceedings…** 1981. p. 212-233.

JAWORSKE, D. A.; KLINE, S. E. **Review of end-of-life thermal control coating performance.** Cleveland, OH, USA: NASA, April 2008. Report NASA/TM – 2008-215173. Available from: < https://ntrs.nasa.gov/citations/20080018585>. Accessed on: out. 2019.

KANG, W.; LEE, Y.; KANG, C.; CHUNG, W.; XU, H.; MATSUMURA, J. Using the inverse method to estimate the solar absorptivity and emissivity of wood

exposed to outdoor environment. **Journal of the Faculty of Agriculture**, v. 56, n. 1, p. 139-148, 2011.

KARAM, R. D. **Satellite thermal control for systems engineers.** Cambridge, MA, US: American Institute of Aeronautics and Astronautics, 1998. 280 p. (Progress in Astronautics and Aeronautics).

LEET, S. J; FOGDALL, L. B.; WILKINSON, M. C. Thermo-optical property degradation of irradiated spacecraft surfaces. **Journal of Spacecraft and Rockets**, v. 32, n. 5, p. 832-838, 1995.

LIU, T.; SUN, Q.; MENG, J.; PAN, Z.; TANG, Y. Degradation modelling of satellite thermal control coatings in a low Earth orbit environment. **Solar Energy,** v. 139, p. 467-474, 2016.

LURA, F.; BIERING, B.; HAGELSCHUER, D. A thermal method for the determination of solar absorptance and thermal emittance of spacecraft coatings. In: INTERNATIONAL CONFERENCE ON ENVIRONMENTAL SYSTEMS, 23., 1993, Colorado Springs, CO, USA. **Proceedings…** 1993. 8 p.

MARCO, J.; REMAURY, S. Evaluation of thermal control coatings degradation in simulated geo-space environment. **High Performance Polymers**, v. 16, p. 177-196, 2003.

MESEGUER, J.; PÉREZ-GRANDE, I.; SANZ-ANDRÉS, A. **Spacecraft thermal control.** Cambridge, UK: Woodhead Publishing, 2012. 413 p.

MILLARD, J. P. **An uncertainty analysis for satellite calorimetric measurements.** Moffet Field, CA, USA: NASA, February 1968. Report NASA/TN – D-4354.

MILLER, S. K. R.; BANKS, B. Degradation of spacecraft materials in the space environment. **MRS Bulletin.** v. 35, p. 20-24, Jan. 2010.

MORAN, M. J.; SHAPIRO, H. N. **Fundamentals of engineering thermodynamics.** 5 ed. West Sussex, UK: John Wiley & Sons, 2006. 847 p.

MURAOKA, I. **Thermal analysis of OSR sample unit (OSRA).** Technical Report no. RBLH-TRP-8043/00(04A). São José dos Campos: National Institute for Space Research (INPE), 2017.

NAEGELI, C. Spacenet I, II 5 years in orbit – review of the thermal trends observable in a passive thermal design of 2 communication satellites. In: AIAA/ASME JOINT THERMOPHYSICS AND HEAT TRANSFER CONFEFENCE, 5., 1990, Seattle, WA, USA. **Proceedings…** 1990.16 p.

NAEGELI, C. Solar absorptance degradation of optical solar reflector radiators on the SPACENET satellites**. Journal of Spacecraft and Rockets**, v. 29, n. 5, p. 741-745, 1992.

NENAROKOMOV, A. V.; ALIFANOV, O. M.; KRAINOVA, I. V.; TITOV, D. M.; MORZHUKHINA, A. V. Estimation of environmental influence on spacecraft materials radiative properties by inverse problems technique. **Acta Astronautica**, v.160, p. 323-330, 2019.Available from: https://doi.org/10.1016/j.actaastro.2019.04.014. Accesso on: 15 Jan. 2020.

OHRING, M. **Materials science of thin films:** deposition & structure. 2.ed. Hoboken, NJ, US: Academic Press, 2002. 808 p.

OZISIK, M. N.; ORLANDE, H. R. B. **Inverse heat transfer**: fundamentals and applications. New York, NY, USA: Taylor & Francis, 2000. 341 p.

PIEGARI, A.; FLORY, F. **Optical films and coatings.** 2 ed. Duxford, UK: Woodhead Publishing, 2018. 862 p.

REMAURY, S.; SERÈNE, F.; NABARRA, P. The THERME experiment: in-flight measurements of the ageing thermal control coatings. In: INTERNATIONAL SYMPOSIUM ON MATERIALS IN A SPACE ENVIRONMENT, 9., 2003, Nordwijk, The Netherlands. **Proceedings…** 2003. p. 585-587.

REMAURY, S.; NABARRA, P.; BELLOUARD, E.; D'ESCRIVAN, S. In-flight ageing of thermal control coatings: the THERME experiment. **Journal of Spacecraft and Rockets**, v. 48, n. 1, p. 27-33, 2011.

SCHAEFER, C. F.; BANNISTER, T. C. Thermal control coating degradation data from the Pegasus experiment packages. In: AIAA THERMOPHYSICS SPECIALISTS CONFERENCE, 1967, New Orleans, LA, USA. **Proceedings…** 1967. p. 457-474.

SHANGHAI INSTITUTE OF SATELLITE ENGINEERING. **Method for predicting on-orbit performance degradation of thermal control coating of satellites.** [S.l.]: SISE, 2015.

SILVA, D. F. **Model for a satellite thermal control project based in experimentation and optimization – application to a 3-axis stabilized satellite** (in Portuguese). 2014. 255 p. (DCTA/ITA/DM-005/2014). Thesis (Master in Aeronautical and Mechanical Engineering – Aerodynamics, Propulsion and Energy) – Aeronautical Technology Institute (ITA), São José dos Campos, 2014. Available from: http://www.bd.bibl.ita.br/tde_busca/arquivo.php?codArquivo=2968. Access in: Apr. 2019.

SHI, F. **Basic theory of magnetron sputtering**. Intech Open, 2018. Available from: https://www.intechopen.com/online-first/63559. Access in: 15 Dec. 2021.

VLASSOV, V. V.; COSTA, R. L. **Combined thermal balance and thermal vacuum cycling test specification for acceptance of OSR sample unit FM SN02.** Technical Report no. RBLH-TES-8006/00(04A). São José dos Campos: National Institute for Space Research (INPE), 2019.

VUOLO, J. H. **Fundamentals of error theory** (in Portuguese). 2 ed. São Paulo, SP, Brazil: Edgar Blütcher, 1996. 250 p.

GLOSSARY

Albedo – solar spectrum radiation energy that is directly reflected by a celestial body, without absorption

Black body – a theoretical body that is able to emit energy at any conceivable wavelength if heated enough

Convection – heat transfer mode that relies on the transit of mass

Lump – physical qualities of a real mass object concentrated in a virtual equivalent representation

Multi-layer insulation blanket – a highly customisable composite material that exhibits super insulation characteristics in a vacuum environment

Radiation – physical phenomenon that also defines a heat transfer mode and occurs by means of photon exchange

Radiator – heat exchange device that issues radiation

Smoothing – post processing of data in order to enhance its interpretability

White noise – theoretical signal characterized by random signals equally distributed throughout the spectrum

APPENDIX A – EXPERIMENT FABRICATION AND ASSEMBLY DETAILS

For reference, the surface available to the samples is a square of 41 mm sides. Dimensions of the sample supports and their material were chosen to reduce the thermal capacity and thus the temperature inertia of the samples as well as good thermal conductivity for temperature homogeneity. Comparable to the box geometry, each sample holder is a one-piece concave part as can be observed in Figure A.2.

In what concerns the geometry of the holders, they have three main distinctive features: a square stand where the samples reside, a square slot carved within the stand, and an octagonal skirt that has four recessed holes available to house the heads of the bolts. They are all electrically grounded.

Figure A.1 - Inside details of the chassis from bottom isometric view.
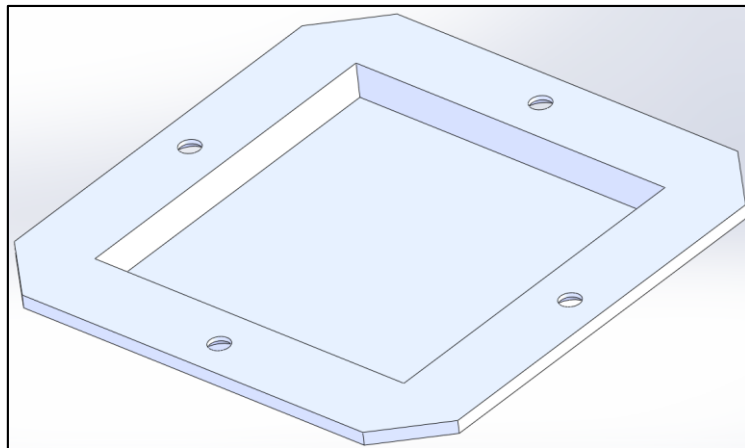
Source: Prepared by the author.

The box is fitted with two space-qualified electrical connectors in the front face: a DA-15 and a DE-9. The purpose of these two connectors is to offer a detachable electrical interface and be part of the circuitry needed for the temperature sensors and heaters to function, respectively. Each of the heaters and sensors is part of an independent electrical circuit fed by the satellite bus.

Internally, when the sample holders are in place their bottom surfaces are visible. Due to the use of FR4 washers as spacers, the bottom surface of the sample holders skirts can be viewed also.

As shown in Figure 3.1, the bottom side of the sample holders is oriented towards the interior of the box. Therefore, the slot faces directly the lid top side, which is also oriented inwards. This slot contains the inner surface of the holders and is available to accommodate heaters and thermal sensors.

Similar to the box, the lid is made of machined FR4 and has a simple geometry that features two main surfaces. It has been conceived to close the assembly without touching the lateral faces of the box, which is done by keeping its edges a constant distance from them. When fastened to the box, the lid is protected with MLI on both sides. Velcro hook pieces glued to both faces hold the insulation blankets correctly in place. Figure A.2 illustrates this part.

Figure A.2 – Bottom Closing Lid.
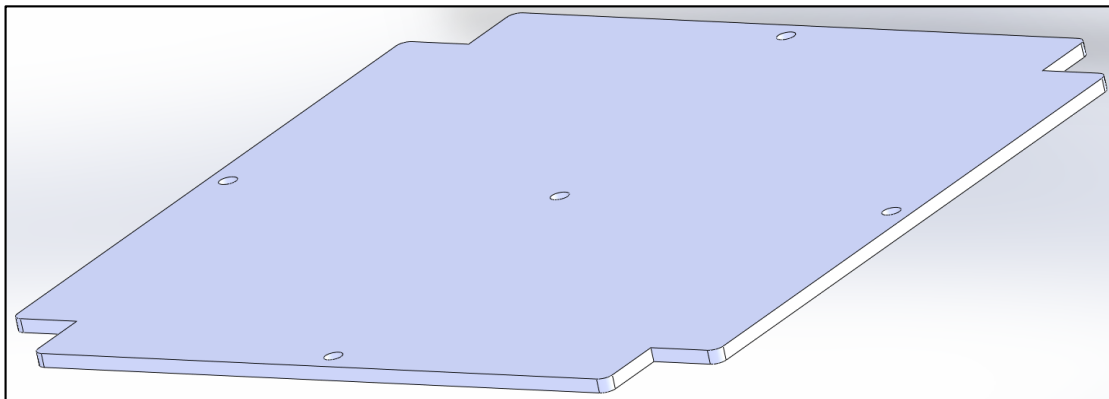
Source: Prepared by the author.

A custom MLI blanket was designed to fit and cover all the externals of the assembly but the exposed samples on the holders. The single piece blanket has been created to protect the outwardly oriented faces. This is why it needs to fold in multiple locations to do that. Multiple reinforced pass-through perforations exist for threads routing. The threads prevent MLI from inflation during the quick ambient pressure drop at launch. MLI has 15 layers 0.25 mil

thick of 2-sided aluminized mylar, all electrically connected to the grounding point.

All mentioned details make the MLI blanket quite complex to manufacture. Although required, those added features were expected to provoke insulation efficiency losses. Figure A.3 it is possible to observe how meticulous they are.

Figure A.3 – Experiment Bottom View with Lid and MLI Blankets Removed.
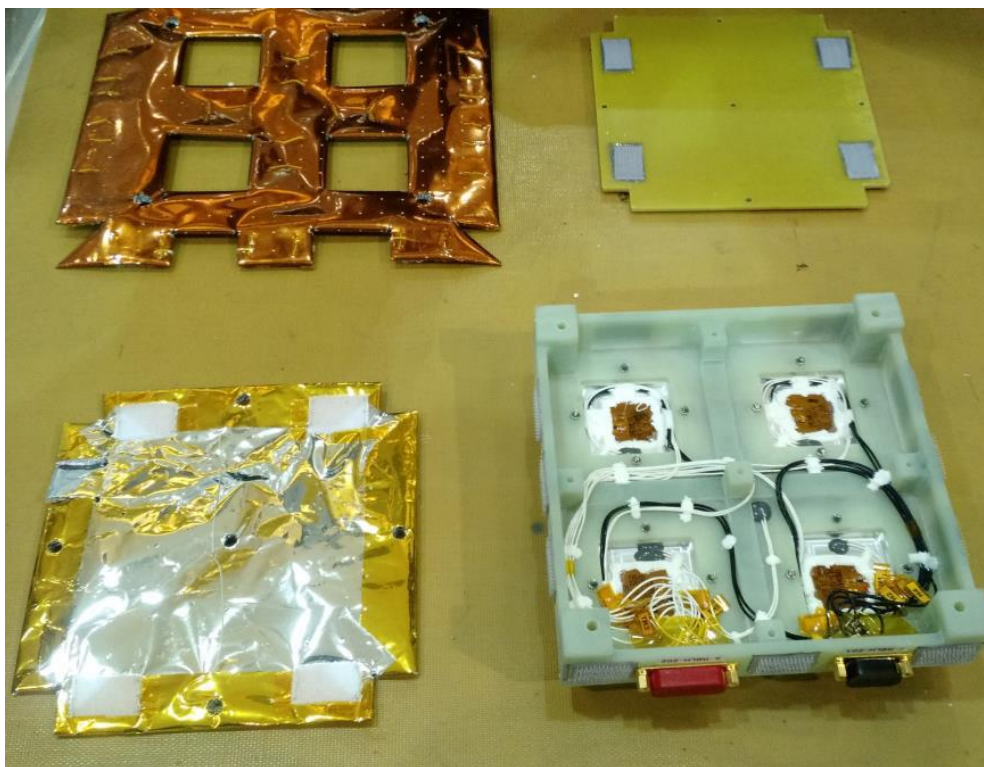
Source: Costa et al (2018).

Alluding again to Figure A.3 it gives an idea on how internal electric cables were routed, being the black coloured cables connected to the heaters and the white cables to the thermal sensors.

In total, four equal resistive skin heater elements were attached to each slot of the sample holders. They are arranged to dissipate 0.4 W approximately when active. Five temperature sensors are glued to the chosen points of interest: four

inside de sample slots, adjacent to the heaters; and the last one is joined to the box in a point close to its geometric centre. Cables are glued to the box along their way to make them less prone to continuity issues induced by vibrations. The temperature sensing elements chosen are NTC type thermistors with resistance of approximately 10 $k\Omega$ at 25°C.

The described assembly was positioned in the zenith oriented Z- face of the CBERS 04A satellite.

Borosilicate glass was chosen to be the substrate material of the OSR samples built. Manufactured OSR substrates are rectangular tiles measuring 20 x 40 mm and 0.12 mm thick. This is a very stable material and is what gives to the samples the infrared emissivity needed.

As mentioned before, the reference configuration is made of three juxtaposed layers of Aluminium, Silver and Chrome were deposited in the substrate, and they have thicknesses of respectively 6 nm, 300 nm and 20 nm. This layout is represented in Figure A.4.

Figure A.4 - Configuration of the Layers in OSR Samples.
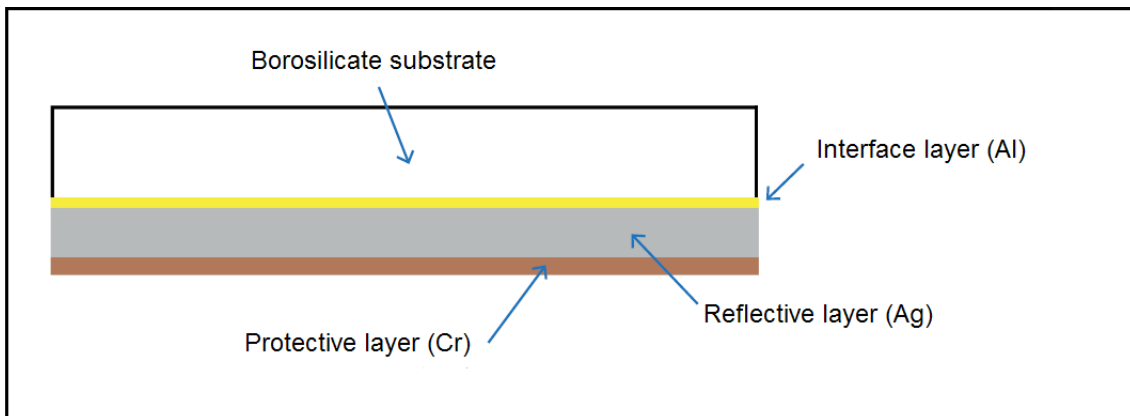
Source: Adapted from Boato et al. (2017).

The aluminized layer does not have optical purposes and serves primarily as a binding interface between glass and Silver. The silvered layer is the most optically active and the one responsible to provide the low absorptivity levels to

166

the samples. Finally, overlaid to the Silver is the Chrome layer that exists to protect mechanically and from oxidation the previous ones. When attached to the sample holders, is the chromed layer the one in contact to the binding glue.

As the dimensions suggest, two tiles are attached side by side to the top of each of the sample holders destined to OSR. Henceforth each pair of tiles installed in the same sample holder will be referred to as one single sample. The OSR tiles are attached to the holders top side by a controlled 0.5 mm RTV566 layer.

During manufacturing, all OSR tiles used in a sample were exposed to analogous conditions and thus are expected to be homogeneous.

Equipment general dimensions of the box and sample holders are shown in Figures A.5 and A.6 respectively.

As the equipment design evolved and tested through time, a simple timeline is presented at Figure A.7 in order to locate some relevant events chronologically.

Figure A.5 – General dimensions of the OSRA equipment box.
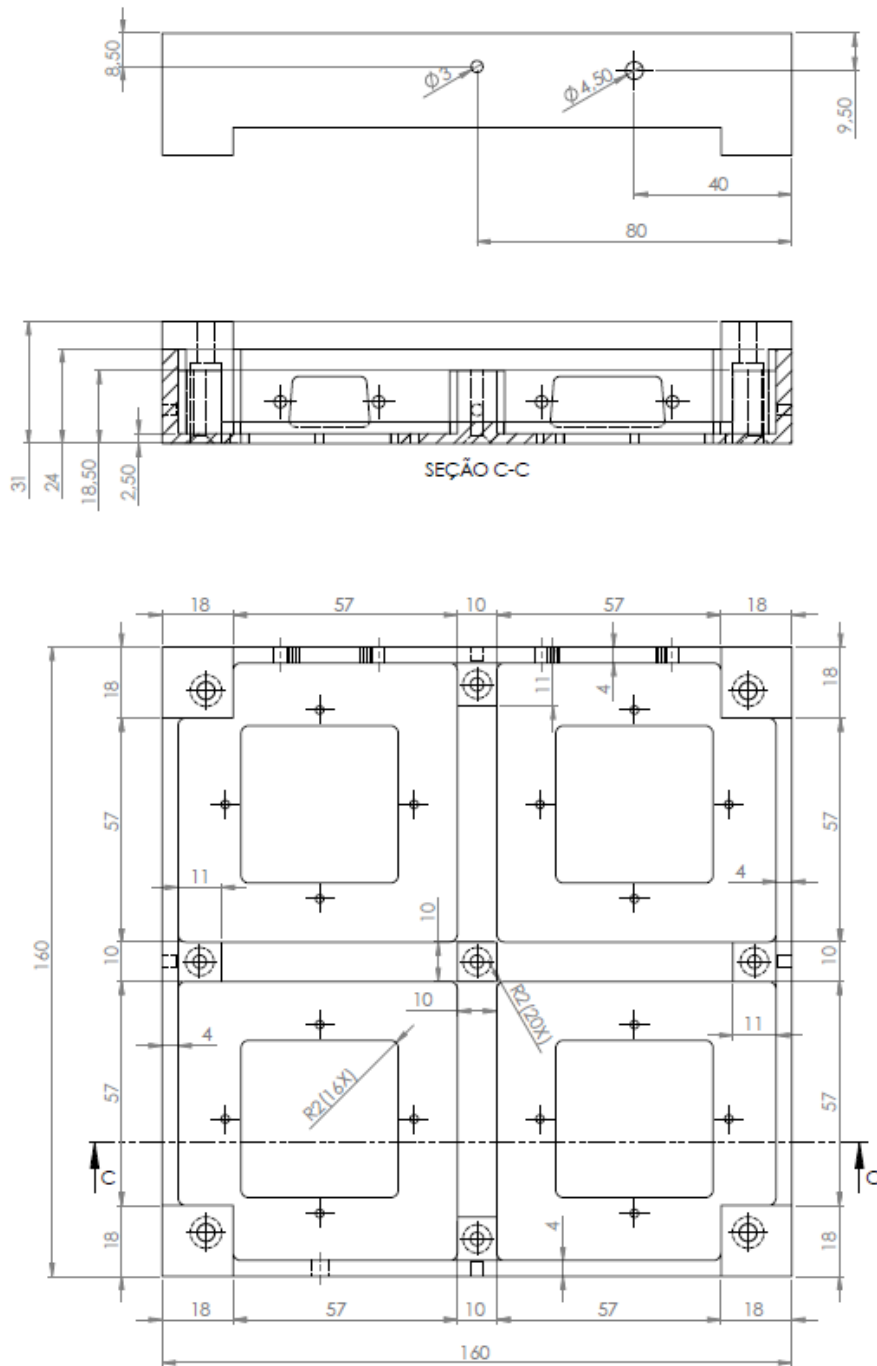
Source: Prepared by the author.

Figure A.6 – General dimensions of the OSRA sample supports.
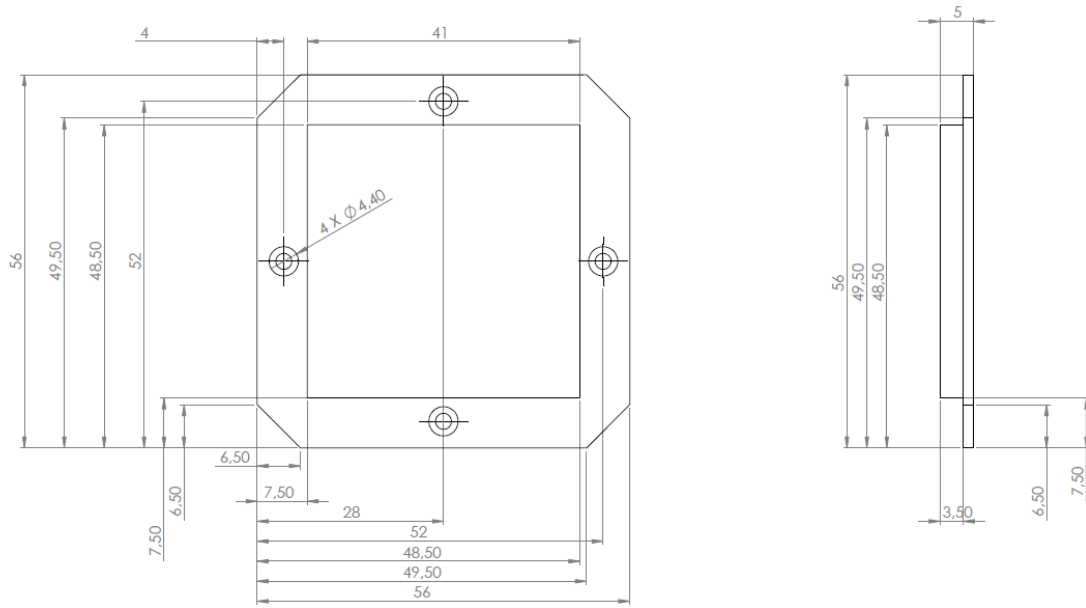
Source: Prepared by the author.

Figure A.7 – Selected equipment design and testing events.

Source: Prepared by the author.

APPENDIX B – OSR SAMPLES FABRICATION

As means of understanding, a brief explanation to the OSR sample fabrication processes follows. Both use PVD techniques that differ in principle: OSR 1 and 2 samples have been prepared via e-beam and ion sputtering, respectively.

The first sample, OSR1, was manufactured by having the cover glass substrate being positioned in a round aluminium baseplate at the top of a high vacuum chamber showed in the Figure B.1. The materials which the thin films are made from are placed inside water-cooled crucibles that are housed on the box-shaped structure at the bottom of the chamber. As shown in Figure B.2, a controlled electron beam is directed towards the crucibles to smelt the materials and produce negatively charged droplets that tend to propagate within the chamber spherically. The equipment used for e-beam deposition is shown on Figure B.4. E-beam samples for the flight equipment were produced by the author (Figure B.5).

Figure B.1 – Electron Beam Vacuum Chamber.

Source: Prepared by the author.

Figure B.2 – Electron Beam Crucible Housing.
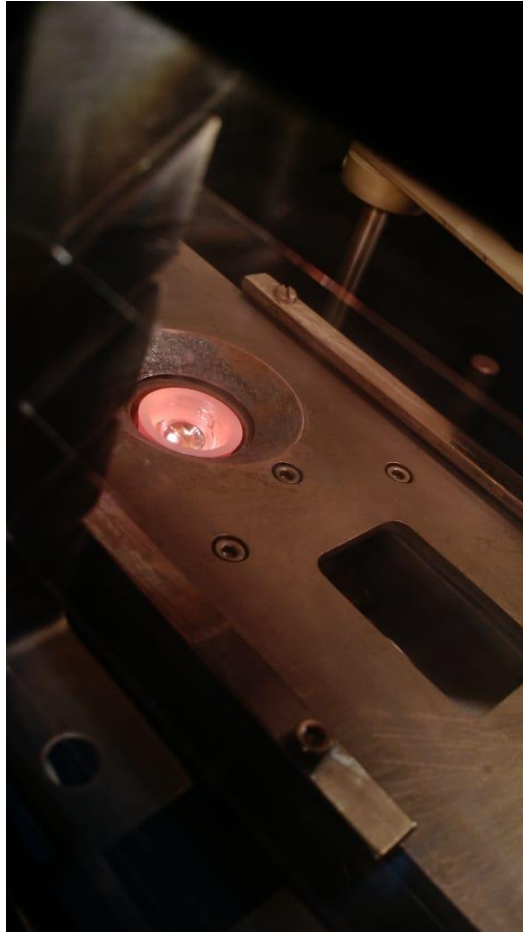
Source: Prepared by the author.

The second OSR sample was build using the sputtering process. In this process, the sample substrate is placed in a support opposite to a target made of the materials of interest. Within low vacuum chamber, ionized gas is directed towards the target that by its turn ejects positively charged particles that propagate spherically. This process tends to produce denser films and is usually faster. However, the layer thickness control is not as refined as via e-beam. Figure B.3 illustrates the sputtering PVD principle.

Figure B.3 – Sputtering PVD Principle.
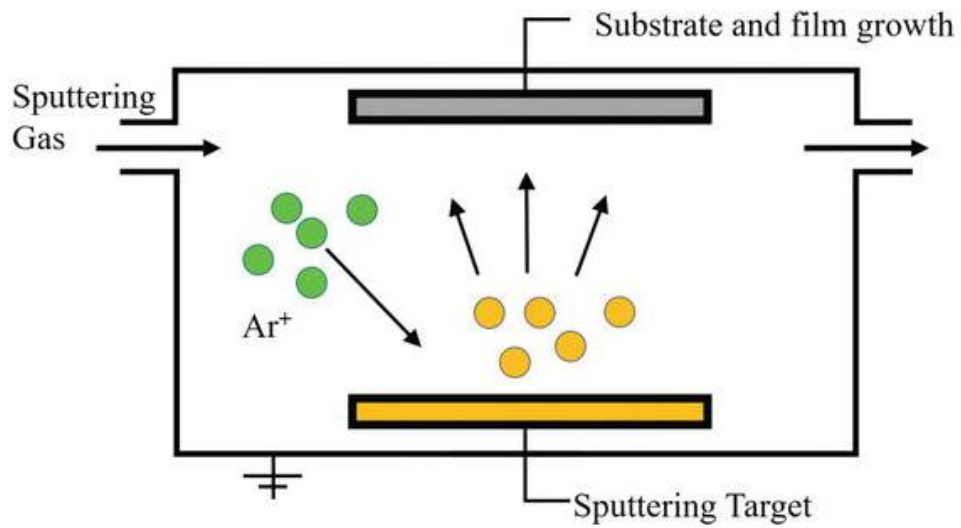
Figure B.4 – E-beam equipment used Edwards AUTO 306.

Figure B.5 – E-beam flight OSR Samples are ready.

Source: Prepared by the author.

APPENDIX C – FURTHER INFORMATION ON ACCEPTANCE AND QUALIFICATION TESTS

In order to verify the OSRA equipment unit survivability at the space environment, thermal shock and vibration tests were carried on to test levels based on the CBERS 04A satellite Environmental Specification.

Placed above a shaker as shown by Figure C.1, which excited mechanically the assembly in a typical launch vibration spectrum. Mechanical joints preservation and parts integrity were evaluated visually then. The thermal tests were carried out after this test.

Figure C.1 – Experiment in a Shaker Setup.

Source: Prepared by the author.

Another important test that has been carried out is the Thermal Cycling Test, which was performed only to the OSR samples within a double deck

temperature chamber. The samples were exposed than to 4 hour plateaus of extreme temperatures (+75 and -75 °C) for 25 cycles approximately. The temperature plateau change used is of high gradient and follows the typical profile shown at picture C.2. The samples were then optically and visually inspected after this test, that has the objective to verify that the coating layers do not delaminate under thermal induced stresses.

Figure C.2 – Thermal Cycling Test Typical temperature profiles.
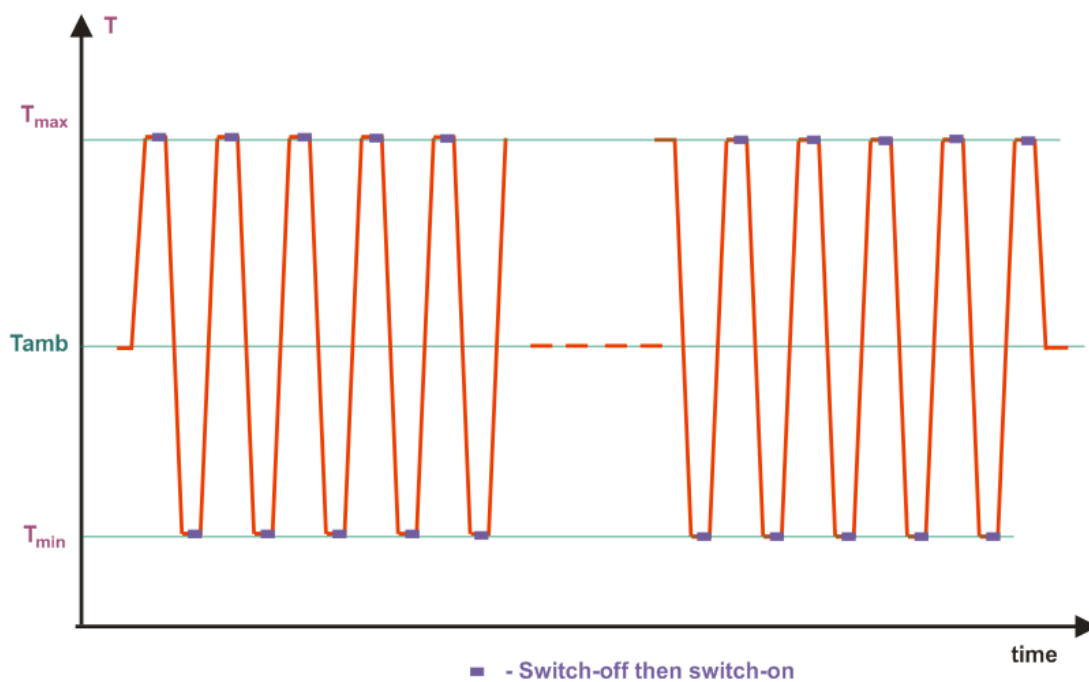
Source: Prepared by the author.

Having the experiment successfully passed the aforementioned steps, it was considered able to be thermally tested by means of TVT and TBT tests. Such experiments have been carried out to gather temperatures responses on different points of the equipment given a set of user defined boundary conditions. Figure C.3 shows the rig used for TVT and TBT procedures. Figure C.4 shows a heat power tuning procedure being carried out.

Figure C.3 – RIG used for TVT and TBT tests.
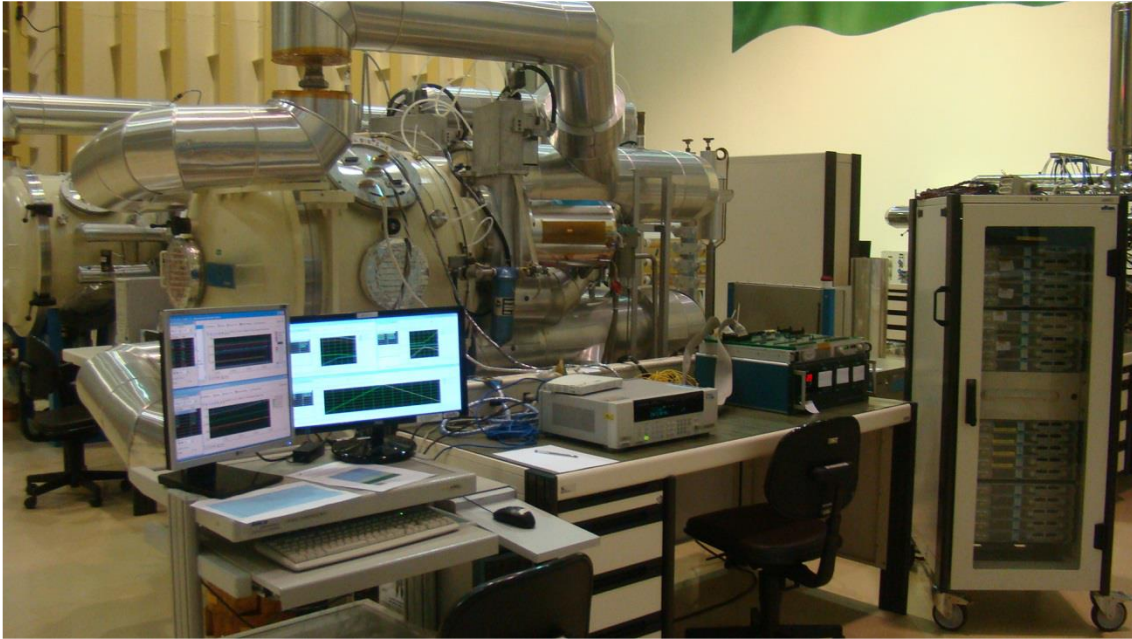
Source: Prepared by the author.

Figure C.4 – Test execution, OSRA heater power tuning.

Source: Prepared by the author.

APPENDIX D – SELECTED EXPERIMENTS WITH SLPM

Some of the performed tests consisted of:

a) Determination of G_L and C_m assuming that all samples had the same conductive couplings and thermal capacity. Only eclipse data was used. For each data point, systems of Equations were defined between the black sample and each of the remaining samples, i.e. 3 systems of Equations per data point. The results were evenly dispersed and resembled a white noise curve.

b) Computation of G_L and C_m again assuming that they were the same for all samples. But at this occasion, the systems of Equations formed were a combination among all samples, resulting in 6 systems of Equations per data point. Resulting calculated values were once again dispersed. G_L and C_m parameters were deemed potentially different for each sample as a result. Hall and Fote (1983) did the same assumption for their experiment.

c) C_m was kept equal for all samples but not G_L in a comparison of analogous data points of subsequent orbital cycles. Unfortunately, only special points with time derivatives equal to zero were usable. For example: temperature maxima. This made the results unfeasible for statistical analysis, since too few points were generated per cycle.

d) Matrix least squares applied to group of heat balance Equations. This method was considered promising, but good agreement between fitted function and data was not reached. It is believed that this method is best suited for balance Equations that are closer to the heat interactions it sample has with its surroundings. A more complex model would be required then.

e) An attempt similar to the one listed on item 'c', using notable points but now considering not only the original heat balance Equation, but also its

second order time derivative. Still, too few G_L and C_m calculated values per orbit cycle were obtained.

f) Similarly to item 'e', considering algebraic expressions obtained from comparison between samples balance Equation and their time derivatives. Fortunately, all data points in an eclipse could be employed. However the cited algebraic expressions were very complex, with many product terms between unknowns and derivatives. This has driven error propagation up and no conclusion could be drawn from the calculations.

APPENDIX E – COMPLEMENTARY TECHNIQUES FOR THE SLPM

Aside from modifying the nodal configuration, other refinements to be proposed to the SLPM solution steps can contribute to enhance its reliability.

Until the present date, unit ground qualification tests temperature data was not employed to deduce some thermo physical properties of the assembly before flight. Such practice was not adopted in order to avoid the decrease in the levels of the algorithm flexibility, because it assumes that the experiment assembly maintains the same thermal couplings at launch.

Indeed, expectations are that these couplings are conserved through launch since consolidated procedures were used on experiment construction. Conversely, there is a remote chance that those couplings had changed slightly while the experiment was exposed to structural loads produced by the launcher. In anyway, as other authors (SCHAEFER; BANNISTER, 1967, and HALL; FOTE, 1983) have used this practice in similar degradation experiments, its incorporation to the solution philosophy should be considered.

Another option to be considered is to revisit the tests where second order thermal balance Equations were employed. The principle is to try solving the systems of Equations using order reduction methods.

Furthermore, evolutionary algorithms (EA) may also be added to the algorithm in different stages. For example, the heat balance Equations and its variations could be employed in EA procedures as objective functions that have to comply with the available data in the best possible way. Alternatively, genetic algorithms (GA) could also serve as means of refining the bootstrap calculated thermo physical properties.

APPENDIX F – TBT DATA FITTINGS

The following Figures compile the temperature response of the experiment unit thermistors. TBT stages 3A and 4; 4A and 5; and 5A and 6 had been grouped and referred as phases 1, 2 and 3 of the TBT.

Prior to presentation on a graphical form, the data points acquired had been selected to depict the probed temperatures evolving from stable boundary conditions; i.e. data collected while the chamber shroud was in transient has been put aside. A data acquisition has been made once each 30 seconds.

Considering a typical exponential solution to the transient cooling problem, exponential curves had been adjusted to the experimental data and had shown good agreement to the temperature data points. As R^2 index suggest, the temperature model represented by Equation F.1 is capable of explaining over 99% of the variance observed.

$$T_i = T_o + A.\exp[R_o t] \tag{F.1}$$

As expected, temperature evolves slower for the box and this is probably to its higher thermal inertia.

Another aspect that can be observed from the data curves is that, even though the measured temperatures are within TBT criteria limits adopted in the industry [1] to be considered stable, a complete steady state has not been reached for any temperature at any stage. This is because that reaching a perfect steady state would require much more time than spent given the high time constants of the system. Unfortunately, such timespans are cost prohibitive.

Even though a complete thermal equilibrium was not reached, the temperatures the points of interest would reach if left to stabilize for an indefinite amount of time can be projected by the independent terms on the fitted temperature versus time Equations.

Figure F.1 – OSR1 sample TBT temperatures of phase 1.

$$T_{o1-3A+4}(t) = 278.244 - 24.418e^{-(2.28449E-4)t}$$
$$R^2 = 0.99889$$
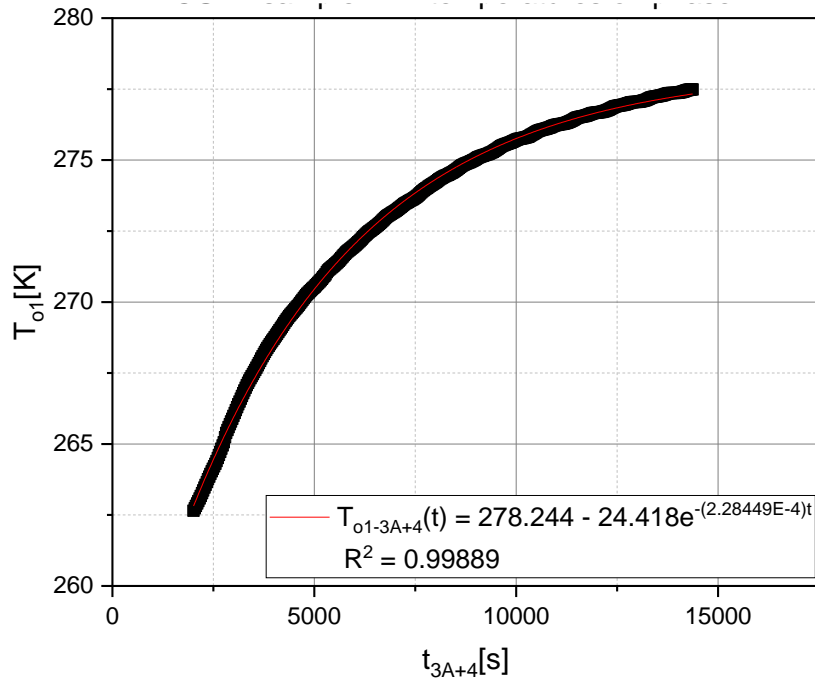
Source: Prepared by the author.

Figure F.2 – White sample TBT temperatures on phase 1.

$$T_{wt-3A+4}(t) = 276.070 - 25.370e^{-(2.50258E-4)t}$$
$$R^2 = 0.99895$$

Source: Prepared by the author.

181
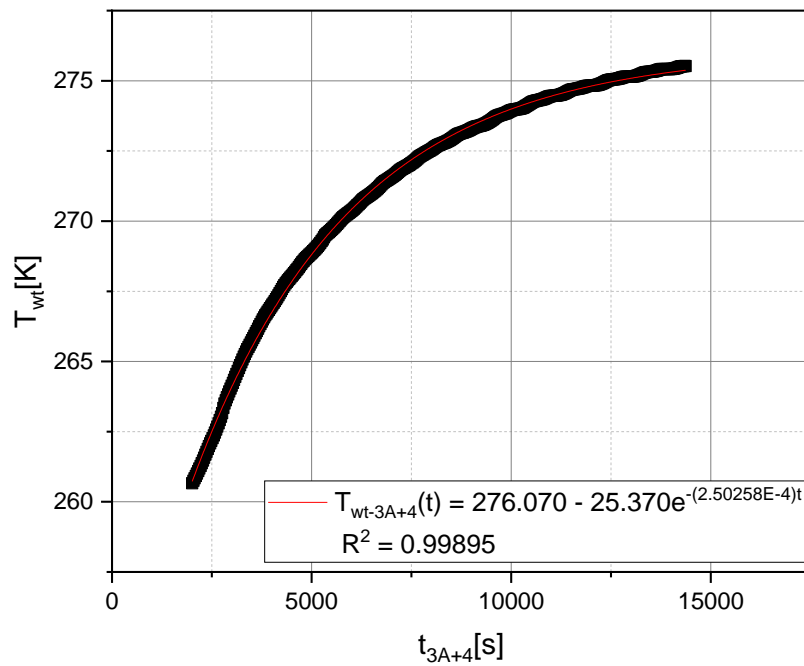
Figure F.3 – OSR2 sample TBT temperatures on phase 1.

$$T_{o2-3A+4}(t) = 276.855 - 25.016e^{-(2.35903E-4)t}$$
$$R^2 = 0.99897$$
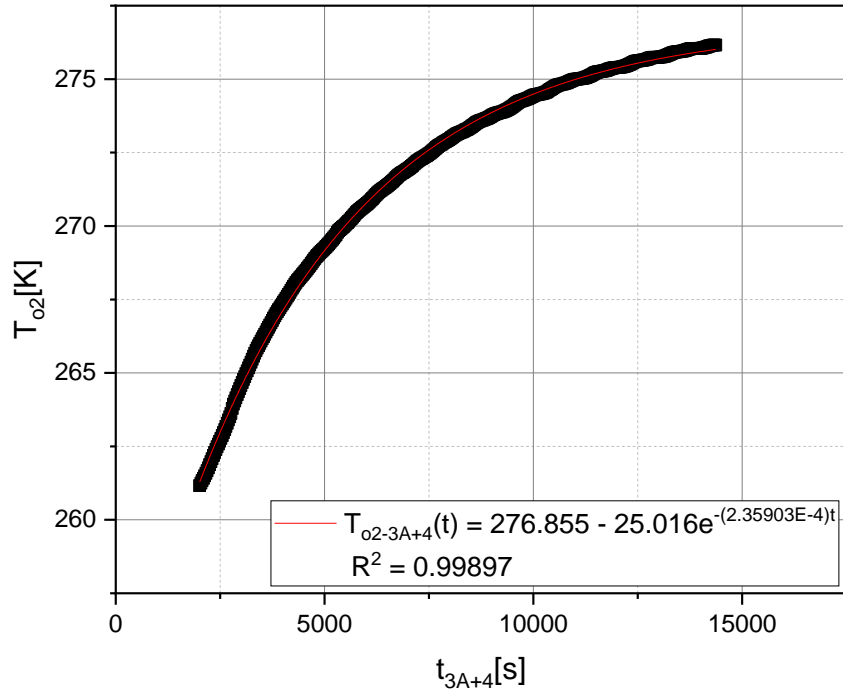
Source: Prepared by the author.

Figure F.4 – Black sample TBT temperatures on phase 1.

$$T_{bk-3A+4}(t) = 279.049 - 22.262e^{-(2.21543E-4)t}$$
$$R^2 = 0.99836$$
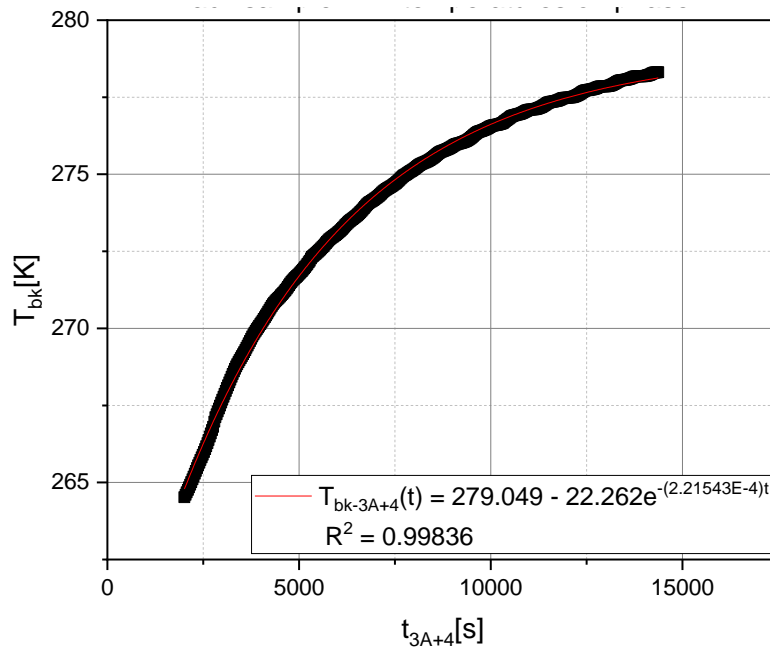
Source: Prepared by the author.

Figure F.5 – Box reference TBT temperatures on phase 1.

$$T_{box\text{-}3A+4}(t) = 270.730 - 30.300e^{-(2.04947E\text{-}4)t}$$
$$R^2 = 0.99951$$
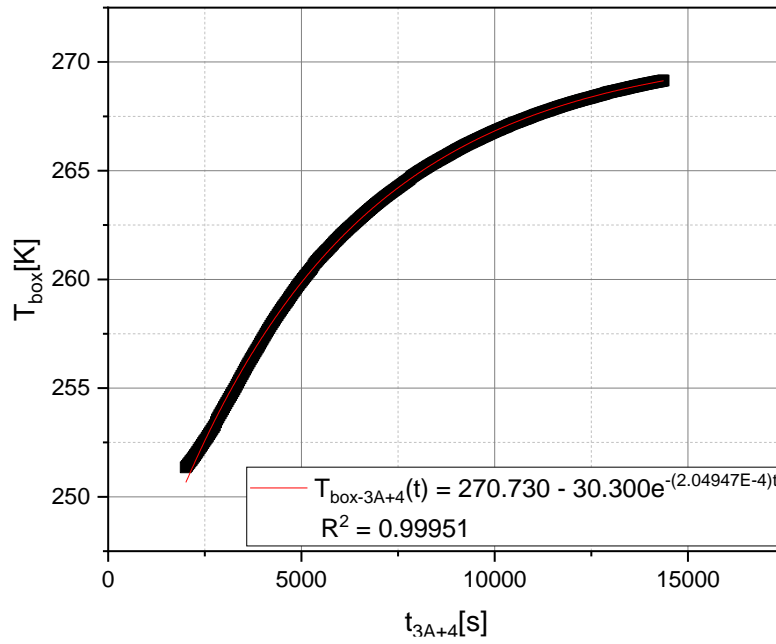
Source: Prepared by the author.

Figure F.6 – OSR1 sample TBT temperatures of phase 2.

$$T_{o1\text{-}4A+5}(t) = 289.317 - 11.660e^{-(2.36994E\text{-}4)t}$$
$$R^2 = 0.99749$$
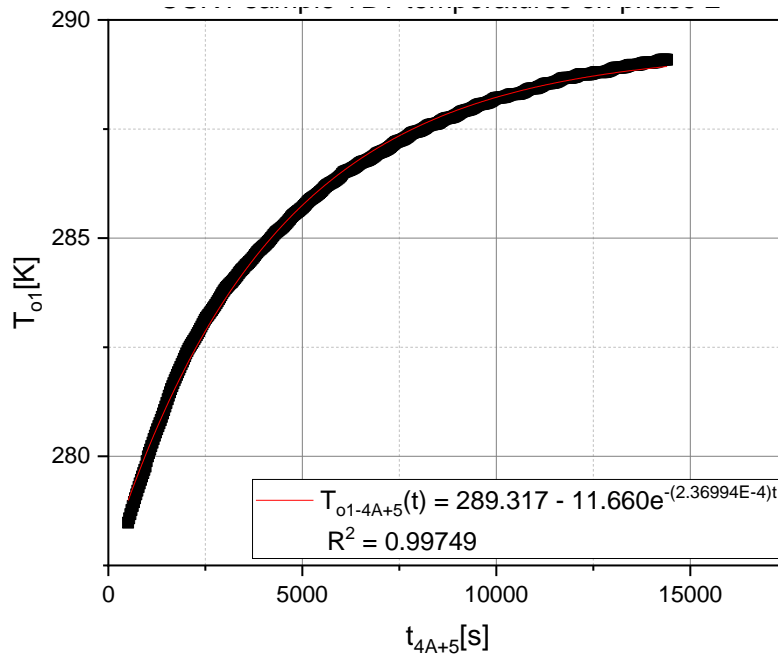
Source: Prepared by the author.

Figure F.7 – White sample TBT temperatures on phase 2.

$$T_{wt\text{-}4A+5}(t) = 287.146 - 11.566e^{-(2.683718E\text{-}4)t}$$
$$R^2 = 0.99749$$
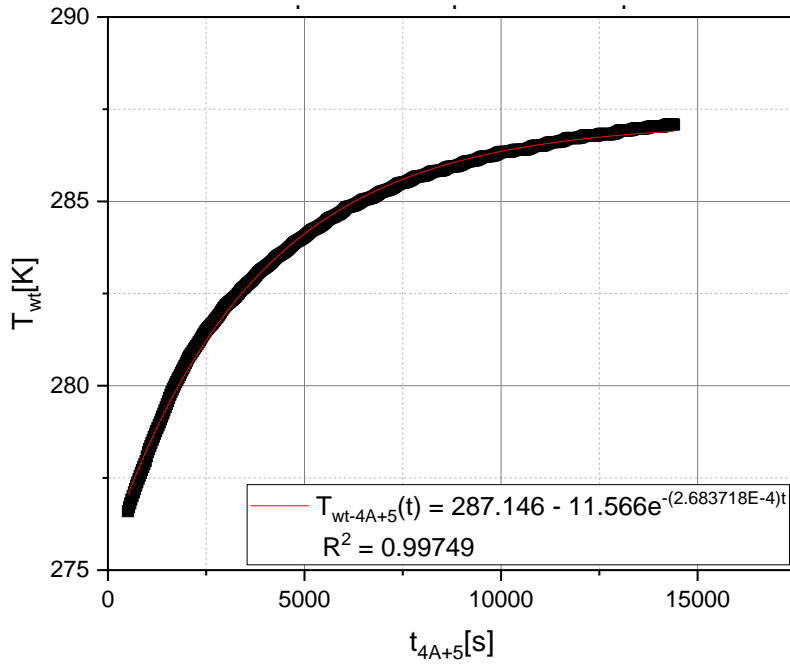
Source: Prepared by the author.

Figure F.8 – OSR2 sample TBT temperatures on phase 2.

$$T_{o2\text{-}4A+5}(t) = 287.987 - 11.666e^{-(2.49947E\text{-}4)t}$$
$$R^2 = 0.99761$$
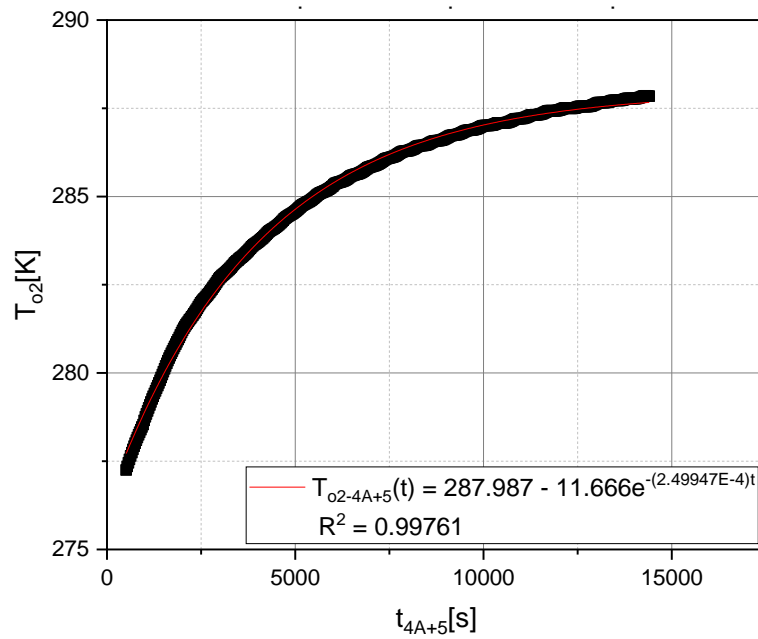
Source: Prepared by the author.

Figure F.9 – Black sample TBT temperatures on phase 2.

$$T_{bk-4A+5}(t) = 289.665 - 10.772e^{-(2.230013E-4)t}$$
$$R^2 = 0.99639$$
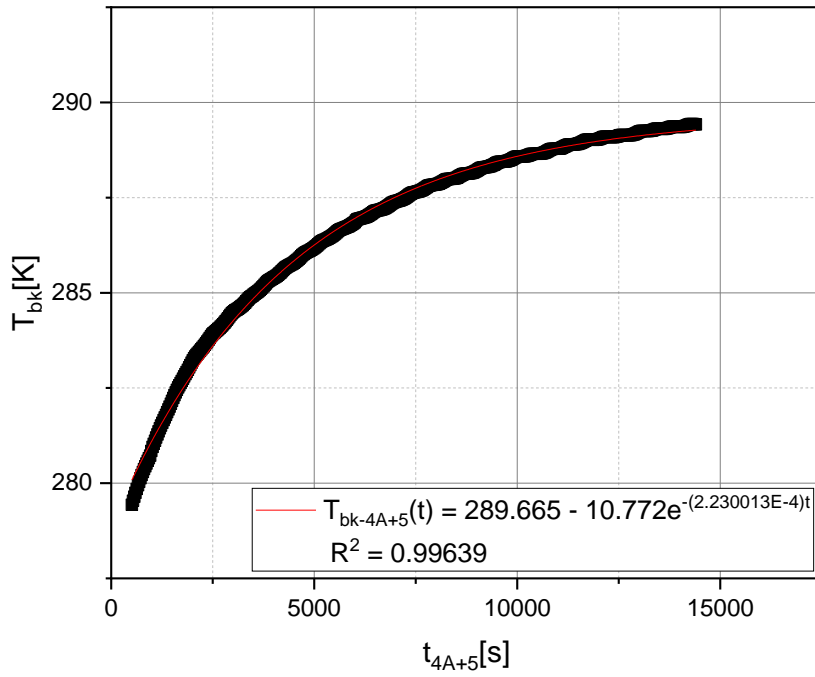
Source: Prepared by the author.

Figure F.10 - Box reference TBT temperatures on phase 2.

$$T_{box-3A+4}(t) = 282.140 - 14.816e^{-(2.13842E-4)t}$$
$$R^2 = 0.99982$$

Source: Prepared by the author.

185
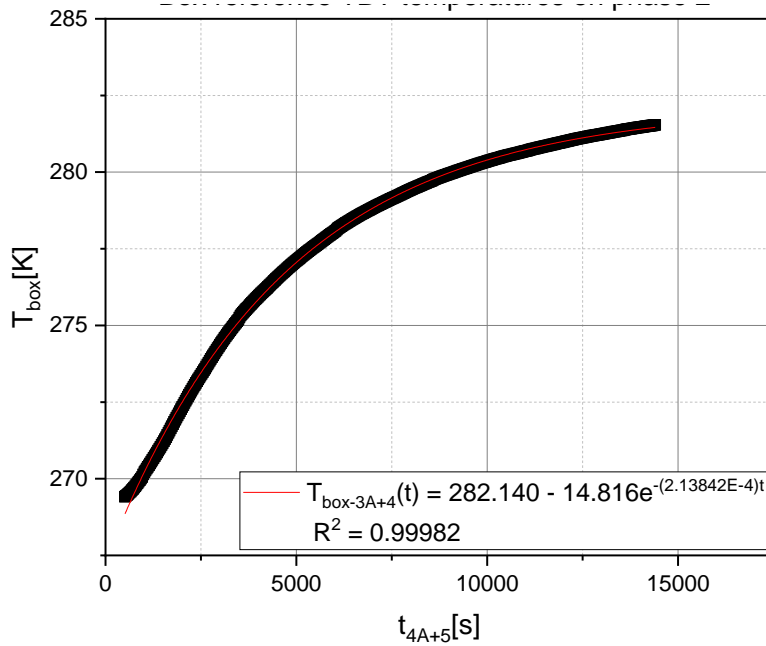
Figure F.11 – OSR1 sample TBT temperatures of phase 3.

$$T_{o1-5A+6}(t) = 306.709 - 40.192e^{-(2.66982E-4)t}$$
$$R^2 = 0.99791$$
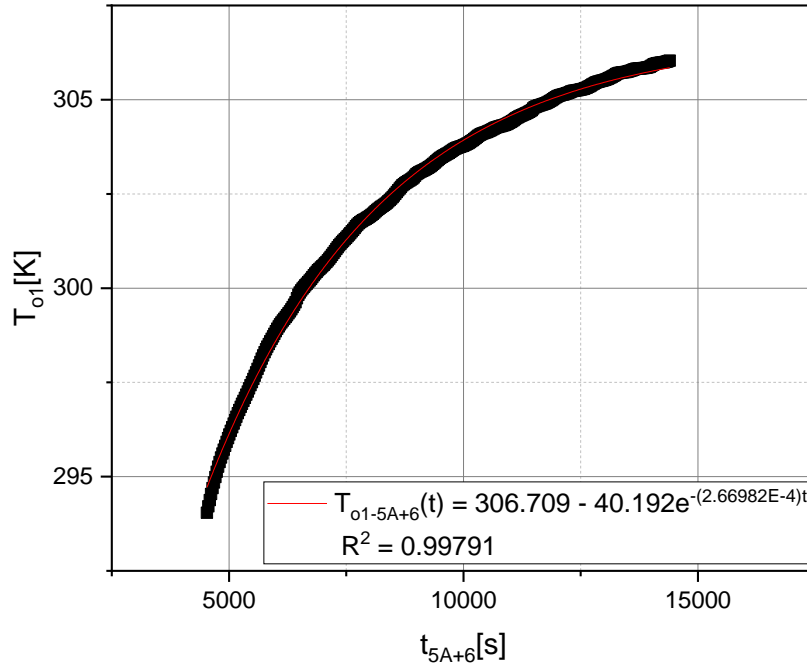
Source: Prepared by the author.

Figure F.12 – White sample TBT temperatures on phase 3.

$$T_{wt-5A+6}(t) = 304.670 - 49.203e^{-(3.18791E-4)t}$$
$$R^2 = 0.99802$$

Source: Prepared by the author.

186
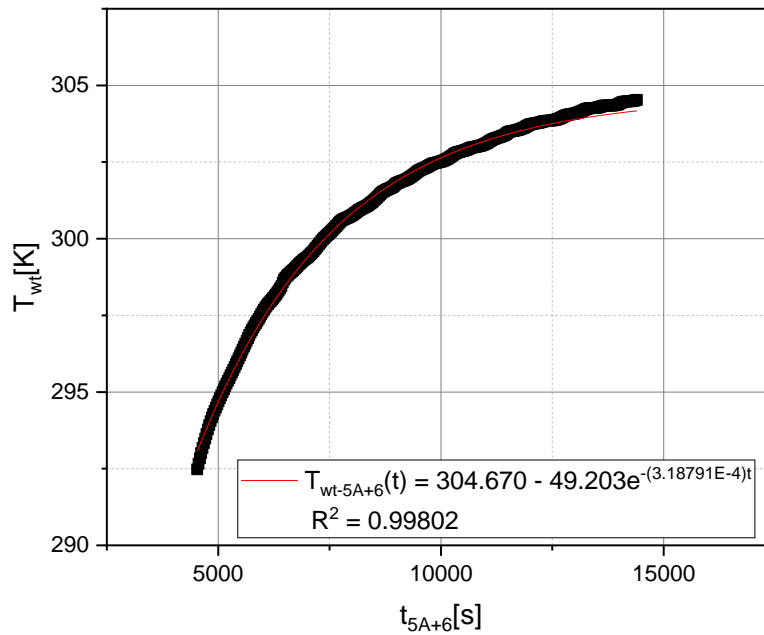
Figure F.13 – OSR2 sample TBT temperatures on phase 3.

$T_{o2-5A+6}(t) = 305.713 - 43.322e^{-(2.83455E-4)t}$

$R^2 = 0.99774$
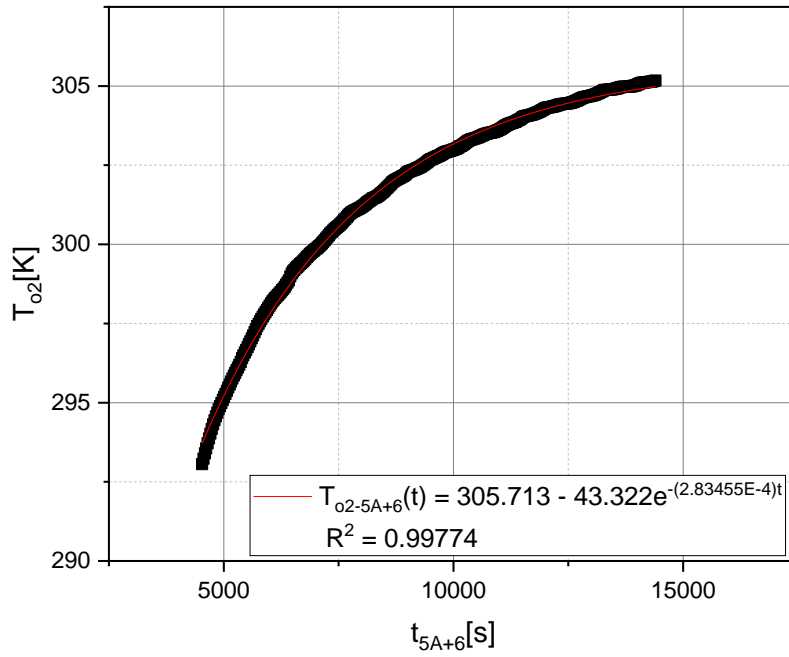
Source: Prepared by the author.

Figure F.14 – Black sample TBT temperatures on phase 3.

$T_{bk-4A+5}(t) = 306.256 - 37.720e^{-(2.72022E-4)t}$

$R^2 = 0.99683$

Source: Prepared by the author.

187
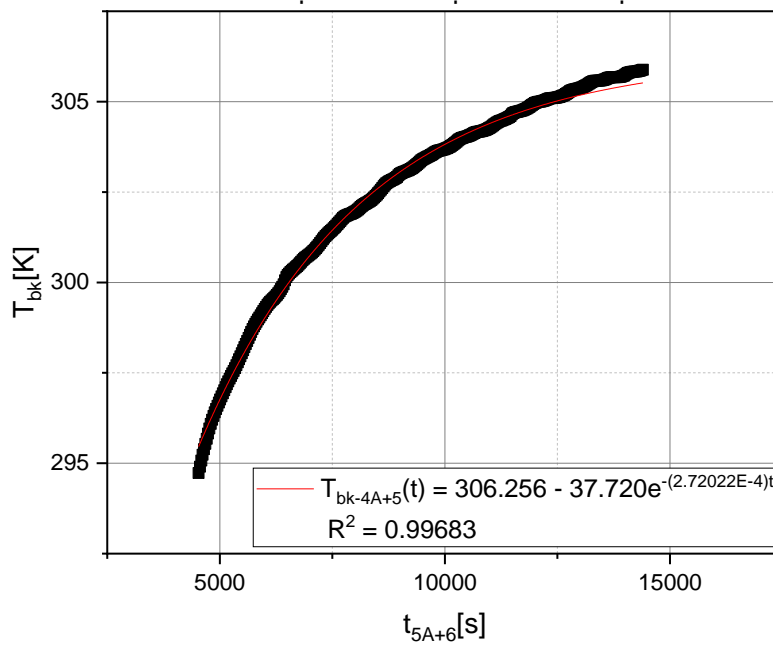
Figure F.15 - Box reference TBT temperatures on phase 3.

$$T_{box-3A+4}(t) = 300.378 - 49.616e^{-(2.44477E-4)t}$$
$$R^2 = 0.99975$$
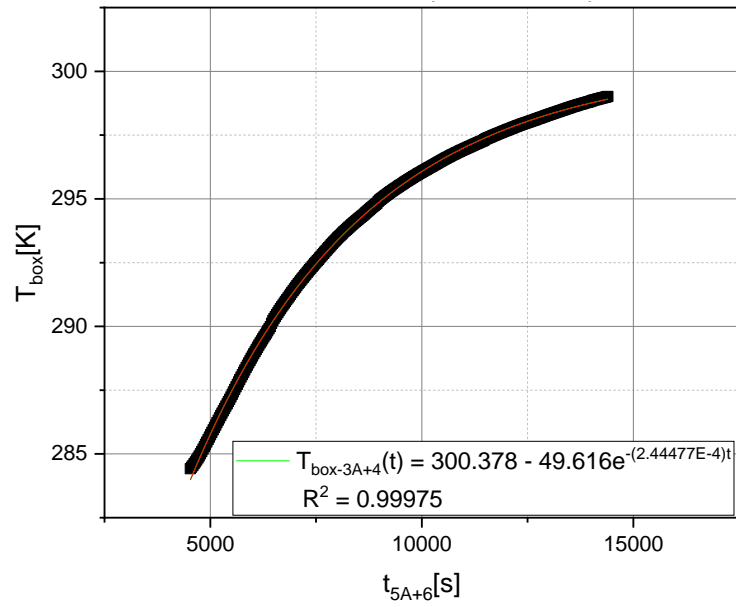
Source: Prepared by the author.

APPENDIX G – TBT TEMPERATURE CORRECTIONS

Prior to use in, all thermistor data gathered in the TBT has been corrected by Equations G.1 to G.4, which correlate the thermistor read temperature to the thermocouple read temperatures. The same corrections had been applied to the telemetry data acquired from flight to obtain the temperatures that could have been read by the same thermocouples used in the TBT if they were kept on the experiment unit. Temperatures to be used in the Equations below need to be in Kelvin.

$$T_{o1\_corr} = \{1 - [-0.04141 + (10E-4)*2.33650*T_{o1} - (10E-7)*3.03321*T_{o1}{}^2]\}*T_{o1} \qquad \text{(G.1)}$$

$$T_{br\_corr} = \{1 - [-0.04845 + (10E-4)*2.82525*T_{br} - (10E-7)*3.75170*T_{br}{}^2]\}*T_{br} \qquad \text{(G.2)}$$

$$T_{o2\_corr} = \{1 - [-0.06685 + (10E-4)*3.82257*T_{o2} - (10E-7)*6.30296*T_{o2}{}^2]\}*T_{o2} \qquad \text{(G.3)}$$

$$T_{pr\_corr} = \{1 - [-0.05564 + (10E-4)*3.41335*T_{pr} - (10E-7)*5.01459*T_{pr}{}^2]\}*T_{pr} \qquad \text{(G.4)}$$

The experiment assembly chassis temperature, or box temperature, was deemed dismissed from correction because its thermistor reads very close temperatures to the equivalent TBT installed thermocouple. The box higher inertia is also likely to contribute to such proximity.

For easier comparison, the original TBT data was also reproduced in this appendix section on Figures G.4 to G.6 and correspond to Figures 10.1 to 10.3.

Figure G.1 – Corrected Experiment Therm. TBT Temperatures for 3A and 4.
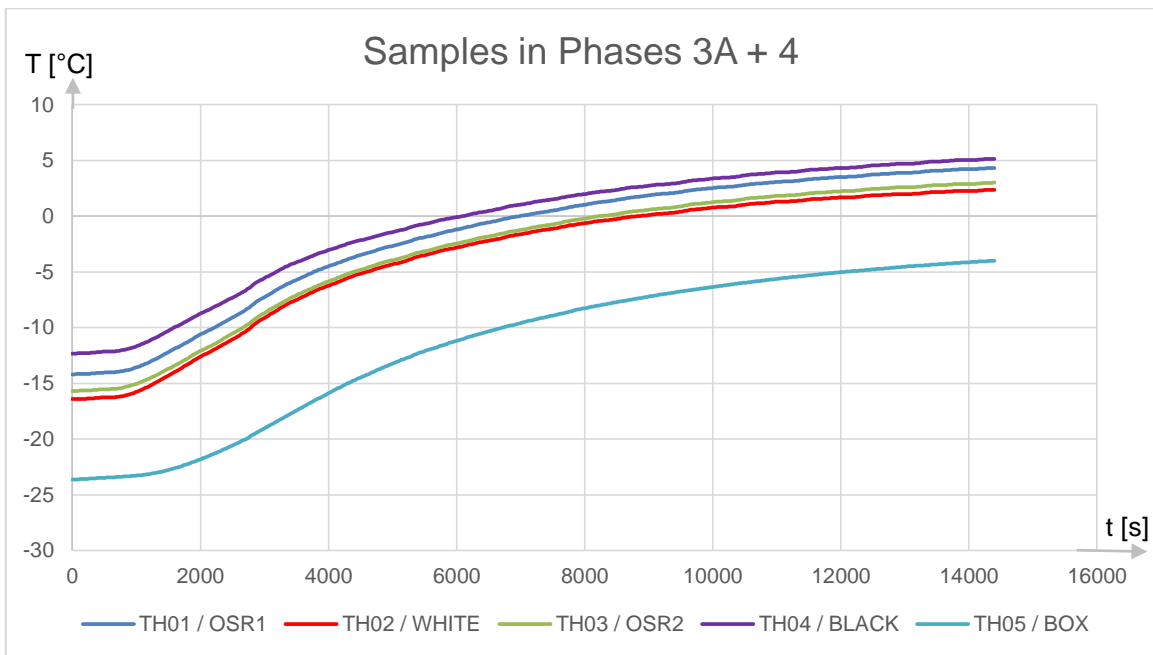
Figure G.2 – Corrected Experiment Therm. TBT Temperatures for 4A and 5.
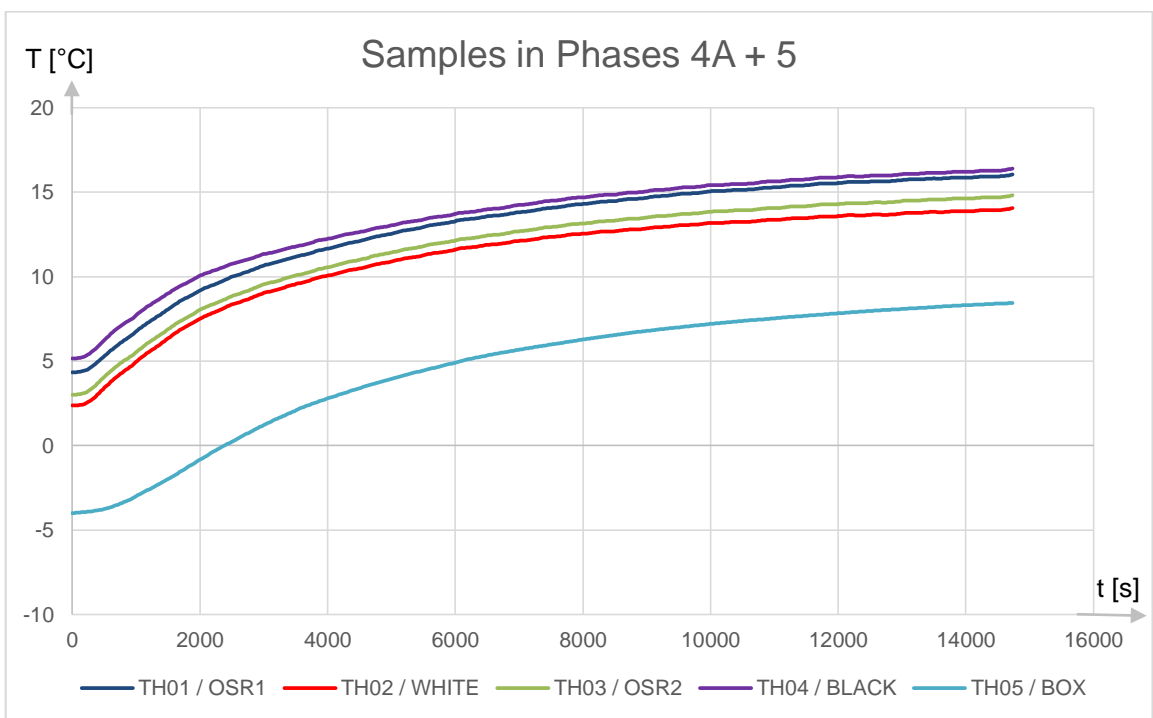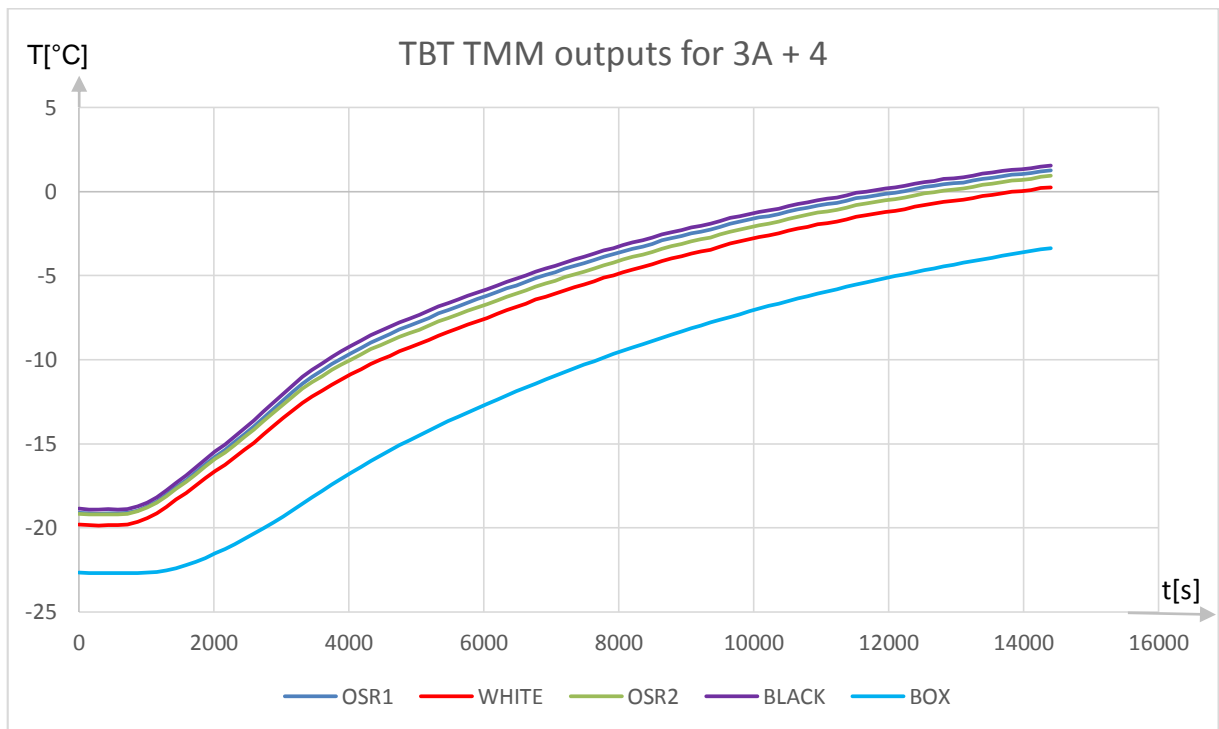
Figure G.3 – Corrected Experiment Therm. TBT Temperatures for 5A and 6.
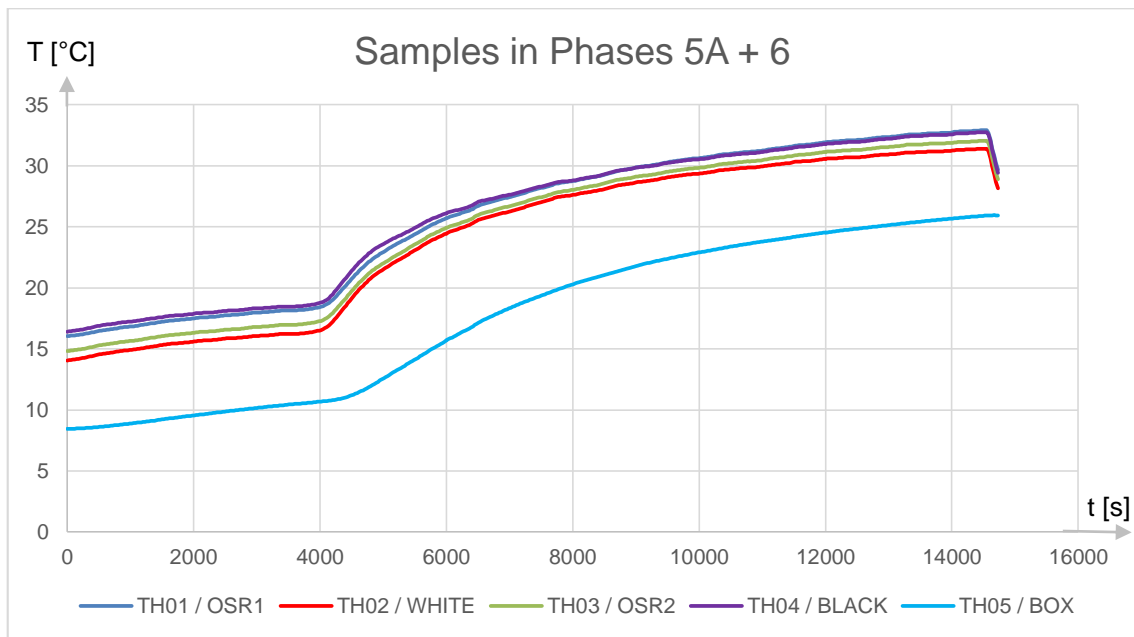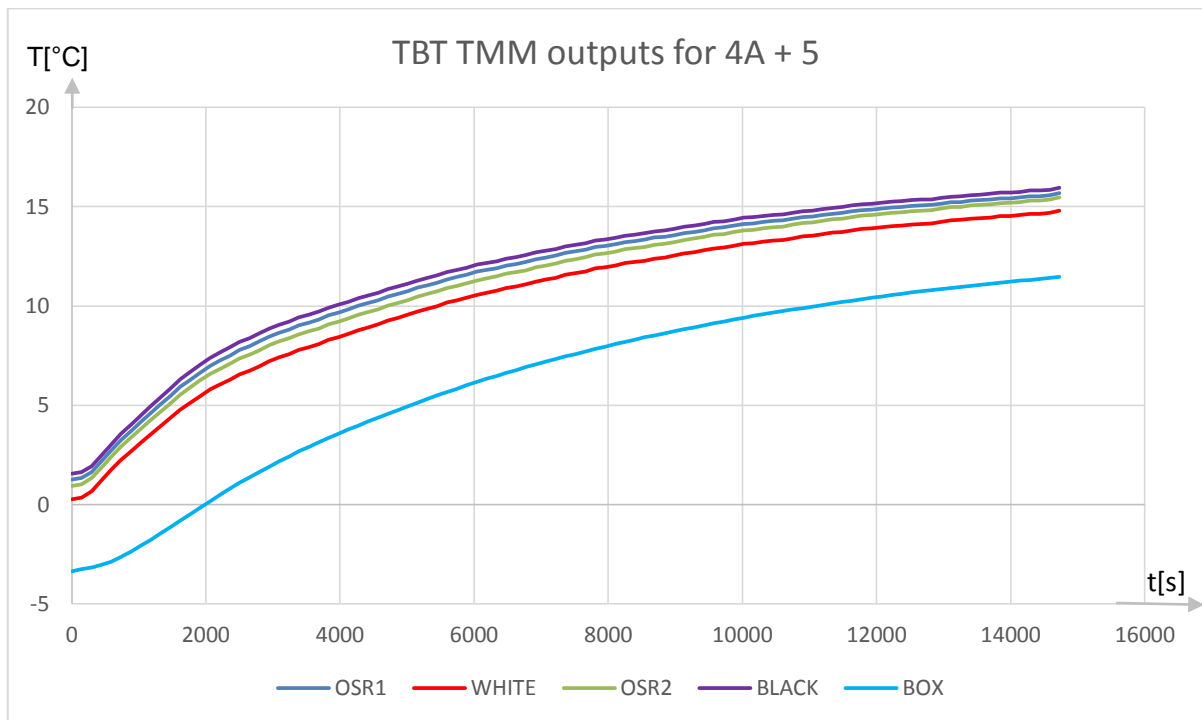

Source: Prepared by the author.

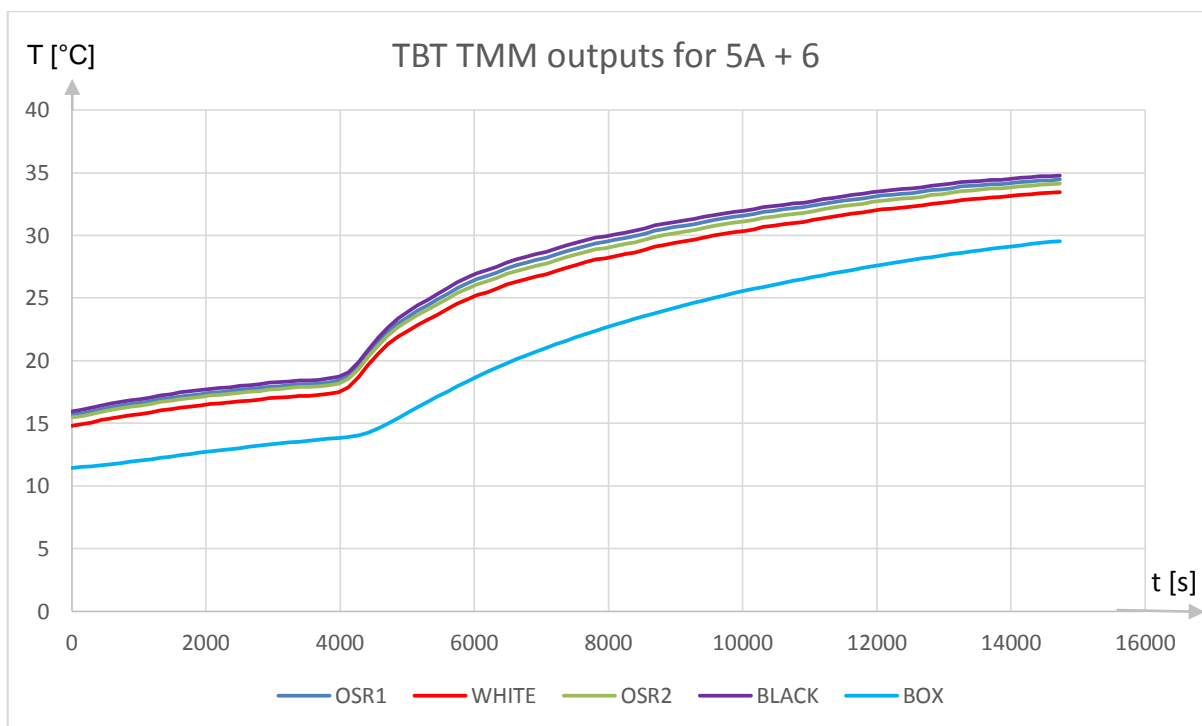Figure G.4 – Temperature curves for the TBT simulation phases 3A+4.

Source: Prepared by the author.

Figure G.5 – Temperature curves for the TBT simulation phases 5A+6.

Source: Prepared by the author.

Figure G.6 – Temperature curves for the TBT simulation phases 5A+6.

Source: Prepared by the author.

APPENDIX H – IN-FLIGHT TELEMETRY DATA SAMPLES

On the following pages is the temperature telemetry data available for the evaluation of the coatings on the present date. Unfortunately, not all points of interest of the mission lifecycle up to date have good quality data.

Data still could be used though with some reservations.

Data reported on the Figure H.3, from February 2020, seems to have temperature data not synchronized with the standard data collection timestep.

Data from Figure H.7, from December 2020, seems to have been collected in a reduced resolution: comparing it to the H.6 general temperatures seem to be lower and this is likely inaccurate due to the enhanced solar heat load. Probably this reduced resolution made the data inaccurate.

Data from Figure H.8, from April 2021, seems OK but still only a very short time span was available.

Figure H.1 – In-flight telemetry sample from 11/01/2020.
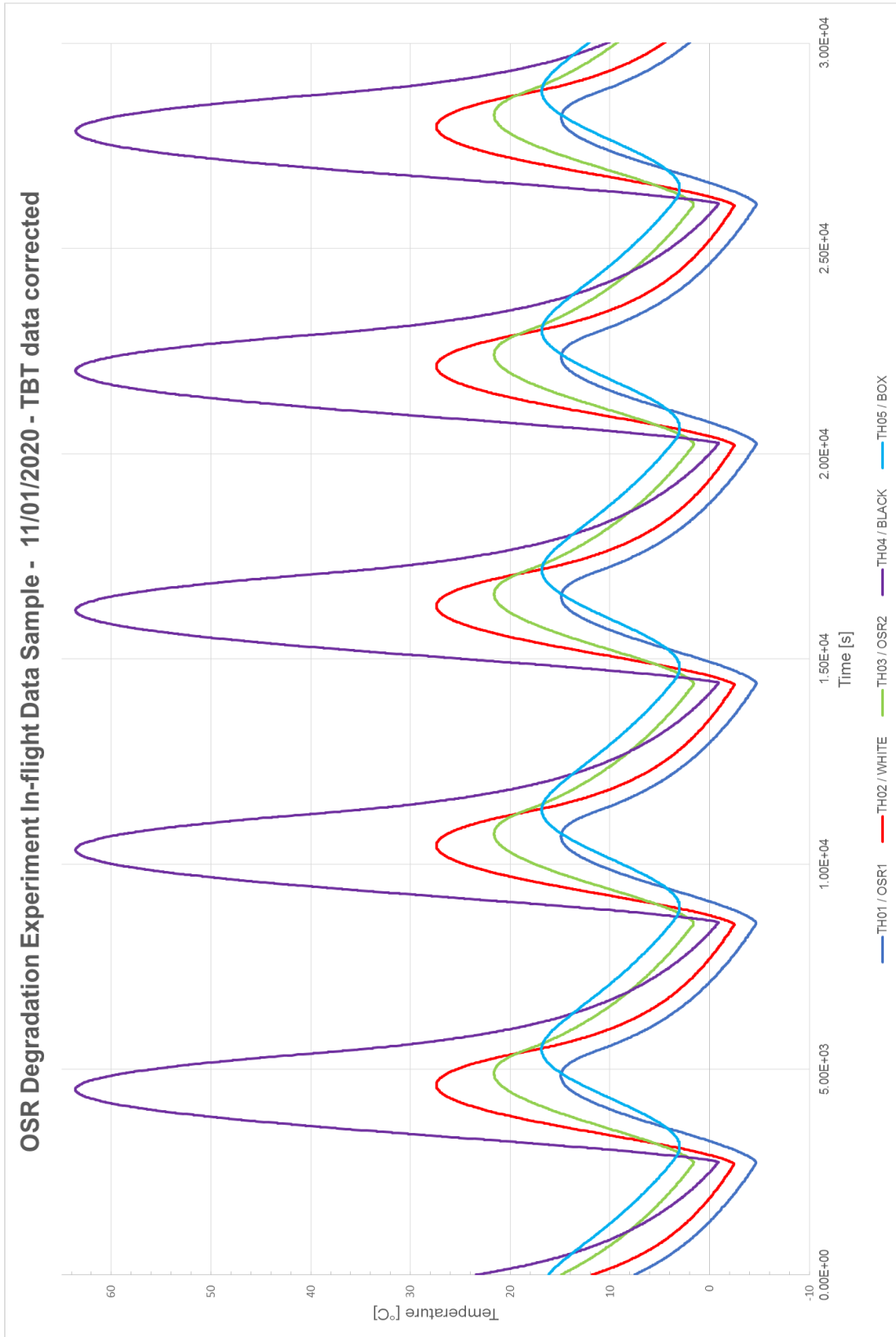
Source: Prepared by the author.

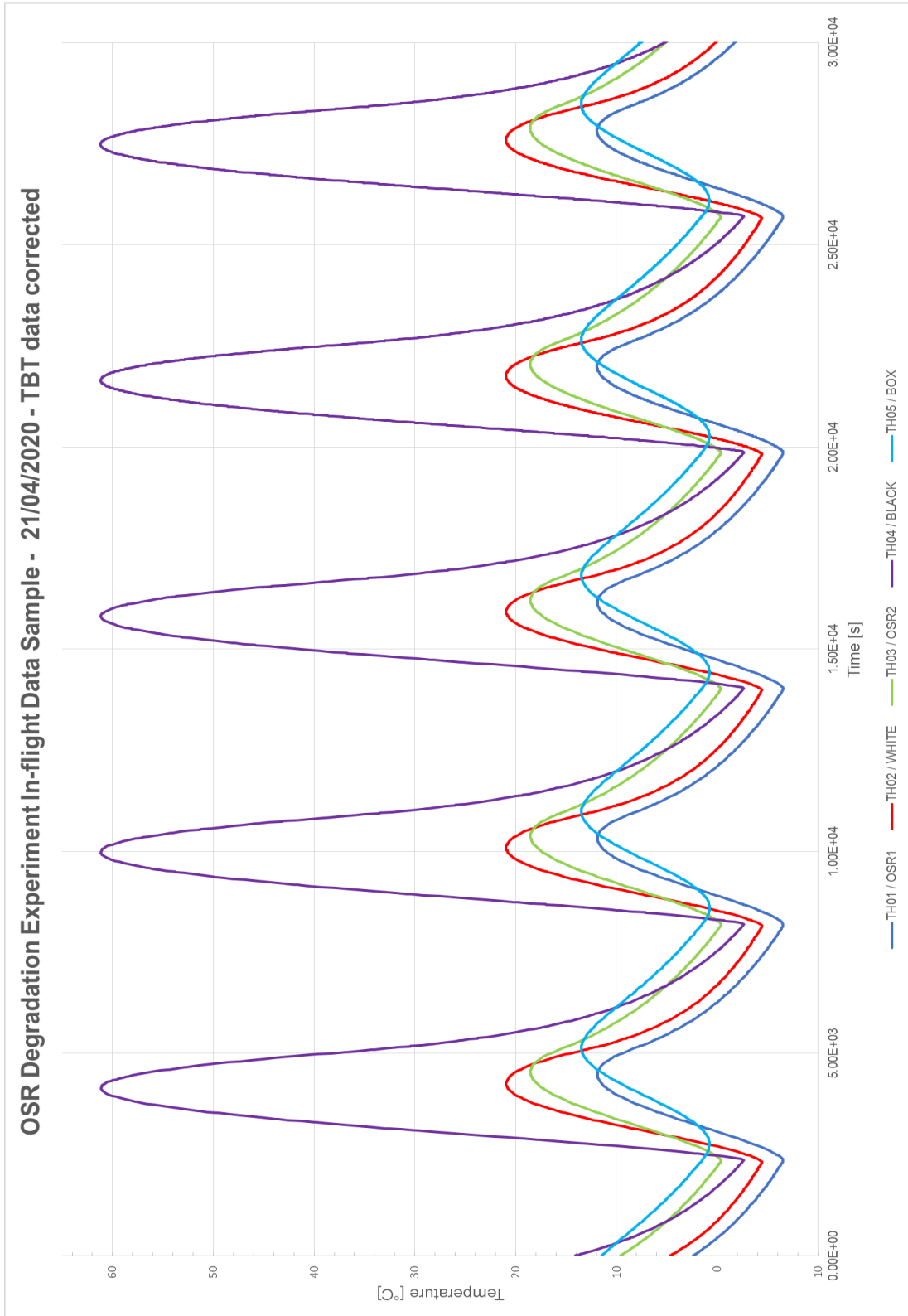Figure H.2 – In-flight telemetry sample from 23/01/2020.
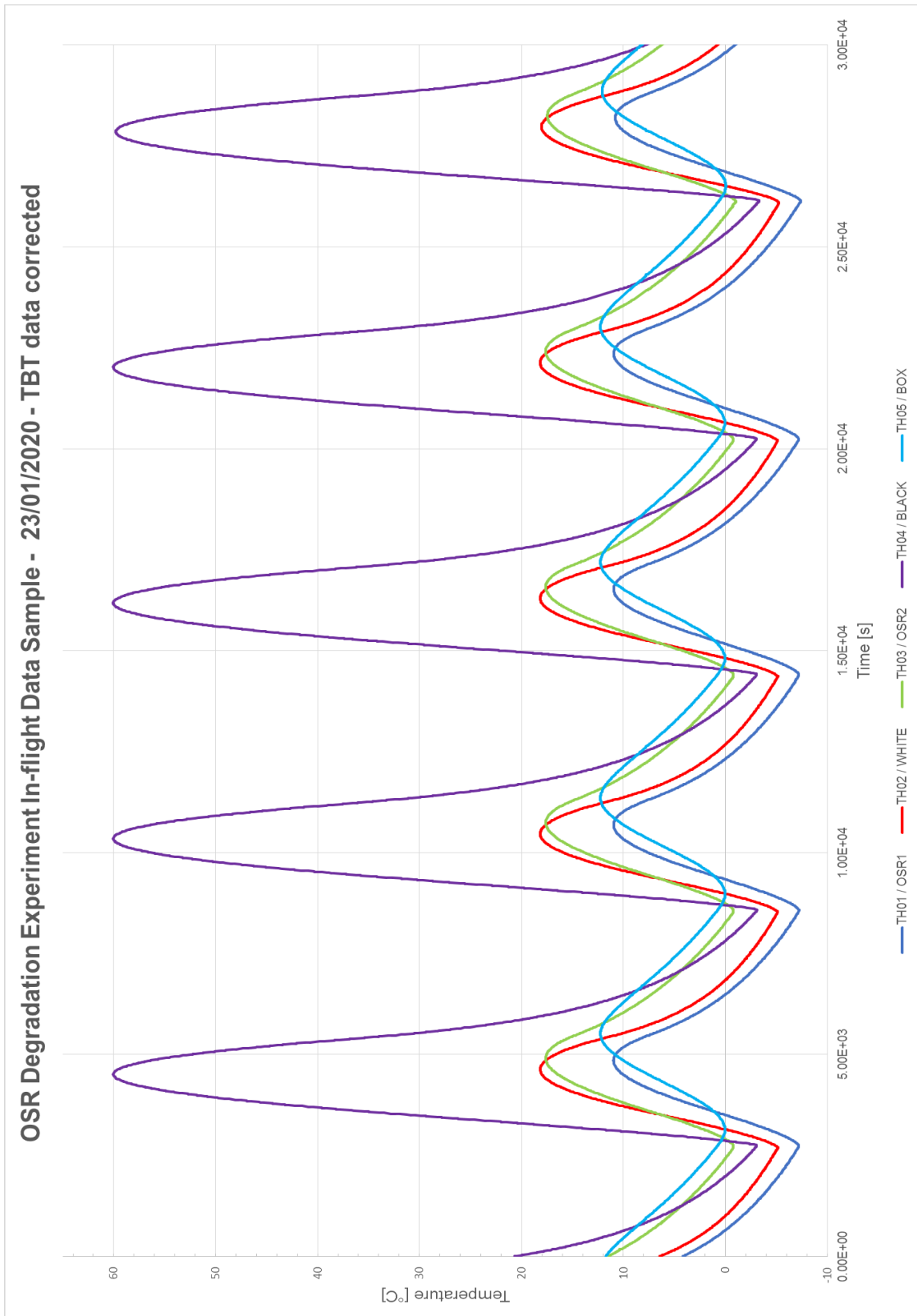
Source: Prepared by the author.

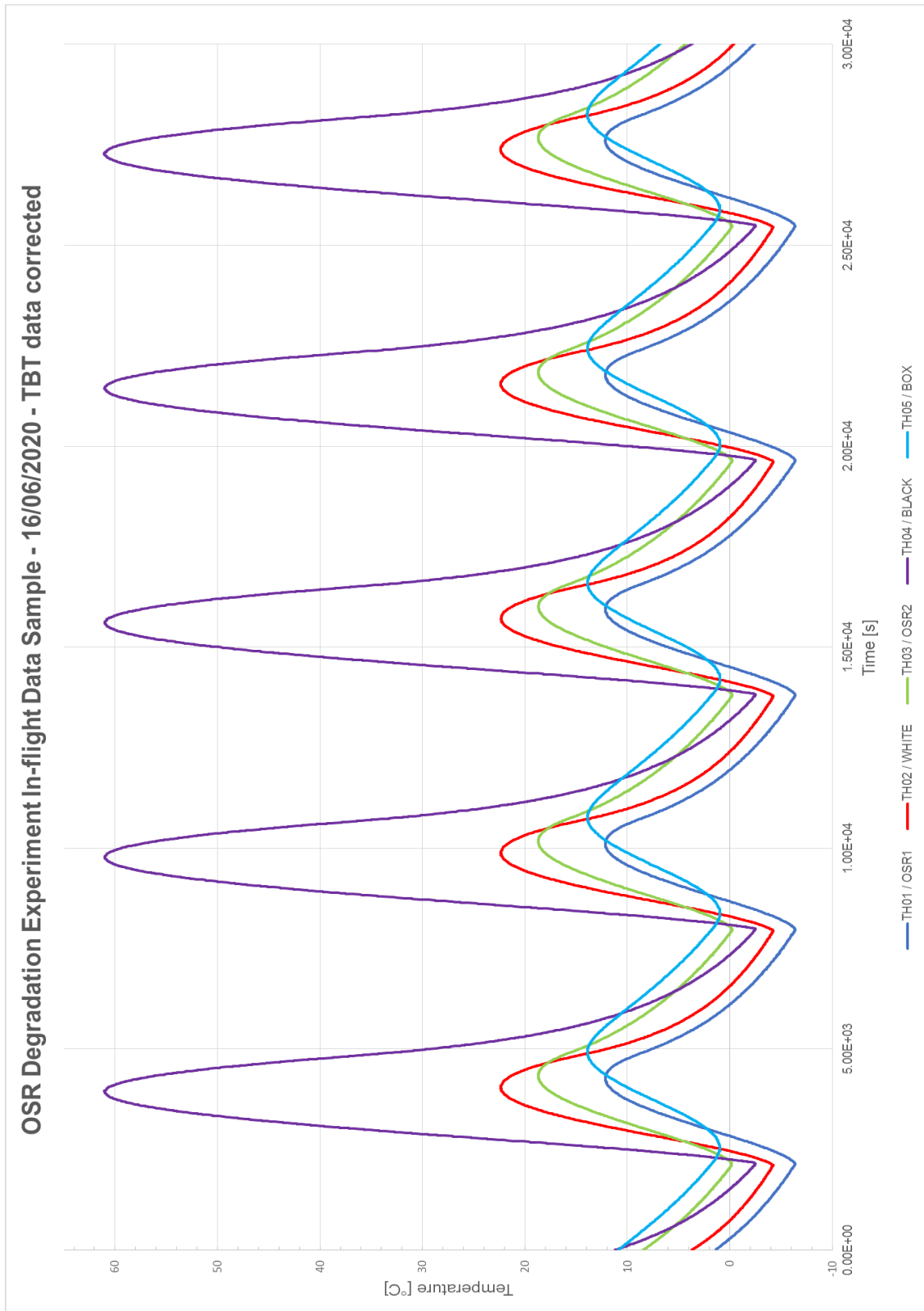Figure H.3 – In-flight telemetry sample from 01/02/2020.
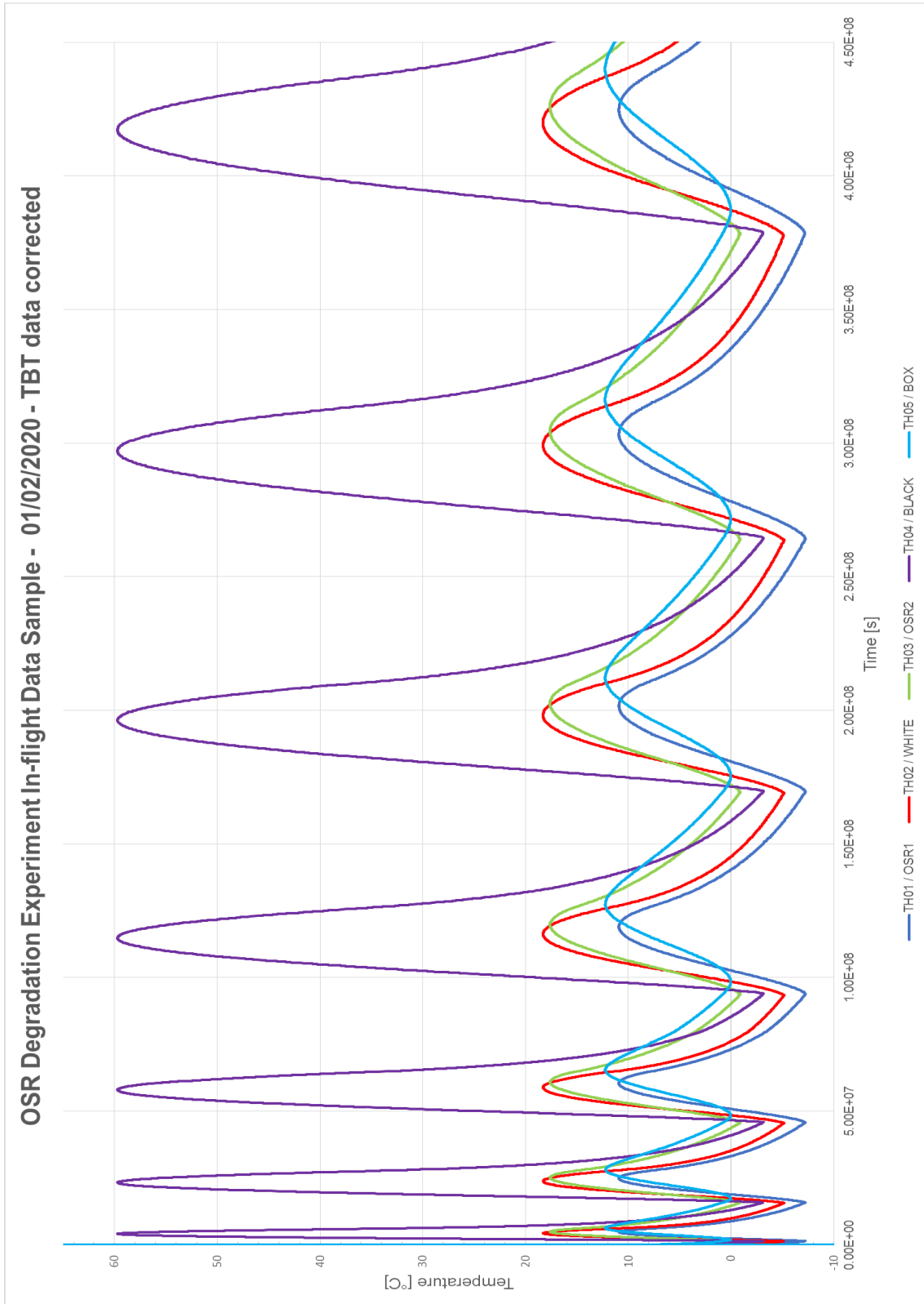
Source: Prepared by the author.

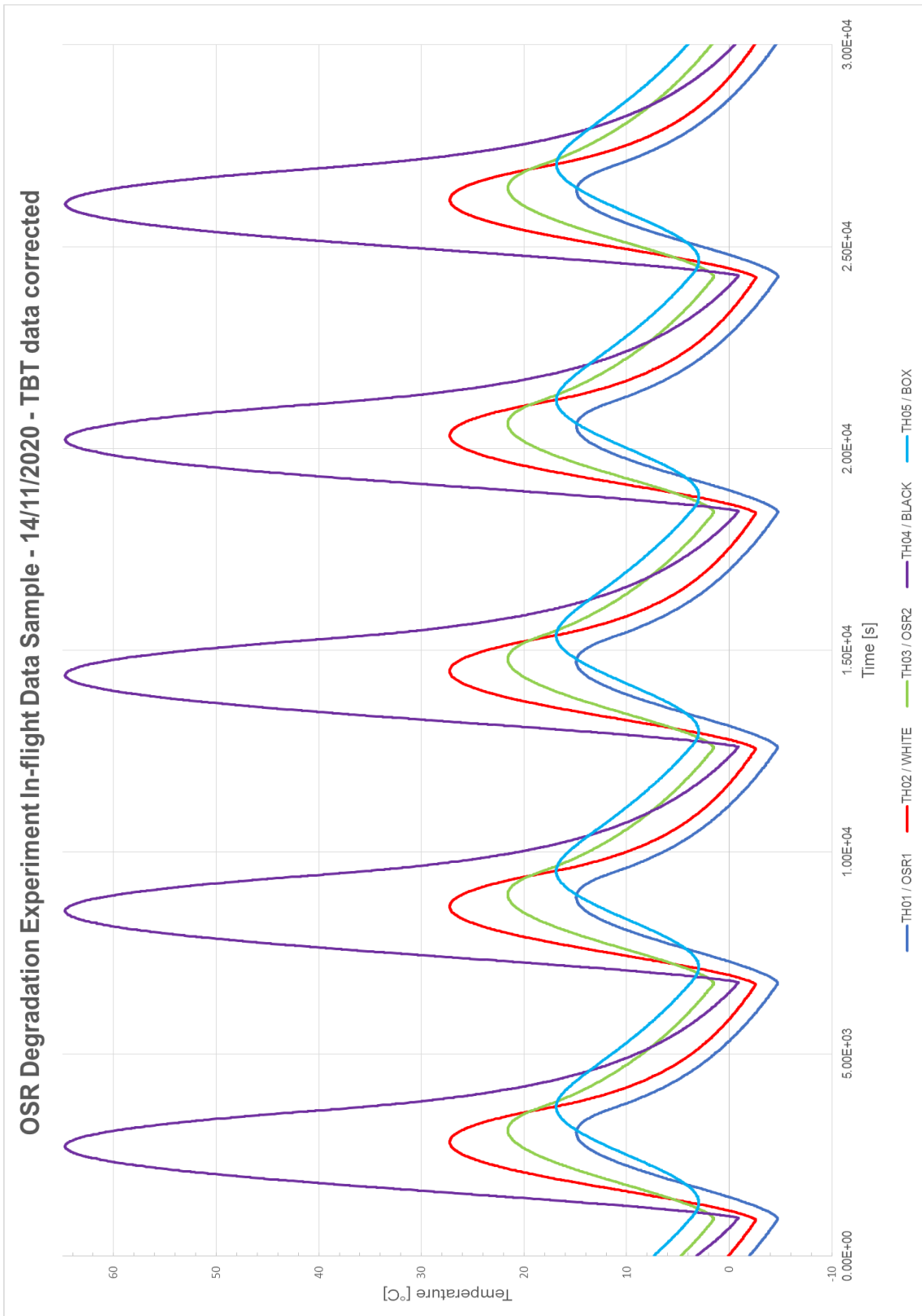Figure H.4 – In-flight telemetry sample from 21/04/2020.

Source: Prepared by the author.

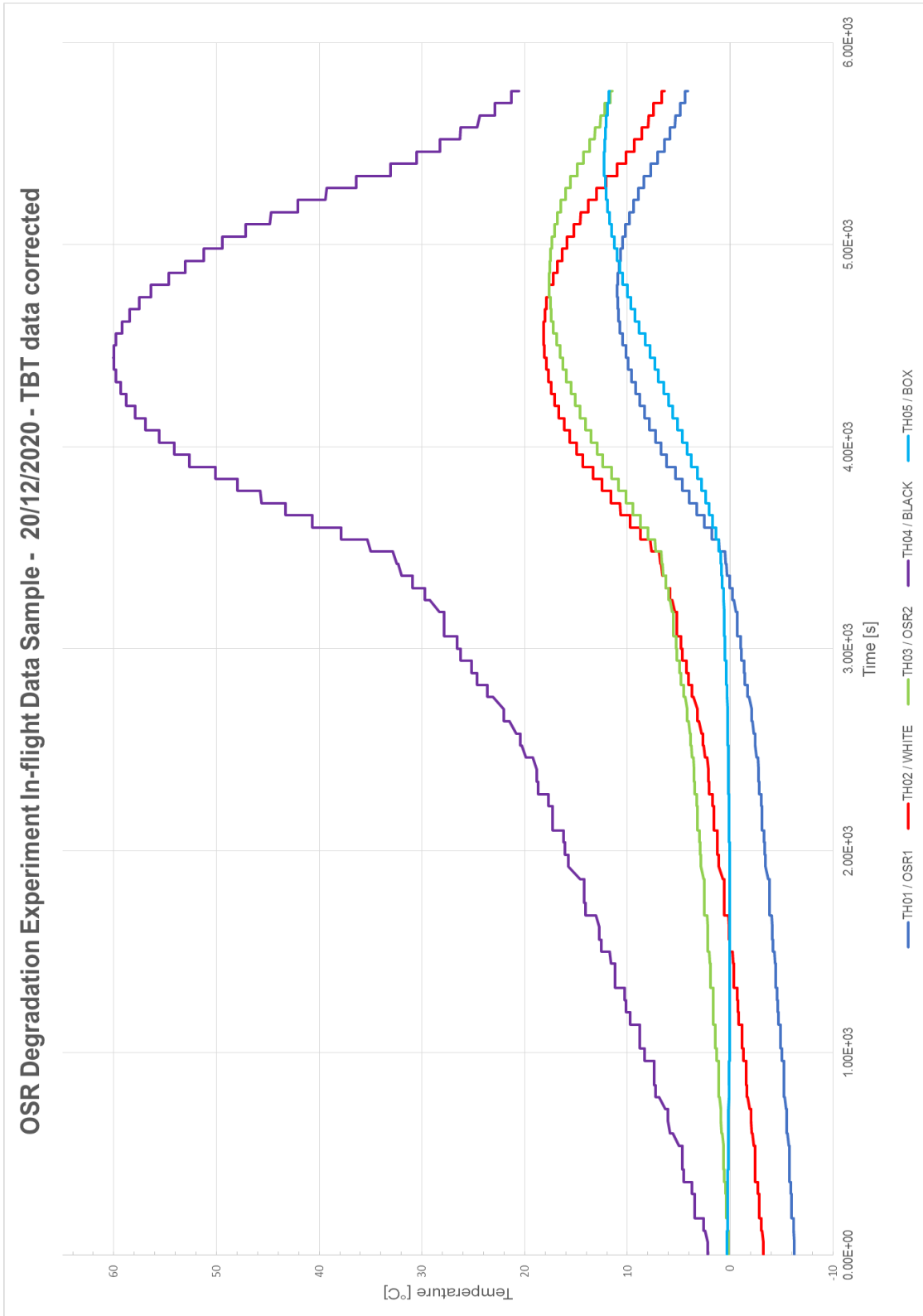Figure H.5 – In-flight telemetry sample from 16/06/2020.

Source: Prepared by the author.

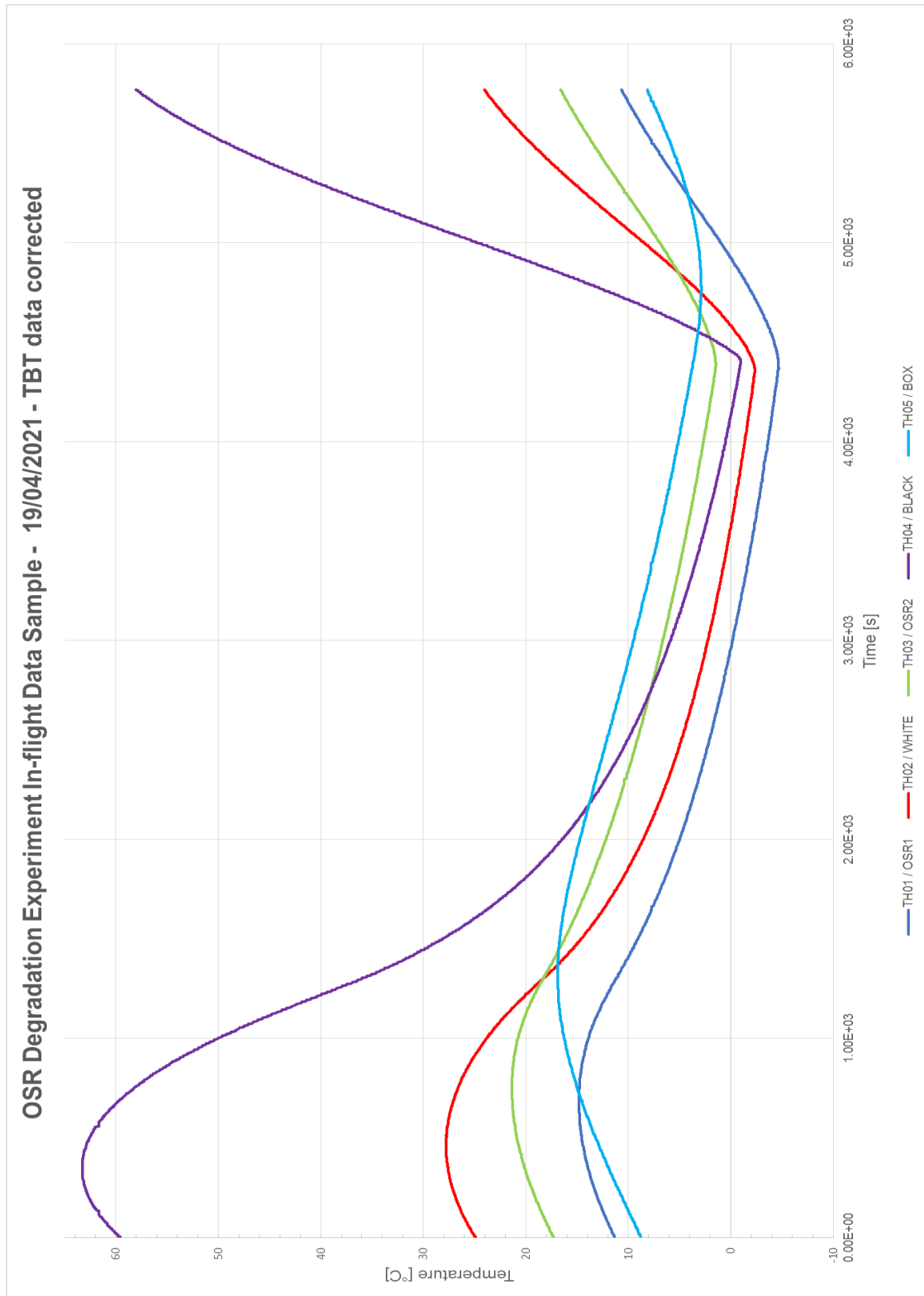Figure H.6 – In-flight telemetry sample from 14/11/2020.

Source: Prepared by the author.

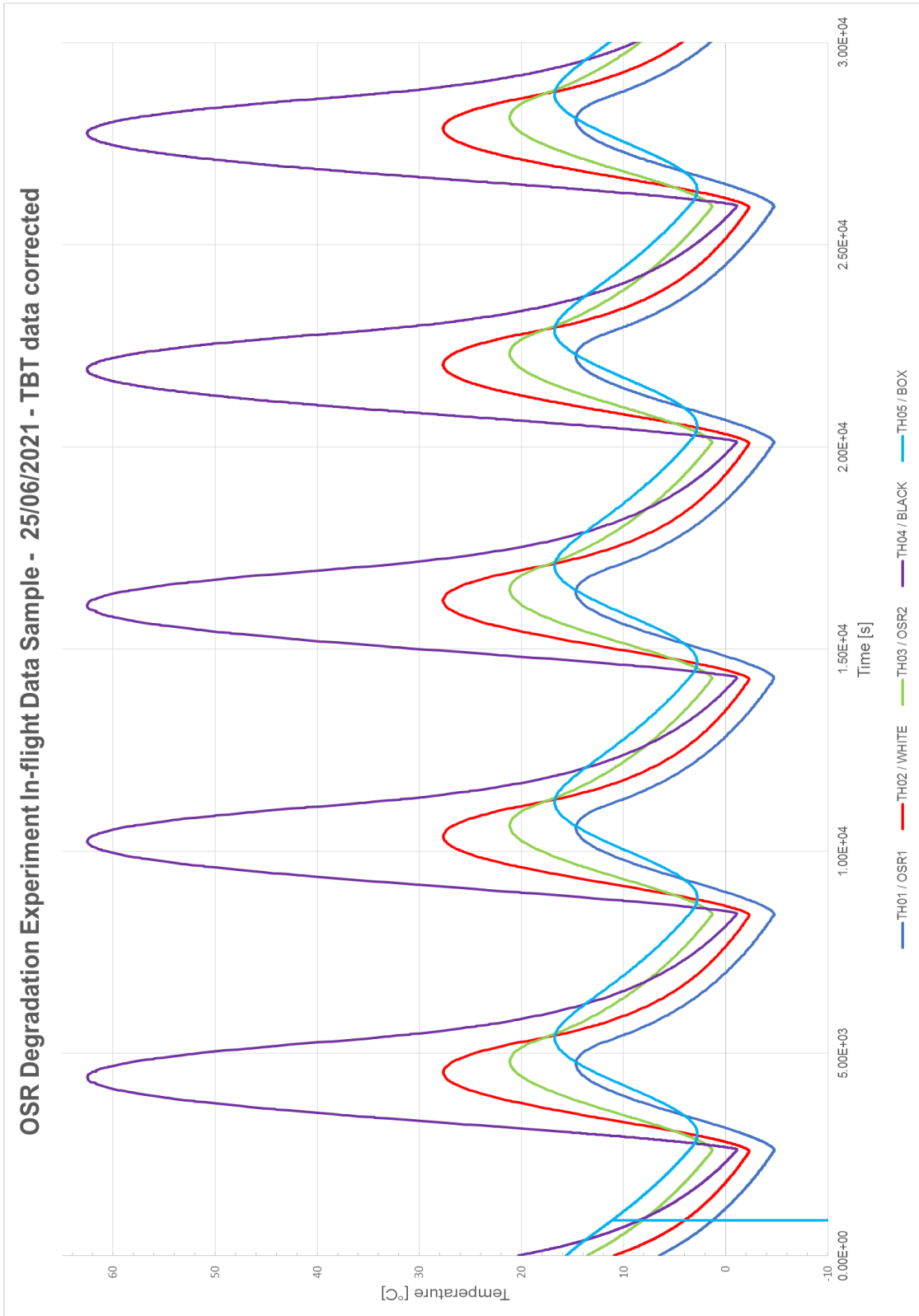Figure H.7 – In-flight telemetry sample from 20/12/2020.

Source: Prepared by the author.

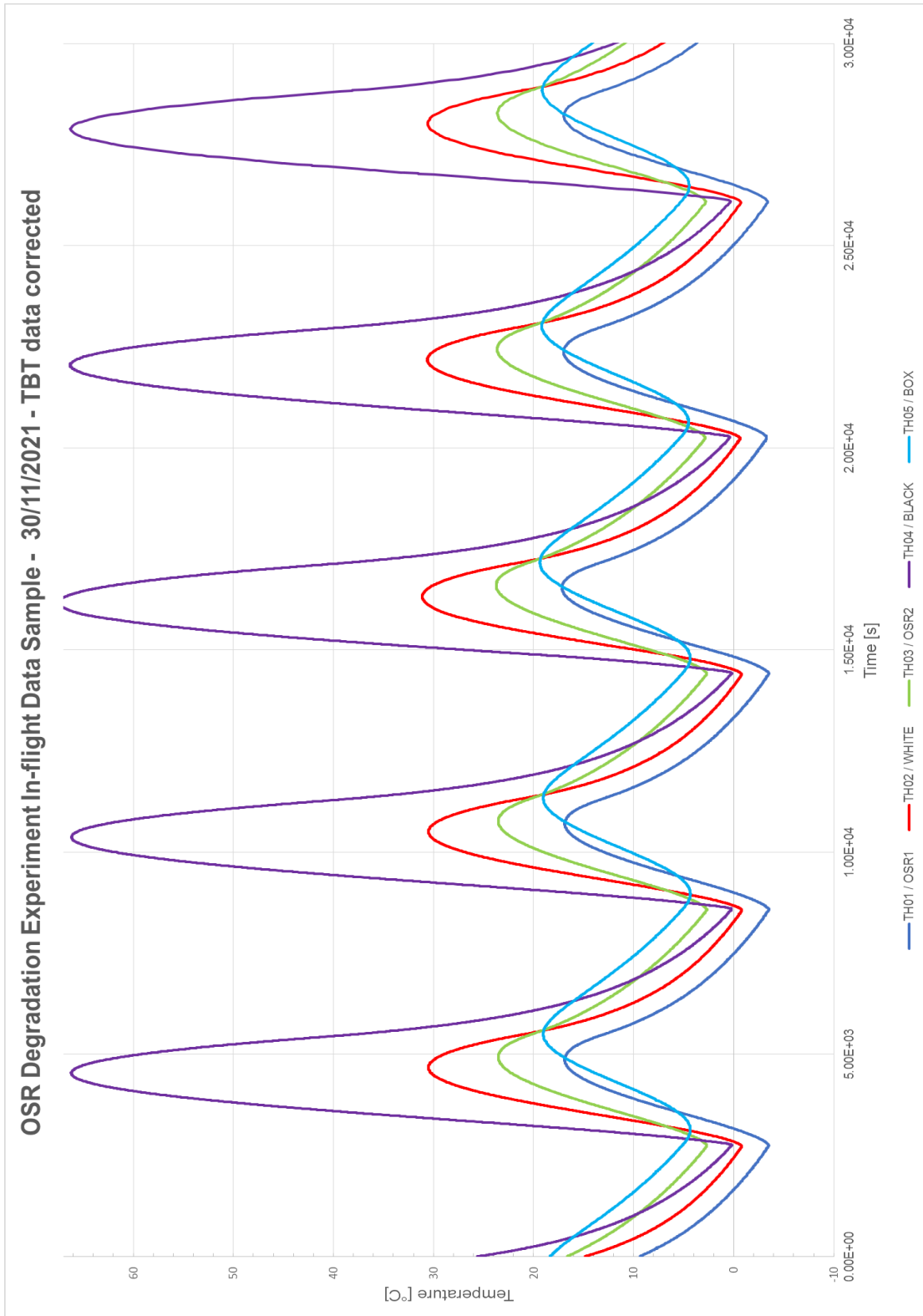Figure H.8 – In-flight telemetry sample from 19/04/2021.

Source: Prepared by the author.

Figure H.9 – In-flight telemetry sample from 25/06/2021.

Source: Prepared by the author.

Figure H.10 – In-flight telemetry sample from 30/11/2021.
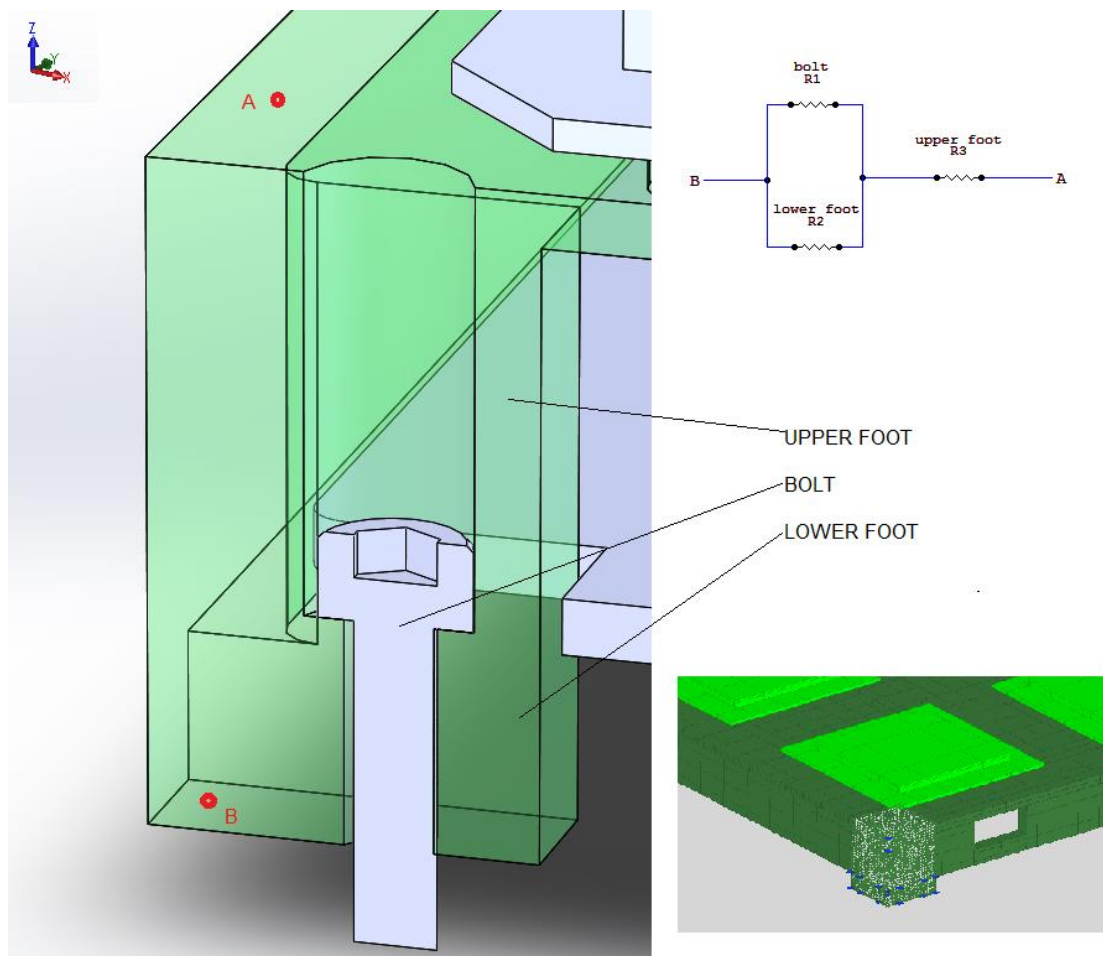

Source: Prepared by the author.

APPENDIX I – EQUIVALENT THERMAL RESISTANCES ESTIMATIONS

The construction of the TMM of a real thermal system requires definition of equivalent properties in the virtual representation. Equivalent resistances were assumed as a means to represent factors such as lack of homogeneity of a solid and presence of interfaces. Precise determination of equivalent resistances were not pursued, but rough estimations were made to kick-start the numerical model setup.

In order to illustrate the adopted procedure, some estimations are presented as follows. Adopting directionality to the estimations was a common practice.

For example, an equivalent thermal circuit between points A and B on the box foot at 'Z' direction can be represented as shown in Figure I.1

Figure I.1 – Foot Thermal Circuit.

Source: Prepared by the author.

Assuming an ideal condition that the bolt is perfectly soldered to the box, the equivalent resistance and conductance to this subset may be calculated as:

$$R_1 = \frac{z_{lower\_foot}}{\kappa_{s\_steel} A_{bolt}} = \frac{0.007 * 4}{(15) * (\pi * 0.004^2)} = 37.136 [K / W]$$

$$R_2 = \frac{z_{lower\_foot}}{\kappa_{FR4} A_{lower\_foot}} = \frac{0.007}{(0.25) * (0.018^2 - \pi * 0.004^2 * 0.25)} = 89.907 [K / W]$$

$$R_3 = \frac{z_{lupper\_foot}}{\kappa_{FR4} A_{upper\_foot}} = \frac{(0.031 - 0.007)}{(0.25) * (0.018^2 - \pi * 0.008^2 * 0.25)} = 350.705 [K / W]$$

$$R_{eq-AB} = \frac{R_1 R_2}{R_1 + R_2} + R_3 = 376.986 [K / W] \rightarrow G_{eq-AB} = 1 / R_{eq-AB} = 2.653 E - 3 [W / K]$$

However, the bolt is not perfectly soldered to the box and its contact to it also produces additional resistances to the real equivalent circuit which were not taken into account.

An additional detail worth noting is that this illustrative procedure only considers the solid bodies, but in reality other factors further enhances the equivalent resistance.

For instance: the torque applied to the bolt produces a pressure in the interface, which influences the thermal coupling. The materials of the interface and finishing of participating surfaces also influence its behaviour. Theoretical models to quantify such influences lack precision and frequently empirical relationships are used instead.

For this reason, it is believed that giving further details regarding the equivalent thermal resistances does not make sense since it depends highly on the real equipment available to future studies. Therefore, if the basic procedure as presented is followed by others while studying the theme, it is possible to achieve reasonable thermal conductances applicable to the peculiar specimen available.